The development of SOFC with perovskite electrodes by co-sintering and co-casting method

Kamil Nowicki

University of
St Andrews

This thesis is submitted in partial fulfilment for the degree of

Doctor of Philosophy (PhD)

at the University of St Andrews

November 2021

Candidate's declaration

I, Kamil Nowicki, do hereby certify that this thesis, submitted for the degree of PhD, which is approximately 69,000 words in length, has been written by me, and that it is the record of work carried out by me, or principally by myself in collaboration with others as acknowledged, and that it has not been submitted in any previous application for any degree. I confirm that any appendices included in my thesis contain only material permitted by the 'Assessment of Postgraduate Research Students' policy.

I was admitted as a research student at the University of St Andrews in September 2017.

I, Kamil Nowicki, received assistance in the writing of this thesis in respect of Y, which was provided by Xiangling Yue.

I received funding from an organisation or institution and have acknowledged the funder(s) in the full text of my thesis.

Date 27/04/2022 Signature of candidate Nowicki Kamil

Supervisor's declaration

I hereby certify that the candidate has fulfilled the conditions of the Resolution and Regulations appropriate for the degree of PhD in the University of St Andrews and that the candidate is qualified to submit this thesis in application for that degree. I confirm that any appendices included in the thesis contain only material permitted by the 'Assessment of Postgraduate Research Students' policy.

Date 27 April 2022 Signature of supervisor

Permission for publication

In submitting this thesis to the University of St Andrews we understand that we are giving permission for it to be made available for use in accordance with the regulations of the University Library for the time being in force, subject to any copyright vested in the work not being affected thereby. We also understand, unless exempt by an award of an embargo as requested below, that the title and the abstract will be published, and that a copy of the work may be made and supplied to any bona fide library or research worker, that this thesis will be electronically accessible for personal or research use and that the library has the right to migrate this thesis into new electronic forms as required to ensure continued access to the thesis.

I, Kamil Nowicki, confirm that my thesis does not contain any third-party material that requires copyright clearance.

The following is an agreed request by candidate and supervisor regarding the publication of this thesis:

Printed copy

Embargo on all of print copy for a period of 1 year on the following ground(s):

- Publication would preclude future publication

Supporting statement for printed embargo request

I wish to publish some of the data from this Thesis in a scientific journal

Electronic copy

Embargo on all of electronic copy for a period of 1 year on the following ground(s):

- Publication would preclude future publication

Supporting statement for electronic embargo request

I wish to publish some of the data from this Thesis in a scientific journal

Title and Abstract

- I agree to the title and abstract being published.

Date 27/04/2022 Signature of candidate Nowicki Kamil

Date 27 April 2022 Signature of supervisor

Underpinning Research Data or Digital Outputs

Candidate's declaration

I, Kamil Nowicki, understand that by declaring that I have original research data or digital outputs, I should make every effort in meeting the University's and research funders' requirements on the deposit and sharing of research data or research digital outputs.

Date 27/04/2022 Signature of candidate Nowicki Kamil

Permission for publication of underpinning research data or digital outputs

We understand that for any original research data or digital outputs which are deposited, we are giving permission for them to be made available for use in accordance with the requirements of the University and research funders, for the time being in force.

We also understand that the title and the description will be published, and that the underpinning research data or digital outputs will be electronically accessible for use in accordance with the license specified at the point of deposit, unless exempt by award of an embargo as requested below.

The following is an agreed request by candidate and supervisor regarding the publication of underpinning research data or digital outputs:

Embargo on all of electronic files for a period of 1 year on the following ground(s):

- Publication would preclude future publication

Supporting statement for embargo request

I wish to publish some of the data from this Thesis in a scientific journal

Date 27/04/2022 Signature of candidate Nowicki Kamil

Date 27 April 2022 Signature of supervisor

Acknowledgements

First of all, I would like to express my gratitude to Prof. John Irvine for taking me into the JTSI group and giving me an opportunity to carry out this work and learn about this extremely interesting and dynamic sector. Thank you for access to a well-equipped laboratory, participation in university life and international conferences, advice, and supervision over my program.

I would like to acknowledge and express my gratitude to Hongyu Zeng, visiting student from Tsinghua University in Beijing, for the work we have done together on the tubular fuel cells. Data obtained from collaborative experiments were used in chapter six to describe the manufacturing and electrochemical testing of tubular cells with composite electrodes. Experimental work with Hongyu inspired new ideas on cell development, described later in the chapter. Also, I would like to thank Hongyu and her supervisors, Shi Yixiang and Ningsheng Cai, for inviting me to visit their University; this exciting trip to China will remain in my memories for a long time.

I would also like to thank all members of the JTSI group for their support, advice, and kindness given to me during my PhD journey. Cristian Savaniu and Paul Connor for advice and discussions and overseeing the proper conduct of experiments. Xiangling Yue, for help in reviewing a final draft of the Thesis. David Miller and Ross Blackley for training on SEM and help with analysis. Candice Mitchell for overseeing the program from the administrative and financial sides, and Julie Nairn for managing the laboratory and helping with practical matters.

Finally, I would like to acknowledge the Engineering and Physical Sciences Research Council for funding [grant number EP/N509759/1];

Aims

Solid oxide cells (SOCs) could become the vital technology in transitioning to a net-zero economy based on hydrogen due to their significantly high efficiency and ability to work in fuel cell and electrolysis mode. However, the high cost and low durability still constrain their full-scale commercialisation, and these challenges are tackled in this project.

The $La_{0.43}Ca_{0.37}Ni_{0.06}Ti_{0.94}O_{3-\gamma}$, (LCNT), a perovskite able to exsolve Ni nanoparticles, proved to be an excellent fuel electrode in high-temperature solid-oxide fuel cells (SOFC); the material could become competitive to a well established Ni/YSZ electrode with many stability issues. Despite showing high performance, the demonstration of cells with an alternative fuel electrode is usually limited to a laboratory scale. In most publications, the research is based on small, well defined planar cells, where the production method involves screen printing of electrodes on YSZ support and multiple thermal cycles. Therefore, the applicability of alternative fuel electrodes remains to be demonstrated in larger devices. The project aims to develop a relatively simple and easy-to-scale manufacturing method for large area SOFC with an LCNT fuel electrode.

The LCNT fuel electrode was used in SOFCRoll and tubular designs. The benefit of SOFCRoll is its very high volumetric surface area, whereas the tubular shape offers a much simpler solution but has smaller electrodes. The simple and easy scalable tape casting and co-sintering method were chosen as the most attractive manufacturing technique.

The report aims to deliver the complete procedures behind the manufacturing and testing of SOFCRoll and tubular SOFC with an alternative LCNT based fuel electrode; in various configurations and assembly. These include the guidelines for material preparation and processing, tapes development, analysis of shrinking profile, cell assembly, set up of electrochemical test, data interpretation and post mortem analysis.

Abstract

The Solid Oxide Fuel Cells (SOFCs) were produced with various geometries by tape casting and co-sintering. Tape casting is a cheap and easily scalable method employed on a large scale for thin layers preparation. In the project, a sequential casting technique was developed where all the function layers in SOFC assembly were cast on each other; co-casting gave a strong interface and reduced electrolyte thickness. Co-sintering further simplified cells manufacturing and reduced processing time and energy demand, making fuel cells more profitable and suitable for mass production. The crucial factor for co-sintering of various-material tapes is to ensure that they have close shrinkage profiles during the sintering step, which usually differ due to individual properties of ceramic materials and pore former's concentration in the slurry. The minor differences create stress between layers, leading to delamination and cracks in the cell's structure. By controlling the composition of the slurry, particle size distribution and sintering temperature, it was possible to produce a cell without any internal structural defects.

The developed method was used to produce SOFC with alternative SOFCRoll geometry and the small tubular cells. SOFCRoll gives the possibility to extend the surface area while keeping the volume low. Up to 27.75 cm^2 of surface area was incorporated in a spiral structure, with a volume of about 2.5 cm^3, thus giving better applicability where size reduction is required and a more robust structure; however, the cell was suffered a performance loss due to complications with the current collection and gas distribution. The structure modification and co-sintering of the current collector with high Ni content into otherwise unavailable part of the cell allowed for optimal use of 12 cm^2 surface area in the smaller version of the cell. Tubular cells are known for their high mechanical and thermal resistance. Tubular cell's surface area was up to 7 cm^2, much lower than in SOFCRoll but more accessible for gas and current collector. The combination of a small tubular design with thermally and redox stable alternative perovskite fuel electrode gave a highly durable device; without noticeable degradation after testing in extreme conditions.

Through the project, composite electrodes were mainly used, co-cast, and co-sintered with electrolyte at 1350 °C. The state-of-art yttria-stabilised zirconia ($Zr_{0.84}Y_{0.16}O_{1.92}$, YSZ) was used as the electrolyte, which offers good performance and commercial availability. The co-sintered active fuel electrode contained the nickel-doped lanthanum calcium titanate ($La_{0.43}Ca_{0.37}Ni_{0.06}Ti_{0.94}O_{3-\gamma}$, LCNT) and YSZ. The co-sintered oxygen electrode was a composite of lanthanum strontium manganate

($(La_{0.8}Sr_{0.2})_{0.95}MnO_3$, LSM) and YSZ. LCNT belongs to the family of new alternative materials proposed to replace highly active but prone to degradation state-of-the-art Ni/YSZ composite. Thanks to its mixed ionic and electronic properties (MIEC) and the possibility of exsolving nickel nanoparticles on its surface, LCNT offers a high activity for hydrogen oxidation whilst possessing great thermal shock and redox resistance as a fully ceramic electrode.

Despite the successful co-sintering of the LCNT/YSZ fuel electrode and LSM/YSZ oxygen electrode into a SOFCRoll and tubular structure, due to limitations related to the sintering temperature and composition, electrodes showed a significant ohmic and polarisation resistance.

In the following experiment, the composite electrodes were replaced. For the development of the next generation of tubular cells, the active material was impregnated into a co-sintered porous YSZ backbone. For impregnated electrodes, LCNT was impregnated on a porous YSZ backbone for the fuel hydrogen side, while on the air electrode, a lanthanum strontium ferrite ($La_{0.8}Sr_{0.2}FeO_3$, LSF). The impregnated electrodes were sintered at a much lower temperature than in state-of-the-art methods, giving more active spatial microstructures with a large surface area. Using this technique in co-sintered cells simplified manufacturing and made a broader range of materials available.

This work contains complete procedures for producing SOFC with various designs, including planar, tubular, and SOFCRoll, by the outlined methods. In addition, it seeks to determine a mechanism of their functionality based on electrochemical tests and DRT analysis.

Legend

List of abbreviations

3PB	triple phase boundary
AFC	alkaline fuel cell
BSE	backscattered electrons
CGO	gaddolinum dopped cerium oxide, $(Ce,Gd)O_{2-\delta}$
CNLS	complex non-linear least squares
CPE	constant phase element
DRT	distribution function of relaxation times
EIS	impedance spectroscopy
FE	fuel electrode
I-V	current-voltage
LCNT	nickel doped lanthanum calcium titanate, $La_{0.43}Ca_{0.37}Ni_{0.06}Ti_{0.94}O_{3-\gamma}$
LCNT/YSZ50	composite fuel electrode (active layer) developed in this thesis, $La_{0.43}Ca_{0.37}Ni_{0.06}Ti_{0.94}O_{3-\gamma}$ (50% vol.)/ $Zr_{0.84}Y_{0.16}O_{1.92}$
LCNT/ P-YSZ	impregnated fuel electrode, $La_{0.43}Ca_{0.37}Ni_{0.06}Ti_{0.94}O_{3-\gamma}$ (50% vol.)/ $Zr_{0.84}Y_{0.16}O_{1.92}$
LSCF	lanthanum strontium cobalt ferrite, $La_{0.6}Sr_{0.4}Co_{0.8}Fe_{0.2}O_{3-\delta}$
LSF	lanthanum strontium ferrite, $La_{0.8}Sr_{0.2}FeO_3$
LSF/ P-YSZ	impregnated oxygen electrode developed in this Thesis, $La_{0.8}Sr_{0.2}FeO_3$ (30% vol.)/ $Zr_{0.84}Y_{0.16}O_{1.92}$
LSM	lanthanum strontium manganate, $(La_{0.8}Sr_{0.2})_{0.95}MnO_3$
LSM/YSZ50	composite oxygen electrode (active layer) developed in this thesis, $(La_{0.8}Sr_{0.2})_{0.95}MnO_3$ (50% mass.)/ $Zr_{0.84}Y_{0.16}O_{1.92}$
MIEC	material with mixed ionic and electronic conductivity
Ni/LCNT50	composite fuel electrode (current collector layer) developed in this thesis, Ni (50% vol.)/ $La_{0.43}Ca_{0.37}Ni_{0.06}Ti_{0.94}O_{3-\gamma}$
Ni/YSZ	state-of-the-art composite fuel electrode, Ni/ $Zr_{0.84}Y_{0.16}O_{1.92}$

Ni/YSZ10	composite fuel electrode (current collector layer) developed in this thesis, Ni (90% mass.)/ $Zr_{0.84}Y_{0.16}O_{1.92}$
OCV	open circuit voltage
OE	oxygen electrode
PAFC	phosphoric acid fuel cell
PEM	polymer electrolyte membrane cell
pO_2	oxygen partial pressure
PSA	particle size analysis
P-YSZ	porous YSZ backbone developed in this thesis, $Zr_{0.84}Y_{0.16}O_{1.92}$
RDS	rate determines step
Redox	reduction-oxidation
SEI	secoundary electron imaging
SEM	scanning electron microscopy
SOC	solid oxide cell
SOEC	solid oxide electrolysis cell
SOFC	solid oxide fuel cell
TEC	thermal expansion coefficient
YSZ	in this thesis 8mol.% yttria doped zirconia, $Zr_{0.84}Y_{0.16}O_{1.92}$
XRD	X-ray diffraction

Notations for SOFCRoll with Ni/YSZ based FE and LSM/YSZ based OE

SRB1-SRB5	the notations for batches of SOFCRoll with Ni/YSZ based fuel electrode

Characteristic of evaluated cells from specified batches:

SRB1	in a batch, cells were prepared strictly following the original method, slurries were tape cast separately and laminated (Figure 4-3 a, Table 4-4).
SRB3	in a batch, cells were prepared with the modified tape's dimension and assembly (Figure 4-3 b, Table 4-4).
SRB5	in a batch, cells were prepared by co-casting, all slurries were cast on previously cast and dry tapes (Figure 4-3 c, Table 4-4).

Notations for SOFCRoll with LCNT based FE and LSM/YSZ based OE

SRB1P-SRB36P	the notations for batches of SOFCRoll with LCNT based fuel electrode

Characteristic of evaluated cells from specified batches:

SRB25P	in a batch, cells were prepared with LCNT/YSZ50 active fuel electrode; and LSM/YSZ50 active and LSM current collector oxygen electrode. Cells were made with the large electrode tapes of 50 cm^2 (Table 5-8), and the co-casting method described in Figure 5-15 a-c.
SRB26P	in a batch, cells were prepared with LCNT/YSZ50 active and Ni/LCNT50 current collector fuel electrode; and LSM/YSZ50 active and LSM current collector oxygen electrode. Cells were made with the large electrode tapes of 50 cm^2 (Table 5-8, Figure 5-16 a), and the co-casting method described in Figure 5-15 a-c.
SRB30P1	in a batch, cells were prepared with LCNT/YSZ50 active and Ni/LCNT50 current collector fuel electrode; and LSM/YSZ50 active oxygen electrode. Cells were made with the small electrode tapes of 24 cm^2 (Table 5-8, Figure 5-16 b), and the co-casting method described in Figure 5-15 d-f.
SRB30P2	in a batch, cells were prepared with LCNT/YSZ50 active and Ni/LCNT50 current collector fuel electrode; and LSM/YSZ50 active oxygen electrode. Additional porous YSZ layer was co-sintered in a spiral part. Cells were made

	with the small electrode tapes of 24 cm^2 (Table 5-8, Figure 5-16 c), and the co-casting method described in Figure 5-15 d-f.
SRB36P	in a batch, cells were prepared with LCNT/YSZ50 active fuel electrode; and LSM/YSZ50 active oxygen electrode. Additional Ni/YSZ10 fuel electrode layer was co-sintered in a spiral part. Cells were made with the small electrode tapes of 24 cm^2 (Table 5-8, Figure 5-16 c), and the co-casting method described in Figure 5-15 d-f.

Table of contents

1 Literature review

1.1 Introduction

This section aims to introduce the reader to the elemental topics related to Solid Oxide Fuel Cells necessary for understanding the experimental part of the report.

The first section of the chapter specifies Climate Change as an imminent security threat, which is the impulse for low carbon energy generation through renewable resources. Next, the mechanism behind the hydrogen economy was briefly summarised, and the role of fuel/ electrolysis cell technology in the net-zero energy system.

The basic principles of thermodynamics and electrochemistry are explained next, e.g. Gibbs energy, Nernst potential and polarisation. Comprehending these topics is crucial for interpreting information from electrochemical analysis, where the main techniques are current-voltage characteristic (I-V), impedance analysis (EIS), which are also characterised in this part.

For the SOFC study, it is necessary to understand the functionality of its components, which include oxygen ion conductive electrolyte, fuel and oxygen electrode. The functionality of materials is outlined by analyzing the state-of-art YSZ electrolyte, Ni/YSZ fuel electrode and LSM/YSZ oxygen electrode. Also, special attention was given to perovskite and functionality in SOFC technology and possible applications as the fuel electrode.

The most common SOFC geometry was characterised in the last subchapter, including planar and tubular construction. Prons and cons of both types were highlighted as manufacturing methods. Finally, the functionality and previous development of SOFCRoll were discussed.

1.2 The energy sector

1.2.1 Climate Change

The expansion of industry and growing population have been requiring increasing demand for heat and power. For generations, energy systems have been based on stationary power plants and internal combustion engines run on fossil fuels. The efficiency of energy production from fossil fuels is limited by thermodynamics and technological limitations. As a result, the significant consumption of fossil fuels triggers the energy crisis due to the depletion of natural resources. Moreover, highly carbon-intensive industrial methods affect the natural environment, e.g. contamination of air, water, and soil, causing the so-called greenhouse effects that are emerging mainly due to the increase in the concentration of carbon dioxide in the atmosphere. The effects are related to the absorption of the solar energy by CO_2 that reaches its atmosphere, leading to rising global temperature (Figure 1-1).

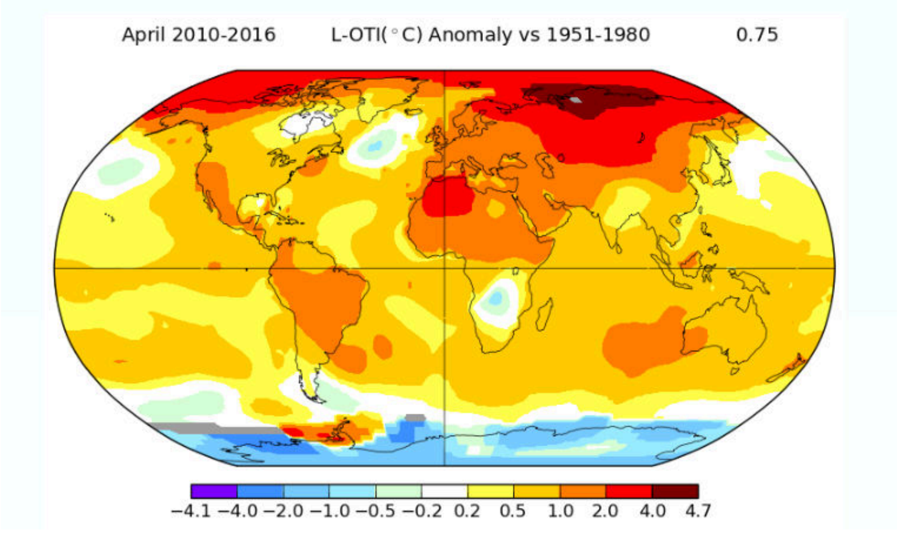

Figure 1-1: The ten-year average temperature anomaly concerning 1951-1980 [1].

Greenhouse gases, primarily CO_2 (more than 80%) and methane (more than 10%), in the overwhelming majority, come from the burning of fossil fuels, but also other human activities such as industry, agriculture, and deforestation [2]. The level of CO_2 in the air atmosphere has increased by more than 45% since the mid-1800 [3]. Global warming tremendously affects the ecosystem and brings all kinds of natural disasters, including storms, floods, droughts, heatwaves, and other weather extremes that directly and indirectly harm animals, crops, and people's communities [4]–[6]. Further increase in temperature is expected to bring even more harmful impacts [7], and global action is needed to protect humanity against this scenario.

Currently, the global average temperature is around 1 °C above pre-industrial times [8]. Under the Paris Agreement, almost every nation signed a declaration to keep global warming well below 2 °C. However, despite these bold declarations, under current actions, the Earth is predicted to warm to around 3 °C by 2100 [9], [10].

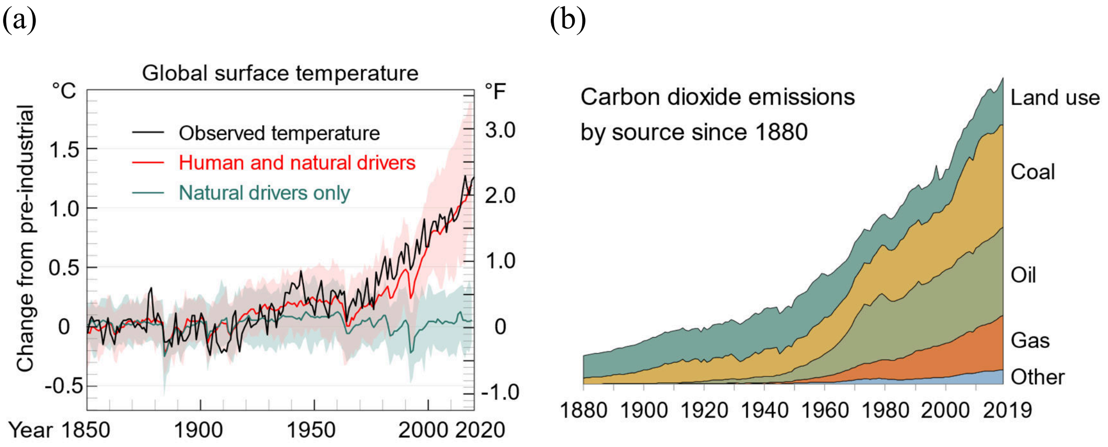

Figure 1-2: (a) The annual average of the change in global surface temperature (annual average), observed and average [11], [12]. (b) Carbon dioxide emissions by source since 1880 [13], [14].

On top of the disasters related to global warming, the world faces challenges associated with the deterioration of air, water, and soil quality that endangers the ecosystem and habitats. Air poisoning is the greatest direct danger to human life. The burning of fossil fuels is associated with the emission of particular airborne matter, which has a massive contribution to the mortality rate [15]; burning fossil fuels was related to 8.7m deaths in 2018 only [16].

In the approach countries adopt, emission reduction mainly relies on developing and implementing low-carbon technologies, e.g., energy generation by renewable resources, energy-efficient technologies, carbon sequestration and storage. As a result, there is a trend in the global economy to move into the “green alternative” as an energy source. Renewable energy systems are becoming essential parts of the economy with rapid growth every year; in 2018, about 63% of newly installed energy capacity was renewable [17]. The global share of renewable energy increases every year and has jumped to 28% in 2020 [7].

Renewable energy derives from processes naturally reoccurring in the environment; they include wind, solar, wave, tidal, fall of water and bio-gas [18]. As the alternative to fossil fuels, their resources renew in the natural processes, practically making them inexhaustible. Most importantly, renewables can substantially decrease the emission of harmful substances to the environment, such as CO, CO_2, VOCs, NO_X, SO_X gases, dust and the generation of various waste products. Renewable energy sources also contribute to the diversification of income sources for producers and farmers, regional economic development, or national energy security. They create an opportunity to reduce fossil fuel imports from politically unstable regions, improve the country’s independence and security, achieve progress in the diversification of energy supply, and reduce dependence on the growth of oil and gas prices.

1.2.2 Hydrogen economy

Renewable energy is more unpredictable in terms of energy supply, as the amount of generated power depends on such factors as time of the day/ year and weather. The changing world's energy supply requires storing capacities to buffer their irregular productions and demand. The vital strategy to support an energy sector based on carbon-neutral technologies is to use hydrogen as the energy carrier to connect individual consumers. Storing energy in the form of hydrogen or hydrocarbons seems to be a desirable option [19]. It doesn't require a large battery capacity, and green fuels produced from hydrogen can be distributed through existing infrastructure, improving the energy system's efficiency and flexibility. Besides the energy storage for electricity generation in stationary power plants, hydrogen could also be injected into a gas grid, used to fuel vehicles, or as the input for the chemical industry and production of synthetic hydrocarbons. Such hydrogen would be "green", as produced through renewable energy from water electrolysis or "blue", produced by traditional methods supplemented by carbon storage [20], [21].

For electricity management, the electrolysers could transfer the electricity surplus into H_2 gas and fuel cells to generate electricity when needed. Among various technologies, the most mature type are alkaline electrolysers, the cheapest option at the moment, and perhaps that is why they dominate the market [22]. The PEM (polymer electrolyte membrane) electrolysers are becoming more popular due to their ability to adapt to variable conditions and improve efficiency. Still, their electrodes use precious metals to catalyse the reaction, which could become a bottleneck to the low-carbon energy technologies' supply chain [23]. Solid Oxide Cells (SOC) only start appearing on the market as commercial solutions, but they can offer the highest efficiency and don't require precious metals due to high operating temperature.

The hydrogen economy to be prosperous must be economically feasible, which, apart from the price of technology itself, depends on the cost of energy from renewable resources. Currently, hydrogen is mainly used as the feedstock for oil refining and chemical industry and, in large part, is produced from fossil fuels, mainly gas and coal. The natural gas reforming and coal gasification used for H_2 production are carbon-intensive but are still the most economical option [22]. The price of hydrogen produced from fossil fuels mainly depends on the cost of natural gas and CO_2 emission; in Europe, it is around 1.5 €/kg, with carbon storage at about 2 €/kg. In comparison, the "green hydrogen" prices generated from renewable resources vary between 2.5-5.5 €/kg [22]. Thus, for green hydrogen to become more competitive, the consumption of fossil fuels must become less profitable.

On the other hand, the cost of electrolysis has to be reduced through the technology development and introduction of system solutions to the energy market. The realisation of these postulates largely depends on governments activities, which take the central role in developing and widespread low carbon technologies; it must create the right environment for future investments through the policy objectives focused on decarbonisation. The price of electrolysis has been reduced by 60%, and a further 50% cost reduction is anticipated by 2030. However, through traditional methods coupled with carbon storage technology, hydrogen production is expected to stay as the main route, which finally would become less economically feasible due to an increase in the price of CO_2 storage [20].

Europe alone has adopted a very ambitious strategy, placing hydrogen as one of the pillars in the transition to clean energy that assumes the minimum reduction of 50% of greenhouse gases emission until 2030 and a carbon-free economy by 2050. Investment in hydrogen would contribute to the creation of new jobs and faster economic recovery from the Coronavirus crisis, so-called "green recovery" [20], [24]. Similarly, the US [25], Canada [26], Australia [27] and East Asia [22] have adopted suitable hydrogen implementation strategies.

The European Strategy is an excellent example of how the hydrogen economy could be gradually implemented. In the first phase, electrolysers would produce hydrogen from renewable energy, mainly from wind and solar, to meet the demand for hydrogen, which today comes primarily from the industry. Ideally, large electrolysers would be installed at industrial centres with a need for hydrogen and powered directly by renewable resources. In the next phase, the production of green hydrogen is anticipated to become more cost-competitive; technology will achieve some maturity. It would play a more prominent role in the energy system, e.g. by processing the surplus of electric energy into hydrogen, or balancing its demand, making it more flexible, e.g. through the possibility of hydrogen storage and transport on large distances. Finally, the technology is expected to reach maturity and be deployed in all carbon-intensive sectors. It is assumed that a quarter of generated renewable energy could be consumed to produce hydrogen [20].

Hydrogen also plays an essential part in the UK decarbonisation strategy as the most cost-effective option [21]. In terms of technology capabilities, the country's asset mainly lies in many patents and high-impact publications, showing the UK Universities' critical role in supporting those innovative technologies [21]. The UK government aims to increase its H_2 production capability to 5 GW by 2030, supporting over 9000 jobs and estimates to attract over £4 billion in co-investment with the private sector. In other estimation, the hydrogen economy could contribute to the creation of 100 000 jobs and generate up to £13 billion in revenue by 2050 [28].

Scotland independently pursues a net-zero emission by 2045 and a 75% reduction by 2030 [29]. In its activities, the Scottish government has also issued a policy on hydrogen. It ensures that it will become a key element in the decarbonisation of the Scottish economy and has set a target of 5 GW of low-carbon hydrogen by 2030 [30]. Hydrogen production will primarily be based on renewable energy produced from wind farms. Scotland owns about 25% of wind resources in Europe and has 1 GW of installed offshore wind farms and plans to expand to 11 GW by 2030; and also has 8.4 GW of onshore wind capacity. Besides, the country has a skilled workforce in the Energy sector and has already demonstrated several hydrogen projects. In the most ambitious scenario, in addition to the use of H_2 in the country, the possibility of exporting the superannuation of green hydrogen to European countries is envisaged. For research and development purposes, the Scottish government intends to allocate 100 million pounds for 2021 – 2026 [30].

1.3 SOFC – working principle and the basics of electrochemical characterisation

1.3.1 Fuel cell technology

The fuel cells are the electrochemical device that converts chemical energy embodied in the gas directly into electricity through a redox process [31]. The fuel cell as a battery is an electrochemical cell to generate power; however, instead of storing chemical energy, they work on a constant fuel supply. The half-cell reactions occur on the porous electrodes (separated by the ion conductive membrane), where hydrogen is usually the fuel, while oxygen from the air is an oxidising agent. This technology can generate an energy current from H_2 and even other fuels containing carbon [32] without an intermediate step – combustion; bypassing the carbon cycle increases process efficiency [33]. Fuel cells with very low CO_2 emissions and other harmful substances, including NOx and SOx, are more beneficial in converting fossil fuels to electric energy than conventional power plants do.

The electrochemical cells are truly flexible devices which may revolutionise the energy sector which we know today. Apart from cleaner and more efficient energy generation, they also allow storing of energy through electrolysis when the current is reversed.

The theoretical functionality of the fuel cells was first introduced by the German chemist Friedrich Schonbein in 1838. In 1839, William Grove successfully experimented with energy generation from the fuel cell system [34]. Through his experiment with two platinum electrodes submerged in diluted sulphur acid and sealed under a hydrogen and oxygen atmosphere, the author noticed that connecting the electrodes by voltameter raised the liquid level in the hydrogen compartment. In 1942 William Grove developed his first working fuel cell that generated energy from H_2 oxidation; he also conducted a reversible reaction and showed that H_2O could be turned into H_2 and O_2 by providing electrical current [35], which today is the basis for energy conversion through water electrolysis. In 1932, Francis Bacon invented the first alkaline fuel cell (AFC) with the nickel fuel electrode; the developed system generated 5 kW of electric power. The AFC were the first fuel cells used in the actual application. NASA, since 1960, had successfully incorporated alkaline and polymer membrane fuel cells into the space technology for the Apollo and Space Shuttle missions [36], [37].

Nowadays, various kinds of fuel cells are exploited; they differ in such characteristics as materials, operating conditions and fuel being used to generate the current [38]. The first group of fuel cells can operate at relatively low temperatures. Polymer Electrolyte Membrane (PEM) Fuel Cell has a polymer electrolyte (e.g. Nafion) that can conduct H^+ proton and has about 60% efficiency for direct energy generation from H_2 [39] and 40% efficiency for reformed fuel [40]. PEMs work at low operating temperatures (below 100 °C); hence they become attractive for transport or portable application to assure quick start-up/ turn-off. The low operating temperature also brings fewer problems with materials and their selection. However, they use expensive noble metals as catalysts, which are not resistant to impurities. AFC uses the porous medium saturated with an alkaline solution as the electrolyte, e.g. KOH, where the charge carrier are OH^- ions. AFC also can operate below 100 °C and has an efficiency of up to 60% [41]. They are popular due to the low cost of manufacturing and the wide range of materials. Still, they are sensitive to CO_2, and there are management problems with the liquid electrolyte. Phosphoric Acid Fuel Cell (PAFC) fuel cells use phosphoric acid as the electrolyte where the charge carrier is H^+ proton; similarly, as in AFC, the liquid electrolyte is introduced into porous media or membrane. The range of operating temperature is between 150 °C and 200 °C. PAFCs was developed in early 1960, and since then, they have had a long history of application, typically for stationary power generation [38]. The platinum catalyst in PAFCs is more tolerant to CO_2 and CO than in AFCs, due to higher operating temperature; therefore, it broadens the choice of fuels. On the other side, they are much less sensitive to sulphur than PEM or AFC.

Molten carbonate fuel cells (MCFC) and SOFC belong to a high-temperature group of fuel cells. MCFC uses molten carbonates in porous media such as molten lithium, sodium or potassium carbonates. The MCFC usually operates at a temperature between 600 °C and 700 °C and could achieve 60% chemical conversion efficiency to electrical.

In contrast, SOFC uses a solid electrolyte made of ionically conductive ceramics. The operation temperature in SOFC is even higher (up to 1000 °C) due to the limitations of solid electrolytes at a lower temperature; the efficiency of power generation in SOFC could exceed 60% if generated heat is captured and reused, the actual efficiency could be higher.

1.3.2 *Principles of operation in SOFC*

SOFC comprises three essential ceramic elements, a gas-tight ion-conducting electrolyte and two porous electrodes on opposite sides, with electrochemical activity for the redox process [42], [43]. In the state of the art devices, the yttria-stabilised zirconia ($Zr_{0.84}Y_{0.16}O_{1.92}$, YSZ) is used as dense oxygen ion conductive electrolyte, Ni/YSZ composite as the fuel electrode and LSM/YSZ composite ($La_xSr_{1-x}MnO_3$ - $Zr_{0.84}Y_{0.16}O_{1.92}$) as the oxygen electrode [31], [44]. SOFC has a solid ceramic electrolyte to conduct oxygen ions from cathode to anode placed between two porous electrodes.

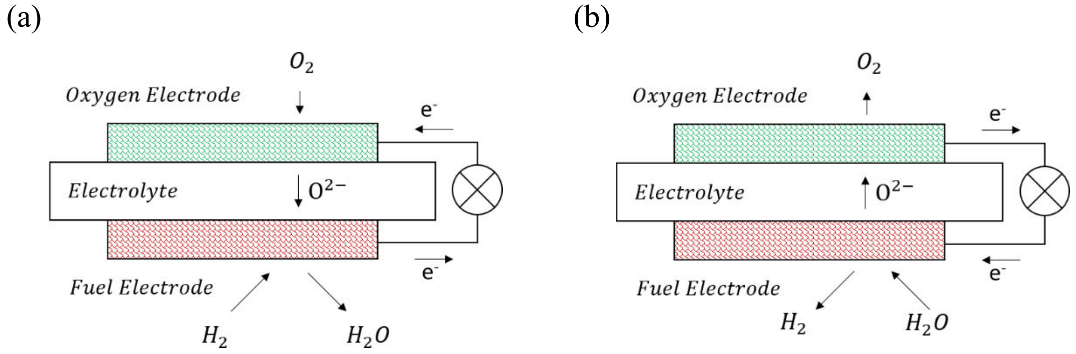

Figure 1-3: Solid Oxide Cell (SOC) reversible operation. (a) Fuel Cell (FC) mode. (b) Electrolysis Cell (EC) mode.

During the fuel cell operation, oxygen ions are generated on an electrochemically active oxygen electrode, and travel to the fuel electrode, where they participate in the electrochemical oxidation of fuel, which in this example is hydrogen, Figure 1-3 a. Electrodes must be porous to allow for a gas transfer and have well developed triple phase boundary (3PB) where gas, the ionically conductive media and electric conductor meets to fulfil conditions for the electrochemical reaction [44]. If the current is reversed, the cell works in electrolysis mode (Solid Oxide Electrolysis Cell, SOEC), and the current is being consumed to produce H_2 and O_2 gas from the H_2O splitting reaction Figure 1-3 b.

The whole mechanism for SOFC could be reduced to simple reactions:

$$\frac{1}{2}O_2(g) + 2e^- \leftrightarrow O^{2-}$$ **(air side)** **Equation 1-1**

$$H_2(g) + O^{2-} \leftrightarrow H_2O(g) + 2e^-$$ **(fuel side)** **Equation 1-2**

$$H_2(g) + \frac{1}{2}O_2(g) \leftrightarrow H_2O(g)$$ **(overall reaction)** **Equation 1-3**

The ceramic electrolytes used in SOC require high temperatures to achieve ionic conductivity sufficient for the cell's operation. The cells with state-of-the-art yttria-stabilised zirconia (YSZ) electrolyte usually operate in the temperature range between 700 °C – 1000 °C, depending on the application, microstructure, and other materials being used [31]. Such a temperature makes ceramic cells challenging to adapt to specific operating conditions, such as small portable or transport applications, and brings several issues related to their stability [45]. On the other side, at SOFC operating conditions in a high temperature, the activation energy for electrochemical reaction on the electrodes is lower; hence, noble metal catalysts are not required, making SOFCs cheaper and more resistive to poisoning. The advantage of the oxygen-ion conductive membrane, rather than proton conductive, and the higher temperature is the possibility of using a whole range of fuels other than hydrogen, including higher hydrocarbons [46], [47], carbon oxide [48], and even coal [49].

Theoretically, SOFC can achieve more than 60% efficiency in chemical-to-electrical conversion in operational conditions, and efficiency is defined as the ratio of Gibbs energy and enthalpy for the reaction [50]. Additionally, if the heat from SOFC operation is utilised, the theoretical efficiency could increase to 90% [31], [51]. The heat from exothermic fuel oxidation can be reused for maintaining the operating temperature of SOFC itself, for parallel processes, e.g., the endothermic reforming of hydrocarbons, or can be treated as a product from the so-called combined heat and power generating unit (CHP) or to power a gas turbine to produce electricity in the hybrid system, [52]. The SOFCs have many advantages in comparison to other types of fuel cells. A common problem with the fuel cells with the liquid electrolyte is management and corrosion in other cell parts. The SOFC is made of solid components which don't bring such difficulties.

1.3.3 Thermodynamics of SOFC

The Gibbs free energy, $\boldsymbol{G}$ [53], is the chemical energy of the system available to do work. At given conditions, $\boldsymbol{G}$ is the sum of the chemical potential of system components, $\boldsymbol{\mu}$, multiplied by their molarity $\boldsymbol{N}$ [54]:

$$\boldsymbol{G = \mu_1 N_1 + \mu_1 N_1 + \cdots \mu_n N_n} \qquad \textbf{Equation 1-4}$$

Where $\boldsymbol{\mu_1, \mu_2, \ldots \mu_n}$ and $\boldsymbol{N_1}$, $\boldsymbol{N_2}$, $\ldots\boldsymbol{N_n}$ are the chemical potential and number of moles of a specific component. The chemical potential of the element determines its thermodynamics, e.g. their tendency to change, like stability, reactivity or migration; thermodynamically, the Gibbs free energy is defined as:

$$\boldsymbol{G = H - TS} \qquad \textbf{Equation 1-5}$$

T is the temperature of the system, $\boldsymbol{S}$ is entropy, $\boldsymbol{H}$ is enthalpy, defined as:

$$\boldsymbol{H = U + pv} \qquad \textbf{Equation 1-6}$$

Where $\boldsymbol{U}$ stands for the internal energy, $\boldsymbol{p}$ for pressure, $\boldsymbol{v}$ for volume.

To see how Gibbs free energy changes when the system parameters are changed above function could be differentiated [55], and with the use of the first and second laws of thermodynamics for an ideal gas, Gibbs free energy under certain conditions could be expressed by:

$$\boldsymbol{G = G^0 + RTln(\frac{p}{p^0})} \qquad \textbf{Equation 1-7}$$

$\boldsymbol{T}$ is the temperature in K, $\boldsymbol{R}$ is the universal gas constant, 8.314J K^{-1} mol^{-1}, $\boldsymbol{G^0}$ is the Gibbs free energy at standard conditions and pressure $\boldsymbol{p^0}$. The standards values are lower integration constants; they result from the fact that the system is arbitrary [55].

The free energy change $\boldsymbol{\Delta G}$ is the difference of free energy between the product of the reaction and reactants. If the free energy of the product is lower than that of the reactants, it will become the driving force of the reaction. As an example, the chemical reaction for hydrogen oxidation could be considered:

$$\boldsymbol{H_2(g) + {}^1\!/_2\, O_2(g) \leftrightarrow H_2O(g)}$$ **Equation 1-8**

In standard conditions (25 °C, 1 atm), the free energy both for oxygen and hydrogen is 0, while for water is −228.61 kJ mol^{-1}, using the equation

$$\boldsymbol{\Delta G = G_{H_2O} - G_{H_2} - G_{O_2}}$$ **Equation 1-9**

The free energy change in standard conditions ΔG^0 for Eq. 1-9 is −228.61 kJ mol^{-1}; the negative sign means that the reaction is spontaneous.

In SOFC, the oxygen and hydrogen compartments are separated by an oxygen ion conductive membrane. Potential E resulting from the chemical potential of species at both sides of the cell is defined as the decrease in Gibbs free energy per coulomb of charge transfer, which leads to the relationship:

$$\boldsymbol{E = \frac{\Delta G}{-zF}}$$ **Equation 1-10**

E is the cell's potential, z is the number of electrons in reaction, F is Faraday’s constant 96485C mol^{-1}. In general, E represents the reversible work associated with moving charged particles from the region at higher pO_2 to lower [48] and becomes a driving force for the process.

Equation 1-7 and Equation 1-10 give the so-called Nernst equation, which takes the form:

$$\boldsymbol{E = E^0 - \frac{RT}{zF} ln(\frac{p_{anode}}{p_{cathode}})}$$ **Equation 1-11**

Where p_{anode} and $p_{cathode}$ correspond to oxygen activity at both sides of the cell, while E^0 is a potential in standard conditions.

The introduction of the electrochemical potential $\bar{\mu}$, could explain the flux of the carrier j in SOC, which is proportional to the already mentioned chemical potential μ and electrostatic potential of charged particles $\boldsymbol{\Phi}$, $\boldsymbol{z}$ is the charge number and $\boldsymbol{F}$ Farraday constant [56], [57]:

$$\bar{\boldsymbol{\mu}}_j = \boldsymbol{\mu}_j + \boldsymbol{zF\Phi}_j \qquad \textbf{Equation 1-12}$$

At open circuit conditions (open-circuit voltage, OCV), the difference of electrochemical potential between electrodes is spatially constant, while the external voltage will result in an electrochemical potential gradient $\boldsymbol{\nabla\bar{\mu}}$ and net flux of charge carriers $\boldsymbol{j}$ will be expected, as the system always strives to equilibrium. For steady-state mass flow under an electrochemical gradient, the driving force could be either chemical or electric [57], [58]. The flux of charged particles will be proportional to the gradient of the electrochemical potential in the electrochemical cell and could be expressed by the fundamental transport equation [56]:

$$\boldsymbol{J}_j = \frac{\boldsymbol{\sigma}_j}{\boldsymbol{z}_j^2\boldsymbol{e}^2}\boldsymbol{\nabla\bar{\mu}} \qquad \textbf{Equation 1-13}$$

Equation 1-13 is derived from the general transport equation and could refer to any particles (either neutral or charged) being under a potential gradient. The particular case of eq. 1-13 is Ohm's law when the spatial gradient of chemical potential $\boldsymbol{\nabla\mu}$ is 0 and Fick's law of diffusion for $\nabla\Phi = 0$ [57]. In the equation, $\boldsymbol{z}$ is the charge number, $\boldsymbol{e}$ the elementary charge, while $\boldsymbol{\sigma}_i$ is a total electric conductivity of the material, which is proportional to the total concentration of charge carrier $\boldsymbol{c}$ in material and mobility of particles $\boldsymbol{u}$:

$$\boldsymbol{\sigma}_i = |\boldsymbol{z}_i|\boldsymbol{c}_i\boldsymbol{e}\boldsymbol{u}_i \qquad \textbf{Equation 1-14}$$

In solid conductors, the charged particles could be electronic particles (eon) or ionic defects (ion); when the transport in solid is considered, one kind of particle is usually more mobile, and the partial lattice of immobile species is taken as the reference. For the mixed conductors, the electrical conductivity is treated as the sum of both electronic and ionic species, transported independently of each other [57], [58]:

$$\boldsymbol{\sigma}_i = \boldsymbol{\sigma}_{ion} + \boldsymbol{\sigma}_{eon} \qquad \textbf{Equation 1-15}$$

1.3.1 Electrode kinetics and impedance analysis

The electrochemical process on the electrode consists series of steps. Usually, starting with the diffusion of gases into/from the vicinity of active material, next is adsorption/desorption and formation and transport of intermediate species for charge transfer reaction. The kinetic of each step partially contributes to the polarisation losses of the cell, which mainly depends on operational conditions (e.g. temperature, gas atmosphere, pressure, an applied voltage) and the properties and structure of the cell's electrodes (e.g. catalytic activity, the electronic and ionic conductivity of materials, their thickness and microstructure).

The impedance spectroscopy (EIS) is a transient-response technique used to test cells electrochemically [59]–[61]. EIS can be used to separate processes occurring at various speeds (frequency), giving insight into their kinetics, which is especially important when determining the direction of cell optimisation; for example, the rate determines step (RDS) and how changing conditions or structure modification will affect it. In the method, a small sinusoidal signal, either at known current $i(t)$ or voltage $v(t)$, is imposed on the system at fixed bias, e.g. at 0 that is open voltage conditions or any other "operation point" ((I_x, U_x) in Figure 1-4 a). A sinusoidal signal is written by the equation:

$$u(t) = u_0 \sin(\omega t + \varphi(\omega))) \qquad \textbf{Equation 1-16}$$

$$i(t) = i_0 \sin(\omega t) \qquad \textbf{Equation 1-17}$$

Where u_0 and i_0 is the amplitude of the applied voltage or current, ω is the angular frequency, while $\varphi(\omega)$ is a frequency-dependent face shift between AC voltage and current. The excitation signal should trigger a system response without affecting its equilibrium or steady state. At specific voltage amplitude u_0, the corresponding current response, $i(t)$, is recorded, and their ratio is presented as complex impedance $Z(\omega)$ is expressed as the imaginary z_{im}, and the real z_{re} part on a complex impedance chart called Nyquist plot (Figure 1-4 b), (j is an imaginary unit).

$$Z(\omega) = {u(t)}/{i(t)} = {u_0(\omega)}/{i_0}\, e^{j\varphi(\omega)} = |Z(\omega)|e^{j\varphi(\omega)} = Re\{Z(\omega)\} + jIm\{Z(\omega)\} \qquad \textbf{Equation 1-18}$$

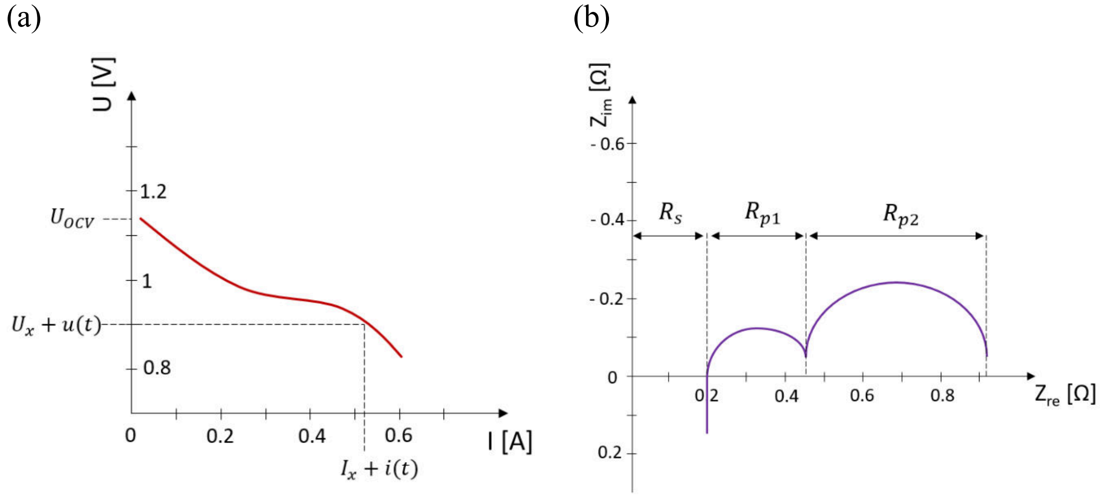

Figure 1-4: Principles of EIS analysis. (a) Position of excitation signal on I-V curve. (b) Illustration of the impedance data on the Nyquist plot.

Processes that take part in cell operation have different kinetics, measured by relaxation time in a given frequency range, e.g. 1 MHz - 0.1 Hz. The ohmic resistance is at the intersection of the impedance curve with the real axis at high frequency. The polarisation processes contain both resistive and capacitive parts, the faster processes, as charge transfer could be visible at a higher frequency, e.g. $\boldsymbol{R_{p1}}$ on Figure 1-4 b, while slower, like diffusion or surface reaction, have longer relaxation time and are triggered at a lower frequency range, e.g. $\boldsymbol{R_{p2}}$ on Figure 1-4 b. Often the magnitude of the capacitance of the polarisation process could help to assign it to the region in the sample and recognise the involved mechanism [60], e.g. processes on the interface are recognised by the electrical double layer capacitance where the typical magnitude of capacitance would be 10^{-5} [F/cm^2]. For EIS spectra to be valid, the system must meet the conditions of linearity, time invariance, causality and finiteness [61]. The linearity requires that the I-V slope at the point where the excitation signal is superimposed is linear. The causality means that the measured response is closely related to the excitation signal. The time invariance is satisfied when the system is in equilibrium during the measurement and does not change its spectrum with time. Fitness means that the impedance has finite values for $\omega \rightarrow 0$ and $\omega \rightarrow \infty$.

The behaviour of analysed impedance spectra can be modelled by combining basic elements of the electrochemical system, e.g. resistor $\boldsymbol{R}$, capacitor $\boldsymbol{C}$ and inductance $\boldsymbol{L}$.

Usually, EIS spectra of SOC consist of more complex responses, showing both resistive and capacitive nature. They are represented by the semi arcs on the Nyquist plot. The ideal semi-arc is modelled by ***R*** and ***C*** connected in parallel (***R/C***). For example, it could represent dielectric relaxation in the bulk of the electrode, with the "non-blocked bulk resistance" and dielectric capacitance [56]. The impedance for the ***RC*** element at the frequency range is modelled by:

$$\overline{Z}_{RC} = \frac{R}{1+i\omega RC} \qquad \textbf{Equation 1-19}$$

At the lower frequency, diffusion restrictions could prevent the ions from crossing the interface; species accumulate at one side of the cell while being used on the other. To model processes where charge carrier diffuses through a material, such elements as Warburg (***W***) could be used [56].

It is visible that in the R/C element at $\omega \rightarrow 0$, the effect of capacitive diminishes; hence, the impedance approach value of DC resistance. The real part of impedance decreases at a higher frequency due to a phase shift between the current going through the resistor and the capacitor (displacement current), while the imaginary part increase [57]. The equation gives the characteristic frequency where both currents are equal:

$$\omega_{max} = \frac{1}{RC} \qquad \textbf{Equation 1-20}$$

In most cases, due to the un-homogeneity of the electrode, arcs deviate from the ideal shape and give a more flattened semi-circle; then, ***C*** is replaced by a constant phase element (***CPE***) [62]. The ***CPE*** element is used in place of ideal capacitance due to the un-homogeneity of the system, e.g. rough or porous sample. The impedance of the ***CPE*** element is expressed by:

$$\overline{Z}_{Q} = \frac{1}{Q(i\omega)^{n}} \qquad \textbf{Equation 1-21}$$

where ***n*** approaches value 1 for the ideal capacitor, ***Q*** is the second fitting parameter.

The approximate capacitance of the Cole-Element could be calculated from the following:

$$C \approx (R^{1-n}Q)^{1/n} \qquad \textbf{Equation 1-22}$$

the value of which became more accurate for $n \to 1$ [63].

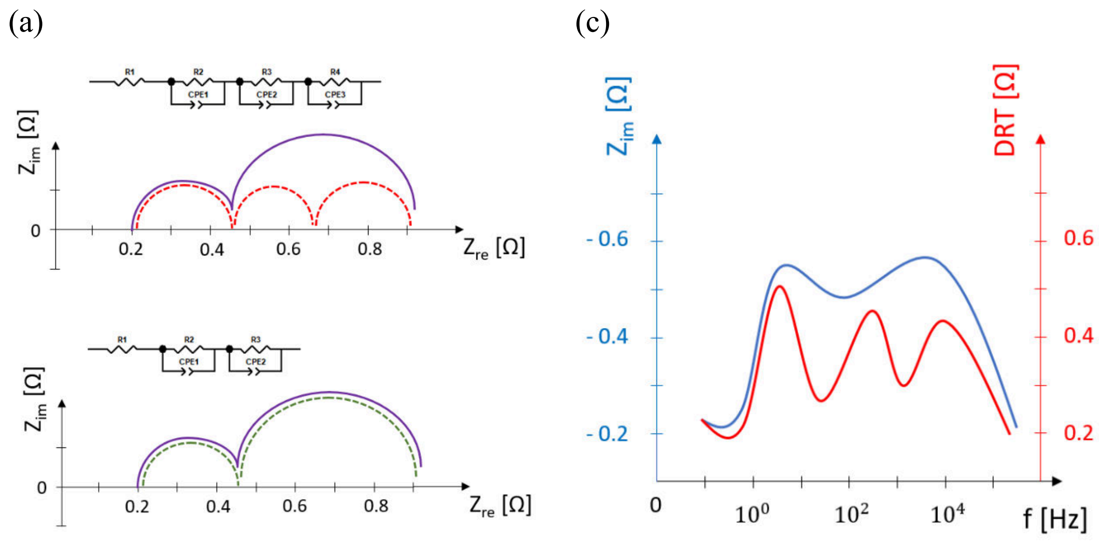

Figure 1-5: Equivalent circuit fitting and DRT principles. (a) The example of Equivalent Circuit with 2 and 3 elements (b) DRT superimposed on Bode plot.

EIS presents the kinetic response of processes on both electrodes. They often occur on a similar characteristic frequency or processes at the same electrode and overlap. In such a case, the equivalent circuit elements could be misinterpreted, and even a substantially different system could give a similar response, Figure 1-5 a. The elements of the equivalent circuit could be predefined with the use of the distribution function of relaxation times (DRT) [64], [65], Figure 1-5 b. The distribution of relaxation times of polarisation processes is the fundamental element of interest in EIS analysis. However, in SOC analysis of a complex system, an impedance at a given frequency could be affected by impedance below and above this point [64]. DRT uses a Fourier transformation to deconvolution EIS spectra, providing a higher resolution than the Nyquist or Bode plot. The method makes it easier to determine the number of individual processes, type, characteristic frequency or resistive contribution. In this way, a whole process could be reversed, parameters obtained from DRT can be used for complex non-linear least squares (CNLS) fits [66] for equivalent circuits or used as the sole representation. There is no need for any initial assumption about the character of the electrochemical processes or their number.

The convolution equation that connects the distribution of relaxation times $\gamma(\tau)$ to impedance data $Z(\omega)$ was obtained by Fuoss and Kirkwood by integral transforms [64], [67]:

$$\boldsymbol{Z(\omega) = R_0 + Z_{pol}(\omega) = R_s + R_{pol} \int_o^{\infty} \frac{\gamma(\tau)}{1+j\omega\tau} d\tau}$$

$$\boldsymbol{\int_0^{\infty} \gamma(\tau) d\tau = 1}$$

Equation 1-23

In the equation, R_0 is a frequency-independent ohmic resistance, $Z_{pol}(\omega)$ is the polarisation part of impedance spectra, and R_{pol} is the polarisation resistance, ω is the angular frequency. In an actual test, the entire spectrum of frequency can not be measured; thus, it is impossible to solve equation 1-23 analytically. Schichlein et al., to calculate $\gamma(\tau)$, used the extrapolation techniques that artificially compute impedance data at the whole frequency range and applied digital filters on the Fourier transform [64]. The method is based on the idea that every polarisation impedance can be expressed as the sum of infinite numbers of small ***R/C*** elements connected in series. Considering first the N number ***R/C*** element, where $R_{pol,k}$ is the ohmic resistance of the k element, the relation will hold $R_{pol,k} = R_{pol}\ \gamma_k$, where R_{pol} is the total ohmic resistance of the circuit. The impedance will look as follows:

$$\boldsymbol{Z_{pol}(\omega) = \sum_{k=1}^{N} \frac{R_{pol,k}}{1+j\omega\tau_k} = R_{pol} \sum_{k=1}^{N} \frac{\gamma_k}{1+j\omega\tau_k}}$$

$$\boldsymbol{\sum_{k=1}^{N} \gamma_k = 1}$$

Equation 1-24

If the infinite number of ***R/C*** elements is assumed at a frequency range 0 to ∞ the equation, 1-24 takes the form of convolution, equation 1-25. In the equation, the expression $[\gamma(\tau)/1+j\omega\tau]d\tau$ corresponds to the part of the entire polarisation between τ and $\tau + d\tau$, meaning that the area under peak corresponds to the resistance of the dynamic process [64]. Before conducting DRT fitting, the quality of impedance spectra should be investigated with Kramers-Kroning (KK) transforms [68], [69]. The good quality data shouldn't show a larger residual than 0.5% [65], [70]. As the real and imaginary parts are connected through Kramers-Kroning transformations [71], only the imaginary part of impedance could be considered; thus, for the infinite number of ***R/C*** elements:

$$\boldsymbol{im\{Z_{pol}(\omega)\} = -R_{pol}\int_0^{\infty}\frac{\omega\tau}{1+(\omega\tau)^2}\gamma(\tau)d\tau} \qquad \textbf{Equation 1-25}$$

The free Matlab-based DRTtool was used in the project, developed by Wan et al. [72]. The program uses novel RBFs discretization regularisation for calculating DRT from the impedance. According to an equation 1-24, the units of DRT are Z/s; thus, for example, in the Schichlein et al. method, the DRT units are [Ω/s]. In Wan et al. method, the authors, instead of dimensional values for function describing relaxation characteristic, uses τ/s for this function; thus, units of relaxation times are in Ω [73]. The data beyond the frequency limits are extrapolated; one should keep in mind that it can lead to spurious or shoulders if not carefully regulated [74]; when checking the correctness of DRT evaluation, the practical approach is to compare DRT made of imaginary and real parts.

1.3.2 I-V characteristic

According to the Nernst equation, a theoretical voltage $\boldsymbol{E_{nerst}}$ at open-circuit voltage conditions (OCV) reaches the maximum for the highest difference in oxygen partial pressure (pO_2) between electrodes and decreases with an increase in operating temperature. For SOFC working conditions, when pure H_2 and O_2 are used, the maximum $\boldsymbol{E_{nerst}}$ is about 1.2V at 800°C. However, open circuit voltage could be lowered due to several reasons [70]. For example, if the leaks are present in the cell, either in the electrolyte or between electrode and surrounding, the voltage would drop due to the decreasing pO_2 difference according to the Nernst equation. Another reason could be partial electronic conductivity of the electrolyte (for example, observed in GDC electrolytes [75]) or low activity of electrodes; thus, the lack of thermodynamic equilibrium at half electrodes compartments.

In a system where external voltage is applied, the current ***I*** flowing through a cell will be proportional to the value of ohmic resistance of electrolyte $\boldsymbol{R_s}$ and polarisation losses on both sides of the cell ($\boldsymbol{\eta_c}$, $\boldsymbol{\eta_a}$):

$$\boldsymbol{E = E_{Nerst} - IR_s - \eta_c - \eta_a} \qquad \textbf{Equation 1-26}$$

The ohmic resistance of electrolyte R_s comes from the limitations of charged particles' flow in the material. In the state of the art SOC, with very conductive Ni/YSZ and LSM/YSZ electrodes, the ohmic resistance is considered to come from the YSZ electrolyte only. The ohmic resistance mainly depends on materials properties and operation temperature, which high value is essential for the ionically conductive electrolytes, as their conduction is thermally activated.

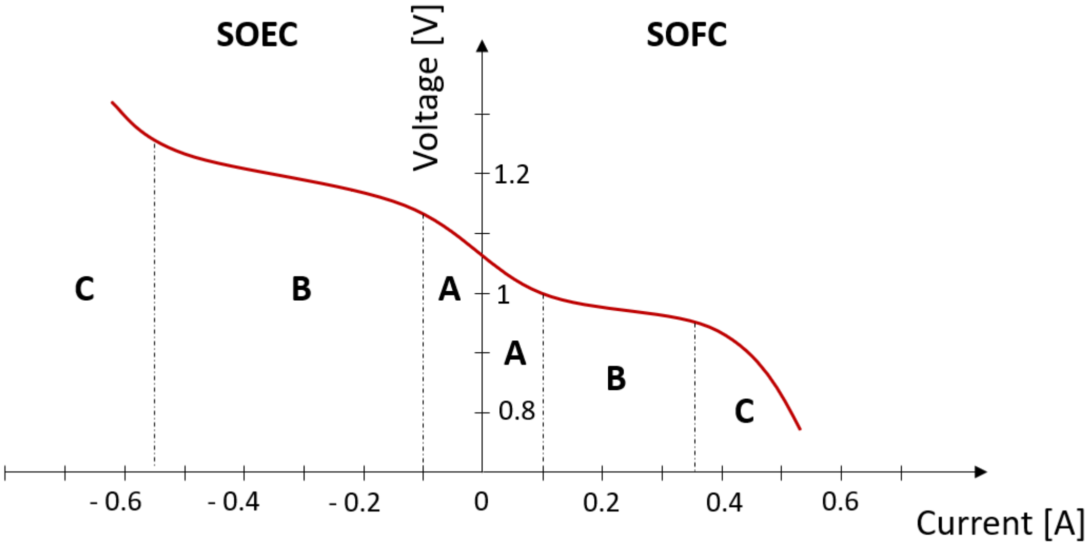

Figure 1-6: The representation of I-V dependency in reversible operation. A – activation region, B – ohmic region, C – concentration region.

The polarisation losses on the cathode and anode (η_c, η_a) result from the current flowing through an electrochemical process at the electrode characterised in the previous section, which is slower than the transport of charged particles [76]. The I-V curve represents the current-voltage characteristic; it presents the voltage dependence on the flowing current (Figure 1-6). When the system is in equilibrium and no external voltage or current is applied, the cell is at OCV conditions, the cell voltage is equal to $E_{nerst,}$ and there is no current flowing through a cell. When the cell's voltage is decreased below $E_{nerst,}$ the cell is switched to a fuel cell mode (SOFC), the cell's fuel electrode will be polarised positively (anodic polarisation), resulting in fuel oxidation [70]. The generated current will travel to a negatively polarised oxygen electrode (cathodic polarisation) through the external circuit to reduce oxygen gas. On the contrary, when the cell's potential increases above OCV conditions, the cell will be switched to electrolysis mode (SOEC). The fuel electrode will be under reducing conditions and the oxygen electrode under oxidising, and the current will be used for steam reduction at the fuel electrode.

The cell's resistance could depend on the applied voltage making the I-V curve un-linear. The resistance could also be different on both sides of the curve, making it asymmetric, e.g. due to various catalytic activity of electrode to reduction and oxidation, or various concentration losses on both sides due to different concentrations of reactants. The most fundamental classification separates three I-V curve polarisation regions: activation, ohmic, and concentration. It is accepted that each of them impacts the current-voltage characteristic A, B, C regions in Figure 1-6. The activation region often appears when switching from OCV to lower potential, and voltage change exponentially with current (area A in Figure 1-6); it concerns processes on the electrode surface [77], which is highly dependent on its charge transfer, catalytical properties. The exponential growth of potential is related to the activation barrier, which needs to be overcome; here, the voltage gradient plays a similar role as the temperature gradient in chemical reactions. Activation overpotential is related to the electrode's electrochemical activity; therefore, it mainly depends on the electrode materials. Often, the current-voltage relation in the activation region could be expressed by the Butler-Volmer equation [77]:

$$\boldsymbol{i = i_0 \left[\exp\left(\frac{\eta_{act,a}}{\beta_1}\right) - \exp\left(\frac{\eta_{act,c}}{\beta_2}\right)\right]} \qquad \textbf{Equation 1-27}$$

Where $\boldsymbol{i}$ is current density, $\boldsymbol{i_0}$ is the exchange current density related to electrode structure, temperature and gas concentration, β_1 and β_2 [78] are the thermal coefficients related to electrode kinetics, while $\boldsymbol{\eta}$ is the activation overpotential on electrodes. After the activation period, the curve could go into linear behaviour, the so-called ohmic polarisation region. Due to linear behaviour, it is difficult to model it by the Butler-Volmer equation, and the cells' potential could be described by electrolyte ohmic resistance ($\boldsymbol{R_E}$) and zero frequencies anode ($\boldsymbol{R_A}$) and cathode ($\boldsymbol{R_C}$) impedance [76]:

$$\boldsymbol{E = E_{nerst} - i(R_E + R_A + R_C)} \qquad \textbf{Equation 1-28}$$

The concentration losses derive from the inability of a porous electrode network to ensure a flow of reactant from its source to interface at specific demand. Concentration losses became visible at higher demand for the reactant (region C in Figure 1-6) and, in addition to gases concentration, are mainly dependent on microstructure and thickness of electrode but more minor on temperature. The concentration overpotential at the fuel electrode during electrochemical oxidation of H_2 can be expressed in terms of the gas concentration gradient between the gas phase in the bulk of electrode and electrode/ electrolyte interface [79].

$$\eta_{conc,a} = \frac{RT}{2F} \ln \left(\frac{p^I_{H_2} p_{H_2O}}{p_{H_2} p^I_{H_2O}} \right) \qquad \textbf{Equation 1-29}$$

Where p^I is the partial pressure at the interface.

1.4 Materials and their functionality in SOFC

1.4.1 Electrolyte

The electrolyte has several requirements [32], [37], [75]. It must have sufficiently high oxygen ion conductivity to provide oxygen ion exchange between electrodes but no electronic conductivity, so there is no short circuit that would reduce the efficiency of the redox process. The electrolyte must be a solid impermeable layer to separate the reducing atmosphere on the fuel electrode and oxidising on the oxygen electrode. Also, like every other component, the electrolyte must be chemically stable in working conditions, which for electrolyte means a vast range of pO_2. Thermal and mechanical resistance is also required, as it allows for more robust and reliable cells.

A standard electrolyte used in SOFC is fluorite-type yttria-stabilised zirconia ($Zr_{0.84}Y_{0.16}O_{2-\delta}$, YSZ), popular due to a relatively high ionic conductivity, excellent stability in both reducing and oxidising conditions, high long term stability in operating conditions, good availability of raw materials and good mechanical strength [47]. The addition of Y_2O_3 to ZrO_2 stabilises the cubic crystal structure and introduces oxygen vacancies, enhancing the ionic conductivity; due to the charge compensation formed after the substitute of Zr^{4+} ions by Y^{3+}, the defect reaction according to Kröger–Vink notation could be expressed by [80]:

$$Y_2O_3 \xrightarrow{ZrO_2} 2Y'_{Zr} + 3O_o^x + V_o^{\bullet\bullet}$$ **Equation 1-30**

It has been reported that the maximum ionic conductivity in YSZ could be achieved by dopping with a minimum concentration of Y required to stabilise the cubic crystal structure [81], [82]. Therefore, the optimal ionic conductivity in YSZ is observed with an addition of 8-11% mol of dopant. At a higher level, Yttrium cations and introduced oxygen vacancies could start ordering decreasing ionic conductivity of the material [75]. Also, zirconates doped with different cations are known for solid oxide electrolytes application, among them doped with divalent (Ca^{2+}, Mg^{2+}) or trivalent cations (Sc^{3+}, Gd^{3+}) [83]. The Sc_2O_3 stabilised zirconia (SSZ) is the most promising as it has a much higher conductivity than YSZ. However, they are less practical due to a higher cost and faster degradation [84].

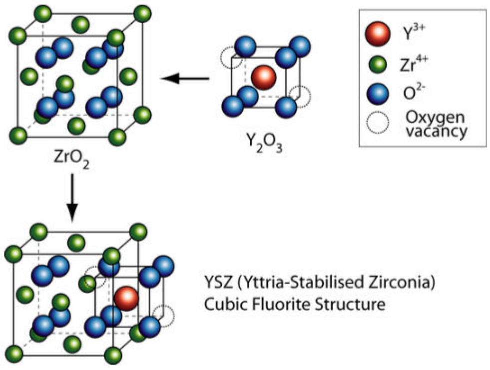

Figure 1-7: Fluorite structure of Yttria-Stabilised Zirconia (YSZ); the image is taken from reference [85].

The transport of ions is a thermally activated hopping process and follows the Arrhenius dependence:

$$\sigma = Aexp(-\frac{E_a}{kT})$$ **Equation 1-31**

A is the pre-exponential factor, ***R*** is the universal gas constant, ***k*** is the Boltzmann factor, and ***Ea*** is the activation energy for conductivity. The theoretical activation energy of YSZ conductivity is around 0.9 eV [86], and the value of YSZ conductivity is 0.08 S/cm at 850 °C [87]. Thermal activation comes from thermal activation of the hopping process and the increase of defect concentration with temperature.

As the SOC technology progresses, alternative materials are being explored to lower operating temperature. The use of electrolytes with higher ionic conductivity would allow more efficient operation at a temperature below 700 °C; among the proposed materials, the ceria-based oxides (CeO_2) [88] and $La_{0.85}Sr_{0.15}Ga_{0.9}Mg_{0.1}O_{3-\delta}$ (LSGM) [89] are the most promising solution [37].

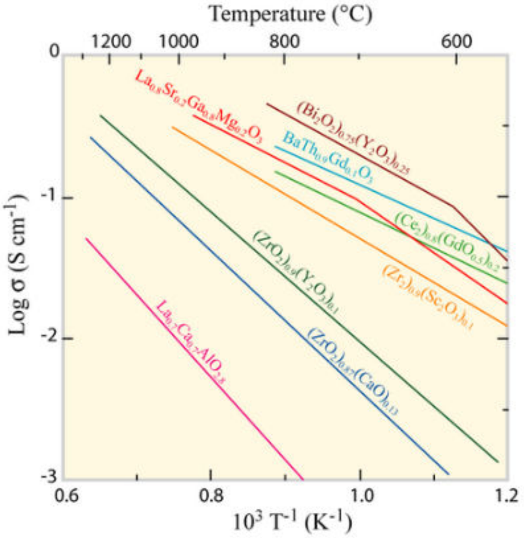

Figure 1-8: The electronic conductivity of various ionic conductors; the image is taken from reference [85].

The CeO_2, with the adequate quantity of a dopant, shows the excellent value of the ionic conductivity, of order 10^{-1} S/cm at 800 ºC. Among the considered materials are Gadolinium-Doped Ceria (GDC) – $Ce_xGd_{1-x}O_2$ and Samaria-Doped Ceria (SDC) - $Ce_xSr_{1-x}O_2$ [90]. The valuable asset of doped ceria electrolytes is their chemical and thermal compatibility with the perovskite structure's cathode material, and very well-matched thermal expansion coefficient (TEC) with the ferritic stainless steel (FSS) used as interconnects [91]. The disadvantage of ceria-based electrolytes is the partial electronic conductivity at a low partial pressure of oxygen, which in fuel cell operating conditions may result in significant performance loss at a temperature above 600 ºC [92]. The electrical conductivity of doped ceria materials results from reducing the Ce^{4+} ions to Ce^{3+}. However, research shows that if the temperature is lower than 600 ºC, the effect of ions reduction is negligible [91]–[93]. Therefore, doped ceria materials are more suitable as electrolytes when the fuel cell operates at intermediate temperatures (400-600 °C). Another solution is using a very thin layer of doped zirconia between the ceria electrolyte and fuel electrode. The zirconia coating isolates the electric current and does not significantly increase the electrolyte's internal resistance [94].

The LSGM is a promising perovskite material used as an electrolyte in low-temperature SOC. Doping of both A and B-sites in LaGaO3 generates many oxygen vacancies, giving this material remarkable oxygen ion conductivity of 6.6 x 10^{-2} S/cm at 1000 K [95], [96]. However, the existing limitation of LSGM is its reactivity with Ni; hence traditional Ni/YSZ composites are challenging to be implemented [97], [98].

1.4.2 Fuel electrode for SOFC

For efficient operation, the fuel electrode in SOFC must have specific technical, physical and chemical properties. The leading factors in the choice of material are the high catalytic activity for electrochemical fuel oxidation, the electronic conductivity to conduct electrons from the reaction site at the triple-phase boundary (3PB) to the current collector and ionic conductivity at the active region, usually not exceeding 20 μm [99]. The fuel electrode should also have sufficient porosity to allow gas transport to 3PB and be chemically, mechanically and thermally stable in operational conditions and with the adjacent materials. Traditionally the composite made of Ni and YSZ is being used as the standard solution (Ni/YSZ) introduced by Spacil [100]. Together with the material's porous structure, Ni/YSZ composite makes a 3PB, where three components of the reaction, fuel in the gas phase, oxide ions from YSZ and electrons from Ni, are in proximity. YSZ also provides the backbone for Ni and stabilises it against agglomeration. Perovskite materials were proposed as the alternative to Ni/YSZ composite. Mixed metal oxides would be less prone to carbon deposition and more resistant to sulphur impurities [96], [101]. Thanks to their mixed ionic and electronic conductivity (MIEC), and catalytical activity, the active region could be maintained by a single-phase material, extending the reaction zone to the whole surface [47], [99], [102], [103].

1.4.2.1 Ni/YSZ composite – traditional electrode for SOFC

The high temperature in SOFC operation gives the advantage over the low-temperature fuel cells as the reaction's kinetics are improved at a higher temperature so that highly active noble metals are not needed and can be replaced by cheaper and often more reliable materials. Due to its excellent performance, good mechanical properties and relatively low cost, Ni/YSZ is still the most widely used solution [104]. However, despite the many advantages, some problems hinder their full commercialisation. The most common anode material, Ni/YSZ, loses its long-term operating performance due to Ni migration and agglomeration. Also, it has a low tolerance to sulphur poisoning [105] and is prone to carbon deposition [106]. Operating on fuels containing carbons requires a complex system, narrow temperature regimes, and strict control over operational conditions, as Ni enhance a carbon formation that could be destructive to the fuel electrode [47], [107], [108]. Moreover, the Ni/YSZ composite is thermally and redox unstable; therefore, it could be damaged during changes in operation conditions, e.g. to emergency shut-down [37] or too fast start-up and shutdown.

The content of Ni must be sufficient to provide continuous conductivity through the metal face, while its excess could lead to agglomeration, decreasing porosity and reducing the length of 3PB [99]. Also, the high Ni content could result in a significant thermal expansion coefficient (TEC) difference between the layers, which for pure nickel is 16.9×10^{-6}/°C [109], while for YSZ, about 10.9×10^{-6}/°C [110]. Studies show that a ratio of 40/60 of Ni/YSZ is optimal, assuring high conductivity and low difference in TEC with YSZ electrolyte [33].

The 30% is the minimum value of porosity that would bring the gaseous fuel to the reaction zone and assure proper water discharge outside the anode [104]. A too high porosity value could result in poor mechanical strength and low 3PB. The Ni/YSZ fuel electrode is usually made from NiO/YSZ composite, which, when under reduction, changes to Ni/YSZ. The volume change of about 30% in the NiO phase provides the required porosity, which could be supplemented by adding pore-formers, such as carbon or starch, that burn during composite sintering.

Materials must offer long-lasting and optimal performance for the commercial solution, e.g., a slow rate of catalyst deactivation and other characteristics. A stable cell is more durable in operating conditions, more flexible in handling and opens the perspective to other applications than stationary power units [37]. Many believe that Ni/YSZ fuel electrode is the most vulnerable part of SOFC [83], [111]. The SOFC operating conditions exert partial water pressure on Ni, leading to volatile $Ni(OH)_2$. The $Ni(OH)_2$ can migrate, leading to a change in the electrode's microstructure due to Ni diminishing or agglomeration [112], [113]. Another drawback is mentioned already the varying TEC of Ni and YSZ. The Ni/YSZ composite, especially under changing conditions, tends to develop micro-cracks between components over time. The effect is strengthened in tubular cells due to the large temperature gradient [114]. Moreover, due to significant volume change during Ni to NiO conversion, the Ni/YSZ electrode is not redox stable, which is even more harmful than rapid temperature changes [115]. The oxidising condition at the anode side may result from interruptions in fuel delivery, emergency system shutdown and leakage, and re-oxidation during start-up and shutdown [114]. Another challenge with Ni-YSZ anodes lies in the drop in cell performance due to nickel agglomeration, poor tolerance towards carbon deposition and sulphur poisoning, limiting its lifetime and cost-effective exploitation [116]–[118]. In this regard, SOFC technology calls for a new alternative anode, which needs to address those issues.

The hydrogen oxidation process on the nickel/ stabilised zirconia (Ni/SZ) system was studied multiple times. The hydrogen oxidation on the electrode was treated as a series of elementary steps; there was a debate about the reaction path and the slowest step in the process, a rate-determining step (RDS) [119]. RDS controls the electrode's kinetics, assuming that the fast processes are in equilibrium [57]. In Theory, each step could be RDS depending on the electrode's material, microstructure, or testing conditions. Mogensen [120] concludes that the H_2 dissociation and proton migration to SZ is the most probable mechanism, Figure 1-9 [121], [122].

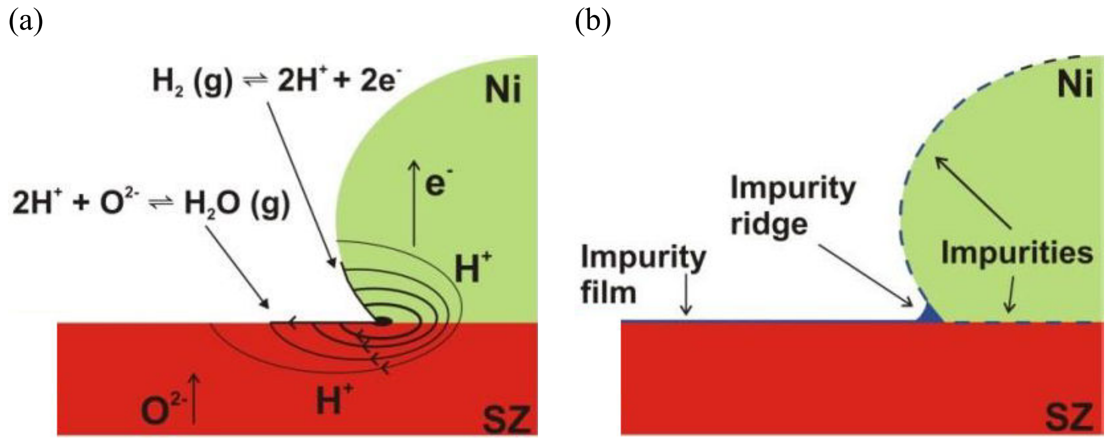

Figure 1-9: Mechanism of H_2 reduction on Ni/SZ. (a) Mechanism of proton migration for H_2O formation. (b) Influence of impurities at interfaces [103], [120].

Such a mechanism would involve the diffusion of H_2 gas to the vicinity of the Ni surface and its adsorption/dissociation on Ni. In the next step, H^+ species migrate to SZ for steam formation. Steam could be formed through the hydroxyl ion, e.g., in a two-step process. The authors pointed out the importance of acknowledging the impurities forming on SZ and Ni surfaces and interfaces, Figure 1-9 b. Most likely, the impurity film covers the whole surface of SZ, and the ridge is located at the 3PB. Also, some impurities are situated in the Ni/SZ interface and on the Ni surface. Therefore, the reaction must occur either through the impurity phase or around it, affecting the specie's mobility within a system.

1.4.2.2 Materials for perovskite fuel electrode

Aside from efforts to increase the Ni/YSZ lifetime, either through microstructural modification [112], the gas pre-treatment [100] or by adjusting the gas composition, e.g., adding the steam into the hydrocarbon fuels [108], other candidates for the next generation of fuel electrode were proposed. Ideally, the alternative electrodes would be single-phase ceramics, which, apart from having a good activity, would exhibit mixed ionic and electronic conductivity (MIEC), facilitating the species exchange and stretching the reaction zone from 3PB to the whole surface [103].

The rare-earth-doped CeO_2 electrodes were proposed as a promising material for SOFC anode [43]. Besides catalytical activity, CeO_2 is an excellent ionic conductor and has a certain level of electronic conductivity at low oxygen partial pressure due to the reduction of Ce^{4+} to Ce^{3+}. Moreover, the performance was considerably improved by adding a low concentration of precious metal catalyst [123]. However, due to the low electronic conductivity of about 0.08 S/cm at 800 °C [124], the material was not considered suitable for practical application [47]. Marina et al. [125] achieved excellent performance from gadolinium doped ceria (GDC), comparable to Ni/YSZ in a hydrogen atmosphere and good activity for methane oxidation without carbon formation. However, the thickness of the electrode was decreased to 10-15 μm while its whole area was covered with the silver-based current collector, meaning that the activity of the electrode was basically dependent on it [47]. Some of the work was focused on Cu/CGO, where cooper would control the electrode's electronic conductivity. This material proved high performance, especially in hydrocarbons, but suffered from performance loss due to poor stability related to the low melting point of Cu [47].

The perovskites have gained attention as the alternative fuel electrode, thanks to their thermal, redox and mechanical stability, good chemical and physical compatibility with electrolyte, electrochemical activity and MIEC properties [99], [126]–[128]. Those and many more useful physical and chemical properties are related to accumulating elements with multiple valence states and various defects [128]. For instance, the B-site position could be occupied by transition metals, which usually provide catalytical activity to perovskite. Simultaneously, pairs of B-site cations on various oxidation states give the material's electronic conductivity and introduce oxygen deficiency responsible for the ionic conductivity. Perovskite lanthanum strontium manganate (LSM) is a well-known air electrode, mainly due to its p-type conductivity that increases with higher oxygen partial pressure. However, a different characteristic is required for the fuel electrode, which has to be conductive in reducing conditions; thus, the n-type conductive perovskite was proposed as the candidate for a fuel electrode [99], [129], [130]. Many architectures for perovskite fuel electrodes were proposed, including one phase perovskite electrodes with mixed ionic and electronic conductivity, the composite of ion conductive fluorite and perovskite MIEC material, or perovskite MIEC electrodes with deposited catalyst, either through infiltration or exsolution [103]. For the fuel electrode application, the perovskite with Fe, Mn, Cr and Ti on the B-site position seems to be a good choice, as it can produce some level of electronic conductivity; for which the requirement was set to be at least 1 S/cm for relatively thin layers with a good distribution of current collector [99].

Several early work was concerned with chromites perovskites with lanthanum on A-site position [131], well-known as good electronic conductors that are stable in both oxidising and reducing conditions; therefore often used for interconnects [31]. However, chromites show relatively low catalytical activity for fuel oxidation and p-type conductivity. The performance could be improved by doping various transition metals on the B-site position (V, Mn, Fe, Co, Ni), presented for methane oxidation [132]. The best performance was attained with 10% Ni doping, most likely due to the Ni exsolution [99]. However, there were doubts about the stability of exsolved anodes at this point of their development. Replacing Cr by Mn in $La_{0.75}Sr_{0.25}Cr_{0.5}Mn_{0.5}O_3$ (LSCM) fuel electrode gave an excellent performance, comparable to Ni/YSZ composite for wet H_2 and good performance for CH_4 oxidation [130]. The low performance of chromium-based electrodes was related to the strong affinity of Cr to hold six-fold coordination; thus, difficulties with introducing oxygen vacancies and the associated oxygen ion conductivity. The addition of transition metals cations, such as Mn, Fe, Co, Ni, and Cu, which can hold various valences, could create a path for oxygen ion conduction. Perhaps the major limitation of LSCM is its p-type conductivity which decreases below 1 S/cm at reducing conditions.

Among the others, perovskites containing Ti have attracted attention due to the ability of Ti cations to remain mixed valent in a reducing atmosphere (Ti^{4+}/Ti^{3+}). The redox couple is stable to accept electrons from dissociative adsorption of hydrogen or hydrocarbons, and Ti^{4+} takes a 5-fold coordination number to allow the removal of oxygen ions from the lattice [133]. These electrodes show sufficient electronic conductivity, good chemical and physical compatibility with YSZ, redox stability and good resistance to sulfur poisoning [134]–[137]. Nevertheless, titanates have relatively low oxygen ion conductivity, as Ti cations prefer octahedral coordination in bulk. The introduction of cations stable at lower coordination with oxygen (Mn^{2+}, Ga^{3+}) facilitated the vacancy diffusion [138], [139].

Despite promising, the oxide electrodes often have too low electrochemical activity to be proposed as a good candidate for fuel electrodes. The research community suggested a slow adsorption/dissociation process as RDS in various oxide fuel electrodes, either in-perovskites or ceria based electrodes [139]–[142]. Often, metal catalysts have been added to improve the H_2 absorption/dissociation process on oxide electrodes [141]. Usually, the metal catalyst is infiltrated through precursor solution and fired. Cations became metallic particles after reducing at a high temperature [102]. These electrodes show high activity; however, due to the weak interaction of metallic particles with the substrate, they tend to move and agglomerate, which reduces their surface area, thus, activity [103].

First proposed by Daihatsu and Toyota [143], the exsolution of nanoparticles on perovskite surface has been found to be an elegant way of metallic catalyst preparation. In recent years, the exsolved material found interest as the fuel electrodes for SOC due to their excellent activity and stability of metal catalyst [144]–[151]. The strong interaction of exsolved metal nanoparticles with oxide surface is advantageous, giving those materials better stability and coking resistance [149], [152]. The process involves doping of transition metal to be exsolved into B-site position. Such cations are randomly distributed in a lattice and tend to be released as metal on the surface of perovskite.

In developing exsolved $La_{0.43}Ca_{0.37}Ni_{0.06}Ti_{0.94}O_{3-\gamma}$ (LCNT) fuel electrode, Myung et al. used a high potential in electrolysis mode to produce a network of nickel nanoparticles on the surface. The process has been termed “switching” and proved to be much more efficient and faster than gas-driven exsolution [153]. The LCNT predecessor $La_{0.4}Ca_{0.4}TiO_3$ (LCT) was proposed by Vashook et al. as an alternative fuel electrode for SOFC [136], [137]. Besides n-type conductivity, LCT has no visible short or long-range ordering; hence, the material could be advantageous in using the in-situ exsolution method. The smaller Ca^{2+} ions potentially have less tendency to segregate to the surface in A-site rich layers than, for example, bigger Sr^{2+}. It is well known that the reconstruction of native perovskite surfaces can hinder exsolution due to A-site rich surfaces [149].

1.4.2.3 Perovskite structure and properties

It is impossible to understand the principle of perovskite electrodes without familiarising with the fundamentals of these materials. Therefore, perovskite's crystal structure and properties will be briefly characterised, with a particular focus on its functionality in SOC electrodes. Perovskites took their name from the mineral perovskite with stoichiometry $CaTiO_3$; they have a general formula, ABX_3. Usually, the A-site cation holds a 12-fold coordination number connected with four BX_6 octahedral, where X^{2-} ions occupy a face-centred position with the B-site cation in the centre [128]. To achieve electroneutrality, the total charge of A and B cation in the ABX_3 structure is 6. The perovskite oxides with general stoichiometry ABO_3 are the largest group, but fluorides (e.g. $CaRbF_3$) and sulfides (e.g. $BaTiS_3$) are also known [128].

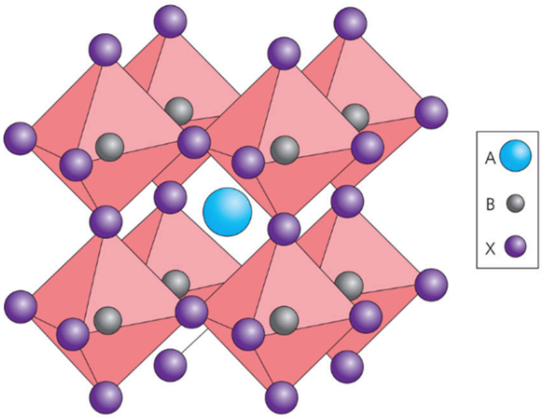

Figure 1-10: The perovskite lattice structure (ABX_3); the image taken from reference [154].

Due to the high lattice energy, perovskite oxides can accept some level of A or O side deficiency; B-site deficiency is also possible [155] but less likely due to strong bonding with oxygen ions. Deficient perovskite adopts general stoichiometry: $A_{1-\alpha}BO_3$, $ABO_{3-\gamma}$, where α stands for A-site deficiency while γ for O-site deficiency. The compounds with A or O site excess are also possible, characterised as $A_{1+\alpha}BO_3$, $ABO_{3+\gamma}$, while the creation of perovskites with deficiency on one site and excess on the other is somewhat unfavourable [156]. Deficiency is accumulated by vacancies in perovskite lattice, while excess by intergrowths. Deficiency, excess and cation substitution, depending on doping level, often determines perovskite's functionality, such as catalytical activity or MIEC properties. Therefore, perovskites properties could be tailored by their stoichiometry (or nonstoichiometric), which could be controlled either during formulation or by different conditions (e.g. reduction at high temperature) [156].

The ABO_3 perovskites can also adopt a wide range of elements on either A or B positions. The larger, lower valency cation occupies the A-site position and the smaller cation B-site position; usually, a transition metal is known for its catalytical activity [157]. The perovskites could accept more than one element on either site, as long as cations are similar in size and their preferred coordination number allows this. The substituted cation often has different valency; therefore, the perovskite attains nonstoichiometric through a charge compensation mechanism to maintain its electroneutrality [96]. For instance, replacing A-site cation with the higher charge cation, depending on the used method, could lead to oxygen excess ($A1_x^{+2}A2_{1-x}^{+3}BO_{3+x/2}$), A-site deficiency ($A1_x^{+2}A2_{1-3x/2}^{+3}BO_3$), or partial reduction of B-site cations ($A1_x^{+2}A2_{1-x}^{+3}B_x^{+3}B_{1-x}^{+4}O_3$). Whereas, dopping the B-site with a higher valency cation could be compensated by oxygen excess ($AB1_x^{+4}B2_{1-x}^{+5}O_{3+x/2}$), oxygen deficiency ($AB1_x^{+4}B2_{1-x}^{+3}O_{3-x/2}$) or mixed valency on A-site.

The ideal perovskite oxides adopt cubic symmetry as $SrTiO_3$, but due to distortion of the crystal lattice, they can accept lower symmetry, e.g. tetragonal, orthorhombic, or even rhombohedral. These often arise from differences between the radii of cations and O^{2-} ions expressed through the so-called tolerance factor $\boldsymbol{\tau}$ [128]. It has been agreed that perovskites can hold their structure as long the parameter $\boldsymbol{\tau}$ is between 0.8 and 1.1. The lattice approaches a cubic system for $\boldsymbol{\tau}$ closer to one.

$$\boldsymbol{\tau} = \frac{(r_A + r_O)}{\sqrt{2}(r_B + r_O)}$$ **Equation 1-32**

Where $\boldsymbol{r_A}$, $\boldsymbol{r_O}$ and $\boldsymbol{r_B}$ are ionic radii of individual elements that could be calculated from an X-ray pattern [158], the average size is taken if multiple cations occupy the site. Deficiency in perovskite also affects the perovskite lattice symmetry. A defect could be treated as doping on a particular position, which has its specific radii and can be included in an equation 1-32 [156]. The distortion in perovskite leading to the tilting of BO_6

octahedra, often changing its properties, can result in ferromagnetism or ferroelectricity. The tilting of BO_6 octahedral in perovskite is the reason behind their substantial flexibility and ability to adopt various cation substitutions. However, due to the significant differences in cation size, their different chemical nature, or accumulation of vacant sides, instead of random positions, the cations and vacancies may start ordering, creating so-called superstructures in perovskites lattice [128]. There are known cases in which many A-site vacancies lead to alternately arranged cation rich and cation deficient layers. The ordering could lead to a change in material properties, which in the case of SOFC electrodes, may reduce their performance, like lower catalytical activity or conductivity [128].

One of the factors perovskite owes its wide range of applications is mixed ionic and electronic conductivity (MIEC), characterised by relatively high conductivity for both electronic and ionic defects [159].

A basis for electronic conductivity in ABO_3 is the ability of B-site cation to hold various oxidation states. Electron holes or electrons result from perovskites nonstochiometry and can cause either p-type or n-type conduction [160]—the charge transfer occurs through defects associated with B-site cation in adjacent octahedra (BO_6). It is generally agreed that in the oxide n-type conductors, the conduction occurs by small polaron transfer [90], [161], [162]. The polaron is a defect created when the electron (or hole) is trapped at a given site due to the dislocation of neighbouring atoms or ions. According to Kröger-Vink notation, the small polaron could be identified as B-site with associated electron $\boldsymbol{B'_B}$, or electronic hole $\boldsymbol{B_B^X}$.

Polaron migration is a thermally activated hopping process [90], [162]. For perovskite n-type conductors, the electronic conductivity will depend on the concentration of negatively charged B-site cation $[\boldsymbol{B_B^{'}}]$, the charge of electron $\boldsymbol{e}$ [As] and the mobility $\boldsymbol{u}$ [cm^{2}×V×s$^{-1]}$].

$$\boldsymbol{\sigma_n} = [\boldsymbol{B_B^{'}}] \times \boldsymbol{e} \times \boldsymbol{u} \qquad \textbf{Equation 1-33}$$

The mobility is thermally activated and takes the form:

$$\boldsymbol{u} = (\frac{B}{T})\boldsymbol{exp}(-\frac{E_H}{kT}) \quad \textbf{Equation 1-34}$$

where $\boldsymbol{E_H}$ is the activation energy for polaron hopping, and $\boldsymbol{B}$ is a constant [90], [162].

Hence, the dependence on conductivity takes the form:

$$\boldsymbol{\sigma_n} = (\frac{A}{T})\boldsymbol{exp}(-\frac{E_H}{kT}) \quad \textbf{Equation 1-35}$$

where $\boldsymbol{A}$ is a constant.

The n-type conductivity increase in a more reducing environment, whereas p-type conductivity increase in more oxidising conditions; this dependence could be expressed by eq. 1-36 and 1-37, where n is a natural number and $\boldsymbol{\sigma_n^0}$ and $\boldsymbol{\sigma_p^0}$ are constants [163], [160].

$$\boldsymbol{\sigma_n} = \boldsymbol{\sigma_n^0}\mathbf{exp}\,(\boldsymbol{P_{O_2}^{-1/n}}) \quad \textbf{Equation 1-36}$$

$$\boldsymbol{\sigma_p} = \boldsymbol{\sigma_p^0}\mathbf{exp}\,(\boldsymbol{P_{O_2}^{1/n}}) \quad \textbf{Equation 1-37}$$

The dependency of p-type and n-type conductors from pO_2 is associated with the defect equilibrium of material. Low pO_2 reduces neutral oxygen in the perovskite lattice ($\boldsymbol{O_O^X}$) leading to the release of molecular oxygen and the formation of oxygen vacancies; for the charge compensation in n-type conductors, the electrons will be produced, equation 1-38. In p-type conductors, the holes will be produced from doping of molecular oxygen in vacant oxygen sites at oxidising conditions, equation 1-39. Therefore, n-type conductivity is preferred for the fuel cell side, as both ionic and electronic conduction improves in the fuel atmosphere, whereas the natural choice for p-type conductors would be the oxygen side.

$$\boldsymbol{O_O^X} \leftrightarrow \frac{1}{2}\boldsymbol{O_2} + \boldsymbol{V_O^{\cdot\cdot}} + \boldsymbol{2e^-} \quad \textbf{Equation 1-38}$$

$$\boldsymbol{O_O^X} + \boldsymbol{2h^{\cdot}} \leftrightarrow \boldsymbol{V_O^{\cdot\cdot}} + \frac{1}{2}\boldsymbol{O_2} \quad \textbf{Equation 1-39}$$

The ionic conduction takes place via oxygen vacancies by hoping process; therefore, perovskites with a high concentration of $\boldsymbol{V_O^{\cdot\cdot}}$ are desirable, both in the case of oxygen and fuel electrodes. For oxygen ions to migrate through perovskite lattice, they must be first incorporated from the gas phase via the surface, which is highly dependent on the concentration of oxygen vacant sites on the surface. The ability of the perovskite surface to incorporate molecular oxygen is expressed by the surface exchange coefficient $\boldsymbol{k}$, while the diffusivity by diffusion coefficient $\boldsymbol{D}$. Diffusion and surface exchange coefficients usually are measurable by tracer exchange experiments ($\boldsymbol{D^*}$ and $\boldsymbol{k^*}$) [57]. The method examines the gradient in the concentration of chemically identical tracer atoms, O^{17} or O^{18} [164]. For the known $\boldsymbol{D^*}$, the ion conductivity could be calculated from the Nernst-Einstein equation [165], where $\boldsymbol{q}$ is the charge, $\boldsymbol{f^*}$ is the tracer correlation factor representing the deviation of the atomic jumps and perovskite structure:

$$\boldsymbol{\sigma_{ion} = \frac{4q^2[O_O^x]D^*}{f^*kT}} \qquad \textbf{Equation 1-40}$$

The transport of oxide ions in perovskite lattice is a thermally activated process, and the concentration of mobile vacancies has a dominant effect [164], [166]. Similarly to stabilised zirconates, the oxide ions can migrate through oxygen vacancies if energy for oxygen to jump to the adjacent vacant site is provided to the system [160]. The activation energy for oxygen ion migration could be separated on the enthalpy of vacancy migration, formation and association [156], [166]:

$$\boldsymbol{E_a = \Delta H_f + \Delta H_m + \Delta H_a} \qquad \textbf{Equation 1-41}$$

The enthalpy of vacancy formation ($\boldsymbol{\Delta H_f}$) is related to the energy needed to break up the B-O bond and decrease the coordination number of B-site cation. The energy required for this step is relatively high for a large part of perovskites due to the preferable 6-fold coordination in most B-site cations and the high strength of the B-O bond [167]. Therefore, the perovskite with B-site cations stable in a coordination number lower than 6, such as Mn, Co or Ga, could attain a higher level of conductivity [96], [130], [168]. The enthalpy of oxygen ion migration ($\boldsymbol{\Delta H_m}$) is strongly dependent on the size and electronic structure of A-site cation as the distance of the migration is controlled by their position in relation to each other [167]. Also, $\Delta \boldsymbol{H_m}$ is affected by the lattice; it has been reported that the oxygen ion mobility improves in components with higher symmetry [169]. $\Delta \boldsymbol{H_a}$ is an enthalpy related to the vacancy trapping in perovskite lattice, which results from the association of the same site or various sites vacancies [156]. The trapped vacancies would not participate in the diffusion process, considerably diminishing the ionic conductivity of the material. In A-site doped perovskite, with a significant size mismatch of the dopant and the host cation, the trapping energy is related to a large elastic contribution in those compounds [169].

1.4.2.4 Exsolution of metal nano-catalyst in perovskite

The exsolution involves doping metal into an oxide lattice and exsolving it on the surface in the form of metallic nanoparticles [143], [170]–[175]. The perovskites offer great flexibility to accommodate transition metals and hold a stable structure after exsolution, which often gives them new, unique functionalities to use in various applications, e.g. SOFC [146], [150], [173], or SOEC [175], [176], and catalysis application [149]. The extensive research in this area showed the possibility of releasing various transition metals such as Pd, Pt, Rh, Ru, Ni from many types of perovskites, among others, from the titanates, chromites and chromites manganites [103].

Perhaps, the most significant advantage of these materials when used as the fuel electrode is their remarkable stability and resistance to coking reaction. The research has shown that these features result from the strong interaction of nanoparticles with the perovskite surface, forming a “particle-in-a-pit” structure [149], [175], [177]. During the formation of carbon fibres on the nickel catalyst, carbon chemisorbs on the nickel surface and dissolves in bulk. After that, carbon precipitates from one of the nickel planes [178]. Without the strong Ni anchoring, carbon nanofibers grow from their bottom, lifting it (the tip-growth of carbon nanofibers) [179]. The submerging of exsolved particles could be about 30% of the perovskite surface (Figure 1-11), preventing them from uplifting. The anchoring changes the nature of carbon formation to base growth. The fibres are released from the side of the particle; without tip-growth, the fibre’s size significantly decreases [149].

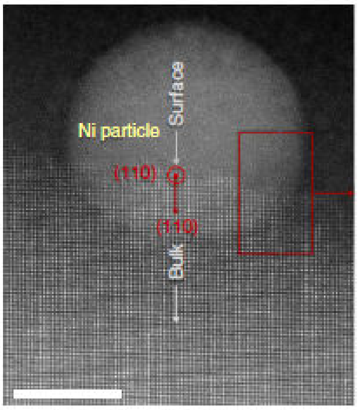

Figure 1-11: The anchoring of exsolved particles into oxide surface; the image is taken from the reference [149].

The driving force for exsolution is the difference in pO_2 between bulk and surface, leading to the reduction of perovskite lattice [147], [149], [174]. In the chemical exsolution process, pO_2 is controlled by gas composition and temperature. The exsolution could also be triggered electrochemically by applying a high cathodic polarisation to the fuel electrode [148], [153], [180]–[183]. The method has been proved to be much more efficient than gas reduction, being much faster and giving a larger population of nanoparticles. According to Myung et al. [153], the same physicochemical laws control both methods; in both cases, the driving force of exsolution is the oxygen partial pressure. According to the Nernst equation, the partial pressure of oxygen in the gas-induced exsolution was 10^{-19} while for exsolution in potential pO_2 was equal to 10^{-35}, therefore higher efficiency of the method. The low pO_2 applied on the perovskite surface results in the desorption of molecular oxygen and the creation of oxygen vacancies and electrons. The generated electron would change the oxidation state of B-site cations. Ni and Ti cations would be reduced for nickel doped titanates, and oxygen vacancies would be generated [147], [153].

The formation of nanoparticles is likely to begin at the surface as the nucleation barrier is lower than in bulk [103], [149], [174]. Next, reduced cation diffuses to the surface and supports particle growth due to the compositional gradient. There are reports about larger particles in the bulk of perovskite [152], [184], demonstrating that reduced metal atoms could also start to connect and grow in bulk.

The defect chemistry of perovskite oxides controls the exsolution of transition metals. The perovskites with A-site deficiency have higher exsolution than their stoichiometric counterparts [147], [149]. There are two explanations for this phenomenon. Firstly, the A-site vacancies facilitate the diffusion of metal particles through perovskite bulk. The second is that A-site deficiency causes the stoichiometric excess of B-site ions. The system attempts to achieve equilibrium and releases this excess from the lattice as exsolved nanoparticles [147], [149].

Another functional property of the exolusion is its reversibility; it was proposed that redissolving exsolved particles into the crystal lattice can be a way to regenerate the material [143]. However, some evidence has shown that process is not entirely reversible [172]. New research suggests that re-exsolution is affected just as in the case of the exsolution itself, which is very much controlled by the defect chemistry [185].

In conclusion, the exsolution sets a new path in preparing ceramic catalysts with metallic nanoparticles. The agglomeration of metallic catalyst and carbon formation is suppressed in the exsolved system. The exsolution is an in-situ method that could be faster, cheaper and gives better access to unreachable locations than conventional methods. Moreover, the method provides better control over the amount and distribution of deposited particles.

1.4.3 Perovskite air electrode

Perovskites have been successfully implemented as the standard solution on the oxygen side, such as popular strontium doped lanthanum manganese (LSM), $La_{1-x}Sr_xMnO_3$, usually with x in a range of 0.15-0.2 [44]. Dopping Sr^{2+} into an A-site occupied by La^{3+} requires a charge compensation that could lead to partial oxidation of Mn^{3+} to Mn^{4+} or formation of oxygen vacancies, depending on temperature and pO_2 [186]–[188]. In the oxygen electrodes atmosphere, the oxidation of B-site cation is predominant, the formation of oxygen vacancies is possible at very low pO_2 below 10-12 bar [187], [188]. Due to the existence of the Mn redox couple, LSM has a very high p-type electronic conductivity, approaching 100 S/cm, at 800 °C in the air [186], [189], but relatively low ionic conductivity, below 10^{-6} S/cm and oxygen exchange coefficient (***k****) as low as 10-8 cm/s, [165]. Therefore, in most cases, LSM is used with YSZ as a composite layer

(LSM/YSZ), where the reaction occurs at 3PB [190]. Usually, about 30% vol. of LSM to YSZ gives the optimal length of 3PB [86]; it is also a minimum to achieve LSM percolation, thus electronic conductivity path through the bulk of electrode [191]. The lanthanum manganate-based oxygen electrodes have a tolerable TEC of 11×10^{-6} [192], [193] and are stable with YSZ at operational temperature. However, LSM and YSZ could react at higher temperatures to form poorly conductive pyrochlore phases, LZO (La_2Zr_2O) and SZO ($SrZrO_3$) [194]–[197]; therefore, the preferable sintering temperature is below 1200 °C. The amount of produced LZO increases with time and sintering temperature and decreases with lower A-site content [195]. Mori et al. suggested that the formation of LZO may be related to the difference in solubility limit of Mn and La in doped zirconia [196] and excess of La react immediately with zirconia; therefore, to suppress the creation of zirconates A-site deficient LSM is being used.

The perovskite $La_{0.6}Sr_{0.4}Co_{0.8}Fe_{0.2}O_{3-\delta}$ (LSCF) [92] [198] is the most studied composition in the family of $La_{1-x}Sr_xCo_{1-y}Fe_yO_{3-\delta}$ used as oxygen electrode in SOFC; it gives superior performance compared to the classic LSM/YSZ oxygen electrode. Very high electronic conductivity has been reported, up to 1500 S/cm in Co rich stoichiometries [199], [200]; which decrease with the Fe doping and achieve 100-300 S/cm conductivity for widely used Fe rich compounds [201], [202]. LSCF has a very high oxygen ionic conductivity; a value of 0.1 S/cm has been reported in the air at 800 °C [203], which increases with Co and even more with Sr content. The oxygen exchange coefficient ($\boldsymbol{k^*}$) is much higher than for LSM, as high as 1.5×10^{-6} [204]' giving LSCF excellent activity for oxygen reduction. The drawback of LSCF is its reactivity with YSZ at a temperature much lower than LSM, which makes it challenging to produce a good interface between YSZ and LSCF without having the insulating zirconates (LZO, SZO) that substantially decrease the performance of the cell [205], [206]. In most applications, to prevent reaction between those components, the additional barrier layers of doped ceria are used [207]. Doped ceria oxides can provide high ionic conductivity and do not react with LSCF. Another issue is a large TEC of LSCF, $19.5 \times 10^{-6}\ K^{-1}$, between 500 and 900 °C. TEC is usually related to the change of perovskite lattice parameter and is associated with defect chemistry, where the oxygen vacancies take a significant part [208].

The lanthanum strontium ferrite electrode (LSF) is also most often used with 20% of Sr doping $La_{0.8}Sr_{0.2}FeO_3$. The advantage of the electrode compared to LSCF is lower reactivity with YSZ; thus, the CGO layer is not required and avoids the carcinogenic cobalt. The disadvantage is much lower electronic conductivity than LSM or LSCF, about 0.75 S/cm for LSF with 20% Sr doping [208], but still sufficient for SOFC electrode purpose [37] if the thin layer is used. However, LSF has a significantly higher oxygen ion conductivity and the oxygen exchange coefficient of its surface than LSM, giving this material a great activity. LSF in the range of 15-25% strontium doping has TEC between 12.8 - 15.2 ($10^{-6}K^{-1}$), which is lower than for LSCF, but still may bring some long-term degradation [208]. Due to a charge compensation mechanism, the electronic and ionic conductivity of LSF increases with higher Sr^{2+} doping, which is the case up to a certain level, as Sr^{2+} cation could start ordering at high levels. Ordering of Sr^{2+} cation and oxide ion vacancies on the surface may reduce the degree of coverage by B site ions and changes in their position in relation to oxide vacancies, which may also play a role in the oxygen reduction mechanism [208].

Air electrode takes part in oxygen reduction reaction (ORR) in fuel cell mode. Similarly, as on the fuel electrode, the series of electrochemical steps on the oxygen counterpart may include gas-phase transport, adsorption, dissociation, transport species along with the electrode and charge transfer reaction [193]. The oxygen gas diffusion into the vicinity of the cathode surface depends on the porosity of the electrode and pO_2, which, if too low, may lead to a limitation at high current density. Usually, 40% of porosity offers the best compromise between gas flow and the size of the surface area/length of 3PB [209]. In most applications, atmospheric air is used as the source of O_2, where pO_2 is equal to 0.21. Two possible paths are considered for oxygen gas reduction, surface and bulk path, depending on the material activity and oxygen ion conductivity [193]. In the surface path, oxygen species would be transported to 3PB and incorporated in electrolyte oxygen vacancies (steps 1-2-3-4 in Figure 1-12). Such a mechanism is proposed for LSM/YSZ electrode, where LSM is considered purely electronically conductive. The predominance of the surface path in LSM/YSZ is related to faster exchange kinetics on the surface of LSM than bulk diffusion [191].

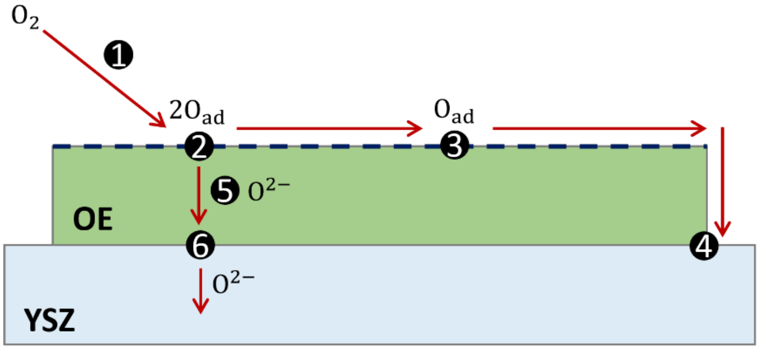

Figure 1-12: Possible mechanism of O_2 reduction on the oxygen electrode (OE) and YSZ electrolyte.

In contrast, the bulk path is suggested for materials with higher oxygen incorporation efficiency and oxygen ion conductivity (as LSF or LSCF), where oxygen will be incorporated in the bulk of perovskite and transported to the electrolyte as oxygen ions (steps 1-2-5-6 in Figure 1-12). The incorporation of oxygen ions is not restricted to the electrolyte/electrode interface but could be stretched to the perovskite surface. Both surface and bulk processes could run parallel; however, the surface path is negligible for good ionic conductors [57]. The primary condition that perovskite must fulfil to attain large ionic conductivity is the high concentration of the oxygen vacancies, through which oxygen transport is performed. There is evidence of a correlation between surface and bulk transport, indicating the involvement of oxygen vacancies in surface diffusion of oxygen species; hence, higher value of surface kinetics for good ionic conductors [57], [164], [210]. Another factor determining electrode activity to oxygen reduction is the type and concentration of B-site cation on the perovskite surface and perhaps their position against oxygen vacancies [208].

1.5 The geometry of SOFC

The fundamental requirement for the construction of SOFC is to assure that the fragile, thin ceramic layers will not crack during production, handling of the system and long term operation. Better cell strength could be achieved by transferring all mechanical load on one of its elements, leaving the other complying with electrochemical functions. Traditionally, cells were supported by a thick electrolyte, bringing significant ohmic resistance [211]. In the electrolyte supported cell, the supporting layer is usually between 150 -300 μm thick [212]. In the next generation of SOFC, the drive to decrease operating temperature required using of electrolytes with higher ionic conductivity, such as Sc_2O_3 stabilised zirconia (SSZ) [213] or lowering the thickness of the electrolyte and the transfer of the mechanical load on the thick electrode, making the latter fully responsible for the strength of the cell [92]. The benefit of lowering the operating temperature in a cell's operation is the reduction of thermomechanical stress and the reactivity between components [99], [214], [215].

Consequently, electrolyte supported cells became the least desirable solution, and the most common are electrode supported, while other solutions rely on inert ceramic or metal supported [31], [37], [216]. Due to relatively high strength and electronic conductivity in the state-of-art cells, the Ni/YSZ support is the most common. Usually, the electrode supported cells are 250-1000 μm [212]. However, thick Ni/YSZ support makes the cells less resistant to rapid temperature changes or re-oxidation [217] and brings a significant mismatch of TEC between the fuel electrode and electrolyte [218]; also, it could affect gas diffusion; therefore, usually, its thickness is reduced to the required minimum.

The use of the oxygen electrode as the load-bearing was also investigated, with some pros and cons. For example, LSM/YSZ oxygen electrode has lower mechanical strength than Ni/YSZ and lower electronic conductivity but is more resistant to redox cycles and temperature changes. The ceramic support is another emerging design, perhaps the cheapest solution but has the highest ohmic resistance [219].

Due to its price, strength, and high conductivity, metal-supported cells [94], [220], [221] could be an ideal design; however, there are problems with their manufacturing. The material proposed for metallic support in SOFC is ferritic stainless steel (FSS). The stainless-steel supported cells have a much higher resistance to multiple thermal and reduction-oxidation cycles. Furthermore, the steel is much cheaper than ceramics used in SOC; replacing a large part of them reduces the cost of the cell [221]. Usually, the ceramic cells are sintered in the oxygen atmosphere at temperatures up to 1500 °C, required for densification of an electrolyte; for metal-supported cells, sintering requires a protective atmosphere, which may be pure hydrogen or its mixture with argon. Also, there is a risk of inter diffusion of Ni/YSZ fuel electrode with the support material and blocking of the reaction zone by chromium [222].

The choice of support may be driven by production method or stack construction. For instance, electrolyte and Ni/YSZ are often co-sintered for large planar cells due to similar, preferable sintering temperatures, followed by printing of LSM/YSZ oxygen electrode and sintering. During a process, the cell must have adequate strength to not break during further processing; therefore, the anode support seems to be an obvious choice [219]. On the other hand, the choice of the cathode support could be dictated by the stack design, as in Siemens/ Westinghouse tubular cells. The use of oxygen electrode support produced a more reliable connection between the cells, requiring a high amount of noble metals, such as silver [52], [223].

There are several different types of SOC geometries. The most common type used by the vast majority of research is the planar construction, Figure 1-13 a. Most of the manufacturing practices of these cells are traditional methods of ceramic materials preparation, such as film casting or screen printing [219], [224], [225]. These methods allow the production of planar cells on an industrial scale. The SOFC with the planar construction is known for their high achievable power density (up to 2 W/cm^2) and relatively simple configuration [216]. In this type, the additional elements called interconnects in the form of bipolar plates join adjacent cells. Interconnects have special channels for the inlet of reagents (to the oxygen from one side and fuel on the other) and provide electrical connections between the single cells. As for other materials used in SOFC, there are several requirements for interconnects/ bipolar plates. They must have high thermal and electrical conductivity, be gas-tight, have chemical, thermal and mechanical stability in cells set-up and operating conditions and preferably have a low cost. Often, conductive ceramics are being used for this application; the most common are the chromium and lanthanum perovskite oxides doped with strontium or calcium $(Ln_{1-x}M_x)CrO_{3-y}$ where M is Sr or Ca [96]. However, planar stacks are difficult to seal due to the high temperature and large perimeter between the electrolyte and electrode interface. High operating temperature requires thermally resistant sealing materials compatible with other cell elements [219]. The low mechanical strength and thermal shock resistance make them difficult to be used in portable or transport applications, where the fuel cells are exposed to vibrations and mechanical stress or abrupt temperature changes [45].

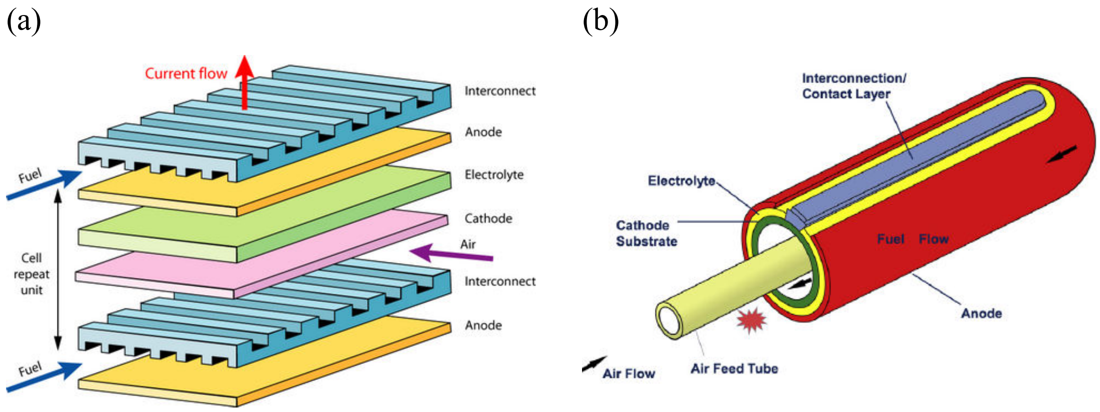

Figure 1-13: The SOFC types by geometry, a) The planar system. b) The tubular cell. Images were taken from ref. [219], [226].

The interest in tubular geometry started from the well-known early design of Siemens Westinghouse tubes, which developed several working systems between 0.4-200 kW, and demonstrated high efficiency during many years of operation [219]. A tubular configuration has much better thermal and mechanical capabilities than planar cells, making SOFC promising to be used in more flexible operating conditions [37]. The tubular geometry introduces more straightforward and more reliable sealing solutions, where an open outlet could be used to burn out unused fuel mixture [51], or the sealing is outside the hot zone of the system [227]. The Micro Tubular Solid Oxide Fuel Cells (mSOFC) were proposed as the alternative, which due to a small diameter, exhibited excellent thermal shock resistance and much higher volumetric power density [45]. The ability to adapt to temperature changes was identified as the most crucial benefit of mSOFC. The small tubular cells have been proposed to be used in different applications than the stationary power unit, as auxiliary power units (APU), including transport applications, typically inaccessible for SOFC [45], [228], [229].

The SOFCRoll design, developed at St Andrew's University, is investigated in this research as alternative geometry. SOFCRoll could be produced entirely by tape casting and co-sintering, methods usually reserved for making planar cells, combining the advantages of thick film manufacturing techniques of the planar system and the high area and robustness of the tubular design [230].

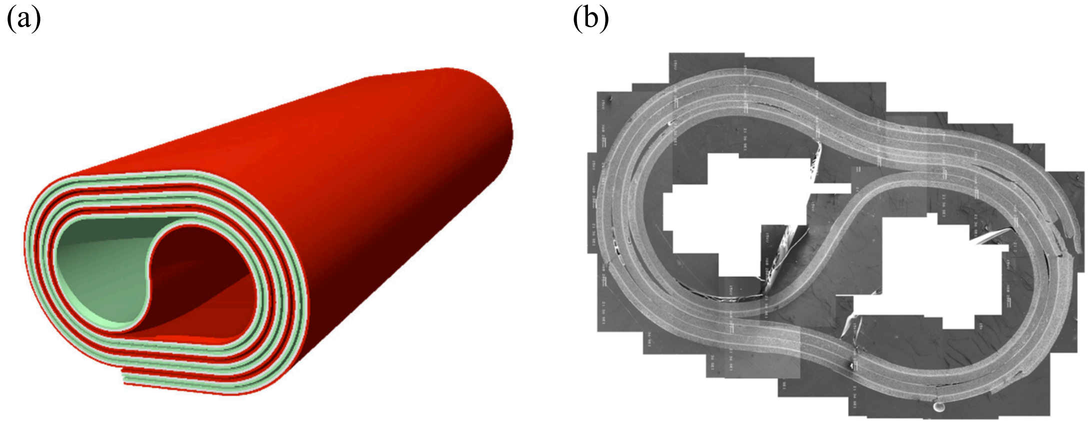

Figure 1-14: The SOFCRoll cell developed at St Andrew's University. (a) Schematic image of the SOFCRoll. (b) A montage image of the overall cell’s crosssection. Images are taken from reference [231].

The work on the SOFCRoll dates back to 2000 when Fran Jones, in her PhD, has developed the manufacturing method, produced the first cells and analysed their microstructure and electrochemical performance [232]. The process was based on tape casting, where all tapes were cast separately, next, hand-laminated rolled and co-sintering in a single thermal step. Most of the active area in SOFCRoll is sandwiched between other layers in a spiral part, thus not available for the external current collector. Therefore, the current collection layers with a high Ni and LSM content were used on top of the standard Ni/YSZ and LSM/YSZ active electrodes. The maximum power generated from cells was about 0.6 W at 925 °C, and the maximum OCV was close to 1 but below the theoretical value [230].

A number of the projects followed the SOFCRoll concept [231]. In his PhD Tesfai [233] produced a bundle with 30 SOFCRoll cells, with the maximum generated power reaching

6 W at 800 °C. Because of the inconsistent cell performance at this time, the quality control test was required to separate cells with comparable performance and gas flow, making them suitable to be used in a bundle. The quality control consisted of three stages: measurement of gas leakage, cathode resistance, and back pressure difference. The average power output from the single cell was 0.5 W, and OCV of 0.935 V. Apart from tape casting, which is a primary method of SOFCRoll manufacturing, screen printing was considered for producing a thinner YSZ electrolyte [234]. The produced layer had a thickness below 10 µm, substantially decreasing the ohmic resistance enabling the cell to work at lowered temperature, down to 700 °C. The total resistance decreased to 0.34 Ω at 700 °C and 0.22 Ω at 800 °C. However, this modification caused many issues, e.g. absorption of the solvent from screen-printed to tape cast layers. The printed layers required longer drying times at a higher temperature (80-100 °C), and they were less flexible and prone to cracking [231]. Attempts were also made to improve the gas flow by introducing channels or chevron patterns in a spiral part of the cell [234], [235], aiming to get more even gas flow in the cell, thereby better gas distribution within a whole SOFCRoll bundle. The chevron patterns were printed on current collector layers, burning off. The new design faced several problems, including the weak bonding and delamination resulting from overlaying YSZ and graphite patterns and handling the tapes due to their rheology [231]. Finally, the concept was simplified and replaced by a tape cast single porous separator YSZ mounted on the cell outlet [236], [237]. Also, co-casting was investigated in SOFCRoll preparation [231]; however, the research did not produce satisfying results. The scope of the proceedings covered the casting of the thin layer of electrolyte on the previously cast electrode and the simultaneous casting of all layers on one tape. The challenges that hindered the realisation of this assignment were mainly issues related to the casting of the tapes with different widths [231]. Nevertheless, progression was to co-cast of dense YSZ layer and porous YSZ layers on both sides. The application of such a construction was the ceramic scaffold for impregnation with active materials on electrode sides. However, due to low porosity, the material concentration inside the porous scaffold was too low to obtain acceptable performance [238], [239]. Consequently, the following projects focused on developing porosity within those layers and aqueous tape casting methods [240]–[242].alternately with solid YSZ and graphite inks, producing YSZ chevron channels after

2 Experimental techniques

2.1 Introduction

Firstly, the chapter summarises experimental materials preparation techniques, processing, and characterisation. The procedures behind those methods have been described in detail. The solid-state synthesis was chosen for LCNT synthesis, while the materials for YSZ electrolyte and LSM-YSZ oxygen electrolyte were purchased. For the tapes preparation and co-sintering purpose, input ceramics were often pre-sintered or/and ball-milled. For slurry formulation, an analysis of the size of ceramic particles was necessary; this was done through PSA analysis.

Next, the techniques for the analysis of the cells were described. Electrochemical measurements and scanning energy microscopy (SEM) were the basis of the conducted characteristics. The SEM technique was employed to identify the microstructure of produced layers and the cell's macrostructure. The last section concerning the electrochemical method clarifies the cell's testing set-up and conditions.

2.2 Material preparation and characteristic

2.2.1 Solid-state synthesis for LCNT preparation

The $La_{0.43}Ca_{0.37}Ni_{0.06}Ti_{0.94}O_{3-\gamma}$ (LCNT) perovskite was prepared using modified solid-state synthesis [156]. The precursors were dried overnight, La_2O_3 (Pi-Kem, >99.99%) at 800 °C for water evaporation and CO_2 desorption, while $CaCO_3$ (Alfa Aesar, >99.5%), and TiO_2 (Alfa Aesar, >99.6%), at 300 °C. For the preparation of 10 g of LCNT, the precursors were weighted while hot (300 °C) and mixed with $Ni(NO_3)_2*6H_2O$ (Acros, >99%) in an 80 mL beaker. The mixture was homogenized with acetone (20 mL) and non-aqueous Hypermer KD-1 dispersant (0.05 wt. %) for 30 min in an ultrasonic probe Hielscher UP200S, operated at 60% of wave frequency and amplitude. After acetone evaporation, the powder was transferred into a crucible and calcinated at 1000 °C for 12 h; at this stage, calcium carbonate and nickel salt decompose to oxides, and materials start to form the perovskite phase. Calcinated material was deagglomerated with isopropanol with a planetary mill operating at 350 rpm for 1 h. After evaporation of isopropanol, the material was pressed into 20 mm pellets and sintered at 1400 °C for 12 h.

2.2.2 Preparation of pre-sintered materials

To prepare 10g of $(La_{0.8}Sr_{0.2})_{0.95}MnO_3$ - $Zr_{0.84}Y_{0.16}O_{2-\delta}$ (LSM/YSZ) composite, the 5g of LSM (Pi-Kem) powder was mixed with 5g of YSZ (Pi-Kem) in an 80 mL beaker with acetone (20 mL) and non-aqueous Hypermer KD-1 (0.05 wt. %) dispersant. The mixture was homogenized in an ultrasonic probe Hielscher UP200S operated at 60% of wave frequency and amplitude for 10 min. After evaporation of acetone, the material was pressed into 20 mm pellets and sintered at 1200 °C for 5 h.

The YSZ with a large particle size for porous layer manufacturing was produced by sintering YSZ pellets. In the method, 5g of the commercial YSZ powder was pressed into 20 mm pellets and sintered at 1350 °C for 5 h. After sintering, pellets were crushed to homogeneous powder in a mortar, and the material was ball milled for the required time to produce a homogenous powder with a specified size of particles.

The YSZ or LSM powder was placed in the crucible and pre-sintered at the required temperature and time for powder agglomeration to prepare the pre-sintered material. Where required, pre-sintered material was deagglomerated by ball milling in a roller mill overnight at 160 rpm in deionised water.

2.2.3 Ball milling and particle size analysis (PSA)

The sintered pellets were crushed with a stainless-steel mortar and ball milled in a planetary mill at the required speed with the addition of isopropanol for the required time to produce a homogenous powder with a specified size of particles.

The size of such prepared powders was analysed with a laser diffraction-based method, in isopropanol, following the breaking of the agglomerates in the ultrasonic bath. Laser diffraction is a standard method for particle size measurement, and Malvern Instruments Mastersizer 2000 PSA analyser was used for analysis. Two essential elements are included in the measuring unit, optical batch and sample dispersion unit [243]. When the laser beam passes particles suspended in the carrier in the optical bench, it scatters, and the intensity of the reflection is analysed by a series of detectors for both red and blue wave lights and a wide measuring angle. The sample is dispersed mechanically and by ultrasonic waves in a dispersion unit containing appropriate suspension, e.g. isopropanol or deionised water.

2.3 Scanning electron microscopy (SEM)

SEM microscope produces the sample image by scanning it with the electron beam. The electrons interact with the sample at a certain depth producing signals that reveal the sample image and information about its topography and composition [244]. Scattered electrons could produce various signals, including secondary electrons (SEI), backscattered electrons (BSE), Auger electrons, X-rays, scattered electrons, diffracted electrons, and transmitted electrons [245].

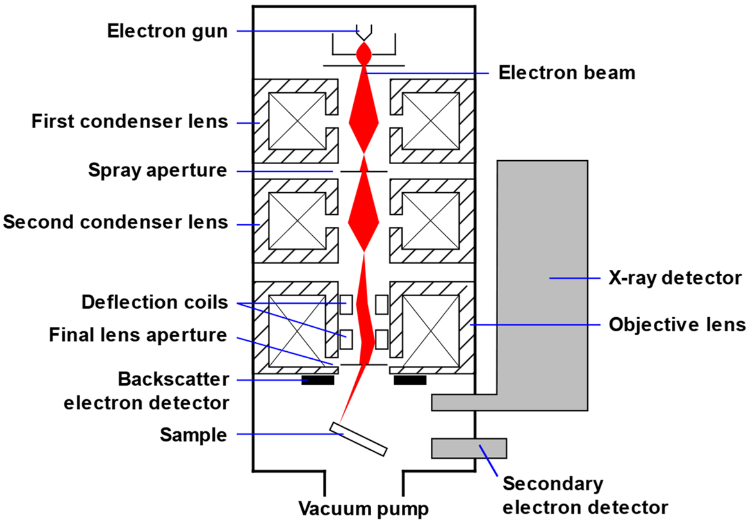

Figure 2-1: Diagram of Scanning Electron Microscope. The image is taken from reference [246].

The SEI and BSE methods were used to acquire images of analysed samples through the project. SEI detects atoms excited by an electron beam; secondary electrons have relatively low energy; hence, they can escape from only a few nanometers of the sample's surface. The secondary electrons are highly localised on the measured point (point of contact with an electron beam), giving the high resolution and magnification image. The backscattered electrons are reflected from the sample via elastic scattering. With higher energy than secondary electrons, they emerge from a deeper location, and as their intensity is dependent on the material's atomic number, they could give information about the distribution of various materials within the analysed sample [245].

The images were acquired with FEI Scios, JEOL JSM 6700 and JEOL JSM 5600 electron microscopes. The high-magnification SEI analysis was used to obtain information about the morphology; the sample was mounted on the holder with carbon tape and a silver current collector. Gold or carbon coating is often used on poorly conductive ceramics to prevent electrostatic charge accumulation and obtain a better quality image with higher magnification. Many of the analysed samples were tested without any coating, as the method could give false information about some of the sample properties, e.g. size and geometry of metallic particles or surface morphology. When ceramic material has low conductivity, analysis at low voltage gives the best image quality. The electron microscopy using the BSE imagining gave information about the cell structure, such as the thickness of ceramic layers, the microstructure, and defects. BSE method is advantageous, where a high contrast between the materials is required, e.g. for the porosity analysis. For the analysis sample to be placed in the resin and polished, the contrast between resin and ceramic gave information about the material structure.

2.4 Conductivity measurement

For the conductivity measurement, the rectangular pellets were pressed and sintered at 1350 °C for 5 h. The samples were 5 x 15 mm in area and 5 mm in thickness. The golden wires were attached to four locations on the sample and consolidated with golden paste and ceramic sealant.

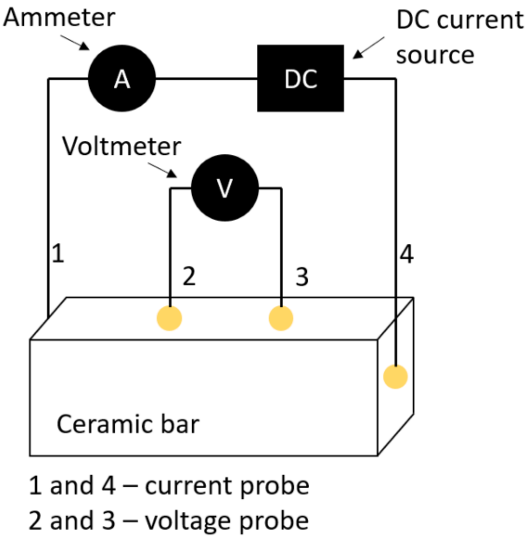

Figure 2-2: Diagram of the four-probe method for conductivity measurement [247].

The conductivity was measured with the four-probe method. Two outer probes were connected to the current source, and a digital voltmeter measured the voltage across the inner probes [247]. The conductivity of the sample was calculated from the equation:

$$\sigma = \frac{I}{V} \times \frac{S}{A} \ [\mathrm{S/cm}] \qquad \textbf{Equation 2-1}$$

Where ***I*** is the current at outer probes, ***V*** is the voltage measured on the inner probes, ***A*** is the sample's cross-section, and ***S*** is the distance between two inner probes.

2.5 X-ray diffraction (XRD)

The XRD analysis was carried out with PAN analytical X-ray diffractometer with CuKα1 radiation (λ = 1.54056Å) in the range 2θ = 20-100.

The XRD method uses the intensity of the scattered X-Ray beam from the sample as a function of the angle. XRD is a primary method to study the crystal structure of the materials, lattice cell parameters, the presence of a secondary phase.

2.6 Electrochemical testing

The silver paste was used as the current collector for all cells, and, depending on the type, the cell was mounted on the appropriate rig and sealed with Ceramic cement (Ceramabond 552, Aremco). The lead wires attached to the steel tubes were connected to the testing station Solartron 1287 Electrochemical Interface and CorrWare v3.2c software (Scribner Associates).

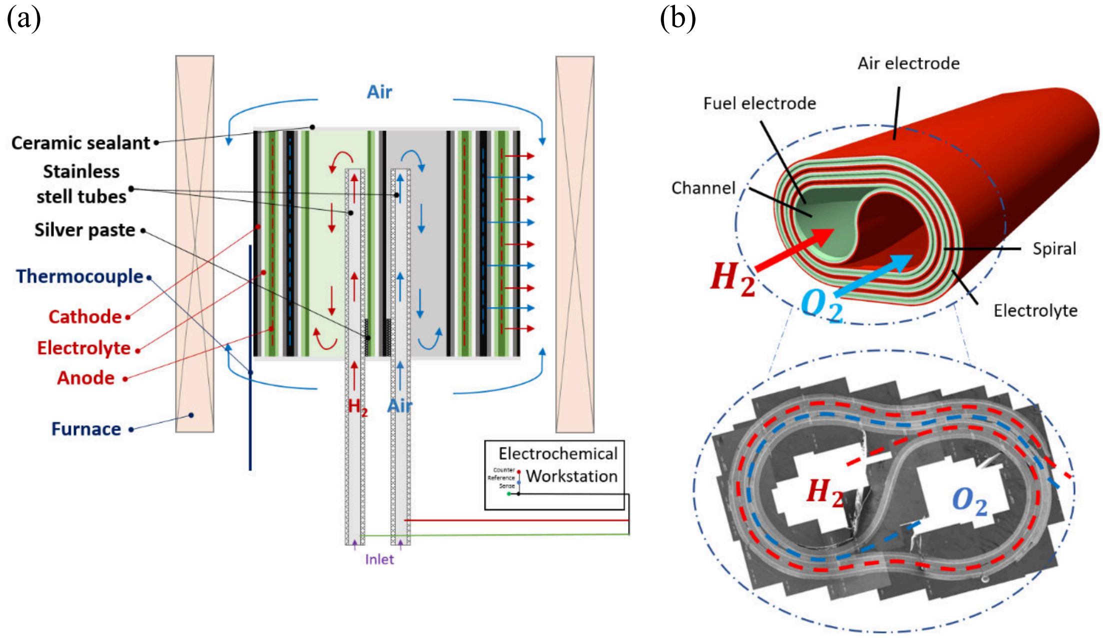

Figure 2-3: SOFCRoll principle of operation. (a) Cell's set-up and diffusion path. (b) Front view and diffusion path.

In the SOFCRoll, the layers were laminated together and rolled in a spiral shape consisting of two main inlet channels for the air and hydrogen-based fuel. The silver paste was used as a current collector to improve connectivity between a cell and stainless-steel tubes inserted into cell channels. The silver paste was applied pointwise to connect the steel tube with the current collector layer in the original design. The role of the steel tubes was to supply the reaction gases and collect the current. Ceramic sealant was used between the steel tubes and the cell. During the operation, gases travelled from the tubes to the cell's inlet channels and through the porous network of electrodes along the spirals to the outlet along the cell's length, Figure 2-3.

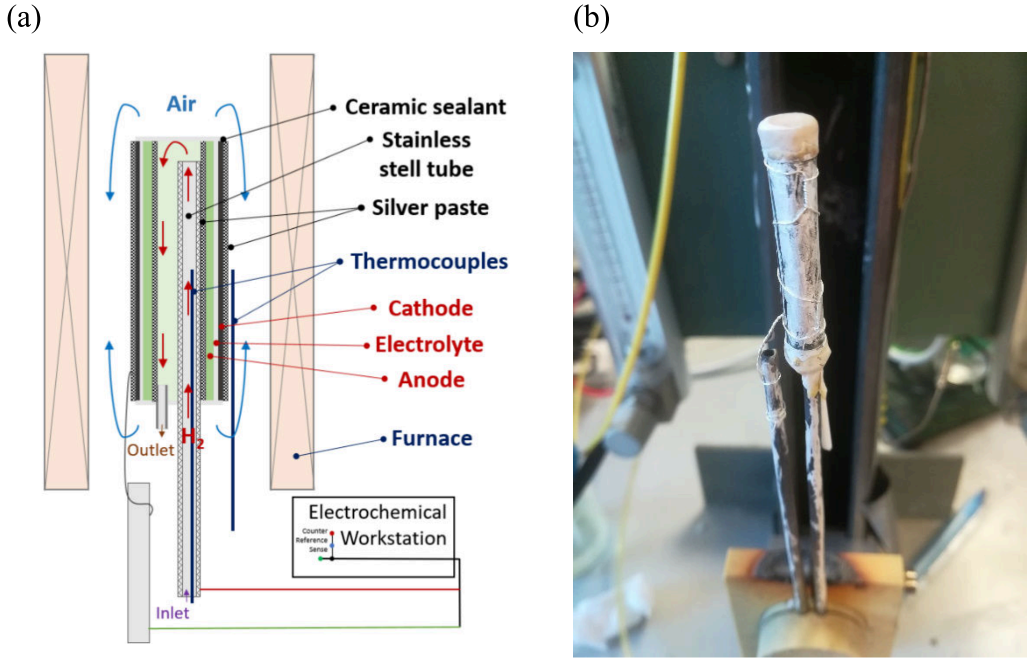

Figure 2-4: The testing set-up of the tubular cell. (a) Schematic image of tubular cell mounted on the testing rig with the gas flow. (b) Image of tubular cell mounted on the testing rig.

The central channel of the tubular cell is a fuel chamber, while the outer layer makes the cell's oxygen electrode, Figure 2-4. Fuel goes in by a stainless-steel tube to the main compartment during the operation. Unreacted gas is discharged outside through the outlet at the bottom or top of the cell and burned off. For the electrochemical tests, the entire surface of the electrodes was covered with the silver paste used as a current collector. The top part of the stainless steel tube used as the fuel inlet and connected with the measuring equipment was inserted into the cells channel and sealed. The oxygen electrode was in contact via the silver wire with measuring equipment. The cell was sealed with the ceramic sealant applied among the steel tube and gas outlet; and at the top of the cell. A K-type thermocouple placed next to the cell at its half-width monitored the temperature inside the tubular furnace.

Figure 2-5 illustrates a schematic graph of the symmetrical sample and the configuration of the testing rig. Before the electrochemical test, a silver current collector paste was painted to cover all electrode surface and connected through silver wires with testing equipment (Figure 2-5 b). The planar cells were attached to the alumina tube of the rig. The cell was fully sealed for testing the planar fuel cell, and H_2 gas was directed through the ceramic tube to the cell fuel electrode; for the measurement of symmetrical cells with oxygen electrodes, the samples were not fully sealed to test in the air atmosphere.

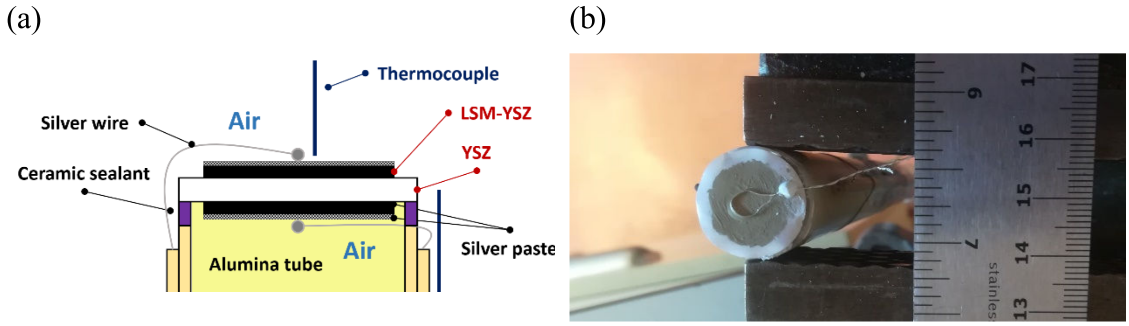

Figure 2-5: The testing set-up of the planar cell. (a) Schematic image of symmetrical LSM/YSZ planar cell mounted on the testing rig. (b) Image of YSZ planar cell with the silver current collector.

Standard measurement was carried out at a temperature between 700 °C and 800 °C. Usually, wet hydrogen (3% H_2O/H_2) was used for a fuel cell operation as the fuel (dry H_2 was directed through a bubbler at room temperature) and air for the oxygen electrode. The electrochemical impedance spectroscopy (EIS), the current-voltage (I-V) and the potentiostatic measurements were carried out with the use of Solartron 1255 Frequency Response Analyser, Solartron 1287 Electrochemical Interface, CorrWare v3.2c and ZPlot v3.2c software (Scribner Associates). For a standard measurement, the impedance spectra were taken in 100000 Hz – 0.1 Hz frequency range, with 10 or 7 points per decade and the excitation voltage amplitude equal to 20mV.

The inductance and resistance of the silver wires were determined from the measurement of short-circuit analysis. The modelled data of planar cells were corrected by the inductance value equal to 8.11×10^{-7} and the rig's resistance of 0.24 Ω. While SOFCRoll and tubular cells by the inductance equal to 5.2×10^{-7} and the ohmic resistance of rig equal to 0.1 Ω.

The impedance spectra were fitted using Z-view software to the equivalent circuit made by model elements of individual processes, which uses complex nonlinear least-squares (CNLS) approximation [66].

3 Manufacturing techniques

3.1 Introduction

The main objective of this work is to produce an operative SOFC using the chosen methods and techniques; therefore, a separate chapter is devoted to manufacturing methods employed in the project.

The first part concerns the theory behind tape casting and its applications for thick film processing in SOC manufacturing; it gives an overview of the various materials used for slurry preparation and describes the preparation of the tape casting set-up and its control during the casting. The slurry preparation for organic tape casting consists of multiple steps, and they are fully characterised by the details of materials, equipment and working conditions. The primary way of cell assembly is described next; with the development of cells, the method has been improved, and all details are described in the following chapters.

Cell preparation is based on the co-sintering of multiple layers in a single thermal step. Following the original method, the technique was characterised. Crucial for the method is to control the shrinking profile of individual layers while optimising their microstructure; those parameters were controlled by particle size and slurry composition. The new technique was developed for shrinking profile analysis, based on in-situ analysis of the tape placed in a tubular furnace and photographed during thermal treatment. This chapter provides details on setting up the experiment and how to analyse the data.

The chapter also includes a description and guidelines for the impregnation to produce the fuel cell's electrode, investigated in the final part of the project.

3.2 Tape casting method for SOFC preparation

For the production of SOFC, thick film processing, usually, tape casting and screen printing, are the method of choice. The popularity of tape casting and screen printing for SOFC preparation comes from their widespread use and commercial availability in other industries, such as paper, plastic, paint and electric boards [248], [249]. Those two techniques allow producing a wide range of materials with porous or dense microstructure and a broad range of thicknesses. The produced layers are primarily deposited on the planar, smooth surfaces and could be easily adapted to produce a planar type of SOFC. For the fabrication of curved and uneven surfaces in tubular cells, other technics based on slurry deposition are preferable [212], including extrusion, jet printing, dip coating, spraying and spin coating [207], [220], [250]–[252].

Screen printing involves the ink deposition through the fine mesh to fill the pattern, and the printing machine distributes the ink over the entire surface of the screen [225]. The ink contains the organic carrier and material to be deposited. The material is pressed through the mesh directly onto the substrate; therefore, screen printing can not be used independently, for example, for a supporting layer in cell assembly. The thin layers down to 5 µm could be produced [212]; the multiple printing steps are being used for thicker layers, which, when finished, are being sintered.

Tape casting allows producing thin and uniform layers with a large surface area by a simple and easily scalable methodology. An extensive review of the technique and methodology of producing ceramic layers could be found in the well-known study by Missler [248]. Figure 3-1 shows the basic principle for tape manufacturing on the laboratory scale, reflecting the tape casting method used in many industrial processes, with the most characteristic elements being a stationary doctor blade, moving carrier and drying chamber.

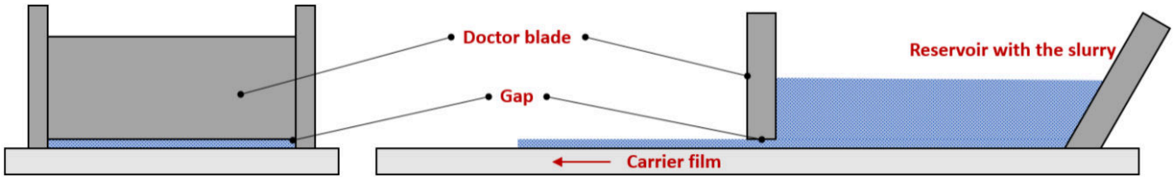

Figure 3-1: The principle of tape casting.

The recommended thickness of the green tapes is between 0.025 and 1 mm [248], but even thinner tapes have been reported, down to 10 µm [212], [253], [254]. Such thin tapes are difficult to handle and easily crack if, after sintering, they are subjected to other deposition methods like screen printing; therefore, they must be cast or laminated on another green tape and co-sintered.

Multiple ceramics could be mixed in the slurry to produce either one-phase or composite layers. The type of ceramic particles used for slurry preparation determines the functionality of the layer. Distribution of the ceramic particle's size and shape and used pore-former, tailor the microstructure of ceramic layers, like the length of 3PB or porosity. The size and shape of ceramic particles determine their position and thus the length of adjacent surfaces and the free spaces between them. Small particles with high surface area and wide particle size distribution are preferable to produce a densely packed bed, as adjacent surfaces are prone to sintering, and small particles fill space between larger pieces [248], [255]. With a more regular shape, the larger particles produce a higher porosity. The addition of pore formers could additionally tailor the microstructure of ceramic layers, e.g. graphite or starch, which burns out, producing additional space between particles.

Besides solid components, the slurry contains organic ingredients, such as solvent, binder, plasticizers and dispersant, which function is to obtain castable slip that holds ceramic particles together, which after drying will produce the strong, homogeneous and elastic tape [248], [255]. The solvent distributes the slurry ingredients homogeneously and gives a "fluidity" to the solution [256]. There are two fundamental techniques in tape casting, depending on the chosen solvent, which could be organic or water-based. The solvent selection determines other components of the green body of the tapes; and often the type of pore former. The water-based slurries are less harmful, but organic-based solutions are more popular because of green tape's quick evaporation and better physical properties [212]. The binary solvent is often used for slip formulation for organic tape casting due to its better ability to dissolve the individual compounds [257]. The binary solvents also give better control over the drying rate of the tape. In the mixture of MEK and ethanol used here, the ethanol increases the drying rate, allowing effective handling of the slurry and reducing the formulation of a "skin" on the top of the slurry reservoir [258]. The binder's role is to hold the solid particles in the slurry together in a polymer matrix. The binder determines a green tape's physical properties, such as its strength, elasticity or smoothness. Butvar B-98 (Sigma Aldrich) is a tradename of polyvinyl butyral (PVB), the most popular binder used in the field [248]. Plasticisers in the slurry enhance tape characteristics, making them more flexible or plastic, enabling them to bend and making them less prone to cracking [248], [259]. The first type of plasticiser, so-called "Type 1", dissolves in a binder and chemically softens polymer chains of the binder, allowing them to stretch. Whereas "Type 2" plasticisers physically affect polymer chains between particles, it works as a "lubricant" that allows the reversible deformation of the matrix. For the slurry formulation PEG was used as Type 1 and DBP as the Type 2 plasticiser. For YSZ electrolyte slurry, a dispersing agent was used to prevent their agglomeration due to the very high surface area of YSZ ceramic particles (Triton). Thus they can be evenly coated by other slurry ingredients, offering a lower viscosity and generally better quality of electrolyte. Besides organic polymer and solid particles, a third primary phase in the tape is porosity formed due to the solvent's evaporation. Some porosity is reduced during the drying process and almost entirely disappears when organic compounds are burned [248].

3.3 Slurry formulation and tape casting

All cells were fabricated by the organic tape casting technique used by Fran Jones in her PhD thesis [260]. For the slurry preparation, the mixture of Methyl ethyl ketone (2-butanone) (MEK, Fisher) and Ethanol was used as the organic solvent (3:2 by weight). The fine ceramic powders were mixed with a solvent, pore former, graphite or its mixture with starch for the electrode slurries. The mixture was homogenised with 30 zirconia balls in the 125ml Nalgene bottle in a roller mill at 160 rpm for a minimum of 18 h. In the second step, the mixture was ball milled for 4 h at 100 rpm with plasticisers, the Polyethylene glycol (PEG, Sigma-Aldrich) and Dibutyl phthalate (DBP, Sigma Aldrich) binder Butvar B-98(Sigma Aldrich). This step is to mix the organic components and dissolve the binder thoroughly. The electrode layer could be cast after the second stage of mixing. For the YSZ electrolyte preparation at the first stage, the dispersant Triton Q-44 (Sigma Aldrich) was added, but not pore former. All mixing steps were the same as for electrode slurry, but after the second step of mixing, the slurry was kept for 24 h at 10 rpm to break possible air bubbles.

A slurry is poured into a reservoir adjacent to a doctor blade, placed on a moving carrier, or previously cast and dry tape on the carrier for co-casting. The polymer film (Mylar^{TM} foil) is used as the carrier, on one side covered with an agent allowing the separation of produced tape. The carrier's speed and viscosity of the slurry should be maintained to ensure the even distribution of the liquid. The size of the casting gap, slurries viscosity and carrier's speed are the main factors maintaining the thickness of produced tapes.

3.4 Cells assembly

Tapes either were laminated or cast successively in required order on each other, with different arrangements described further in the experimental chapter for cell preparation.

Symmetrical planar cells were prepared by lamination. Tapes were cut into a circular shape with a diameter of 2.5 cm for electrolyte and smaller size, 2 cm or 1cm electrodes and co-sintered at standard conditions used in the project. The cell was assembled so that electrode was in the centre of the electrolyte. Assembly had two electrolyte layers and a cathode layer on each side of the cell.

The small tubular cells were rolled on an 8 mm stainless steel tube and reinforced with 0.5 x 10cm electrolyte stripes. Similarly, SOFCRoll, but two tubes were used, and tapes were rolled in between them into a double-circle/ spiral shape. Various method of assembly was investigated, characterised in the following chapters.

3.5 Co-sintering for cell manufacturing

Due to the sintering temperature of YSZ, the conventional planar SOFC is usually produced with at least two thermal steps, where the sintering of YSZ electrolyte and Ni/YSZ fuel electrode is followed by applying and sintering of LSM/YSZ oxygen electrode [261], [262]. The YSZ starts to densify above 1200 °C and creates a fully dense layer at a temperature above 1400 °C; the exact temperature depends on the dwelling time and size, and surface area of YSZ powder. In contrast, LSM based oxygen electrodes are typically fired at temperatures 1200 °C and below, primarily due to LZO and SZO creation at higher temperatures [194]–[197] also LSM sintered at a higher temperature decreasing the length of 3PB. Wang et al. [263] reported much higher polarisation in cells with co-sintered LSM/YSZ than in the cells where LSM/YSZ was sintered in a separate step at 1200 °C. Even without detection of LZO or SZO, the co-sintered cell had about 30% lower performance than one sintered in a multiple-step. The co-sintered oxygen electrode had a substantial contribution at the low frequency, which was argued to be related to the reduction of 3PB.

Following the Jones method, Ni/YSZ fuel electrode was co-sintered with LSM/YSZ oxygen electrode and YSZ electrolyte. Next, the Ni/YSZ fuel electrode was replaced with LCNT based fuel electrode. All layers were co-sintered at 1350 °C [260]. The chosen temperature was a compromise to achieve a sufficiently dense electrolyte. In the last investigated design, the composite electrodes were replaced with porous YSZ backbone and impregnated afterwards, eliminating problems related to co-sintering and allowing to attain the better activity of electrodes. As only YSZ electrolyte and porous YSZ backbone were co-sintered, the temperature was increased to 1450 °C, ensuring much better densification of electrolyte material.

Co-sintering is the method of choice for SOFCRoll preparation, as due to quite elaborated structure, the individual layers cannot be deposited separately and sintered in the lower temperature. However, for the preparation of tubular cells, co-sintering of tapes is also an attractive alternative [49], [264]. The standard way to produce a tubular cell is to extrude tubular support first and dip-coating to deposit other layers, which could be sintered in the following step [252]. The drawbacks of extrusion are the long drying time of extruded tubes and the high capital cost. In contrast, co-sintering of tapes brings several benefits, such as improvement of interface between materials, simplification of the manufacturing process and cost reduction [107], [221], [265]. Soydan et al. [266] analysed the production costs of microtubular cells and reported that sintering is the most expensive parameter to consider after material cost. By decreasing three thermal steps to two, production costs dropped by 9%. The drawback of the method is the possibility of mentioned earlier reaction between materials and development of defects, for instance, wrapping, delamination and cracks, if co-sintering is not well controlled. The co-sintering method requires controlling the sintering rate of individual materials; otherwise, stress is built in the cell's structure [267]. The rate of densification could be controlled by the size of ceramic particles and slurry composition.

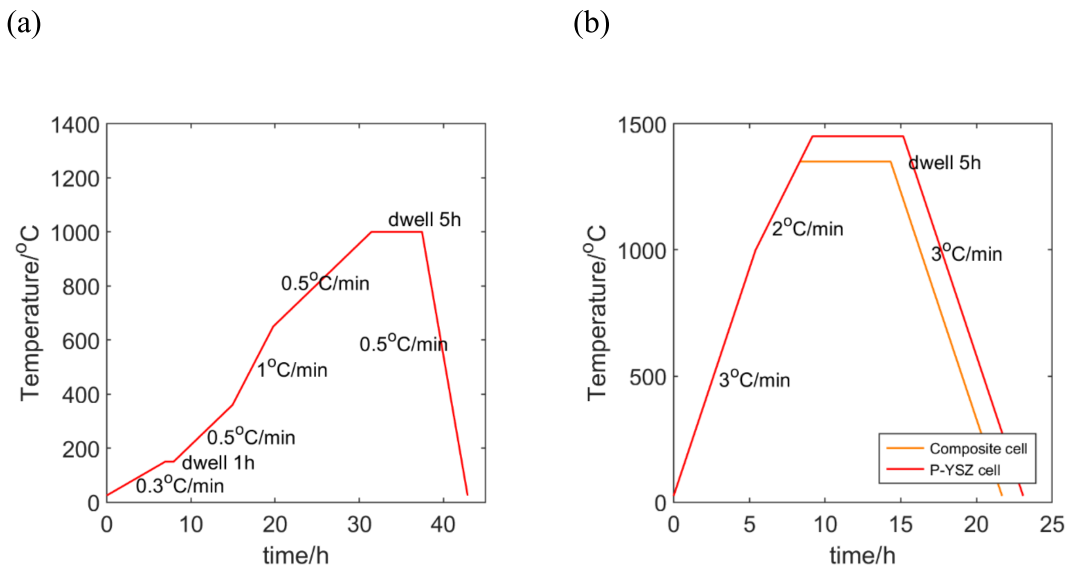

Figure 3-2: Heating profile for fabrication of the cells. (a) Calcination step. (b) Sintering step.

The heating profile includes two thermal steps; at the first step, cells were heated up to 1000 °C at a prolonged rate (Figure 3-2 a) to burn off organics and pore-formers and densify ceramic particles to produce a structure that is possible to handle. To prevent flattening, at this stage, both tubular and SOFCRoll cells were sintered horizontally, with their channels placed on thin alumina tubes, while the planar cells were sintered under the alumina plate to prevent bending and produce flatter surfaces. After dwelling for 5 h, cells were cooled down to room temperature with 3 °C/min cooling rate. At the next stage, the cells were sintered at 1350 °C for 5 h, Figure 3-2 b.

3.6 Analysis of shrinking profile

During thermal treatment, tapes change their volume due to the burning of organic ingredients and the densification of ceramic materials. Due to their composition and properties of ceramic material, the tapes included in the cell's assembly shrink at different rates and degrees, leading to structural defects. The previous work on SOFCRoll revealed that it feasible is to control the shrinkage profile, so the volume change of materials is as close as possible [230], [232].

At the first stage of the heating process, up to 300 °C, the first change of size occurs due to the burning of the organic compounds (binder and plasticisers), which holds the tape's green body in solid colloidal suspension. Between 1000-1350 °C, depending on the material, comes to a further reduction in volume resulting from material densification. Consequently, in the first stage, the main feature affecting the volume change of the green tapes is the quantity of individual organic ingredients, while in the second stage, the amount, size and type of ceramics powders and pore formers in the slurry.

The primary technique to characterize the shrinking profile of tapes used for SOFCRoll preparation depends on measuring the tape's dimension at increasing temperature steps when placed in the muffle furnace and cut into rectangles [232]. The tape rectangles were heated up to the specific temperature step, cooled down and measured when removed from the furnace. The method let many samples be measured at once, and good reproducibility was achieved [232]. However, the technique was rather long and had a high energy requirement; also, it was not entirely accurate. Tapes may interact with the surface on which they are located (in this case, the alumina plate), which distorts their shrinking profile; the tape could also bend or change its shape. Dilatometry is another way to measure material volume changes during thermal treatment. In the method, constant pressure is applied to the sample through a pushrod. A change of its position shows shrinkage of the material [268]. However, dilatometry also brings difficulties in determining the shrinking profile of tapes [260]. A few percent errors could be produced, mainly due to the sample curling and low thickness. Other errors are also possible, such as adhesion of the tapes to the spacers when organics burn off and sintering the material to the spacers, artificially increasing shrinking.

Therefore, more accurate for dilatometry is the testing of shrinkage of ceramics only, using dense pellets, which is not correct compared to the shrinkage of the tape. The shrinking of the electrode tape will differ from dense pellets due to using a pore-former. While in the case of tapes of dense material, e.g. YSZ electrolyte tape, dilatometry and tapes analysis gives similar final shrinking, but its profile is unlike, likely due to using an organic carrier and due to different alignment of particles to each other in both cases (Figure 3-3).

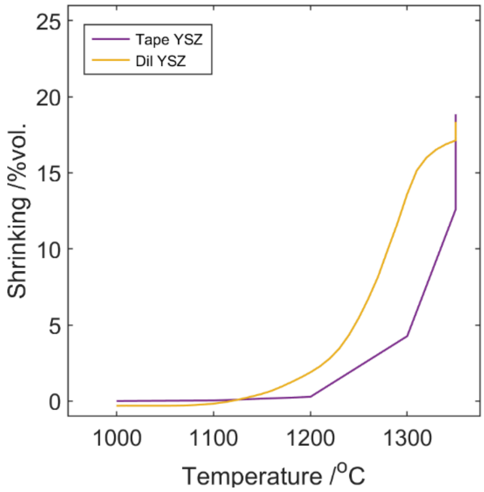

Figure 3-3: Comparison of measurement of YSZ particles in tapes and with dilatometry.

In the presented research, to analyse the shrinking, a new method was developed based on the rectangle's measurement but allowed for continuous in-situ analysis without interacting with the measured sample. The sample tape was attached to the sample holder and placed in the centre of the tube furnace, Figure 3-4 a. Next, the furnace was heated under a set profile, and the sample was photographed during the whole process by the digital camera. The heating rate was 1 or 2 °C, depending on the adopted method; the image was taken every 25 minutes, up to 1350 °C and dwelled for 5 h. The low-temperature heating profile differed significantly from the one in which the cells were sintered. Primary this difference was related to the limitations of the tube furnace controller, where 1 ° C/min was a minimum heating rate. However, as experience showed, the faster heating rate was sufficient to visualize the behaviour of tapes when heated to prevent defects; and significantly reduced the time of the experiment.

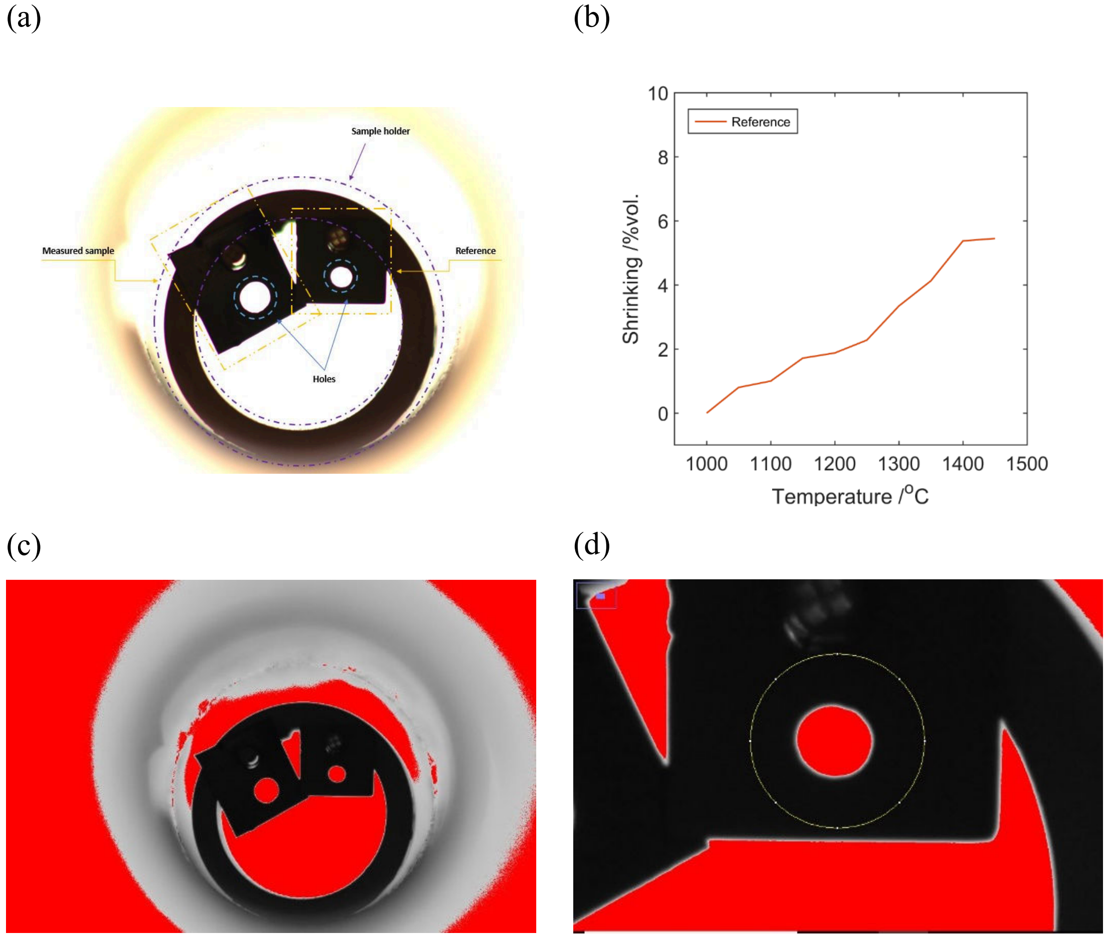

Figure 3-4: The shrinkage measurement with the use of ImageJ software. (a) Sample holder and test set-up for high-temperature tube furnace shrinking measurements. (b) Measurement of reference size at the constant threshold. (c) Image with 8-bit grayscale and under the applied threshold. (d) Closed-up of reference hole.

Afterwards, the tape's size was analysed on the successive photos with ImageJ software [269] to calculate the dimension change. The shrinkage profile comes from measuring the size of the hole in the centre of the sample. In the method, the 1×1.5 cm square of 4 layers of laminated tape of analysed material was hung on the alumina bar in the sample holder, next to the ceramic square of already sintered tape, which is a reference in the experiment. The reference is required, as during the heating up, changing light intensity interferes with the experiment by artificially changing the size of measured holes; as in Figure 3-4 b, at a constant threshold and changing temperature, the measurement shows the 6% shrinking of reference size, but the size of reference sample does not change.

With the use of ImageJ, the size of the hole could be measured. First, the image was converted to the 8-bit grayscale. In an 8-bit grayscale, a picture has an assigned 0 - 256 scale, corresponding to the different intensities of grey [270]. The intensity 0 makes the pixel black, while 256 represents white. Next, a threshold is applied to the picture (Figure 3-4 c), which divides an image into separate classes of pixels, usually called "foreground" and "background" [271]. Threshold separates the pixels with the desired intensity from the background, and it becomes possible to measure the number of pixels in the area of interest (Figure 3-4 d). As the intensity of light changed during the heating up of the sample, the amount of the measured pixels changed. Therefore, the threshold is adjusted at every step regarding the number of pixels from the reference. After the whole area is measured, its diameter is calculated, change in the diameter shows the shrinkage behaviour of the tape.

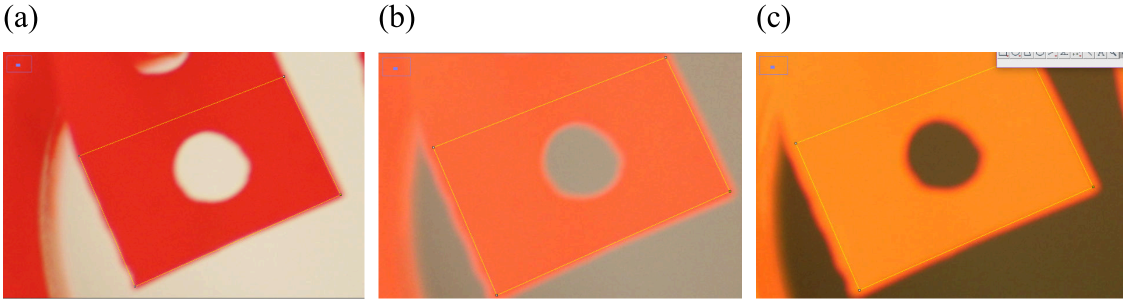

Figure 3-5: The reference sample at various temperatures. (a) 700 °C, (b) 800 °C, (c) 900 °C.

The advantage of the method over the measurement of rectangles is the ability to conduct it in-situ without interacting with the sample, not exposing it to damage. Also, as the sample is suspended on an alumina bar, the main body does not interact with other material, changing its shrinking profile and obstructing its movement. The sample did not bend, which brought the highest error in other methods [232]. Moreover, many readings could be attained; the rectangles measurement gave a small number of measured points, as more points would require many thermal cycles. The drawback of the method is the possibility of measuring only one sample at a time due to the tube's size in the furnace.

Another problem is a significant error in the range of temperature 700 °C – 1000 °C. Due to the change of light source of the picture, from external light to the internal light from the sample, sample holder and the tube, when it starts to shine due to the high temperature. Generally, even when comparing already sintered tape, the expansion of the ceramic is visible (compare the change of the sample size in relation to the orange rectangle in Figure

3-5); such a dimensional change is not possible for the reference; the sample also does not bend. After reaching a temperature of 1000 °C, the measurement stabilises. Therefore, the measurement using this method was divided into two temperature ranges: one for the low-temperature measurement between 0 – 600 °C, and the second for the range 1000-1350 °C and higher.

3.7 Impregnation

The 0.5M solution of $La_{0.43}Ca_{0.37}Ni_{0.06}Ti_{0.94}O_{3-\gamma}$ was prepared by dissolving high purity precursors $La(NO_3)_2•6H_2O$ (Alfa Aesar, >99.9%), $Ca(NO_3)_2•4H_2O$ (Alfa Aesar, >99.0%), $Ni(NO_3)_2•6H_2O$ (Acros, >99%) and $C_6H_{18}N_2O_8Ti$ (Alfa Aesar, 50% w/w aq. soln.) into deionized water according to stoichiometric proportions. Similarly, for preparation of 0.5M $La_{0.8}Sr_{0.2}FeO_3$ solution, $La(NO_3)_2•6H_2O$ (Alfa Aesar, >99.9%), $Sr(NO_3)_2$ (Merck, >99.0%), and $Fe(NO_3)_2•9H_2O$ (Merck, >98.0%) precursors were dissolved in deionized water.

The solutions were placed on the magnetic stirrer to accelerate the dissolution of salt and for homogenisation. The porous YSZ backbone with porosity exceeding 80% has been co-sintered on a dense YSZ electrolyte layer and impregnated with a nitrate solution by micropipette or painting with the brush. Beforehand, another cell side was painted with a viscous liquid, e.g. glycol or nail polish, to prevent possible leaking of the solution through micro-cracks or pinholes in the electrolyte. After every impregnation, the material was calcinated at 700 °C and sintered in the last step (850 °C for LSF and 1100 or 1200 °C for LCNT). The sample was weighted to determine the amount of impregnated material, and multiple cycles were conducted to acquire the required volume concentration. The amount of impregnated solutions was measured by the weighting of the sample after the sintering step. The aimed amount of impregnated LSF was 30% by vol., while for LCNT, 50% by vol.

4 SOFCRoll with Ni/YSZ based electrode

4.1 Introduction

The chapter concerns the research done on SOFCRoll with a Ni/YSZ based fuel electrode. In those early trials, the cells were produced with an original method and had up to six ceramic layers made of state-of-art materials stacked together and laminated.

The original production method was described, and such cells were produced. Next, the modifications of the assembly method were proposed, starting from the alternative cell's assemblage by lamination ending with the first attempt to co-cast all layers.

The cell's structure was investigated using SEM analysis, which exposed the changes in the structure with the modifications in the production method. The defects that arose during the cell's co-sintering were revealed. Also, the shrinking profile of produced tapes was analysed with the previously presented method.

The cell's performance was characterised by I-V and EIS analysis, and various batches were compared; in addition, the DRT was employed to make it easier to determine the number of individual processes, type, characteristic frequency or resistive contribution.

4.2 Slurries preparation for SOFCRoll with Ni/YSZ based electrode

The large part of the SOFCRoll electrodes is sandwiched between other layers and is not physically available, making it unfeasible to apply the current collector mesh or silver paste on the whole surface area of electrodes. Therefore, co-sintering of the highly conductive current collector layers on the active layers was proposed [232].

SOFCRoll based on a Ni/YSZ fuel electrode was assembled with standard YSZ electrolyte, Ni/YSZ fuel electrode and LSM/YSZ oxygen electrode. Every electrode had two layers in the investigated design, the current collector and the active layer.

The electrolyte had one or two of the same layers laminated together; the cell had up to six layers.

Table 4-1: Concentration [% vol.] of materials in the solid part of slurry for original SOFCRoll with Ni/YSZ electrode [232].

Material	Electrolyte (YSZ)	Active OE (LSM/YSZ50)	Current Coll. OE (LSM)	Active FE (Ni/YSZ60)	Current Coll. FE (Ni/YSZ20)
Graphite	-	62.16	63.94	40.5	50.5
YSZ	100	19.75	-	27.9	6.35
NiO	-	-	-	31.6	43.16
LSM	-	18.07	36.06	-	-

The concentration of the solid particles in the original slurries for preparing SOFCRoll with conventional Ni/YSZ electrode gives Table 4-1 [232]. The YSZ electrolyte slurry was made with YSZ powder only. The slurries for electrodes were made from a mixture of YSZ, the relevant active materials and graphite as the pore former. In the sintered LSM/YSZ active oxygen electrode, the volume concentration of LSM was 47.3%, the mixture of two components was used to maximize the length of the triple-phase boundary (3PB) [209]. Only LSM was used to attain better electronic conductivity for the current collector. The composition of the fuel electrode tapes followed the same principle. The current collector layer had a high concentration of NiO, with a small amount of YSZ to improve its sintering capabilities with the active layer, which had an optimal NiO to YSZ ratio. NiO concentration in the active layer gave 40% of Ni by volume concentration after gas reduction, while in the current collector layer, 80% of Ni. The pore former concentration in the fuel electrode layer was lower than in the oxygen electrode, as additional porosity is created after NiO reduction. Pore former concentration for active layer was increased to improve gas diffusion through the SOFCRoll spiral part [232].

The concentration of ingredients in the organic medium of the slurry stayed unchanged for most of the slurries developed in the project, Table 4-2 [232]; such concentration ensures that all components are correctly dissolved in the organic body of the tape. In general, the solvent dissolves other organic ingredients; hence its concentration must be sufficient, but slight modifications were possible (e.g. +/- 10%) to adjust the slurry's viscosity.

Table 4-2: Concentration [% mass] of ingredients in the organic medium of the original slurries [232].

Ingredient	Electrolyte	Electrode
MEK/ E-OH	65.78	66.52
Triton Q-44	1.12	-
PEG	10.08	10.19
DBP	9.07	9.17
Butvar	13.96	14.11

In the original slurries, the volume ratio of organic medium (Table 4-2) to solids (ceramics and pore formers) was 4.7 for electrodes and 5.16 for electrolyte slurry, which produced accurate slurries consistency. The powders with the particles made of a higher surface area give a more viscous slurry; therefore, this ratio was adjusted to formulate the new slurries for new materials used in the project (Chapter 5).

The slurry formulation procedure, already described in the manufacturing section (Chapter 3.3), remained unchanged. The SOFCRoll with Ni/YSZ fuel electrode were prepared with the ceramic materials "as provided" without any structural modification (Figure 4-1).

Graphite has the largest particles and form of flakes; the size of graphite particles is much larger than the size of ceramic particles; the PSA measurement shows an average of 12.59 μm (Table 4-3). The Graphite particles are reduced during the slurry preparation as the soft material becomes fragmented by milling balls [232]. The increase of the surface area of graphite is indicated by the change of the electrode slurries viscosities after 1st stage of milling; it becomes more viscous due to fragmentation of pore former. As further analysis shows, the graphite particles tend to stack horizontally due to their shape, creating longitudinal pores along with the layer, which could be unbeneficial for gas exchange. The YSZ particles are small and regular in shape (Figure 4-1 d), ideal for preparing the electrolyte layer, offering a good densification rate due to the high surface area [248]. The SEM analysis reveals the grain size of around 0.2 μm, while the average particles from the PSA analysis are around 1 μm. Most likely, the small nano-size grains create larger agglomerates. The average size of LSM particles is 1.451 μm. They are quite irregular in distribution (Figure 4-1 b), containing a significant fraction of nano-particles with the maximum at 0.1 µm and large agglomerates up to 10 µm; overall, they also have a quite low surface area. The NiO also has a wide distribution in size, indicated by PSA analysis.

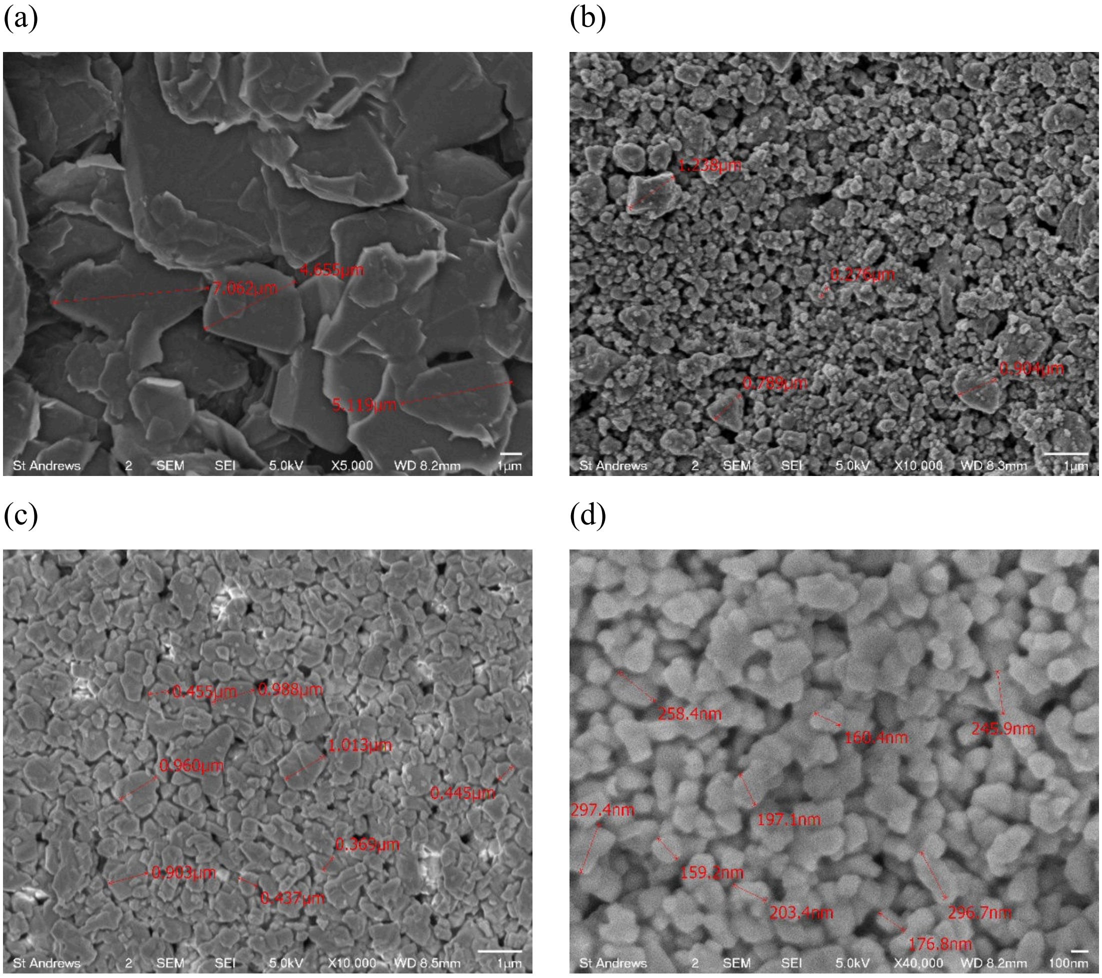

Figure 4-1: The SEM (SEI) analysis of ceramic particles and graphite pore former used for slurries preparation. (a) Graphite (-325 flakes, Alfa Aesar, >99.8%). (b) 5% A-site def. LSM (Pi-Kem). (c) NiO (Pi-Kem). (d) YSZ (Pi-Kem). Note the various magnitude.

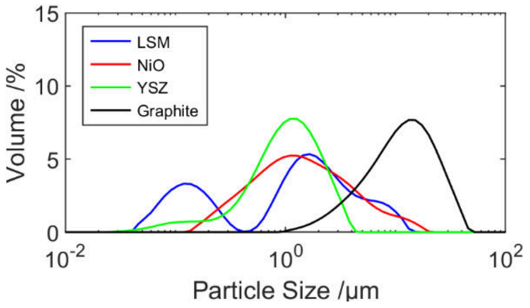

Figure 4-2: The PSA analysis of the materials used for slurry preparation in SOFCRoll with Ni/YSZ FE.

Table 4-3: The PSA analysis of the materials used for slurry preparation in SOFCRoll with Ni/YSZ FE.

Material	D10/µm	D50/µm	D90/µm	SSA/m^{2}g
LSM	0.104	1.451	6.014	2.76
NiO	0.399	1.434	5.849	6.39
YSZ	0.337	1.109	2.482	10.2
Graphite	4.183	12.590	28.113	0.695

All slurries were cast separately and laminated at the initial phase, strictly following Jones's method (SRB1, Figure 4-3 a) [232]. Next, the technique was modified in terms of tape dimension and assembly (SRB3, Figure 4-3 b), and finally, the co-casting technique was used, and slurries were cast on previously cast and dry tapes (SRB5, Figure 4-3 c). Modifications resulted in simplification of the process and better quality of cells with more consistent performance.

After the assembly, green tapes were rolled into a spiral SOFCRoll shape (Figure 4-4), reinforced on the edges with the electrolyte stripes and sealed with the YSZ slurry at one end, keeping another end unsealed for the stainless tubes gas inlets at the last stage cells were co-sintered during the thermal stage (Chapter 3.5).

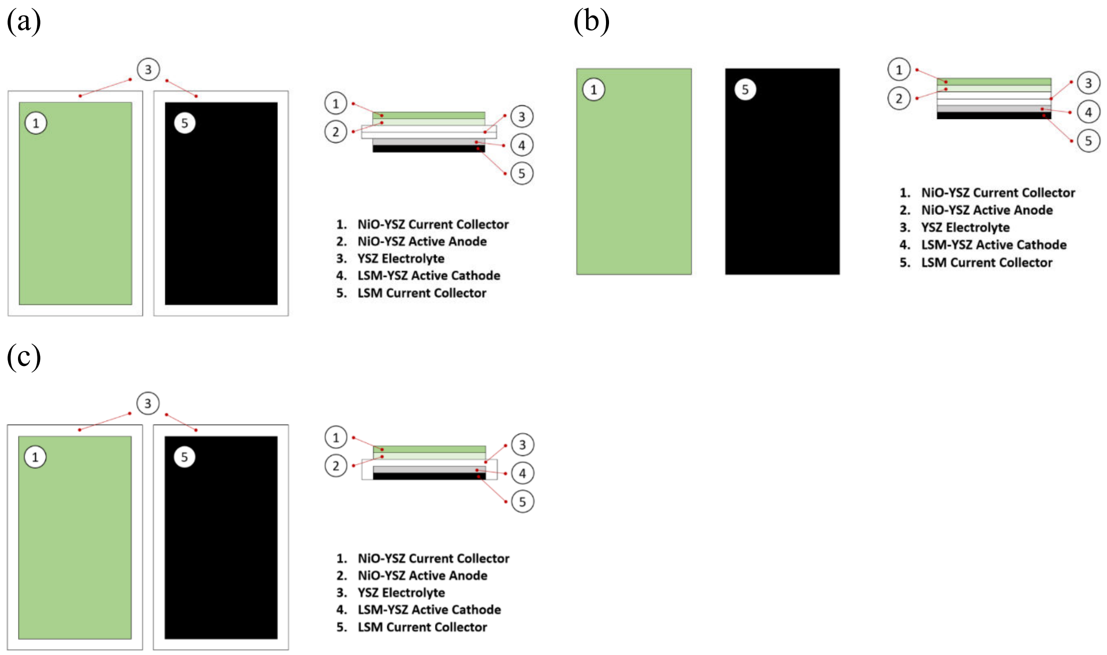

Figure 4-3: Assembly of the layers in particular batches of SOFCRoll with Ni/YSZ anode. (a) Original method (SRB1). (b) Alternative cell assembly method by lamination (SRB3). (c) Co-casting method (SRB5).

Table 4-4: Dimension of green tapes used to assemble SOFCRoll with Ni/YSZ fuel electrode.

Cell	Electrodes	Electrolyte
SRB1	5 x 9 cm	6 x 10 cm
SRB3	4 x 9 cm	4 x 9 cm
SRB5	4 x 8 cm	5 x 9 cm

For SRB1 and SRB3, all tapes were cast separately with the same doctor blade gap of 12 thou (304.8 µm). Dry tapes were laminated while placed between protective Mylar^{TM} film. In the SRB1, between an edge of electrodes and electrolyte was about 0.5 cm space to prevent possible contact between both sides and silver current collector crossover, leading to short-circuit (Figure 4-3 a). Tapes were handled manually and precisely assembled before lamination in the original method. The technique was slow, and large pieces of tape often bent and stuck to each other. As a result, it was difficult to laminate two tapes without forming imperfections or air bubbles. Even from the same batch, material and preparation method, the cell's performance often varied. In the SRB3, the design was simplified; all layers had the same dimension. Instead of cutting tapes into small pieces, large layers were laminated and cut afterwards, which simplified their preparation (Figure 4-3 b, Table 4-4). A problem occurred with the current collector, which was applied from one side of the cell on metal tubes, in some cases resulting in a short circuit, as both channels were separated only by the thickness of the layered assembly.

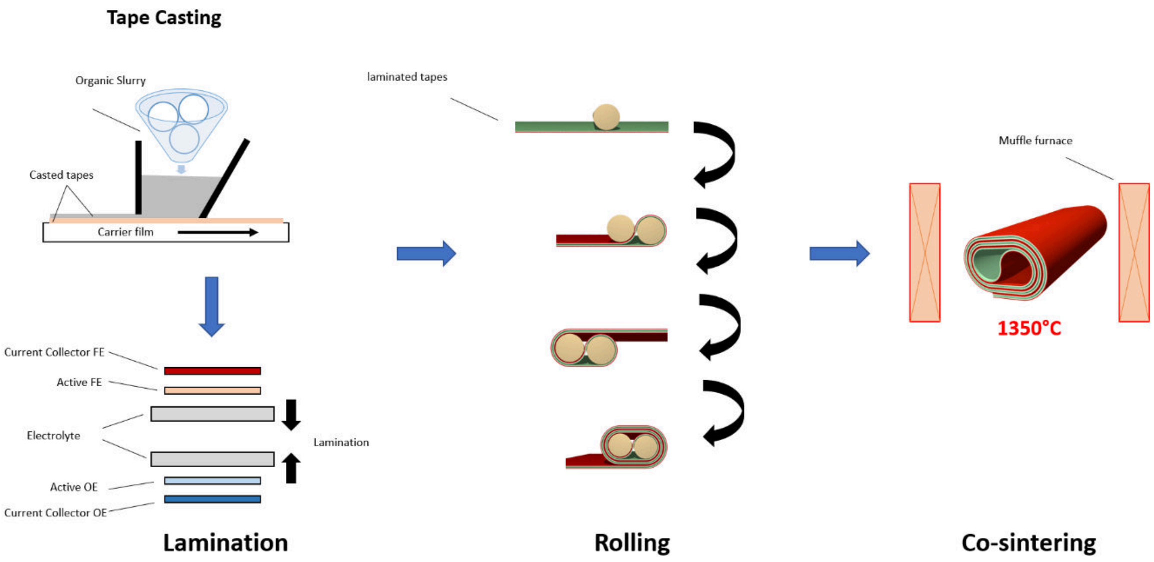

Figure 4-4: The original method of SOFCRoll preparation [232].

Eventually, the first attempt to use the co-casting method was made in SRB5, where slurries were cast over the previously cast, dry tapes. As the co-cast tapes do not need to be laminated, the acquired material should have fewer defects, often emerging at this stage, and better bonding between the layers [272]–[275]. First, the current collector and active oxygen electrode were cast over masked Mylar film. Next, the mask was removed. Two electrolyte layers were cast over the oxygen electrode and masked again to cast fuel electrode slurries with the same dimension as the oxygen electrode. After removing the mask, the co-cast tape was cut into single cells.

4.3 Shrinking/ sintering analysis of tapes used for the production of SOFCRoll with Ni/YSZ based fuel electrode

In the SRB3 batch, there was an attempt to control the slurry's shrinking profile at low temperature (up to about 300 °C when the organic ingredients burns). When the green body of the tape burns away, the tape is at a very fragile stage, as particles did not agglomerate yet [212]. Potentially differences between shrinking of individual layers at this stage could create defects; therefore, the slurries recipes were modified. The shrinking profile at a low-temperature step was controlled by slurry composition, more precisely by changing the ratio of organic compounds of the slurry to the concentration of the solid particles. The change in organics quantity must be carefully controlled as the modification of the ratio between organic ingredients could result in low quality of the green tape, or even un-castable slurry, due to wrong viscosity. Therefore, the concentration of individual organic compounds in the organic medium remained unchanged for most of the slurries developed in this work (Table 4-2). For example, in the method, the concentration of solvent, binder and plasticisers was increased by 10%, leaving a concentration of solids (ceramic particles and pore formers) unchanged; such adjustment results in modification of shrinking at the lower temperature but no structural changes in the sintered tape. The modification would also affect slurry viscosity and eventually a final product thickness; a higher ratio of organics (binder + plasticisers)/ solvent gives a more runny slurry, producing thinner green tapes that shrink more. The changing of plasticisers or binder concentration only is not recommended; the wrong ratio of binder/ to plasticisers could create binder agglomerates or too plastic tapes, difficult to cast and sticky when handling. The change of solvent concentration only leads to a change in the slurry viscosity; more runny tapes would be produced with a higher amount of solvent; the produced tape also would be thinner. If considered, the change of solvent concentration must be reasonable, e.g. +/- 10%, regarding the original recipe, as it could lead to wrong viscosity or, if too low other compounds could not be dissolved. Such modification also could bring some changes in the structure of sintered tape, as a higher concentration of binder/ in the slurry would increase the space between solid particles in the green body of the tape [276], [277]. However, the microstructure change would be only noticeable in tapes with a significant adjustment in the binder/plasticiser concentration [232]. Jones reported that a 50% increase in binder content in a mixture of YSZ with Graphite gave a 5% increase in shrinking and about 10% in porosity.

In the SRB3, the organics/ solid ratio in the original electrodes recipes was altered to the point equal to 5.16, the same as in YSZ electrolyte slurry.

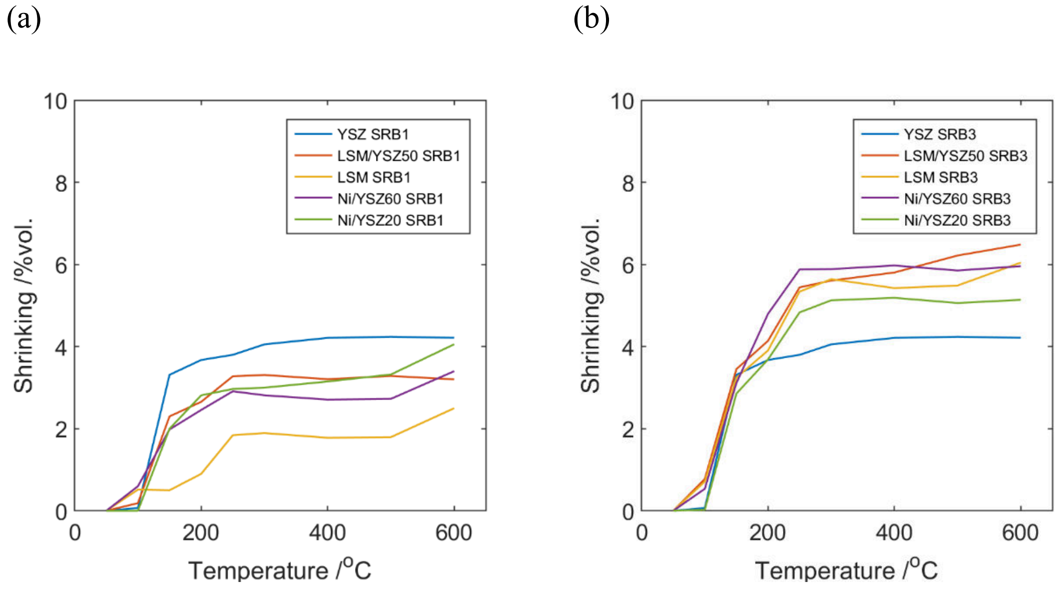

Figure 4-5: The low-temperature shrinkage profile (up to 600 °C). (a) The basic slurries (SRB1). (b) The slurries with modified content of organics (SRB3).

The comparison of shrinking profiles analysed with the described method (Chapter 3.6) shows in Figure 4-5. Both sets of tapes were analysed under different temperature profiles (as the method was still under development) with a 2 °C/min rate for SRB1 (Figure 4-5a) and 5 °C/min for SRB3 (Figure 4-5 b). Therefore it was only possible to construct the dependency of shrinking from temperature to compare those tapes. The slurry modification increased the shrinking of all the electrodes (Figure 4-5 b) and gave more minor differences between them, while the electrolyte slurry remained unmodified. Electrode tapes were made of the larger, more irregular particles and very high pore former concentration; thus, they shrink more, and their shrinking profile seems to be close at the same organic content; while electrolyte slurry with very small YSZ particles is more "packed"; hence, shrinking was lower (Figure 4-1). It could be concluded that the shrinking profile at the low temperature largely depends on the organic concentration in slurry, but also on the solid's size and shape, which affect the distance between them in the body of the green tape.

The high temperature's shrinking profile was analysed for tapes in batch SRB1 and SRB3 (Figure 4-6). As the variation of organic content at such low concentration seems not to affect the shrinking profile at the high temperature, also confirmed in further research, the comparison shows the behaviour of tapes when subjected to various heating rates.

The current collector LSM and LSM/YSZ active layers start shrinking first, already at 1000 °C. The LSM/YSZ layer is shrinking the most and almost the same as the pure LSM, indicating a high sintering rate between LSM particles and between LSM and YSZ. The heating rate does not much influence the shrinking of those layers. The LSM current collector, when heated to 1300 °C for 150 min, shrinks by 13.8% in SRB1 tapes, while when heated to the same temperature for 60 min in SRB3 shrink by 14%. The shrinking rates of those layers are very high at the 1000 – 1300 °C temperature range and are almost linear; most of the shrinking comes from this range; the rate increase between 1300 and 1350 °C. When samples are dwelled at 1350 °C, shrinking continue with a lower late, and not much volume change is noticed after about 2 h of dwelling; the maximum shrinking for those layers is about 23%. The LSM based tapes heated with a higher rate shrink to a slightly greater extent. Those measurements clearly show that LSM based layers could bring the highest stress in co-sintered cell assembly, especially at a temperature between 1000 and 1200 °C when they already shrink by about 10%, whereas other layers show volume change around 1200 °C. At this stage, variation in shrinking could be most damaging for the cell's structure; the assembly is fragile, as other particles are not firmly connected.

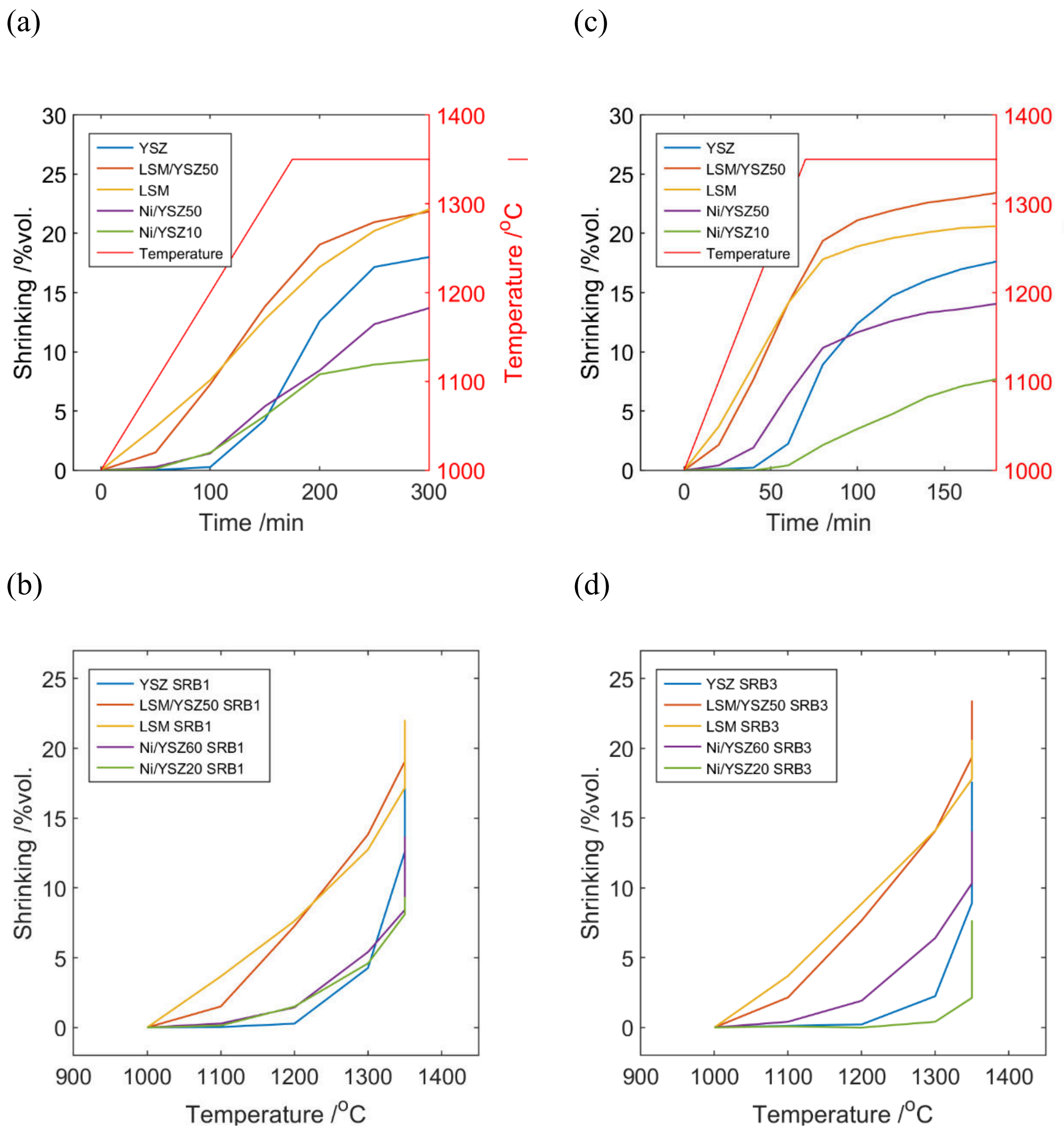

Figure 4-6: The high-temperature shrinkage profile of the slurries used for the SOFCRoll preparation. (a)-(b) Shrinking/Time and Shrinking/Temperature dependence of tapes for SRB1. (c)-(d) Shrinking/Time and Shrinking/Temperature dependence of tapes for SRB3.

Ni/YSZ60 active layer has a lower shrinking, up to about 14% when sintered at 2 °C/min rate and similarly for 5 °C/min heating rate. Again, the shrinking rate seems to increase with a faster heating rate. Ni/YSZ20 current collector, when sintered at 2 °C/min heating rate, has a similar shrinking profile but, when dwelled, achieves a lower maximum shrinking of about 10%. When sintered at a higher rate, it started to agglomerate quite late at 1300 °C and agglomerated the most during a dwelling step; those differences likely are due to errors in the experiment or different "local" composition in the sample, e.g. some agglomeration of material. At 2 °C/min, Ni-based layers have quite close shrinking to YSZ electrolyte, the start to agglomerate to a small extent already at about 1100 °C, while YSZ does not show much volume change below 1200 °C. Above 1300 °C, the sintering rate of YSZ increases, and YSZ shrinks most during a dwelling step, which could bring stress between the electrolyte and assembled electrodes.

The tapes shrinking at high temperature is due to the sintering of ceramic material; when sintered, the compacted powder (green body) agglomerates at the elevated temperature, creating a denser structure [278]–[281]. As a result, the material changes its mechanical and physical properties at a macroscopic level, e.g. more compact ceramic regains certain strength, hardness, elastic or thermal characteristics [278], [279]. The typical sintering temperature is below the material's melting point (about 2/3), making it suitable for consolidation materials with a very high melting point [280]. An example could be the sintering of YSZ particles, where under the sintering process at 1450 °C, the ~ 1µm YSZ particles form a dense body of YSZ electrolyte, Figure 4-7.

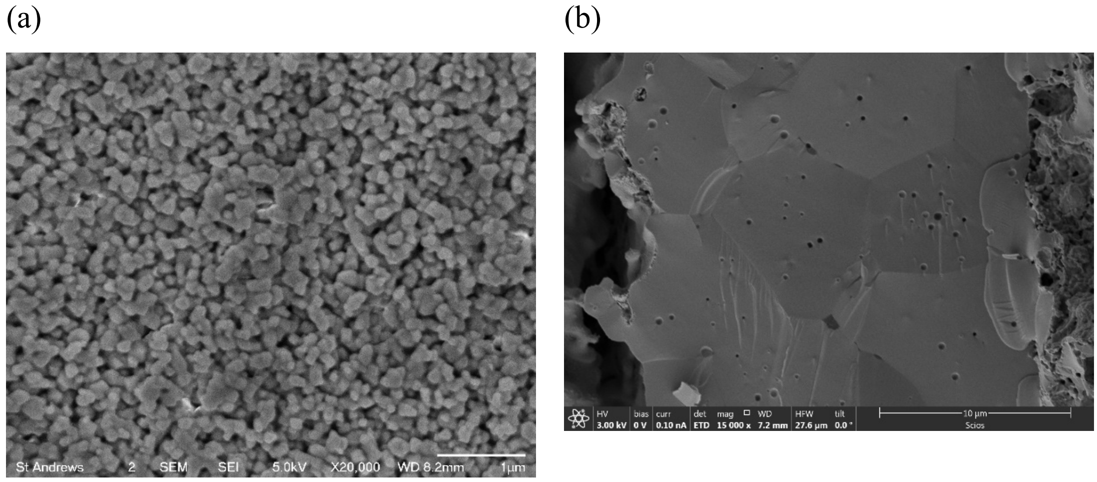

Figure 4-7: The sintering of YSZ. (a) Loose YSZ particles. (b) YSZ sintered at 1450 °C.

In general, there are two stages, including the formation of the neck and material contraction in the further stage of the thermal process; these are the basis of early physical models [279], [282]–[284] that define the interactions between discrete particles, based on which the behaviour of continuous medium is modelled [285]. It is accepted that at the first stage, the particles bond locally, forming a neck, it grows, and mass diffusion eventually leads to filling the "open space" between particles (pores) and at the second stage, the pores are rounded and start to shrink. The models are primarily developed for viscous sintering, the simplest representation of single-phase sintering [278]. The characterisation of the sintering behaviour of ceramic particles adds complexity to the system due to anisotropies of surface energies and the formation of thermal groves, which is due to the non-spherical shape of ceramic particles [278].

On a macroscale, the driving force for strain-free grain sintering is the reduction of excess surface energy per unit volume. The excess surface energy $\dot{\gamma}$ is proportional to total surface energy γ and inversely proportional to particle radius r and material density ρ [278]:

$$\dot{\gamma} = \frac{3\gamma}{r\rho}$$ **Equation 4-1**

In the first stage of sintering, a neck is formed on particles contact, which takes ~0.2 of the cross-sectional area of the particle [279], [283]. The stage is accompanied by several percent of shrinkage and a slight increase in bulk density of the compact body [282], [283]. The neck is characterised by radii of the curvature x, the neck diameter, and minimum radii of curvature of the neck surface ρ [284], Figure 4-8 a.

At the microscopic level, the driving force for mass transport during sintering is the capillary pressure formed at the neck due to surface curvature. The capillary pressure gives the sintering pressure, which typically is between 0.1-1 MPa [278]:

$$\Delta P = \gamma(\frac{1}{\rho} + \frac{1}{x})$$ **Equation 4-2**

At an atomic scale, the driving force for sintering is a gradient of atoms (or defects) between the concave and convex surfaces, effectively increasing their energy and mobility. In the mechanism, the surface acts as the source while the bridge is the sink of the material [286].

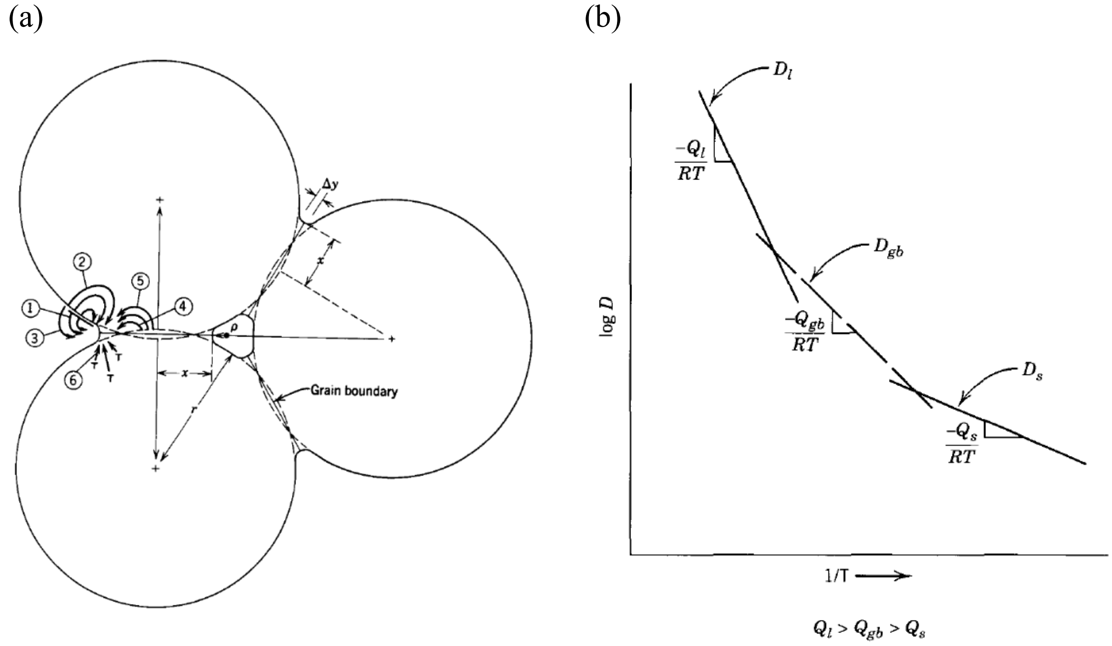

Figure 4-8 (a) Neck formed during sintering of particles and mass transport mechanisms, Table 4-5. (b) Dependencies of diffusion coefficients on temperature. Taken from ref. [278].

A characteristic of the kinetics of the sintering process of ceramic material could be found in the book by Chiang, Birnie and Kingery [278]. Several mechanisms could compete for mass transport during the first stage of sintering, where vapour, lattice, surface, or boundary diffusion are most influential; those could lead to densification or particle coarsening.

Table 4-5: Transport mechanism for sintering and particle agglomeration in Figure 4-8 a [278], [279].

No.	Mechanism Path	Material Source	Process
1	Surface	Surface	Coarsening
2	Lattice	Surface	Coarsening
3	Vapour	Surface	Coarsening
4	Grain Boundary	Grain Boundary	Densification
5	Lattice	Grain Boundary	Densification
6	Lattice	Lattice	Densification

The coarsening involves increasing the neck's surface by decreasing the particle surface without shrinking the material. During the coarsening, the paths for mass transport are surface diffusion and evaporation-condensation. In this mechanism, the excess surface energy is reduced by moving material from the surface to the neck, and those do not shrink as material on the particle's interface is not transferred. The vapour pressure increases exponentially with temperature, thus, strong temperature dependence. During the densification at the first sintering stage, the material shrinks as particles move towards each other. The material is transported from the grain boundary to the neck, along the grain boundary, or through the lattice (lattice or grain-boundary diffusion, Figure 4-8 a). The driving force for mass transport is the tensile pressure caused by the neck's curvature. Tensile stress causes a vacancy gradient between the neck and grain boundary, causing vacancy to diffuse from the neck, which involves the diffusion of atoms from the grain boundary to the neck [278].

After the neck curvature becomes blunted, the driving force for the neck growth decreases, and grain growth becomes possible [283]; the grain growth is considered to terminate neck growth [287].

In the second stage, material densification is governed by the migration of atoms from grain boundaries and intra-granular defects [286]. The driving force for mass transport would be similar to the first stage; at the microscopic level, the curvature, while the differences in surface energy on the global level [286]. At this stage of sintering, the diffusion of the ions is assumed to occur by the reverse flux of lattice vacancies [283]. The intermediate step leads to a change in the dimensions of the pores in the continuous metastable porous matrix of the green body, where grain boundaries intersect all pores. The pore formed between particles could be approximated by a continuous cylinder, which shrinks during this stage [283].

Coble [283] distinguishes two different final stages of sintering. In the first one, closed pores are located on four-grain corners, and such pores shrink evenly and, in time, are reduced to zero. The alternative path is related to discontinued grain growth [288], where the pores are isolated from the grain boundaries; they are rounded, closed and do not interact with the grain boundaries, such as in Figure 4-7 b.

Diffusion of crystal solids during the sintering process could be described as a thermally activated mechanism, where atoms move either on interstitial or vacancy positions [281].

In such a mechanism, a temperature dependence would be associated with the diffusion coefficient, illustrated by the equation:

$$\boldsymbol{D = D_0 exp\,(\frac{Q}{k_B T})} \qquad \textbf{Equation 4-3}$$

D is the diffusion coefficient, ***T*** is the absolute temperature in K, and $\boldsymbol{k_B}$ is the Boltzmann factor; $\boldsymbol{D_0}$ is constant; ***Q*** is the activation energy of the elementary jump. Diffusion coefficient ***D*** would be different for various mechanisms discussed previously; their activation energy ***Q*** could be measured experimentally [286].

The activation energy is usually the highest for grain boundary diffusion and the lowest for the surface mechanism, Figure 4-8 b; as dependence is steeper for lattice and grain boundary diffusion, densification dominates at elevated temperature, whereas the surface process leads to coarsening, dominate at a lower temperature [278]. Consequently, materials are usually fired at a higher temperature to acquire a dense microstructure, while firing at a lower temperature leads to coarsening, producing more porous layers. Possible are exemptions to this dependability, e.g. the system has high activation energy for surface processes; hence, it coarse at elevated temperature. The fast-firing technique is another consequence of the dependencies of diffusion coefficients on temperature [289], pointed out in Figure 4-8 b, where material densification could be promoted, bypassing coarsening step [278]. Such a mechanism could explain a higher shrinking of analysed material for SOFCRoll production when heated at a higher rate, Figure 4-6.

4.4 Microstructure analysis

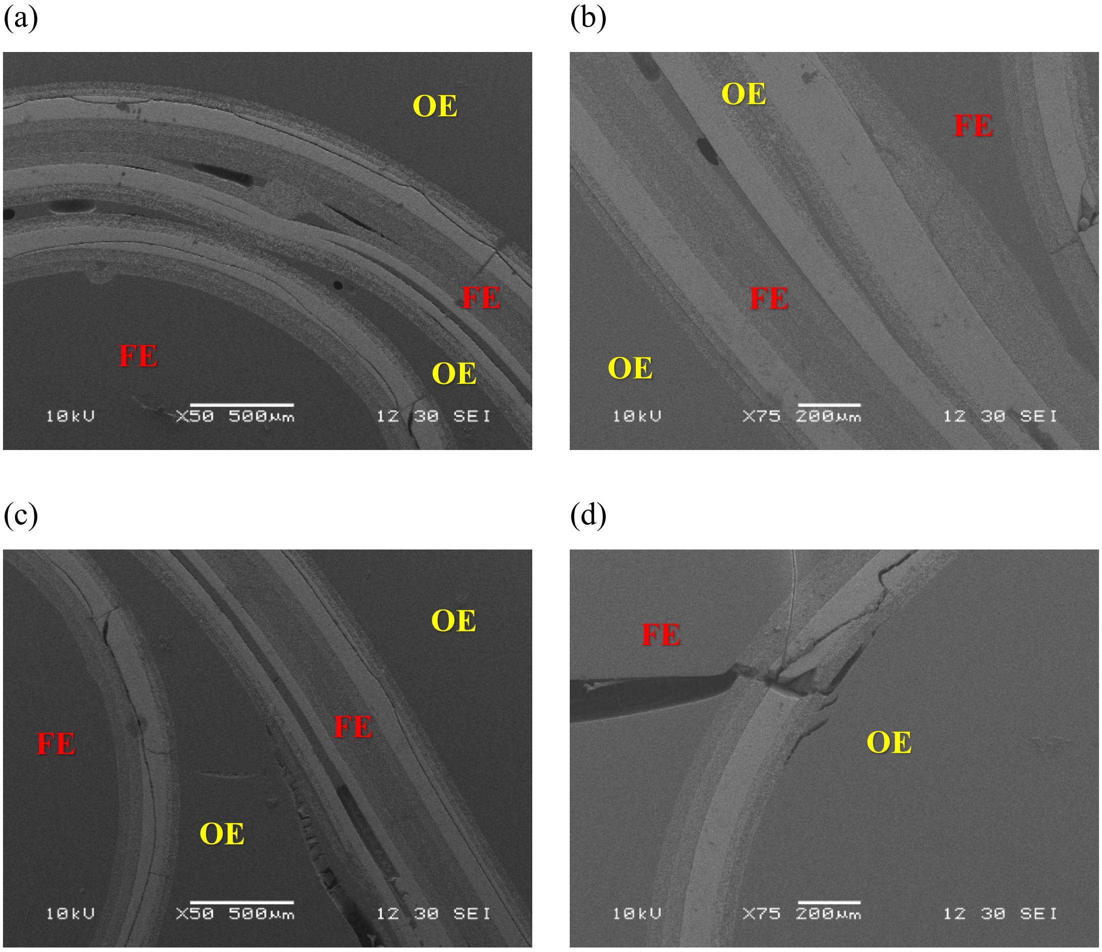

Figure 4-9: (a) – (d) SEM analysis from SRB1 batch of SOFCRoll at various areas in the cell.

The sample made by the primary method using the original slurry recipes (SRB1) has multiple internal defects, Figure 4-9. In some areas, cells show extensive cracking along the electrolyte. Cracks along with the electrolyte would block the flow of oxygen ions, making the area completely inactive; while the cracks across the electrolyte can cause the flux of gases between the chambers; such defects reduce the oxygen's partial pressure difference on both electrodes and thus reduce the OCV according to the Nernst equation. Gas cross-over also could result in lower system performance by changing the material properties, e.g. a drop in LSM conductivity due to reduction; or a drop in fuel electrode activity due to Ni oxidation. Delamination between two electrolyte layers and other active layers is present in several places. Delamination between active layers will result in the blocking of the flow of charged species across a cell. Apart from the shrinking profile, delamination could come from the weak adhesion of tapes during lamination, while cracks most likely are related to internal stress induced during co-sintering.

YSZ electrolyte cracks and delaminates in the middle through its length, indicating a weak point in its structure, where two YSZ tapes were laminated; often, those cracks extend through the large part of the YSZ electrolyte close to the interface with electrodes. Delamination of YSZ through the middle seems to be more pronounced in the inner part of the cell (especially at the inlet from the cell's main channels to the spiral part), and cracks dominate at the outer part, either in the channel or closer to the outer layer of the LSM oxygen electrode. The electrode layers seem not to crack much, crack is visible in Figure 4-9 d, but this seems to be caused by the resin. The electrode layers seem not to crack to a large extent also do not delaminate much; in some areas, slight delamination from YSZ electrolyte is visible, indicating that the interface is not very strong.

The Back Scattering Electron probe (BSE) was used for the porosity measurement to acquire the images with high contrast between the resin and ceramic (Figure 4-10).

Next, the image was converted to the 8-bit grayscale and a threshold was applied to the picture (Figure 4-10 b) with ImageJ software [269]. Threshold separated the ceramic pixels (white) and the resin (black), and the area filled by the resin was measured. Figure 4-10 a & c compare the porosity of the same LSM current collector layer, sintered within SOFCRoll and separately. There are significant differences between the porosity of active layers, even for the same slurries, when sintered in various arrangements, indicating that porosity is not controlled only by the slurry composition but also by the layer location as other layers may limit the movement of material during sintering. Also, there are differences in stress in various cell areas, which would affect porosity (Figure 5-22 in Chapter 5).

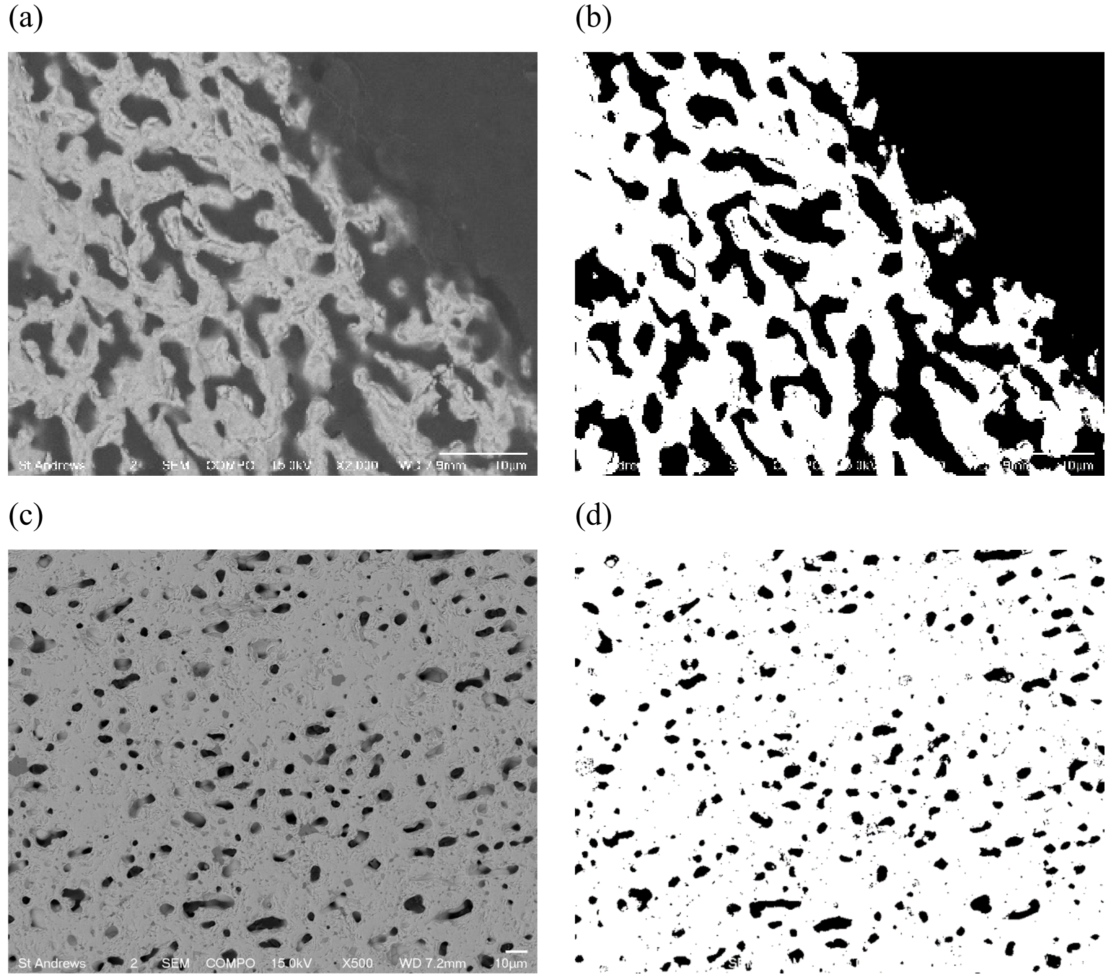

Figure 4-10: Porosity measurement of the LSM layer sintered at 1350°C. SEM (BSE) image and after conversion to a binary scale of the LSM current collector. (a)-(b) Sintered within the SOFCRoll structure. (c)-(d) Sintered separately.

Figure 4-11 shows the microstructure analysis of SOFCRoll produced in the SRB1 batch. The LSM current collector layer had porosity up to 70%, while the value of LSM/YSZ50 porosity was 46%. Pores in the active layer are long and are arranged along with the electrolyte, likely caused by the shape of graphite particles (Figure 4-1 a). Such a structure may be unbeneficial for layer functionality, as pores are not well connected. The current collector layer produces a better structure (Figure 4-11 a).

Both Ni/YSZ based fuel electrodes, after reduction, had a porosity of about 58%. Such a high value was anticipated to limit diffusion losses through the long spiral of the cell. The porosity distribution was relatively uniform, and pores seem to be well connected (Figure

4-11 b). On the fuel electrode images, the large agglomerates represent Ni, while the small grains YSZ.

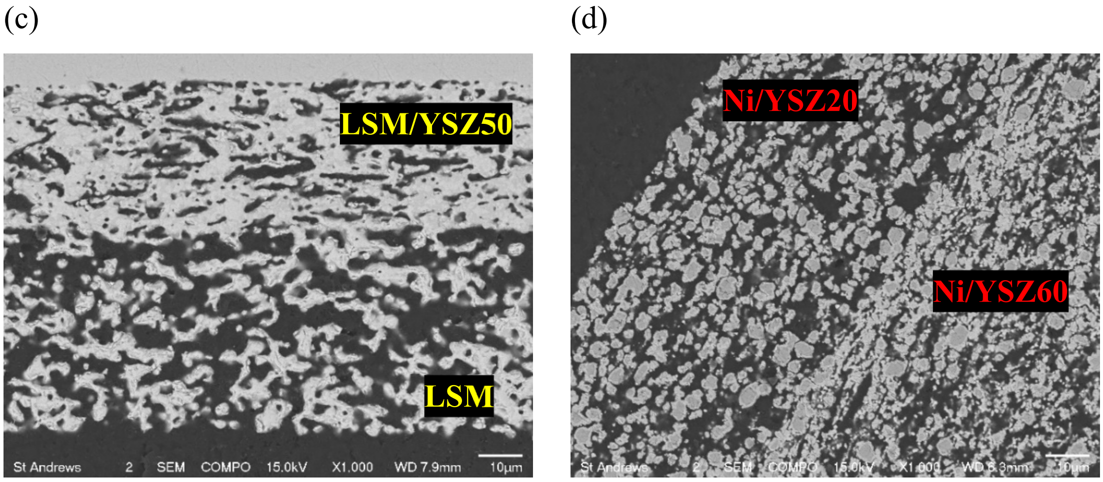

Figure 4-11: SEM analysis from SRB1 batch of SOFCRoll. (a) Image of the oxygen electrode (OE). (b) Image of the fuel electrode (FE).

Although all tapes were cast with the same doctor blade gap, images showed significant differences in their thickness, especially in the oxygen electrode, which is much thinner than other layers. Those variations are likely the result of the difference in viscosity of slurries and the shrinking profile. The more shrinkable LSM slurries produced a thinner tape while fuel electrode layers, where shrinking was lower, were thicker. The average thickness of the LSM/YSZ50 electrode was 30 µm, while the thickness of the LSM current collector was 40 µm. The thickness of fuel electrodes was also similar, 60 µm in Ni/YSZ60 and 55 µm in Ni/YSZ20. The total thickness of electrolyte in the measured location was between 90 - 110µm (the YSZ was made of two tape layers).

Figure 4-12 shows the microstructure analysis of SOFCRoll produced in the SRB3 batch. Some areas have no cracks or delamination (Figure 4-12 a), but the structural defects are present in other regions.

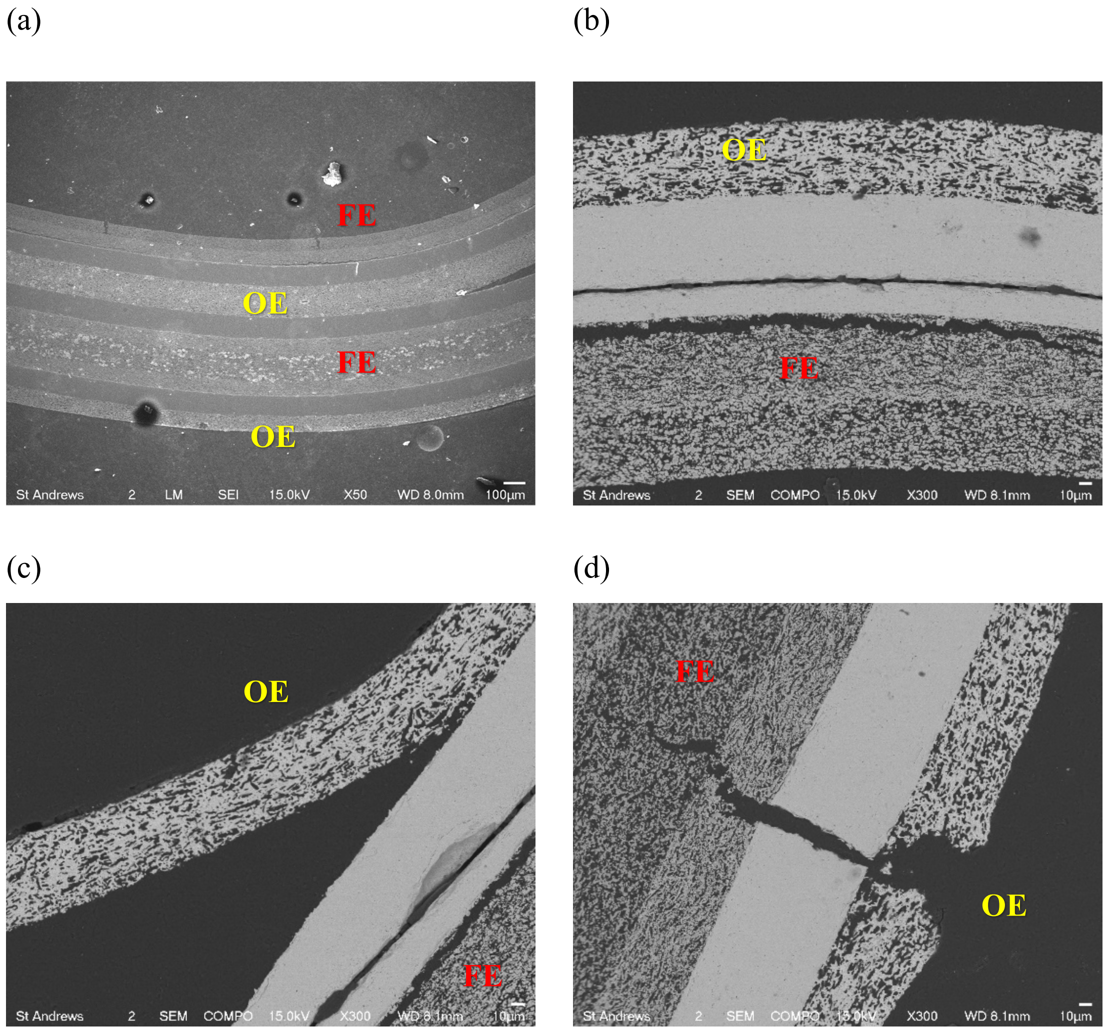

Figure 4-12: SEM analysis of SOFCRoll made in SRB3 batch. (a) SEM (SEI) Image of cell's cross-section. (b)-(d) SEM (BSE) Image of cell's cross-section at various cell areas.

The primary weakness is delamination; the oxygen electrode delaminates the most at the main channel, from the inlet to the spiral (layered part) (Figure 4-12 c). The fuel electrode cracked in many locations at the interface with the YSZ electrolyte (Figure 4-12 b & c). The YSZ developed cracks through its length closer to the fuel electrode side; those cracks coincide with cracks on the fuel electrode interface, revealing stress created in the cell. Also, some cracks are visible across all layers (Figure 4-12 d). However, SRB3 cells have fewer defects overall, and the electrochemical test shows improved performance (Chapter 4.5). Most likely, progress is due to a new preparation method, which simplified the cell's assembly and produced fewer defects during lamination.

The LSM current collector layer had porosity up to 41.5 %, much lower than in the SRB1 batch, where the high porosity value in the OE current collector most likely comes from various stress at a given location. The value of LSM/YSZ50 porosity was 45%. Both Ni/YSZ based fuel electrodes, after reduction, had a porosity of about 50%. Measurements gave a slightly lower value than SRB1; the porosity may also be different due to layer location. However, in both cases structure is very similar (Figure 4-13).

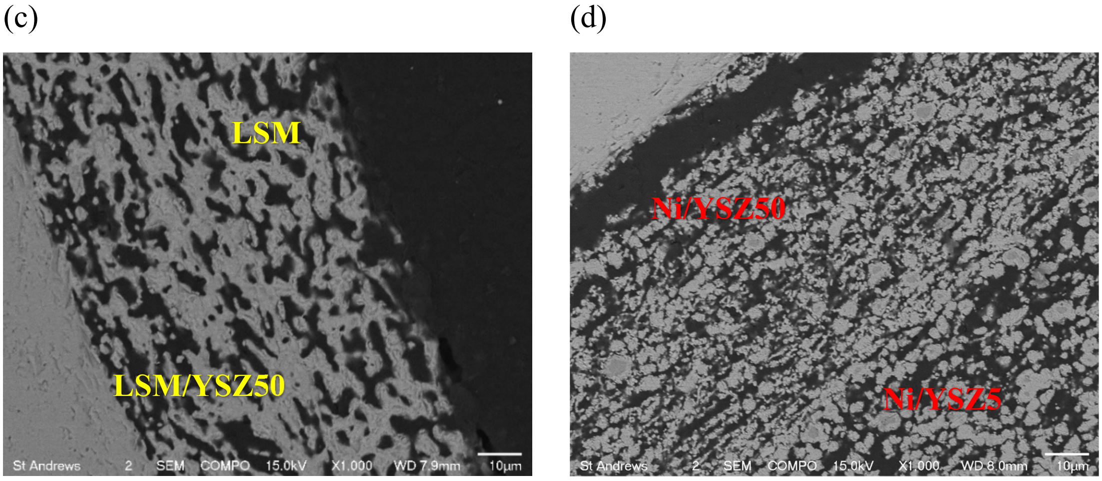

Figure 4-13: SEM analysis from SRB3 batch of SOFCRoll. (a) Image of the oxygen electrode (OE). (b) Image of the fuel electrode (FE).

The co-cast cells (SRB5) had much fewer defects than cells prepared by hand lamination (Figure 4-14) and showed much better performance (Chapter 4.5). The delamination is present between the layers; in some cases, there is substantial delamination of oxygen electrode layers, especially where layers connect at the cell's central channel (Figure 4-14 b). The layers are much thicker than in previously described cells, as different gap adjustments methods were used; such a high variation comes from the additional layer of sticky tape applied between the slurry reservoir and Mylar film to assure that it will not damage the produced ceramic tapes. At the initial phase of the co-casting method development, the control over the thickness of cast layers was poor but improved during the project, where electrolyte as thin as 20 µm was co-cast (Chapter 6.4). The LSM/YSZ50 layer had 60 µm, LSM current collector 50 µm; the fuel electrodes about 150 µm each and YSZ electrolyte 250 µm.

The analysis of co-cast structures shows a much lower porosity of the oxygen electrode layers than in previous examples (only about 30%). The cathode layers were cast first, and then all other layers above it. Perhaps other layers' weight leads to the flattening of LSM based oxygen active and current collector electrodes.

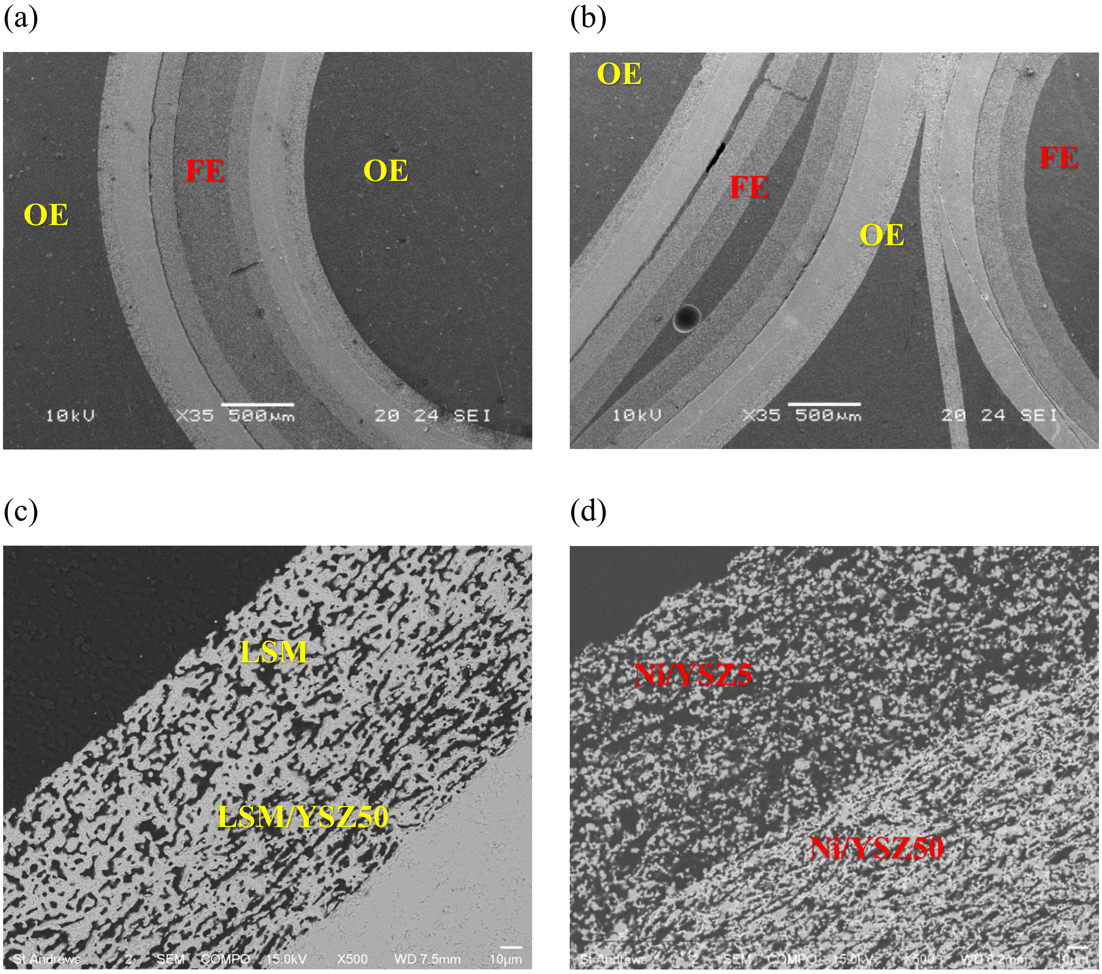

Figure 4-14: SEM analysis of SOFCRoll made with SRB5 method (co-cast). (a)–(b) SEM (SEI) Images at various magnification. (c) SEM (BSE) image of the oxygen electrode. (d) SEM (BSE) image of the fuel electrode.

4.5 Electrochemical test of Ni/YSZ SOFCRoll Cells

The dimension of electrode layers, length of diffusion, and current collector path could be seen in Figure 4-15 b for "unfolded" electrodes, assuming that tapes shrunk by 25% after sintering. For the original SOFCRoll design (SRB1), the total surface area of the fuel electrode was 25.3 cm^2, which includes 5.6 cm^2 in the "Channel" (hatched area) and 19.7 cm^2 in the spiral part of the fuel electrode.

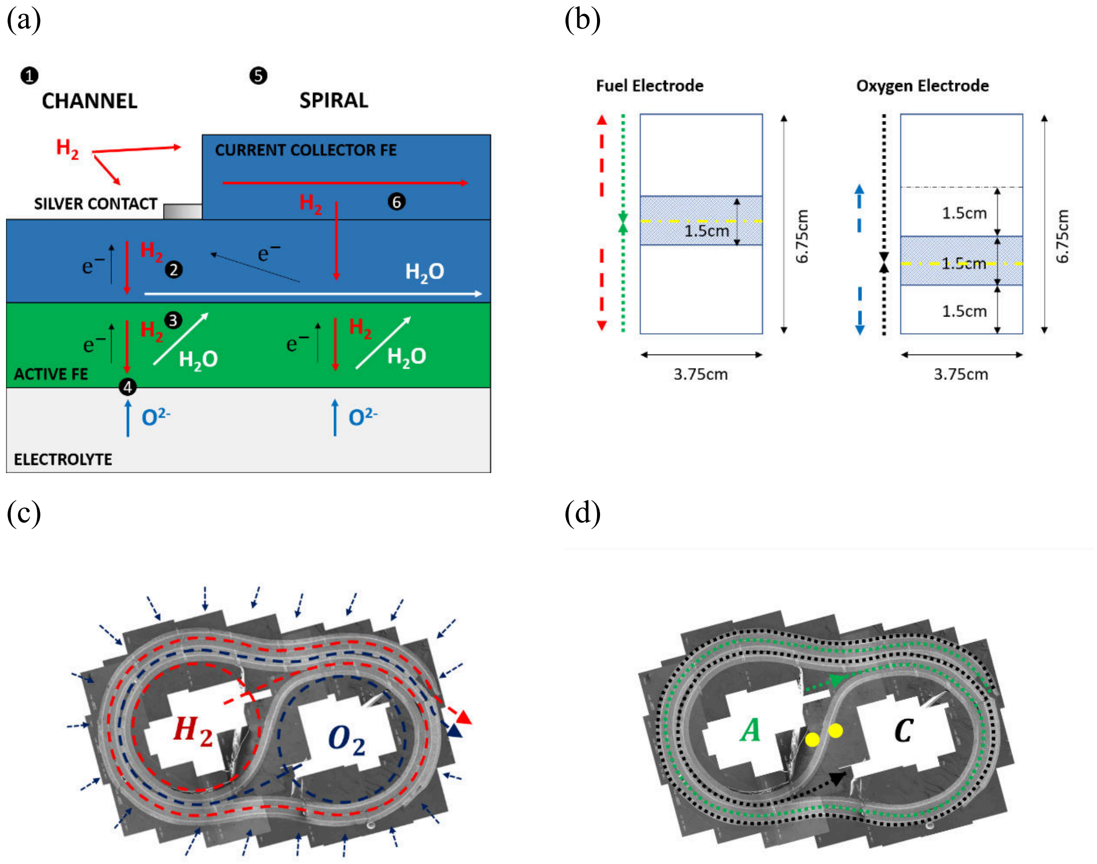

Figure 4-15: Mechanism on SOFCRoll (Original design). (a) Model of cell's functionality at FE side. (b) Electrodes dimension and length of gas and current collector paths. (c) Diffusion paths, in red – H_2, in blue – O_2. (d) Current collector position. In green – current collector fuel electrode layer (FE), in black – current collector oxygen electrode layer (OE), in yellow – silver current collector.

Figure 4-15 shows the mechanism of SOFCRoll functionality on the fuel electrode side. The model cell is divided into two electrochemically active regions, the "Channel" and the "Spiral". The H_2 gas is provided to the channel (1). At the channel, H_2 gas diffuses through the thickness of the current collector (2) and active layer (3), which are around

50μm each. The electrochemical oxidation of H_2 takes place on an active electrode interface with electrolyte (4). Electrons from this area are conducted through a thickness of electrodes (plus distance in the channel) to a silver contact. In the spiral part (5), the H_2 gas must diffuse through the Ni/YSZ current collector layer distance (6), up to 3.375 cm, plus the thickness of the electrodes to the reaction site. The electrons from the reaction would be conducted through the current collector layer for the same distance to silver contact. Water from the reaction in both areas would be discharged through the current collector layer outside the cell; thus, its porosity must be sufficient to assure the exchange of reactive gases. A similar mechanism holds for the oxygen electrode, which has the exact dimension of "Channel", but "Spiral" is shorter, as the outer layer of the electrode is open to atmospheric air. Hence, the "Spiral" is 1.5 cm, which is the length of maximum diffusion distance in the oxygen electrode. Whereas, due to the position of the current collector point (in yellow in Figure 4-15 b & d), the maximum current collector distance is 4.5cm, which is even longer than in FE.

According to the model, gas conditions at "Channel" and "Spiral" are different, and the activity in the "Spiral" will decrease in the x-axis direction, depending on the diffusivity and conductivity of the current collector layer. If those parameters are not sufficient to manage the required distance, or/and the cell has internal defects, the cell's active area in the spiral could decrease due to:

(1) Too low conductivity to transfer electrons through the spiral to silver contact.

(2) Gases are not diffusing or diffusing unevenly through the cell's spiral.

(3) At some point in the spiral, gases mix and burn due to cracks.

(4) Delamination of ceramic layers.

Processes (2) and (3), besides fuel draining, would create unfavourable gas conditions on both electrodes, thus, decreasing their functionality.

For discussion of cell performance, the best working cells with specific characteristics were chosen. However, one should remember that their unstable operation brings errors during the analysis. Cracks and defects change the gas conditions on electrodes, which is manifested by lower than theoretical OCV value and SEM images, apart from changing the concentration and pressure of gases on both electrodes, also changing the oxidation state of materials, decreasing their activity. Moreover, the gas distribution in the cell's spiral may be disturbed due to gas crossover or diffusion losses. Many cells could not achieve a high enough OCV value to be tested in those trials. However, OCV improved with the development of the production method.

Most likely, the area between channels is the most active region. The region is nearest to the silver contact, and gas diffusion is only restricted by the thickness of the electrodes; if the cracks are present, a large part of the spiral could be entirely inactive.

According to the Nernst equation, a theoretical OCV for a cell operating at 800 °C with air and pure hydrogen should be above 1.1 V. SOFCRoll cells with Ni/YSZ electrode had a much lower value of OCV than theoretical (best cells between 0.8-0.95 V), which was considered as the effect of cracks, causing gas to leak between the chambers. The OCV decreases with increasing temperature, with a much higher rate than the Nernst equation indicates. Likely, the loss of potential was related to the change of kinetic energy of gas particles, which will increase linearly with the temperature at constant volume and pressure. The higher kinetic energy will cause more gas to diffuse through a crack.

If the spiral is inert due to lack of conductivity, OCV measurement would only be related to the active area inside the channels, which would explain a relatively high OCV value, even though most cells could be under low pO_2 difference.

Some measurement has been done on the shorter cells, and not much more current was generated; the performance of cells with 3 cm length was close to those with 5 cm length.

Overall, the generated power is low in all tested cells when considering the large area of layers used for cell preparation.

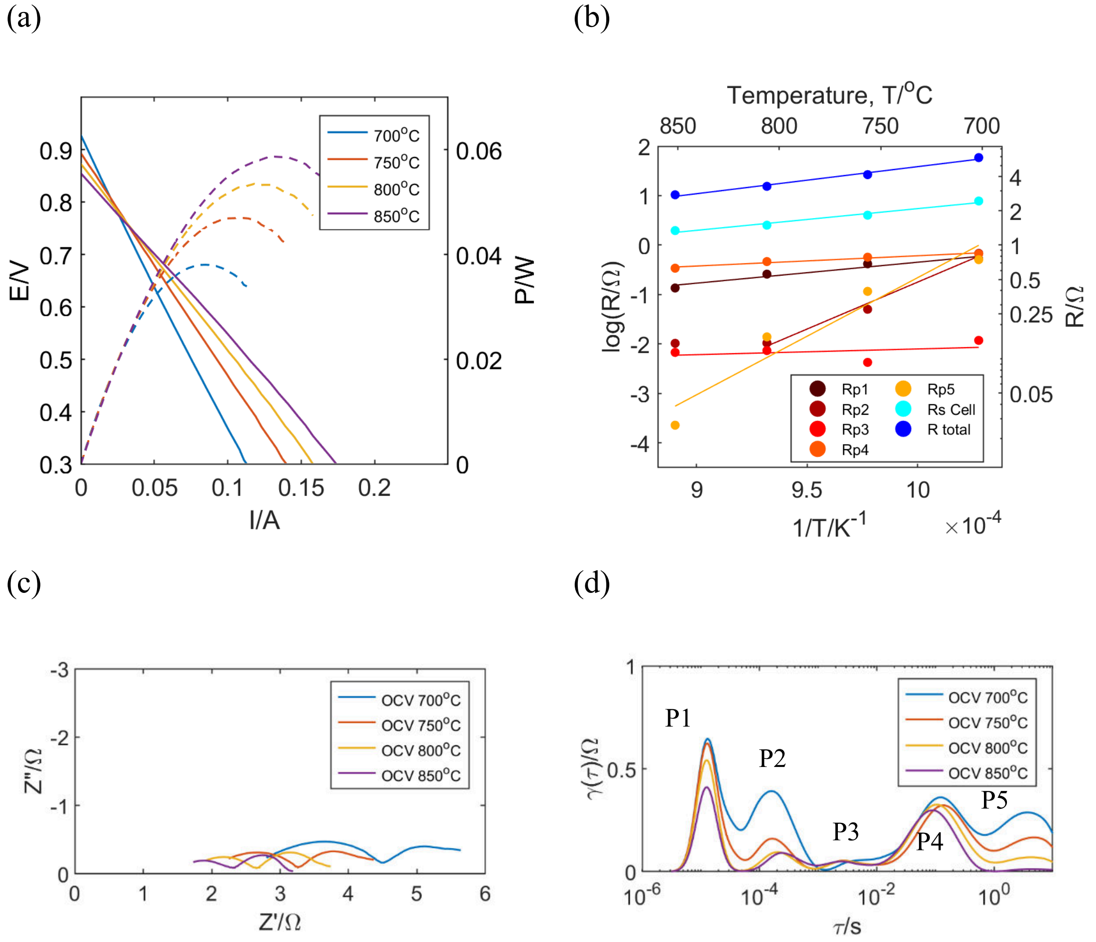

Figure 4-16: The electrochemical performance of the SRB1 SOFCRoll in the temperature range 700-850 °C and the 100 ml/min 5% H_2/N_2 in FE and 100 ml/min of air in OE. (a) I-V curve of cell operating in fuel cell mode. (b) Arrhenius plot of ohmic and polarisation resistance. (c) – (d) EIS and DRT analysis of impedance data at OCV conditions.

The SRB1 SOFCRoll cell has been tested on the 100 ml/min 5% H_2/N_2 in FE and 100 ml/min of air in OE. The small amount of the silver current collector was painted on 1 cm in the metal tube's length. At this point, silver paint was intended to enhance the connection between stainless steel tubes and Ni/YSZ20 current collector layer, not to distribute current through the cell's channel; the Ni/YSZ20 layer with a high content of Ni metal should have provided this (Figure 4-15 d). Figure 4-16 shows the I-V and impedance characteristics of the cell. The EIS and I-V data were not normalised to the surface area, as it is unknown how much surface area is being used; the performance is "per cell".

The recorded OCV for unmodified SOFCRoll cells (SRB1) tested with 5% H_2/N_2 was 0.928V at 700 °C and decreased to 0.856V at 850 °C. The I-V characteristics were taken every 50 °C at 700 – 850 °C; further analysis shows that power gain is lower when heating to 850 °C. In many cases, the power generated at 800 and 850°C was almost the same (Figure 4-19). Such an apparent drop in performance was attributed to the deterioration of the silver current collector at a temperature above 800 °C. The melting point of silver is about 900 °C; thus, silver should not melt; however, a local rise in temperature could be possible, e.g. due to the burning of H_2. The maximum power generated at 850 °C was 58 mW for the 100 ml/min gas flow, giving 8.1% fuel utilisation. The fuel utilisation was calculated from the equation:

$$\boldsymbol{U} = \frac{\boldsymbol{I}}{\boldsymbol{n} \times \boldsymbol{F} \times \boldsymbol{v}} \times \mathbf{100\%} \qquad \textbf{Equation 4-4}$$

Where ***I*** is the generated current in A, ***F*** is Faraday constant 96485C mol^{-1}, n is 2 for H_2 and gas flow ***v*** is in mol/s.

Not much power was obtained when testing at pure H_2, a maximum of 71 mW (test not shown).

EIS spectra of all presented cells show two main arcs developed at high and low frequencies. They are the sum of several processes from both electrodes that merged into single semicircles due to quite close frequencies. To evaluate their number, contribution and type, a DRT was constructed from impedance data (Figure 4-16 d), which clearly shows up to five peaks. In the usual approach to identifying to which electrode and process the peaks on DRT correspond to, their dependency on various conditions could be measured, e.g. by changing one parameter like pO_2 on fuel or oxygen electrode [65]. Theoretically, the parameters could be identified by the value of their characteristic frequencies, capacitance and activation energy.

With the number of elements known, the equivalent circuit was constructed [66], consisting of ohmic resistance (R_s) and five semi-circles (Figure 4-17 d); the inductance ($5.2x10^{-7}$) was calculated from short-circuit analysis and extracted from the data. The intersection point of EIS spectra with the x-axis at high frequency indicates the cell's R_s, which comes from the ohmic resistance of rig (~0.1 Ω), electrolyte and electrodes. The polarisation processes (frequency-dependent) occur in the upper part of the Nyquist plot above the x-axis. The semi-circles were modelled by resistance, and constant phase elements (CPE) connected parallel (R/CPE). R represents the polarisation process's resistance, while CPE represents its capacitive behaviour and is modelled by two parameters.

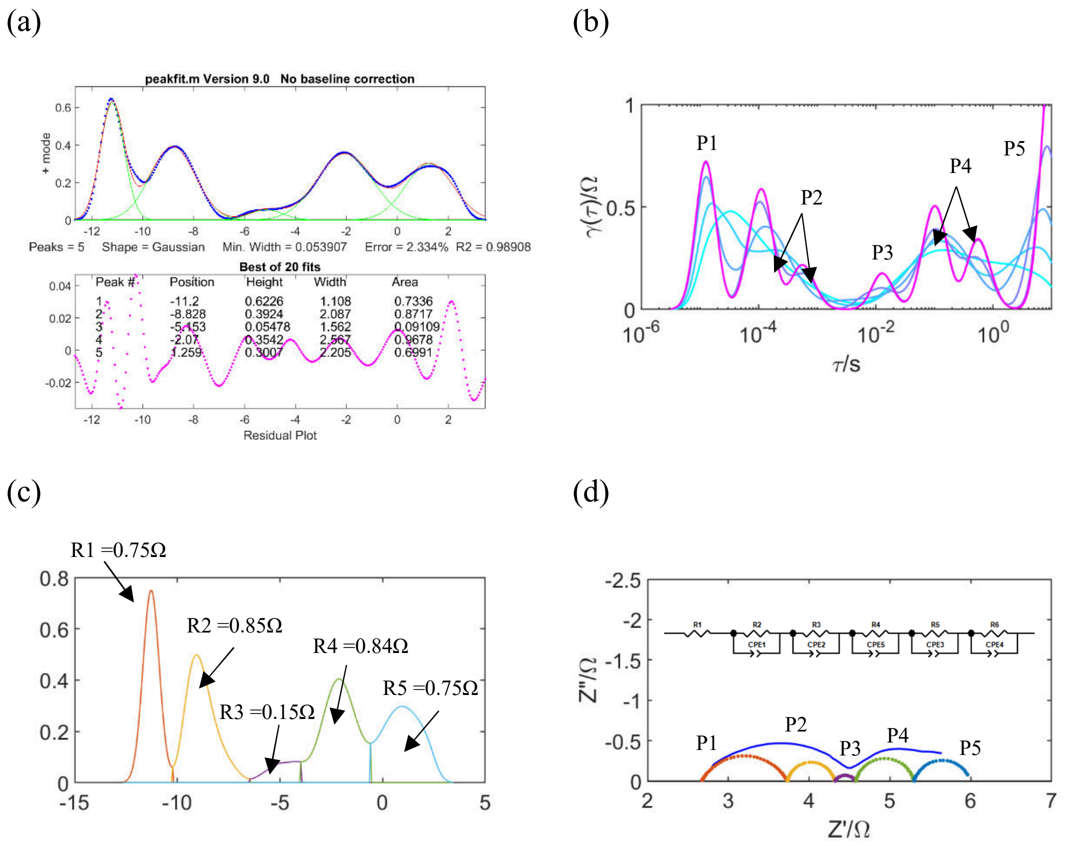

```
Peaks = 5    Shape = Gaussian    Min. Width = 0.053907    Error = 2.334%  R2 = 0.98908

Peak #     Position    Height     Width     Area
  1        -11.2       0.6226     1.108     0.7336
  2        -8.828      0.3924     2.087     0.8717
  3        -5.153      0.05478    1.562     0.09109
  4        -2.07       0.3542     2.567     0.9678
  5        1.259       0.3007     2.205     0.6991
```

Figure 4-17: Development of Equivalent Circuit for impedance analysis in SOFCRoll with Ni/YSZ based fuel electrode. (a) Gaussian fit to DRT of impedance data at 700°C [290]. (b) DRT data is constructed with various values of regularisation parameter λ (between 0.1 – 10^{-7}). (c) The area is calculated under the individual peaks of DRT. (d) Equivalent Circuit with five processes.

The fitting of such a large number of elements in poorly separated impedance spectra requires some parameters “fixed”. For this purpose, the resistances of polarisation processes were calculated from DRT, as the area under the peak corresponds to the ohmic resistance of the dynamic process [64]; this could be done either by determining the integral under the peak area (Figure 4-17 c) or fitting Gaussian peaks into DRT (Figure 4-17 a). The fitting of Gaussian peaks was made with Matlab based free program, a peakfit [290].

Both methods give close values; however, both require good peaks separation. The separation between peaks improves with lowering the regularisation parameter λ of the DRT [291]. The regularisation aims to prevent overfitting by incorporating additional information into the problem under consideration [292]—the method smoothes the data by introducing the additional term to the usual least square regression. The optimal λ would smooth the peaks to the point that they are not oscillating but producing the closest possible DRT to the original DRT. Figure 4-17 b shows the DRT of the impedance data from 0.1 (in blue) to 10^{-7} (in pink) regularisation parameter. A lower value gives better separation and divides single peaks; the area under both peaks still would give the resistive value of the single process, but they do not correctly reflect the system's behaviour. Also, peaks change their frequency; therefore, the characteristic frequency read from DRT with not optimised λ could not be correct. There are methods to calculate the optimal value of this parameter [292]. Due to this problem, the area under the peaks (thus resistance) was chosen as the "fixed" term for EIS fitting, as it does not change to a large extent with chosen λ. While such parameters as capacitance or characteristic frequency were obtained from the equivalent circuit. Another approach was to "fix" resistance first at one of the temperatures (or other conditions) and find the approximate value of "n" in the constant phase element (CPE), which determines the shape of the semicircle. Assuming that shape of the semi-circuits would not change at the whole tested range, an equivalent circuit with constant "n" could be used for all conditions.

Table 4-6: The overview of processes assigned to the impedance of SOFCRoll with Ni/YSZ FE.

No.	Description	Char. Freq./ Hz at 700°C	Ea/ eV 700 - 850°C	Capacitance/ F at 700°C
Rs	The ohmic resistance of the cell	-	0.37	-
P1	Transport of O^{2-} at OE/YSZ interface	17766	0.37	1.3×10^{-5}
P2	Charge transfer at FE	1867	1.6	1.9×10^{-4}
P3	Diffusion process at OE or FE	268	0.1	4.8×10^{-3}
P4	Diffusion process at OE or FE	1.8	0.18	1.3×10^{-1}
P5	Diss./ adsorption and transport at OE	0.15	2	1.7

The cell's polarisation and ohmic resistance after extraction of ohmic resistance (0.1Ω) of stainless steel tubes was plotted on the Arrhenius dependence (Figure 4-16 b). In the fitting, besides polarisation resistance, all other elements were "un-fixed" this determined the values of R and CPE elements which gave the value of capacitance (equation 1-22) and characteristic frequency (equation 1-20). The value of capacitance and characteristic frequencies of polarisation processes and possible interpretation gives in Table 4-6.

The theoretical activation energy of the YSZ electrolyte is 0.9 eV, and the conductivity of 0.08 S/cm at 850 °C [87]; for a 100 μm thick electrolyte, this should give about 0.2 Ω per 1 cm^2. The ohmic resistance of the tested cell was in the range of 2.4 -1.34 Ω and had an activation energy of 0.4 eV between 700-850 °C. Such a large ohmic resistance value could indicate lower electrolyte conductivity due to sintering at 1350 °C or migration of Mn ions into YSZ electrolyte [293] and low active area utilisation. Moreover, in the following measurements, a higher amount of silver was applied to contact between the stainless tube and electrodes to decrease all the resistive contributions, indicating that poor contact between the stainless steel tube and electrodes also affected total resistance.

Numerous processes have been reported on LSM/YSZ oxygen electrodes [190], [294], [295]; which include the transport of oxygen ions through the LSM/YSZ interfaces and the YSZ at high frequency, oxygen incorporation and its transport to interface with the YSZ electrolyte at a medium to low frequency and contribution related to gas diffusion at a very low frequency. The value of capacitance and characteristic frequency of P1 corresponds to the high-frequency process related to oxygen ion transport [294]. Also, the arc does not change when the cell is tested on a different fuel, further supporting the assignment of P1 to the oxygen electrode. The activation energy is much lower than the reported 1 eV, likely due to defects in the tested cell. Another process, likely coming from an oxygen electrode, is P5; the polarisation comes from the dissociative adsorption of oxygen and the transport of intermediates to 3PB. The large value of activation energy points to this conclusion [294]. Also, tests made on symmetrical cells (Chapter 5.5.3.2) confirm the existence of a low-frequency arc at a very low frequency. In LSM/YSZ based materials, the oxygen reduction occurs on 3PB with YSZ, and transportation of oxygen species mainly follows the surface path. In literature, the process associated with dissociative adsorption and transport of oxygen at LSM/YSZ usually is found at a middle frequency, e.g. 150 Hz at 700 °C [296]. Here the drift to a very low frequency is probably due to the high sintering temperature of LSM, as shown in [263].

One or two arcs are reported on Ni/YSZ fuel electrode [113], [296], [297]. The primary response is at a high frequency, usually between 1 and 10 kHz. The process is dependent on the microstructure of the electrode and is associated with the charge transfer between YSZ and Ni. For a "good" fuel electrode, the activation energy would be around 0.8 eV [296]. The charge transfer at the fuel electrode was ascribed to the P2 process with a characteristic frequency and value of capacitance corresponding to theoretical values.

Interestingly, in all analysed cells with Ni/YSZ electrodes, P2 seems to deteriorate at 700 °C. Perhaps, due to gas crossover, Ni starts to oxidise when temperature decreases. The process also seems not to be further activated at a temperature above 800°C, which could be due to the enlargement of cracks or increase in the diffusion of gases through them; hence lower partial pressure difference between gas compartments. P3 and P4 show a very low dependence from temperature, indicating that they are related to concentration losses. Usually, the concentration polarisation on Ni/YSZ electrode is found at a frequency below 100 Hz [125], [296], [298].

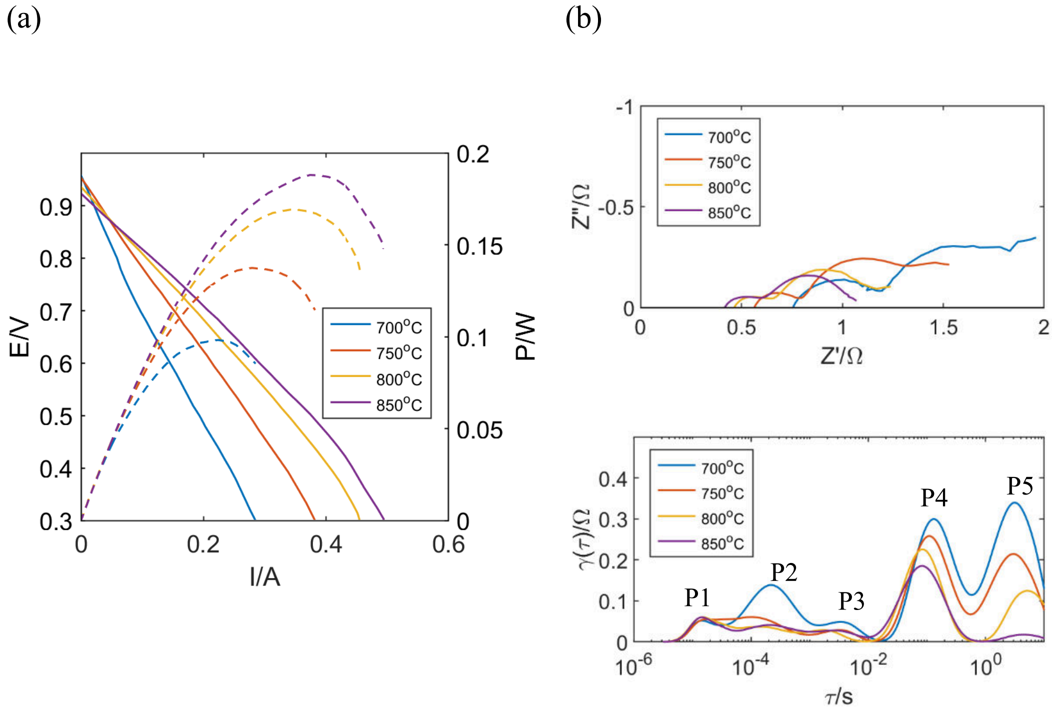

Figure 4-18: The electrochemical performance of the SRB3 SOFCRoll in the temperature range 700-850 °C and the 100 ml/min 5% H_2/N_2 in FE and 100 ml/min of air in OE. (a) I-V curve of cell operating in fuel cell mode. (b) EIS and DRT analysis of impedance data at OCV conditions.

For the manufacturing of SRB3, the long tapes were laminated then cut instead of laminating all layers separately. Performance increased as cells had fewer internal defects (Figure 4-18). Those cells had matched the shrinking profile at a lower temperature (up to 300 °C) due to modification of organic slurry content (Figure 4-5), which may have reduced defects. However, the leading cause can be seen in the new assembly method. It removes the need to apply every single layer separately, which introduces many structural defects into a cell. The electrochemical test of the SRB3 cells had much lower resistance and higher OCV value than SRB1, increasing the amount of generated power up to 190 mW at 850 °C when operating at 5% H_2. Cell achieved one of the highest performances among SOFCRoll with Ni/YSZ based fuel electrode developed in this study, with the fuel utilisation equal to 26.5% at 100 ml/min flow of 5% H_2 in FE.

The ohmic resistance of the cell was between 0.65 Ω at 700 °C and 0.3 Ω at 850 °C. The presented cell had one layer of YSZ electrolyte instead of two, likely decreasing the ohmic resistance per active surface area due to the thinner electrolyte. Moreover, the microstructure analysis showed the possibility of delamination when two YSZ tapes were laminated for cell preparation (Figure 4-9). Such defects entirely blocked the flow of oxygen ions through an electrolyte, effectively decreasing the cell's surface area.

Also, the influence of a higher amount of silver paste on cell performance was investigated. Instead of painting the thin layer of silver on stainless steel tubes, a thick layer of silver was applied. The higher amount of silver decreased the cell resistance more than two times. The paste was still applied pointwise, so the drop of resistance was not coming from an expansion of surface area only from the more reliable connection between the metal tube and the surface of the electrode.

The DRT analysis gave a similar distribution of arcs as previously; however, P4 showed higher activation energy. Both P1 and P2 seem to be much smaller when compared to all other cells, and their activation energy decreased. Also, in this case, at 700 °C, the P2 process substantially increased.

Finally, the performance of co-cast cells was studied. As previously, the amount of the silver current collector on the contact was increased. One test was conducted with the additional stripe of silver painted through the whole channel; however, it did not improve the performance, indicating sufficient conductivity of current collector layers (at least in the channel). The presented cell was tested with 100 ml/min of 5% H_2/N_2. The value of OCV was almost 0.9V at 800 °C. The SEM analysis confirms some internal cracks; however, delamination is the dominant defect. The ohmic resistance of the cell was between 1.11 Ω at 700 °C and 0.8 Ω at 850 °C. Due to poor control of the casting gap in the co-cast cell, the acquired electrolyte thickness was about 250 µm, much higher than in cells where electrolyte was cast separately.

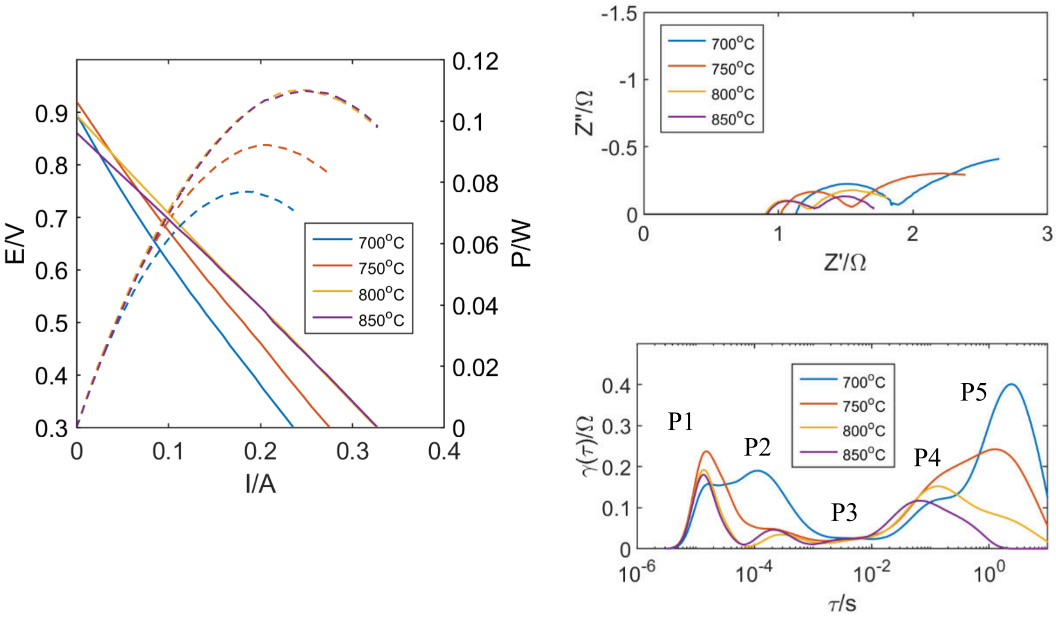
(a) (b)

Figure 4-19: The electrochemical performance of the SRB5 SOFCRoll tested in the temperature range 700-850 °C and 100 ml/min 5% H_2/N_2 in FE and 100 ml/min of air in OE. (a) I-V curve of cell operating in fuel cell mode. (b) EIS and DRT analysis of impedance data at OCV conditions.

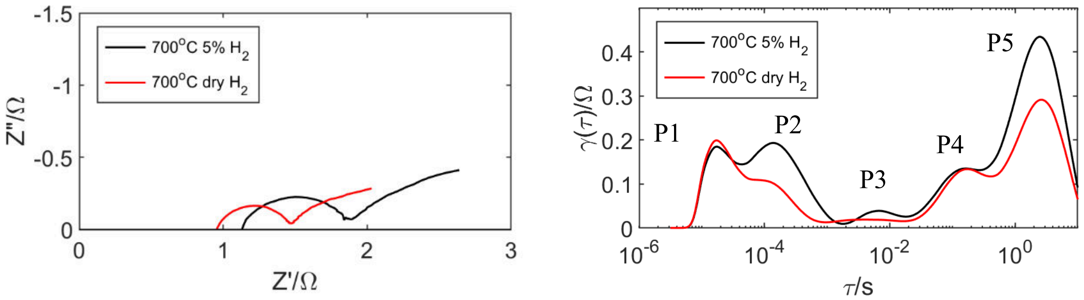
(a) (b)

Figure 4-20: The comparison of impedance data of SRB5 tested at the 700°C and with 100 ml/min 5% H_2/N_2 and 20 ml/min of dry H_2 in FE, both tested with 100 ml/min of air in OE.

The DRT is similar to other cells with five polarisation processes and similar behaviour. P2 increased a lot at 700 °C, but at other ranges has low activation energy, similar to in SRB3. P4 shows moderate activation energy, while P5 has a significant temperature dependency. The test on pure H_2 was conducted on a different cell; therefore, it could bring some errors in comparison; it is also possible that cells produced by hand gave a slightly different performance. Cell with H_2 required a much lower flow to achieve satisfying OCV, around 20 ml/min; the higher flow resulted in a drop in OCV. A 150 mW of power was generated at 850 °C, about 25% more than in 5% H_2/N_2, which worked the best at the higher flow. Cells tested at pure H_2 had lower ohmic resistance and contribution from P2, the prominent peak in the fuel electrode. It is unclear why P5, ascribed to the oxygen electrode, was affected. Perhaps using H_2 decreased pO_2 at the oxygen electrode to a greater extent due to cracks.

4.6 Summary

The initial research on SOFCRoll quickly revealed the challenges with their manufacturing, particularly difficulties with tape assembly, often leading to defects. Moreover, the shrinking analysis of electrodes and an electrolyte indicated the significant differences in its profile during temperature treatment that causes considerable stress inside a cell, forming delamination and cracking.

Employed modifications made the whole process easier and improved the cell's quality. The SEM analysis showed a reduction in the number of defects, even without controlling the shrinking profile. Notably, the co-casting was encouraging; casting tapes directly on each other eliminated the need for lamination and produced a more robust connection between layers.

The electrochemical analysis also showed the better performance of the subsequent batches. Nevertheless, the maximum power was up to 0.2 W, which with such a large area of electrodes, was a poor result, indicating that only a small part of the cell was active. The main factors behind inadequate performance were internal defects, poor current collecting, and diffusion problems.

5 SOFCRoll with LCNT based electrodes

5.1 Introduction

Eventually, attempts were made of replacing Ni/YSZ electrodes with LCNT based material. Subsequently, the shrinking analysis of the electrode layers was controlled to diminish the defects occurring during the co-sintering process.

Due to the delamination of the pure LCNT layer when co-sinter onto YSZ electrolyte, the LCNT-YSZ composite with an equal volume ratio of materials was used as the active fuel electrode (LCNT/YSZ50). Two different solutions were proposed for the current collector layer: Ni/LCNT50 composite sintered on the whole area of the active electrode and Ni/YSZ10 sintered just in the spiral part of the cell. Thanks to the pre-sintering of the LSM-YSZ composite, the oxygen electrode's shrinking profile has also been matched.

The tape casting and cell assembly method were further modified. Both sides of the cells were co-cast separately and then laminated, giving better control over the experiment while obtaining a well-developed interface. Also, the multiple cell designs were investigated, varying in size, gas exhaust and, as already mentioned, with different current collector layers.

As previously, the performance of SOFCRoll was investigated with I-V and EIS analysis, and various types were compared. In addition, the set of planar cells was developed and tested based on materials used for SOFCRoll to separate polarisation from both electrodes and investigate their functionality in a more homogeneous system. Also, a simple mechanism of H_2 oxidation/ H_2O electrolysis on the fuel electrode was proposed.

5.2 Development of LCNT/YSZ50 active fuel electrode

The next step was the implementation of LCNT based anode into the SOFCRoll structure. The LCNT powder was prepared using modified solid-state synthesis (Chapter 2.2.1). Also, trials have been carried out to control the shrinking profile of electrode layers; through a modification of slurry composition and ceramic material used for its preparation, the YSZ electrolyte slurry has not been changed throughout the whole project. A shrinking profile of LCNT based fuel electrodes was regulated by the slurry composition and size of ceramic particles. The collected analyses of LCNT particle size are given in Table 5-1 and Figure 5-1. Besides the milling time and size of milling balls, the rotational speed, the volume of ball milling containers, and the amount of material affecting particle size distribution.

Table 5-1: The analysis of LCNT particle size, ball-milled for various times and milling balls size.

Milling balls size	Time/h	D10/µm	D50/µm	D90/µm	SSA/m^2g
Large, 10 mm	2	0.552	4.606	11.819	0.908
Large, 10 mm	3	0.540	3.445	12.380	0.986
Large, 10 mm	6	0.426	2.289	5.902	1.32
Large, 10 mm	9	0.373	1.408	3.962	1.7
Large, 10 mm	12	0.383	1.128	3.102	1.83
Large, 10 mm	16	0.323	1.058	4.307	2.03
Mixed, 10, 3, 1 mm	3.25	0.236	1.672	3.994	1.45
Mixed, 10, 3, 1 mm	7	0.222	0.798	2.804	2.86
Mixed, 10, 3, 1 mm	10	0.168	0.531	2.561	3.87
Mixed, 10, 3, 1 mm	14	0.169	0.516	2.094	3.93
2 stage, 3 mm	2.5	0.366	2.387	8.648	1.45
2 stage, 3 mm	7.5	0.167	0.788	2.554	3.46
2 stage, 3 mm	10	0.165	0.641	2.167	3.7

For the cell's development, the required small size of LCNT particles was produced either by ball milling with mixed-size balls or two-stage ball milling with smaller balls at the second stage. The particle's size had to be reduced below 0.8 µm to obtain a shrinking of LCNT/YSZ50 composite matching the YSZ electrolyte; however, milling balls with a given size could only reduce particles below a specific value, depending on the material hardness (Figure 5-1 d).

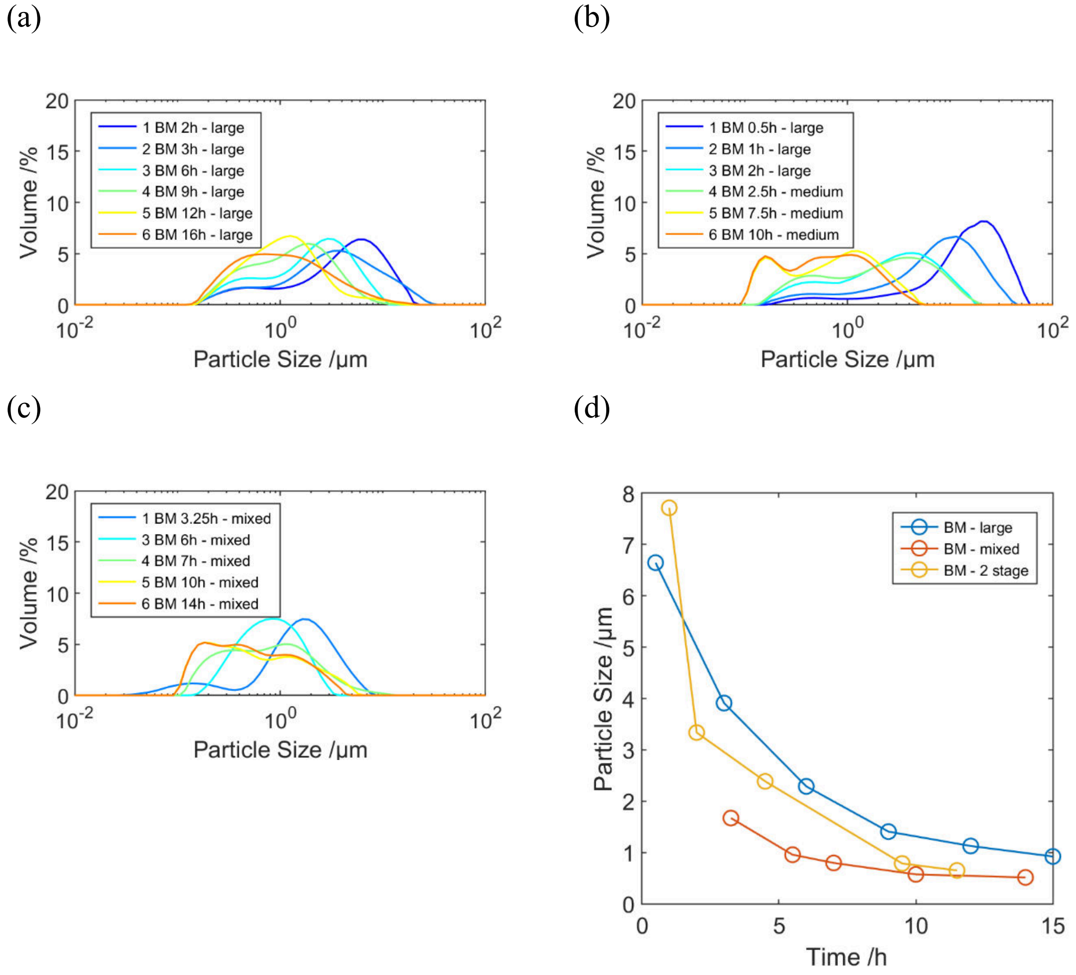

Figure 5-1: Particle size analysis of LCNT powder ball-milled for indicated times at 400 rpm. (a) Ball milled with 10 mm milling balls. (b) 1-3 ball-milled with 7 x 10 mm balls, then changed to 20g of 3 mm balls. (c) Ball milled with mixed balls 4 x 10 mm; 12 x 3 mm; 10 x 1mm balls. (d) Size dependence for various times and milling balls size.

The size reduction rate slows down during the ball milling until it almost entirely levelling off. Milling LCNT material at 400 rpm with 10 mm milling balls had the fastest rate at the initial 2 h and reduced particle size to the 3-4 µm range. Afterwards, even 15 h milling time was insufficient to reduce it below 1 µm. The finest powder could be produced with the small milling balls, but they do not have enough force to break larger particles. To reduce particle size from the initial, grounded material, a mixture of different milling balls may be used or a two-step process, where smaller ones in the second step replace the large milling balls. The first method required 6.5 h ball milling at 400 rpm. No additional peaks were visible on the LCNT pattern after milling with mixed balls, but when such prepared LCNT powder was co-sintered with YSZ, additional peaks were observed near stabilised zirconia peaks in the XRD pattern at 31.6, 34.6, 35.2, 35.53° (Figure 5-2). These peaks correspond to the monoclinic ZrO_2 [299], most likely, coming from zirconia produced from the grinding of zirconia milling balls and walls of containers. The milling procedure was changed to a less intensive, with two stages, where after initial milling, balls were replaced to a smaller size. After 2 h of ball milling at 400 rpm, 10 mm milling balls were changed to 3 mm balls and milled for a further 7.5 h at 400 rpm.

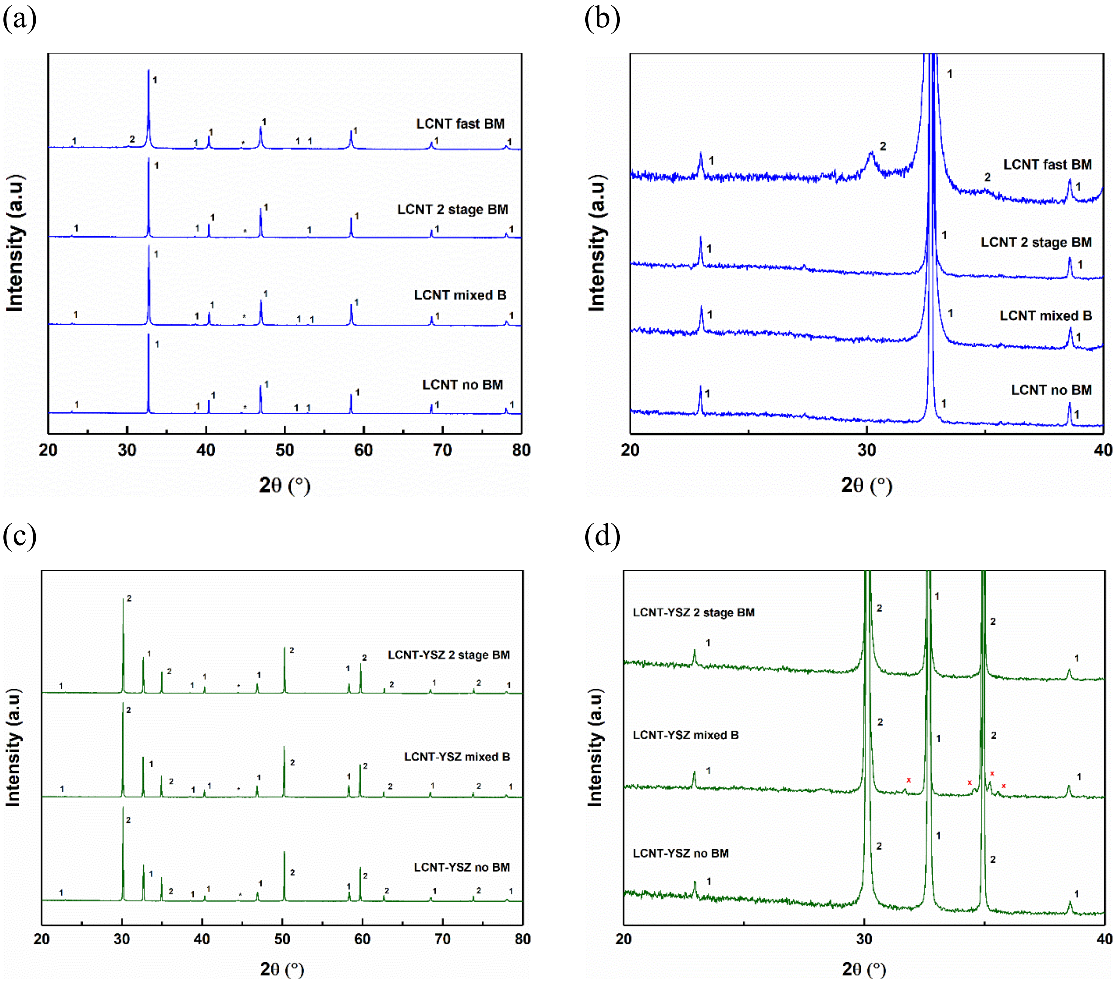

Figure 5-2: XRD analysis. (a) - (b) LCNT ball-milled with various methods. (c) - (d) LCNT/YSZ50 powder prepared with LCNT powder ball-milled with various methods.

The average size of ceramic particles produced by 2-stage milling was about 0.8 µm, and no visible traces of monoclinic zirconia were detected on the XRD pattern of ball-milled LCNT or sintered LCNT/YSZ composite. The process is long and energy-demanding; there was an attempt to reduce the processing time using high-speed ball-milling. The procedure was shortened to 1 h 20 min, with two stages, the first 20 min with large milling balls at 400 rpm and 1 h at 800 rpm with smaller balls (10 mm and 3 mm). However, the produced powder had the most significant ZrO_2 contamination among all methods, visible already on the XRD pattern of LCNT. The size distribution of ceramic particles prepared with various methods is slightly different, but both show the average particle size of 0.8 μm, and the produced LCNT/YSZ50 electrodes shrink similarly. The fine powder produced with mixed balls does not have any large fraction above 6 μm, while produced with the 2-stage method has 1.4% in total, which is not significant and did not influence the quality of produced electrode. The powder produced with the 2-stage method has two peaks, one at 0.18 μm and the second at 1.2 μm, while the distribution of particles milled with mixed milling balls is more levelled.

At the initial phase of LCNT implementation, a pure LCNT layer was considered to be used as the active fuel electrode. However, the layer tended to delaminate from the YSZ electrolyte, even when shrinking was matched, Figure 5-3 a - b. The attempt was also made to produce an LCNT active layer with a small amount of YSZ (e.g. 10% by vol.); however, it decreased a shrinking significantly (to about 2% with the addition of 10% YSZ by volume), Figure 5-3 c-d; this behaviour was unexpected as shrinking of "pure" LCNT with the same LCNT particle size was about 18%. This behaviour suggests that the sintering of LCNT and YSZ is rather governed by coarsening than densification. When LCNT pure layer is co-sintered on YSZ, the neck formed between materials is believed to come from the particle's surface, and as the material is not transported between the lattice and grain boundaries, the strength of the interface is poor. For the material with the addition of 10% YSZ, presumably, the YSZ and LCNT form a homogeneous mixture, where YSZ surrounds LCNT particles. During the thermal treatment, sintering is governed by the surface mechanism between YSZ and LCNT, leading to coarsening, hence low shrinking.

Due to difficulties implementing those layers, the composite electrode with a 50/50 volume ratio between LCNT and YSZ was used. The more significant relative concentration of both materials increases the volume of LCNT and YSZ phases within a composite, and the noticeable shrinking presumably comes from the densification of separate phases. At the same time, the sintering between LCNT and YSZ phases is still believed to be governed by the surface process.

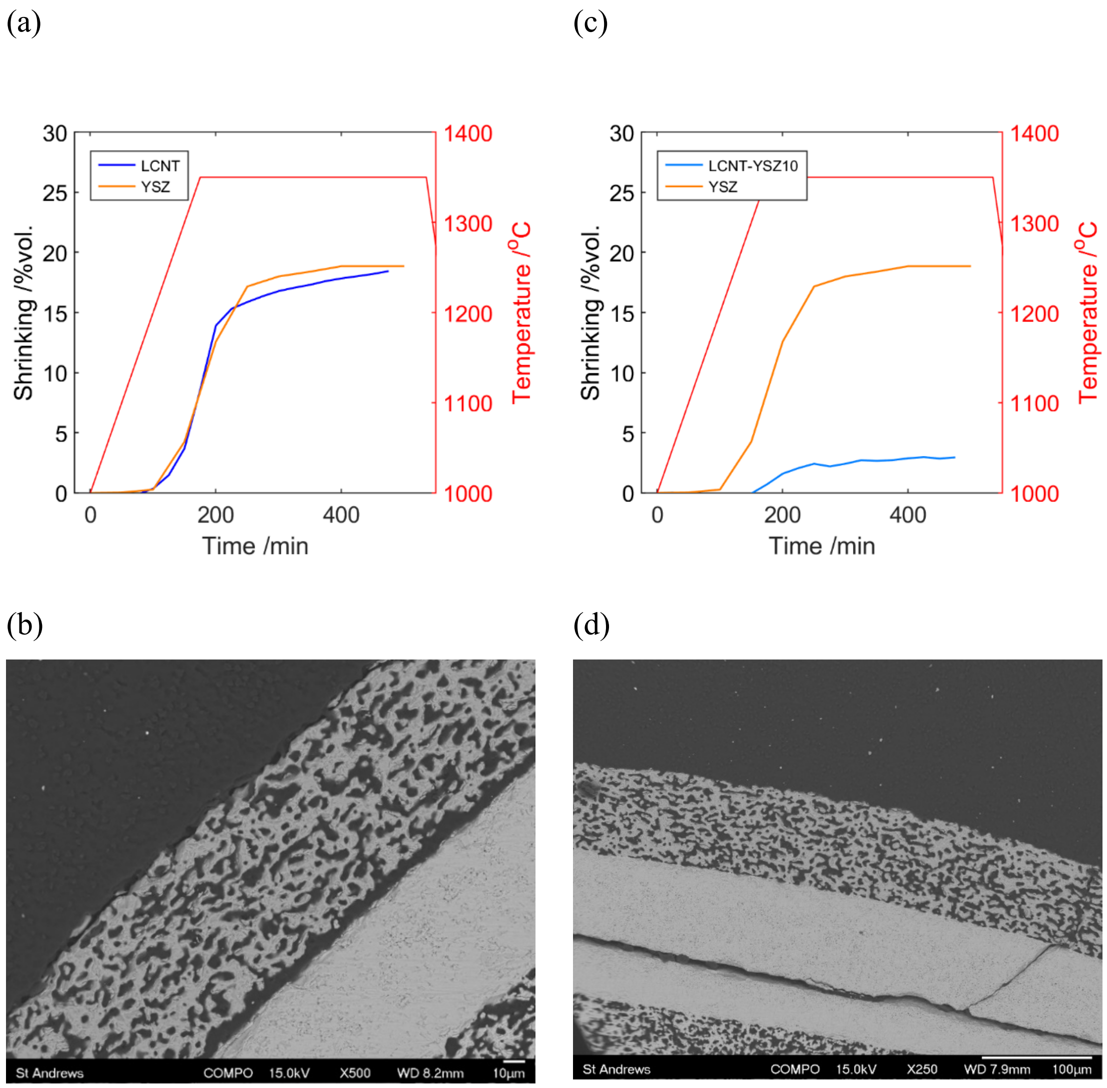

Figure 5-3: (a)-(b) Shrinking profile and SEM Image of LCNT layer co-sintered on YSZ electrolyte in SOFCRoll. (c)-(d) Shrinking profile and SEM Image of LCNT layer with 10% by vol. YSZ content co-sintered on YSZ electrolyte in SOFCRoll.

The YSZ is a pure ionic conductor (IC), where oxygen ions are transferred through oxygen vacancies in its cubic fluorite structure [300]. Presumably, in LCNT/YSZ composite, the activity of metallic particles and MIEC properties of LCNT could be supported by ionic transport in YSZ, and the layer would produce a better interface with the electrolyte. Much better performance was observed with the addition of pure ionic conductors like CeO_2 or YSZ into the perovskite-based fuel electrode [301], [302].

The development of the electrodes layers for co-sintering purposes is not a trivial task. Changing the shrinking profile with particle size will also change the microstructure of the electrode. At the same time, variation in pore-former concentration will change porosity and affect shrinking. Moreover, the slurry viscosity will be affected by pore former concentration and surface area of ceramic material. These parameters must be controlled simultaneously to produce castable slurries that produce cells without defects and the required microstructure and thickness of ceramic layers.

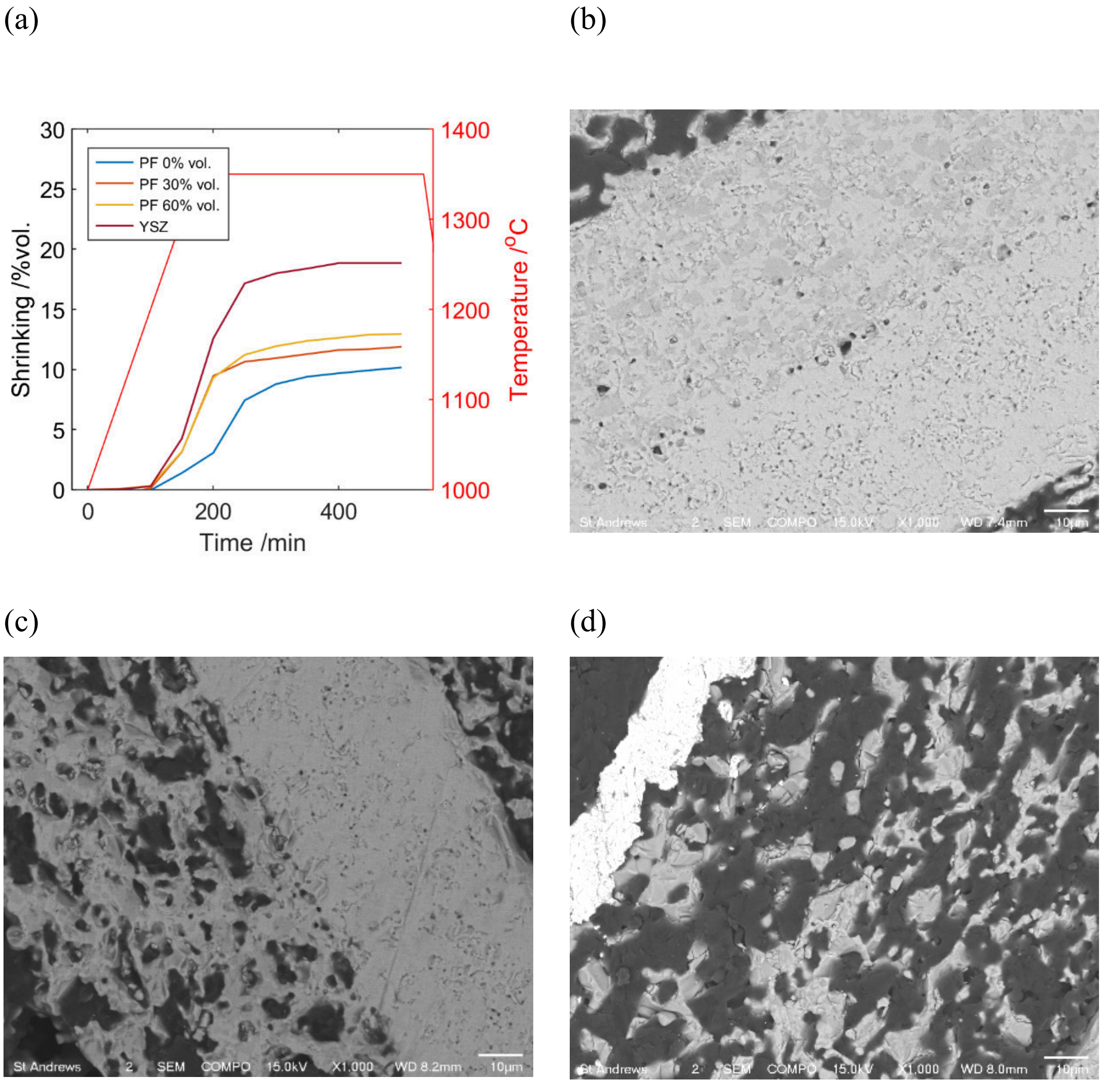

Figure 5-4: Porosity and shrinking measurements of LCNT/YSZ50 with the average size of LCNT particles 4 μm and various pore former concentrations by volume. (a) Shrinking measurement; SEM (BSE) image of the electrode with (b) 0%, c) 30%, d) 60% pore-former concentration.

Table 5-2: The characteristic of the LCNT/YSZ50 layer with various pore former concentrations by volume at constant particle size (4 µm).

Pore Former [%]	Porosity [%]	Max. Shrin. [%]
0	0	10.16
30	39	11.88
60	79	12.9

The study of shrinking and porosity of the ceramic layer at constant particle size reveals the influence of pore former concentration on the shrinking profile and final porosity (Figure 5-4). The layer without pore former is almost entirely agglomerated and shrinks less than samples with pore formers. After adding 30% vol. of pore former, shrinking increase at the full profile and sample develop a porous network. With 60% vol. pore former concentration porous network continues to develop, but the final shrinking profile has only ~ 1% difference compared to slurry with 30% vol. pore former concentration.

The possible explanation for this phenomenon could be as follows. The ceramic particles are irregular; however, for simplification, it could be assumed that they are spherical, as shown in Figure 4-8 a. When the particles are arranged into a bulk, there is space between them; the shrinking of the ceramic layer without pore former is related to the reduction of this "open space" by the transport of the material between the adjacent particles. The maximum distance for the diffusion of the material is limited by the size of those pores and material properties at a specific temperature, e.g. their diffusion coefficients. After adding pore former, more "open space" is created in the bulk of the green body. Thus, the distance of particle bulk movement would not be limited (or limited less) by available space; hence, the shrinking increase. The porosity would be created when material properties limit movement at specific coordinates. More space is created at specific coordinates with the higher pore former addition, which increases shrinking if it is limited by "open space" availability. Perhaps beyond a specific limit of pore former concentration, a diffusion of material is not limited by available space; therefore, shrinking is not increasing, only the porosity.

The study of shrinking and porosity of the ceramic layer at constant pore former concentration reveals the influence of particle size on the shrinking profile and final porosity (Figure 5-5); shrinking increases with smaller particle size, while porosity is reduced. Such behaviour is related to the larger surface area of small particles, and higher bulk density, more surfaces of particles are in contact; hence they agglomerate more. With a larger particle size, fewer surfaces would be adjacent, and the distance between particles would be higher; hence, the porosity increase while shrinking decreases. On the macroscale, the strong dependence of shrinking on particle size is related to the total surface area per volume, decreasing with larger particle size and more equilibrium particle shape (Wulff shape) [286].

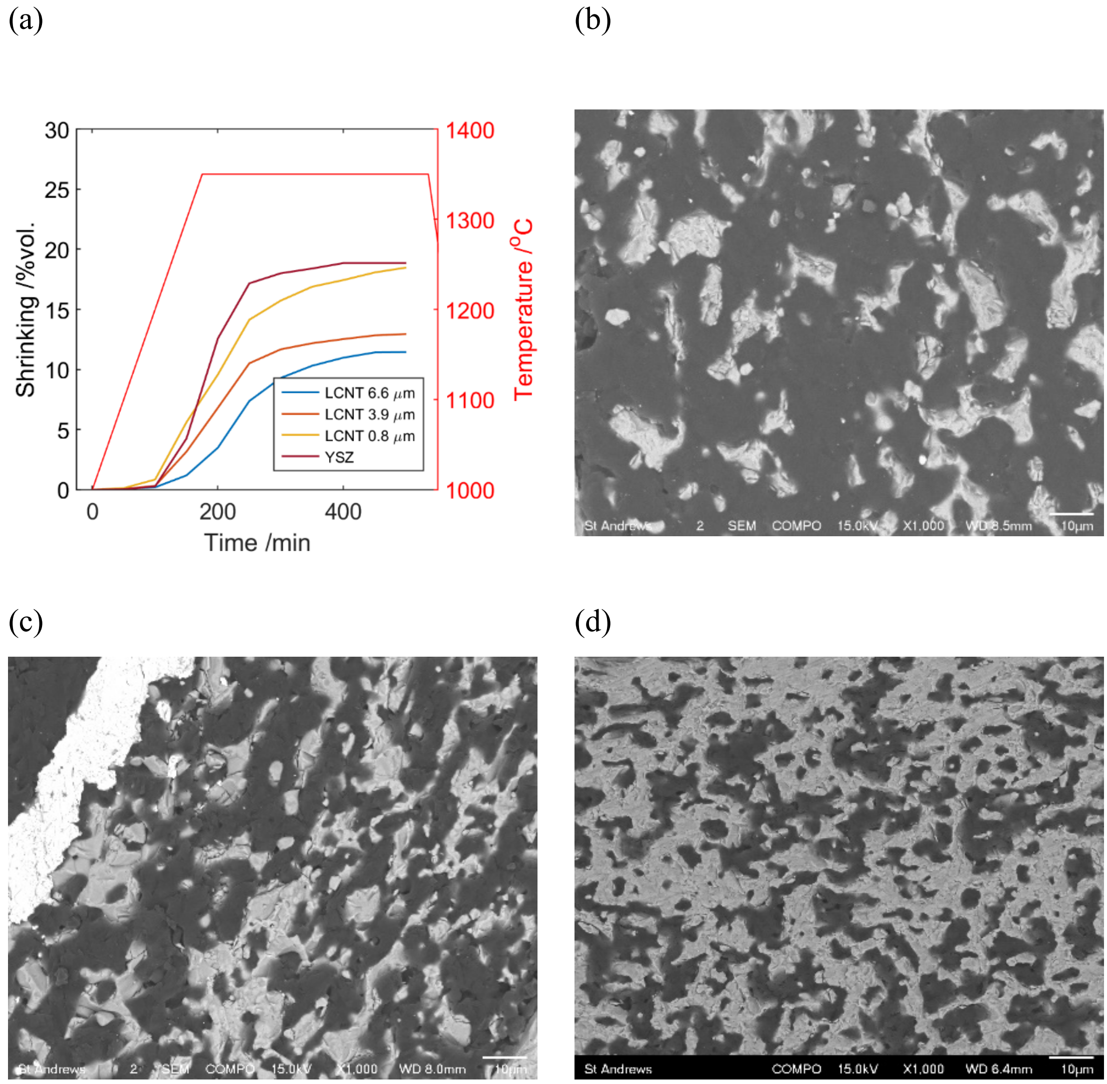

Figure 5-5: Porosity and shrinking measurements of LCNT/YSZ50 active anode with 60% vol. of pore former made with the various average size of particles. (a) Shrinking measurement; SEM (BSE) images of the electrode with (b) 6.645μm, c) 4μm, d) 0.798 μm, LCNT/YSZ particle size.

Table 5-3: The characteristic of LCNT/YSZ50 layer with various particle sizes at constant pore former concentration (60% by vol.).

Particle size [µm]	Porosity [%]	Max. Shrin. [%]
6.6	79	11.4
4	69	12.95
0.8	48	18.46

The investigation of how the particle size and pore former concentration affect the slurry properties and microstructure of sintered materials helped to develop a procedure for formulation of a castable electrode slurry with set porosity and shrinking profile for the co-sintering purpose, which contains the following steps:

1. Mixing ceramic particles (grounded and pre-milled, e.g. 1 h ball-milling) with the pore former in a 40/60 volume ratio.
2. Addition of the solvent in the amount that mixture forms a dense liquid (visual investigation or viscosity measurement).
3. At the second stage of slurry preparation (Chapter 3.3), add plasticizers and binder in concentration at standard binder plus plasticisers/ solvent ratio (Table 4-2).
4. Cast tape, investigate the shrinking profile (Chapter 3.6).
5. Formulate the following slurry, adjust the shrinking profile by changing the size of ceramic particles, keep the same pore-former concentration as in step 1 for slurry formulation. Adjust organic ratio as in steps 2 and 3.
6. Repeat step 5 until the required shrinking profile is attained.
7. For the next slurry, use particle size, which gives the required shrinking profile and adjusts the pore-former concentration to tailor porosity, as explained before, changing the pore former concentration in a range of 30%-60% (investigated for LCNT/YSZ50 only) of its total concentration does not significantly affect shrinking profile, (Figure 5-5). Adjust organic ratio as in steps 2 and 3.
8. Double-check the shrinking profile and porosity modify the slurry if required.

5.3 Development of LSM/YSZ oxygen electrode

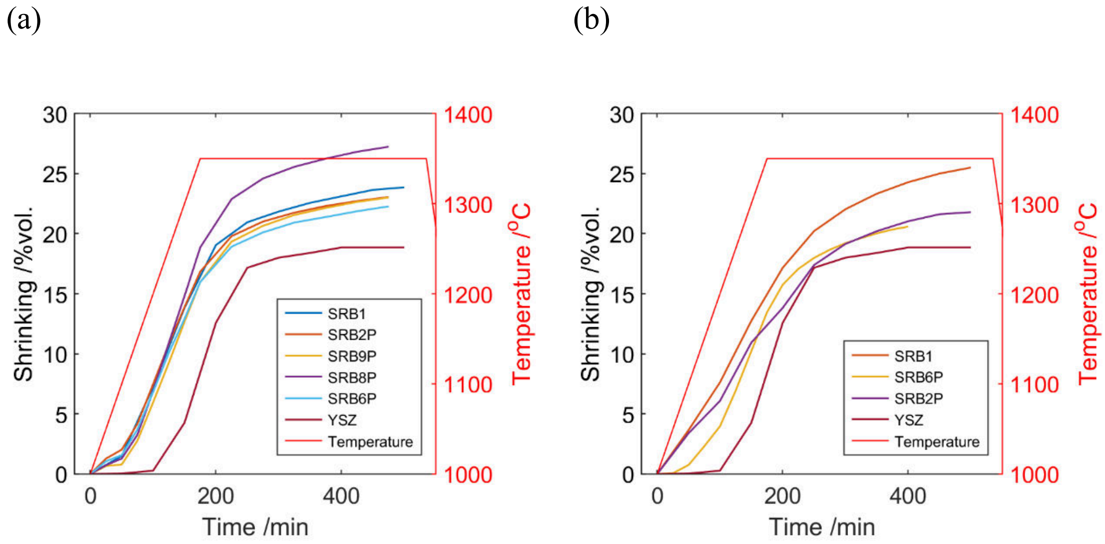

Figure 5-6: Shrinking analysis of oxygen electrode with various particle sizes made by coarsening (Table 5-3). (a) Shrinking analysis of LSM/YSZ50 active layer made of LSM and YSZ powders mixed in the slurry. (b) Shrinking analysis of LSM current collector layer.

Table 5-4: Specification of ceramic particles for LSM/YSZ50 and LSM tapes preparation in Figure 5-6.

Tape	No.	LSM	YSZ	Pore Former/ % by vol.	Por./ %
LSM/YSZ50	SRB1	As provided, B1, 1.45µm	As provided, 1.1µm	Graphite, 60%	47
LSM/YSZ50	SRB2P	Pre-sint., 1000°C, 3.5 m	As provided, 1.1µm	Graph. & Starch, 60%	56
LSM/YSZ50	SRB6P	As provided, B2, 2.03	As provided, 1.1µm	Graph. & Starch, 60%	37
LSM/YSZ50	SRB8P	As provided, B1, 1.45µm	p.s. 1200°C, 1.2 µm	Graph. & Starch, 60%	43
LSM/YSZ50	SRB9P	Pre-sint., 1050°C, 3.3µm	As provided, 1.1µm	Graph. & Starch, 50%	42.6
LSM/YSZ50	SRB1P	Pre-sint., 1200°C, 5.1µm and 1000°C, 3.5µm (1:1)	As provided, 1.1µm	Graph. & Starch, 50%	83
YSZ		-	As provided, 1.1µm	-	2
LSM	SRB1	As provided, B1, 1.45µm	-	Graphite, 60%	36
LSM	SRB6P	As prov., B2, 2.03 µm	-	Graph. & Starch, 60%	54
LSM	SRB2P	As provided, B1, 1.45µm And 1200°C, 5.1µm	-	Graph. & Starch, 60%	57

As indicated in Chapter 4.3, the unmodified LSM and YSZ used directly in the slurry started to sinter already at a temperature below 1000 °C with a very high rate afterwards, significantly deviating from the profile of the YSZ electrolyte, SRB1 in Figure 5-6. The first attempts to modify the shrinking profile of the LSM/YSZ electrode depend on coarsening either LSM or YSZ (increasing particle's size under heat treatment), but the method did not give the desired results.

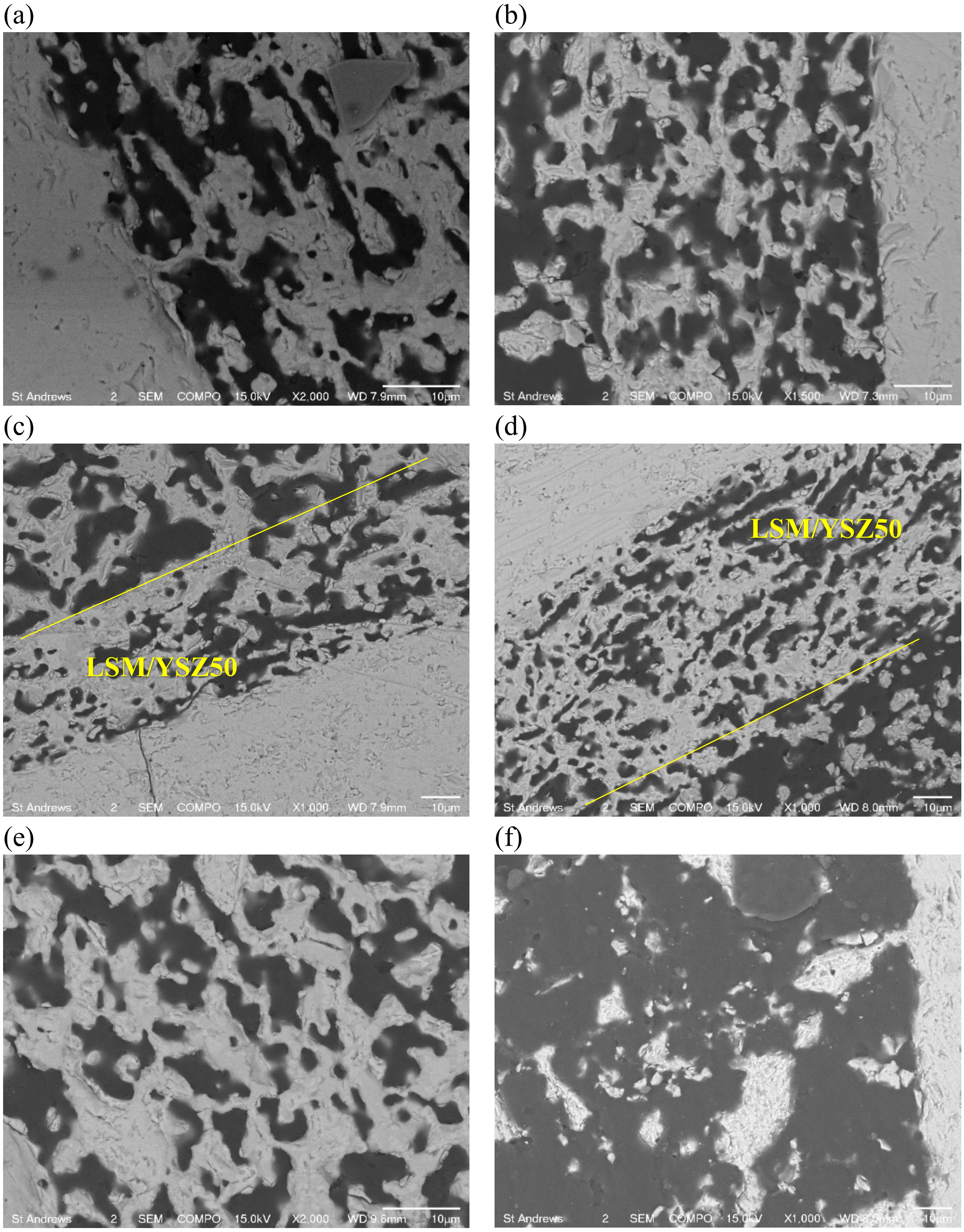

Figure 5-7: SEM (BSE) images of active oxygen electrode LSM/YSZ50 from various batches (Table 5-4). (a) SR1B (b) SRB2P (c) SRB6P (d) SRB9P (e) SRB8P (f) SRB1P.

Pre-sintering of LSM at 1000 °C for 2.5 h almost doubled the size of particles (from 1.4 to 2.8 µm of D50), further thermal treatment at the same temperature (up to 10 h) increased their size only slightly up to 3.3 µm of D50 (Table 5-4). The pre-sintered LSM at these conditions led to an increased layer's porosity (SR2B in Table 5-4), while the shrinking profile was almost unaffected, SRB2P in Figure 5-6. Another layer was produced from pre-sintered LSM at 1050°C; however, neither PSA analysis (Table 5-4) nor shrinking profile showed much difference, SRB9P in Figure 5-6. Similar behaviour was shown in layer SRB6P produced with unmodified LSM but larger particle size (the new batch of LSM, B2, had the bigger particles). To summarise, SRB1, SRB2P, SRB6P, and SRB9P produced a different particle size of LSM, between 1.45 and 3.5 µm and various pore former concentrations between 50-60% by volume, giving almost the same shrinking but diverse porosity, which means that there is a low dependence of shrinking of LSM/YSZ50 composite on LSM particle size (at least for this range of particle size).

Table 5-5: The LSM and YSZ particle size analysis pre-sintered at various temperatures and times. LSM comes from two different batches, B1 and B2.

Material	Temperature/°C	Time/h	D10/µm	D50/µm	D90/µm	SSA/m^{2}g
LSM B1	As provided	-	0.104	1.451	6.014	2.76
LSM B1	1000	2.5	1.260	2.886	11.893	0.363
LSM B1	1000	5	1.237	3.306	22.975	0.338
LSM B1	1000	10	1.284	3.576	18.649	0.324
LSM B1	1050	5	1.853	3.298	5.730	0.305
LSM B1	1100	2.5	1.228	3.369	14.158	0.342
LSM B1	1200	2.5	1.935	5.096	16.325	0.228
LSM B1	1250	2.5	1.961	6.531	28.665	0.201
LSM B2	As provided	-	1.108	2.036	4.674	0.483
YSZ	As provided	-	0.337	1.109	2.482	10.2
YSZ	1200	5	0.472	1.151	3.394	6.43
YSZ	1300	5	0.694	2.545	10.608	3.67

There were trials to increase the size of LSM by pre-sintering them at a higher temperature, at 1000 – 1250 °C for 2.5 h (Table 5-5). The produced size of LSM particles was up to 6.5 µm of D50 at 1250 °C. However, higher temperatures led to their agglomeration, and material had to be sieved to separate larger agglomerates. Screening increased the workload, and the method was not ideal, as large agglomerates still could be visible in the sintered layer, SRB1P, in Figure 5-7. Using higher pre-sintering temperature for LSM decreased the shrinking of the produced layer but was problematic in terms of material pretreatment, and produced layer had low homogeneity. Also, it is not desirable to use coarse powder as an active layer because the surface area decreases [212].

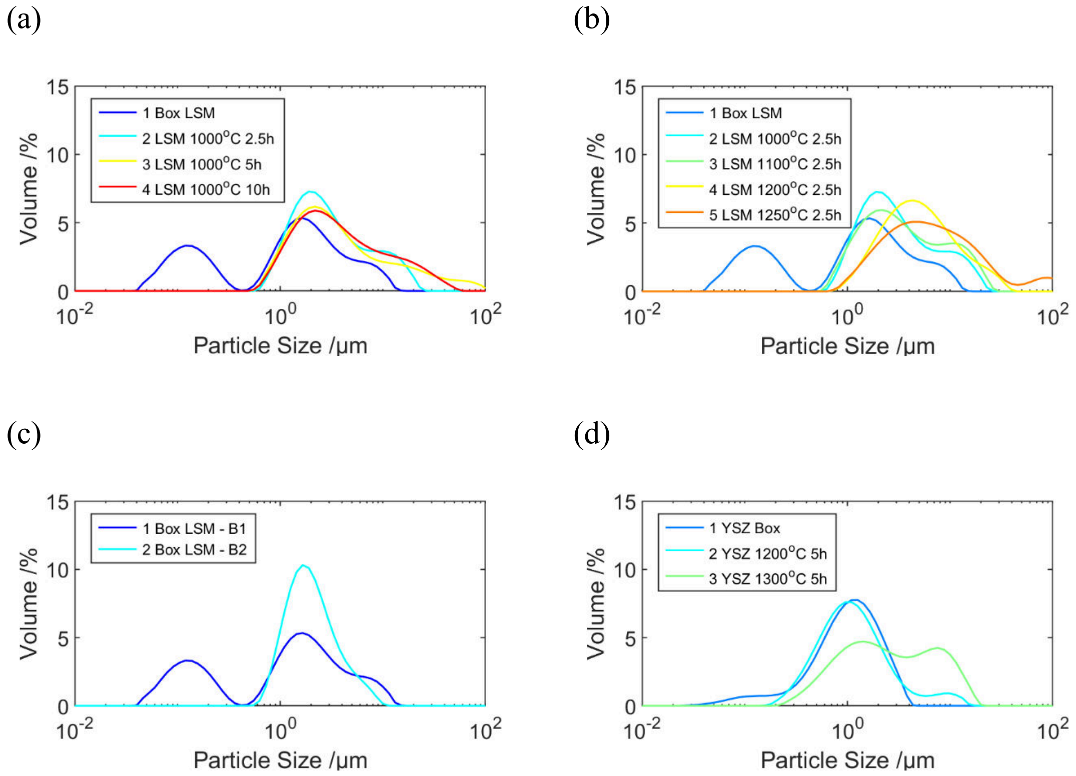

Figure 5-8: The PSA analysis of pre-sintered LSM powder for oxygen electrode preparation. (a) Pre-sintered LSM at 1000 °C at various times. (b) Pre-sintered LSM for 2.5 h at various temperatures. (c) Analysis of untreated LSM from batches B1 and B2. (d) Pre-sintered YSZ for 5 h at various temperatures.

The SRB8P layer was prepared with pre-sintered YSZ at 1200°C (Table 5-4); PSA analysis did not show much difference in particle size or distribution compared to untreated powder (Table 5-5). However, the measured surface area decreased from about 10 m^2/g to about 6 m^2/g, suggesting that YSZ particle changed their shape during pre-sintering under those conditions and became more regular. The SEM analysis of pre-sintered powder may better characterise changes in the size of YSZ particles. Pre-sintered YSZ did not decrease shrinking; it showed the opposite behaviour - shrinking increased, and produced layer had the lower porosity; the shrinking profile is close to the pure LSM layer (Figure 5-6). Meaning that shrinking between YSZ and LSM particles limits the layer's shrinking behaviour; by increasing the size (or changing the shape) of YSZ particles, fewer surfaces between LSM and YSZ are in contact; hence shrinking increases.

There is a higher dependence of shrinking on particle size for the pure LSM layer. The SRB1 produced from LSM with 1.45 µm particles has much higher shrinking than SRB2P produced from LSM with 2.03 µm particle size. Dependence became less determining for bigger particles. Measurement showed that the layer produced from the mixture of course powder SRB2P is close to that produced from untreated powder (SRBP6), Figure 5-6 b.

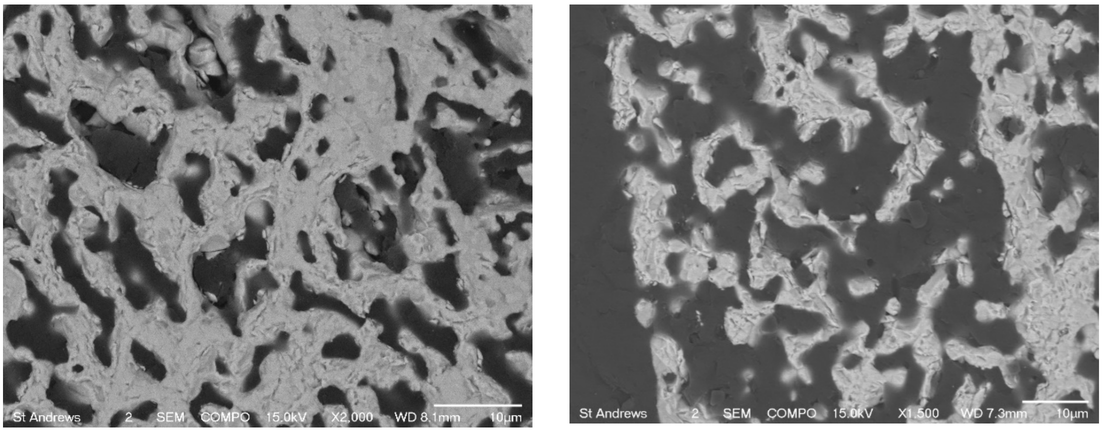
(a) (b)

Figure 5-9: SEM (BSE) images of current collector oxygen electrode (LSM). (a) Batch no. SRB1. (b) Batch no. SRBP2.

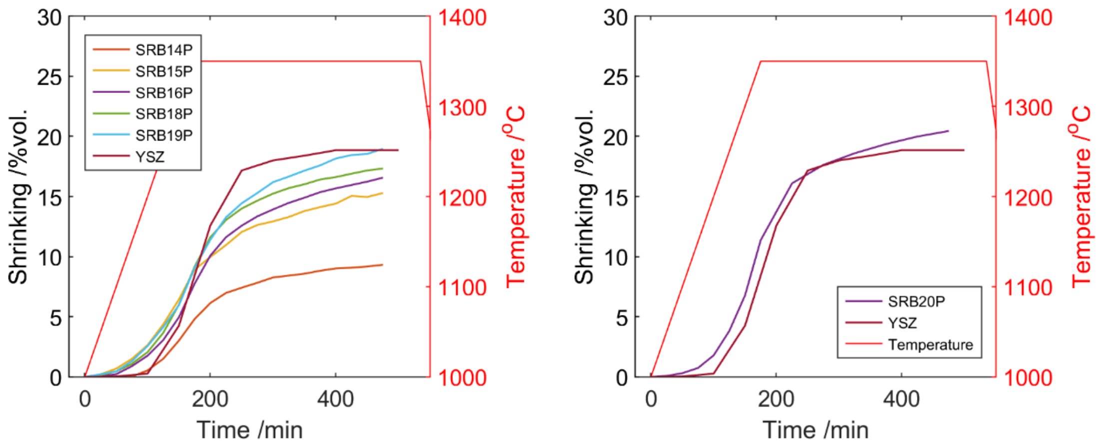
(a) (b)

Figure 5-10: (a) Shrinking analysis of LSM/YSZ50 tapes made of LSM/YSZ50 composite, made with various ceramic particle sizes (Table 5-5). (b) Shrinking profile of LSM/YSZ10 current collector layer made of LSM/YSZ10 composite powder with 3-7 µm particle size.

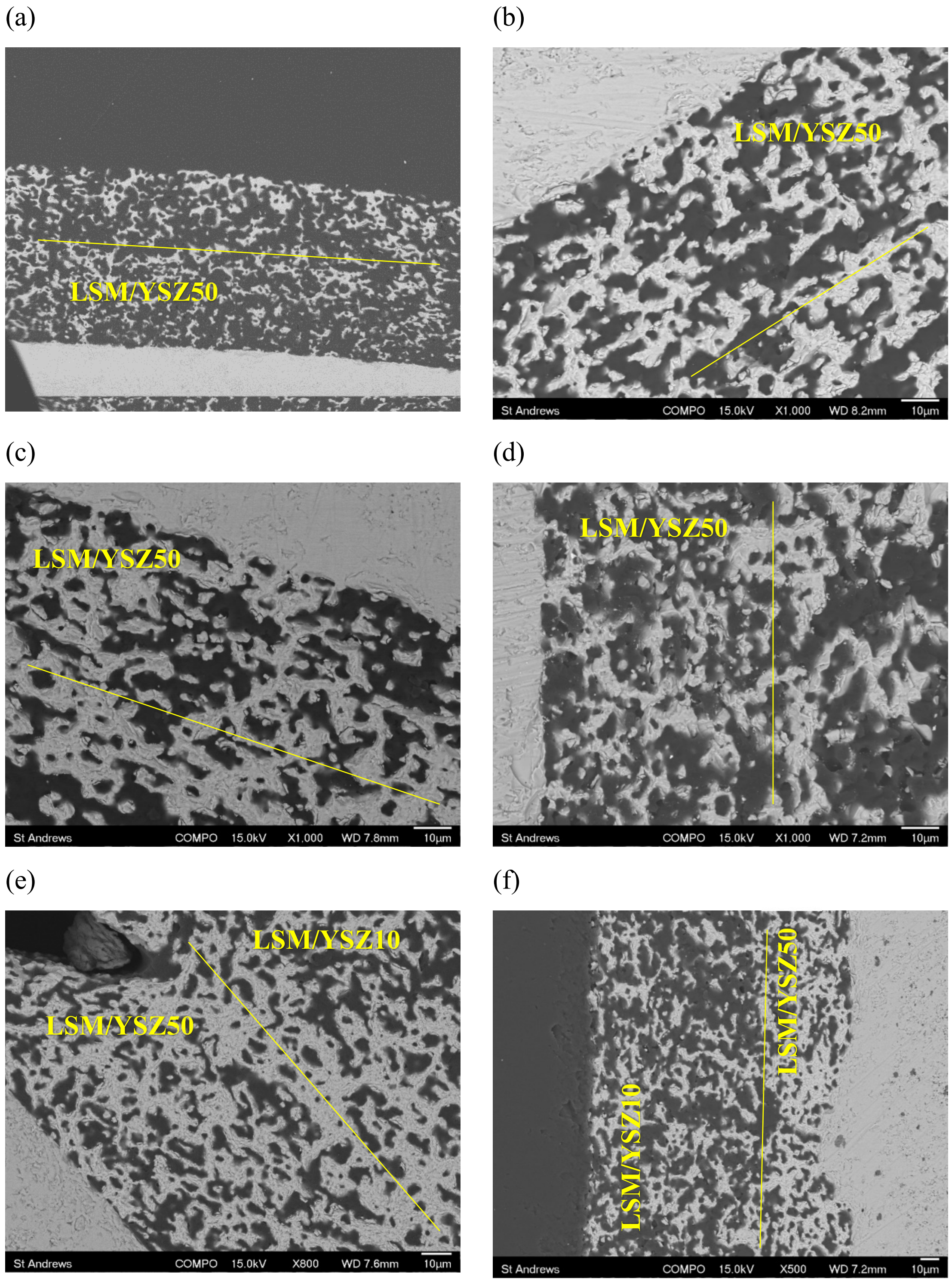

Figure 5-11: SEM (BSE) images of the oxygen electrode (Table 5-5). (a) SRB14. (b) SRBP15. (c) SRBP16. (d) SRBP18. (e) SRB19P. (f) SRB20P.

The turning point was the usage of recycled material. The previously prepared LSM/YSZ50 tapes were collected and sintered at 1200 °C. Next, the formed LSM/YSZ50 composite was ball milled to the ~4 μm of particle size. It was noticed that the shrinkage of the tape produced from composite particles is much lower than when mixing LSM and YSZ particles in the slurry. The pre-sintered LSM/YSZ50 composite reduced the shrinkage of the tape (Figure 5-10) and produced a well dispersed and homogenized composite. In fact, produced shrinking was much lower than electrolyte shrinkage.

Table 5-6: The characterisation of LSM/YSZ50 pre-sintered composite used for tapes production, milled with LB – large balls, MB –mixed balls; and maximum shrinking and porosity of selected tapes. For the production of the tapes, 60% of pore-former by volume was added.

Material	Tape no.	Milling time/ h	D50/ μm	Max Shr./ %	Porosity/ %
LSM/YSZ50	SRB14P	2 (LB)	4.084	9.32	75
LSM/YSZ50	SRB15P	3 (LB)	3.267	15.28	56
LSM/YSZ50	SRB16P	4.5 (LB)	2	16.56	47
LSM/YSZ50	SRB18P	2 (MB)	1.42	17.3	59
LSM/YSZ50	SRB19P	3.45 (MB)	1.13	18.9	42
LSM/YSZ10	SRB20P	0.75 (LB)	3.7	20.4	44

Table 5-7: The LSM/YSZ50 composite particle size analysis, ball-milled for various times and ball size.

Material	Milling balls	Time/min	D10/μm	D50/μm	D90/μm	SSA/m^{2}g
LSM-YSZ	large	25	2.413	6.490	15.544	0.187
LSM-YSZ	large	90	0.91	4.121	10.325	0.988
LSM-YSZ	large	120	0.392	4.084	10.621	1.03
LSM-YSZ	large	180	0.354	3.267	9.553	1.12
LSM-YSZ	mixed	30	1.820	5.088	12.129	0.241
LSM-YSZ	mixed	90	1.356	2.691	5.825	0.382
LSM-YSZ	mixed	120	0.178	1.790	4.555	1.54
LSM-YSZ	mixed	180	0.150	1.573	3.811	1.83
LSM-YSZ	mixed	225	0.110	1.160	2.858	2.7

The matched shrinking with YSZ with ~1 μm particle size, Figure 5-10. Smaller particles of LSM/YSZ50 increased shrinking and reduced porosity, Table 5-6.

The LSM/YSZ50 is much harder than LSM material, thus requiring much longer milling times. The 4.5 h hours of ball milling with large milling balls could not reduce particle size below 2 μm; thus, the particles were changed to mixed size. Finally, the sintering behaviour close to the electrolyte was achieved with the average 1.15 μm particle size of the LSM/YSZ50 composite. The same technique was used for the current collector layer following the active oxygen electrode development. The LSM based current collector layer was first pre-sintered with 10% YSZ by vol. and milled for 45 minutes with large milling balls; LSM/ YSZ10 composite particle size was 3.7 µm.

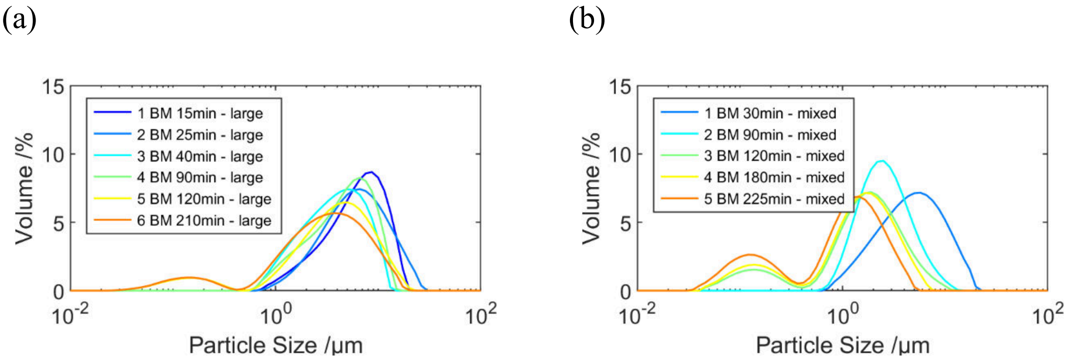

Figure 5-12: The PSA analysis of pre-sintered LSM/YSZ50 composite at 1200° and ball-milled various times. (a) Using large milling balls. (b) using mixed milling balls.

The XRD measurement made on LSM/YSZ50 active cathode material, sintered at 1350°C, showed almost no traces of LZO in the analysed active cathode; in several measurements, a small peak is visible at 28°, which response to the position of LZO, but its concentration is low and should not affect the functionality of electrode.

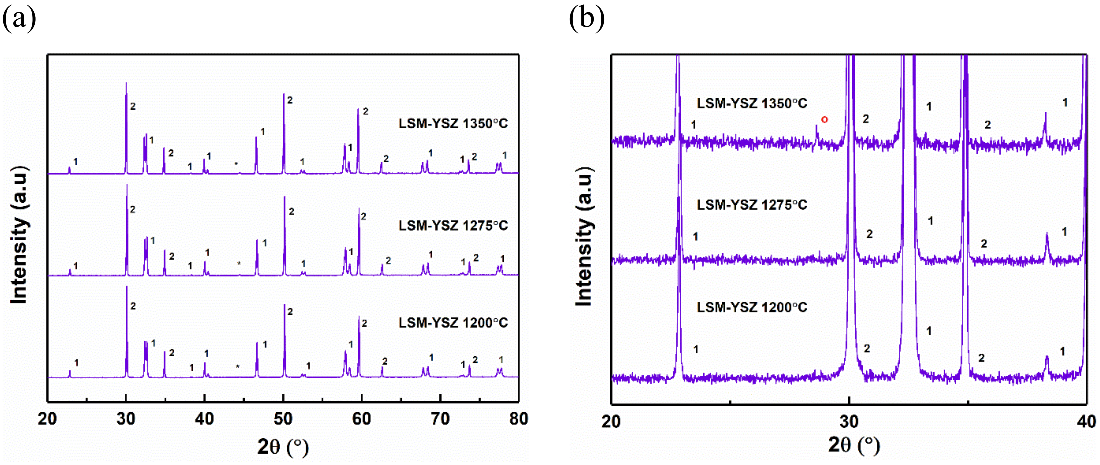

Figure 5-13: XRD pattern of LSM/YSZ50 composite. (a) In the 20-80° range of 2θ. (b) In the 20-40° range of 2θ.

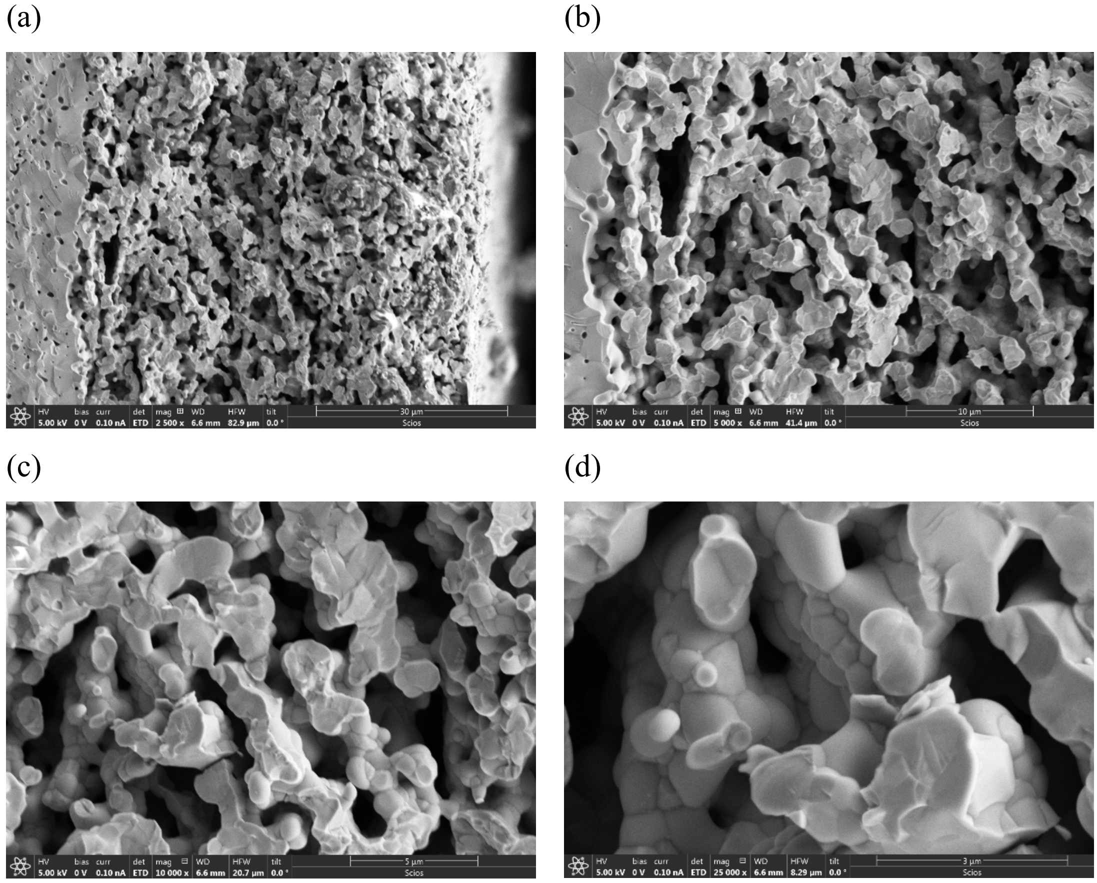

Figure 5-14: (a) – (d) SEM (SEI) of LSM/YSZ50 layer made of pre-sintered LSM/YSZ50 powder with ~1µm LSM/YSZ50 particle size.

5.4 The manufacturing and design of SOFCRoll with the LCNT based fuel electrode.

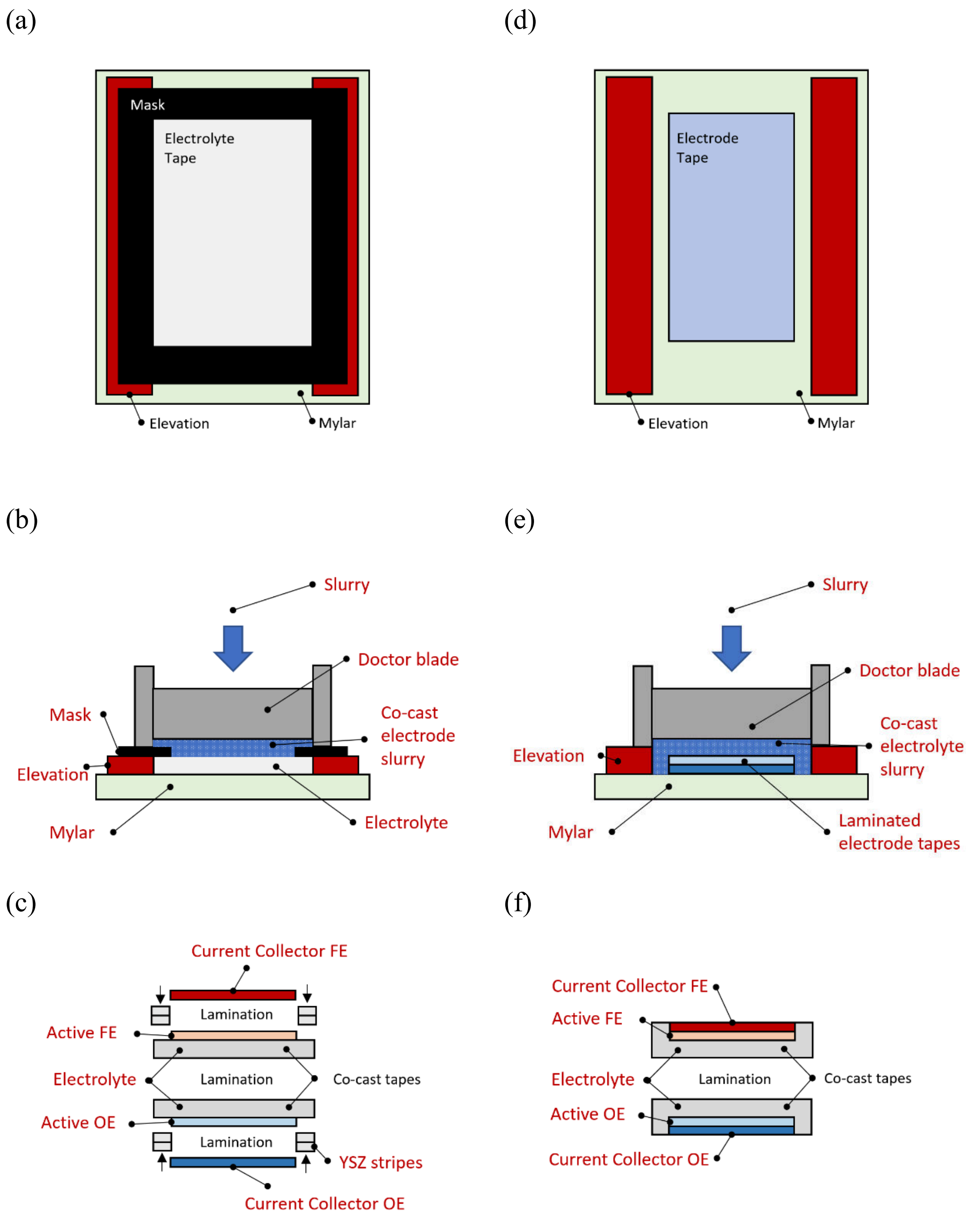

Figure 5-15: Two methods for tapes assembly for SOFCRoll with LCNT based FE. (a) - (c) Active electrode co-cast on YSZ electrolyte and current collector layer laminated afterwards. (d) – (f) YSZ co-cast on laminated electrodes.

Due to difficulties with handling up to 6-layers co-cast into one tape, problematic control of tapes thickness, defects created due to evaporation of the organic solvent, and cracking of very thick green layers when rolled, the co-casting method for SOFCRoll preparation was modified. Instead of casting all layers into one tape, the electrodes for both sides were co-cast with electrolyte separately and laminated afterwards from the electrolyte side.

In the first method (Figure 5-15 a-c), the YSZ electrolyte tape was cast first with a gap equal to 300 µm and dried. Next, the YSZ tape was masked with a Mylar mask with rectangular holes to attain the electrode's shape, Figure 5-15 a. Next, fuel and oxygen active layers were cast over the separate electrolyte tapes, Figure 5-15 b. The tape was laminated on co-cast tapes if the current collector was used. Finally, the oxygen and fuel parts were laminated together from the YSZ side to assemble a complete cell, Figure 5-15 c. The additional YSZ stripes were laminated on both sides of assembly edges to reinforce the whole structure. After the tape's assembly, the green tapes were rolled in a spiral SOFCRoll shape over metal tubes with a diameter of 8mm and reinforced on the ends by 2 of the 0.7x10 cm electrolyte stripes. The size of metal tubes for SOFCRoll rolling was increased at this point; therefore, the cell had larger channels and lower distance in the "spiral"; thus, the available active area for fuel oxidation was enlarged. The cell was sintered in the standard conditions used for all cells, described in Chapter 3.5.

The method was modified in further experiments (Figure 5-15 d-f), and instead of electrode slurry cast on electrolyte, the order was changed, and YSZ electrolyte was cast over previously laminated active electrode rectangles, Figure 5-15 e. The slurry container and doctor blade were elevated with additional layers of Mylar film to protect the tape running underneath, Figure 5-15 d. Such modification removed the need for a mask, which provided better controls of cast tape thickness and simplified the entire process. In addition, the co-cast tape's sides were much thicker, as the YSZ slurry filled the space between the electrode tape and tape's edges; hence, the assembly did not require additional YSZ stripes on the sides, further simplifying the process. Also, it improved the handling of co-cast electrode counterparts, as the exposed side of the electrolyte was less sticky than one when in contact with the Mylar film. Sticky surfaces made it challenging to distribute tapes evenly and, consequently, form imperfections and air bubbles between them. On the other hand, the adhesion between YSZ tapes got worse; hence more prone to delamination; if, for example, tapes were old and lost most of their adhesive properties or were not carefully hot laminated. The SRB25P and SRB26P SOFCRoll cells described next were produced with the first method, whereas SRB30P and SRB36P were produced with the second approach.

Table 5-8: Dimension of green tapes used to assemble SOFCRoll with LCNT based FE (Figure 5-16). All dimensions are in cm.

Cell	Active OE	CC OE	Active FE	CC FE	Porous YSZ	Electrolyte
SRB25P	5 x 10	5 x 10	5 x 10	-	-	5.5 x 10.5
SRB26P	5 x 10	5 x 10	5 x 10	5 x 10	-	5.5 x 10.5
SRB30P1	4 x 5	-	4 x 5	4 x 5	-	4.5 x 6.5
SRB30P2	4 x 5	-	4 x 5	4 x 5	4 x 2.5	4.5 x 6.5
SRB36P	4 x 5	-	4 x 5	4 x 2.5	-	4.5 x 6.5

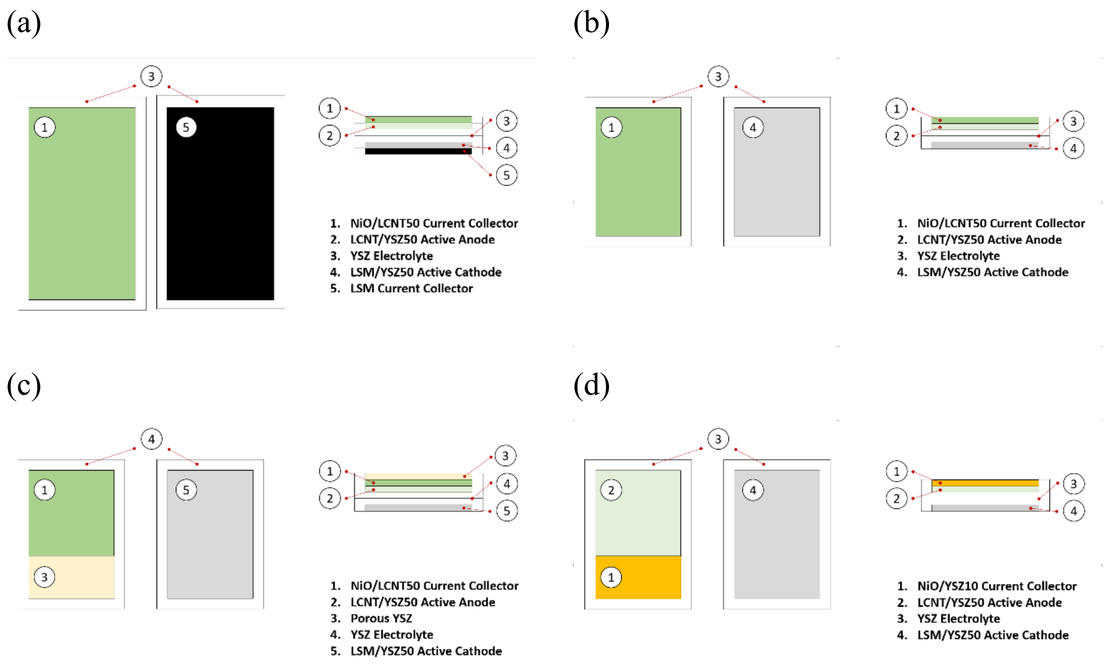

Figure 5-16: Assembly of the layers in various batches of SOFCRoll with LCNT based FE. (a) The large cells with Ni/LCNT50 current collector (SRB26P). (b) The small cell with open OE (SRB30P1). (c) The small cell with open OE and porous YSZ layer (SRB30P2). (d) The small cell with open OE and Ni/YSZ10 current collector (SRB36P).

The SOFCRoll SRB25P and SRB26P had the same size of electrode tapes (Table 5-8), and both were produced with the first described method. The SRB25P had only LCNT/YSZ50 active anode, while SRB26P had LCNT/YSZ50 active anode and Ni/LCNT50 current collector fuel electrode layer. Both types had LSM/YSZ50 and

LSM/YSZ10 oxygen electrode layers; the electrode's shrinking and microstructure were tailored using the explained method.

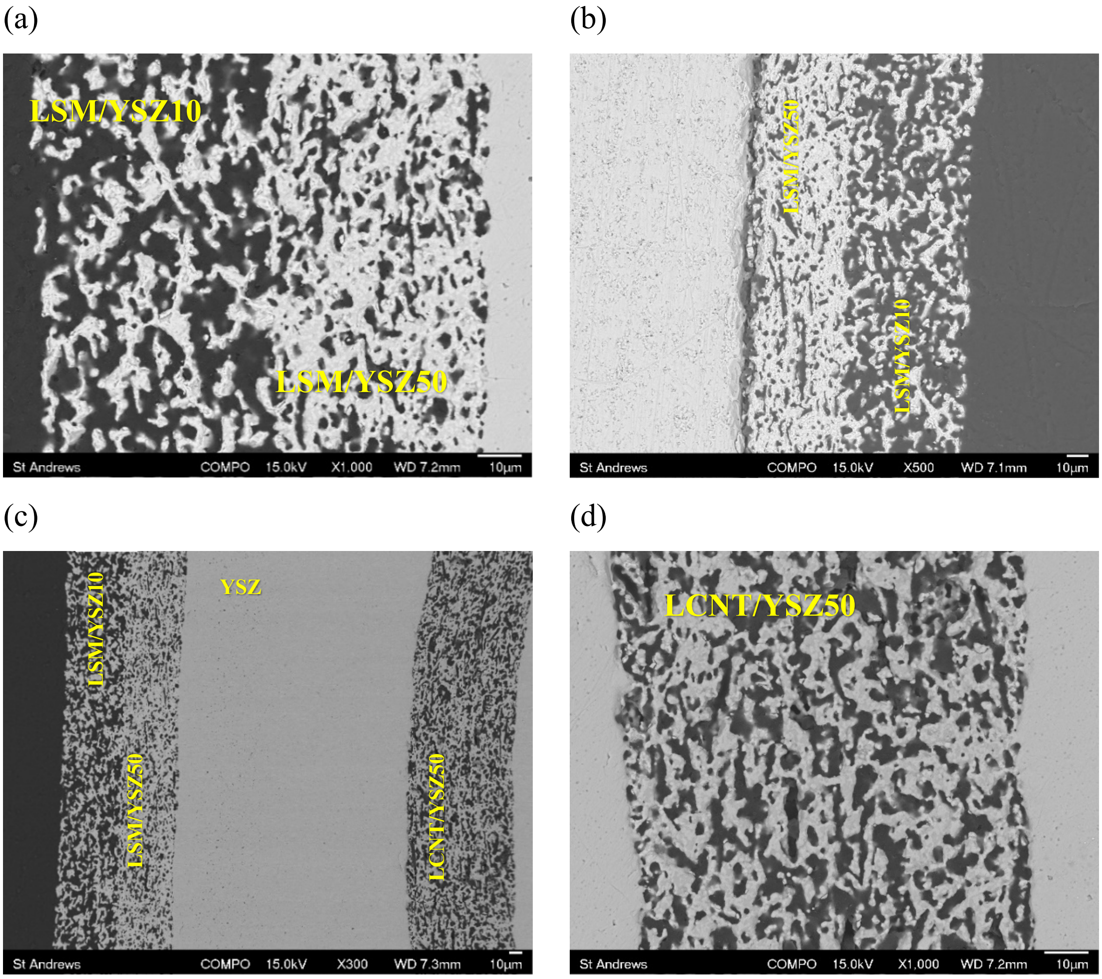

Figure 5-17: SEM (BSE) analysis of cell's fuel electrode with LCNT/YSZ50 active layer (SRB25P). (a) – (b) Active and current collector LSM\YSZ oxygen electrode. (c) Cell's full cross-section. (d) Active LCNT/YSZ50 fuel electrode.

Contrary to SOFCRoll with Ni/YSZ based electrode, where the silver current collector was applied locally, the whole surface area of inlet channels was covered with silver paste. The SRB25P had almost no internal defects in its structure; the fuel electrode did not have any cracks, the oxygen electrode showed minor local delamination in the analysed cell, Figure 5-17 b. The LCNT/YSZ50 active fuel electrode porosity was about 56% in the measured region between the channels. The porosity of LSM/YSZ50 was about 30%, and the porosity of the current collector LSM/YSZ10 layer was 58%. All electrodes had a thickness close to 40 µm, while the YSZ electrolyte was around 180 µm, slightly larger than the usual 110 µm, due to a higher casting gap. The porosity and thickness of individual layers may vary, depending on location, as explained in the following example.

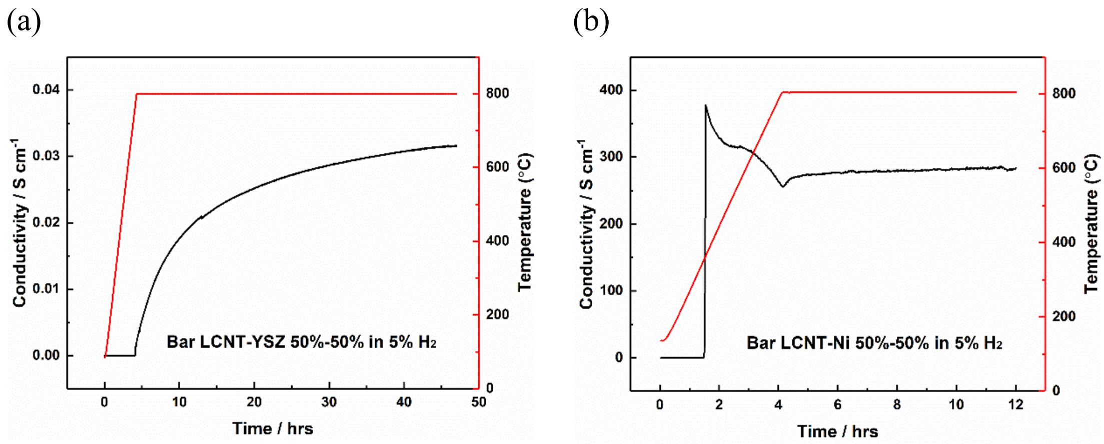

Figure 5-18: Conductivity measurement on solid bars at 5% H_2/N_2 of (a) LCNT/YSZ active FE. (b) Ni/LCNT50 current collector FE.

The LCNT/YSZ50 composite does not have large electronic conductivity (Figure 5-18 a); thus, the current collector layers for a fuel electrode have been developed to extend the active area to the “Spiral” region in the SOFCRoll where silver paste can not be applied. First Ni or Ni/YSZ layer with high Ni content has been considered; however, due to difficulties with the implementation of those layers (significant delamination), NiO/LCNT composite, with a 1/1 volume ratio (NiO/LCNT50), was used at this stage of the project. Ni/LCNT50 achieved almost 400 S/cm of electronic conductivity when reduced in a gas atmosphere; this value dropped quickly below 300, possibly due to changes in microstructure, Figure 5-20. The conductivity test was done on solid bars due to difficulties with the preparation of porous samples made from tapes. The actual conductivity of the materials would be lower than solid bars due to porosity. As explained already, the sintering of the tapes separately significantly reduces their porosity; therefore, they would not reflect the microstructure of layers in the cell. Moreover, the tapes must be laminated to achieve the required thickness for the measurement. The lamination of such a large amount of tapes almost always resulted in delamination.

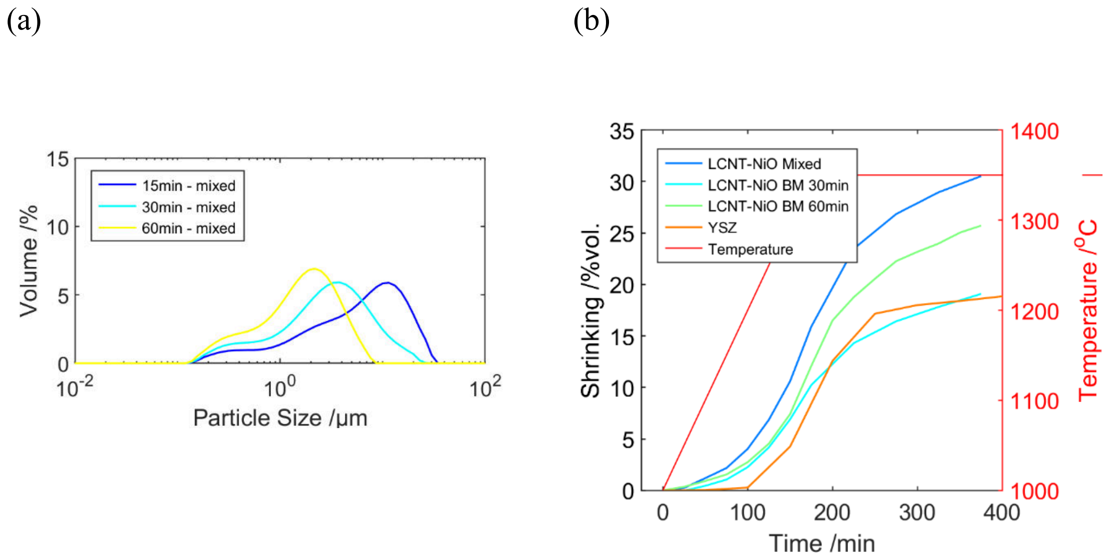

Figure 5-19: (a) PSA analysis of pre-sintered NiO/LCNT50 composite and ball-milled at different times with mixed-size milling balls. (b) Shrinking profile of NiO/LCNT50 tape made of mixed ceramic and pre-sintered composite.

For the preparation of Ni/LCNT50 current collector layer, two different methods were investigated; in the first approach, LCNT was mixed with NiO particles in the slurry; in the second, following the approach taken for the preparation of oxygen electrode, LCNT and NiO were co-sintered first at 1350°C for 5 h to produce NiO/LCNT50 composite and ball-milled to specific particle size. The shrinking of the first tape exceeded 30% (Figure 5-19 b) already with relatively large particle size; therefore, this method was rejected in advance. A more favourable shrinking profile was obtained with the second method.

Analysis showed that shrinking close to YSZ could be produced with an average NiO/LCNT50 particle size of 3.16 μm. The pure material has a large conductivity, and the cell showed much higher performance; thus, at least partially, the layer fulfils its purpose. Unlike Ni/YSZ based current collector layers (as shown next), Ni/LCNT50 does not delaminate and gives a good interface with the active electrode. However, the composite shows a rather peculiar structure. After reduction, gaps appear between LCNT and Ni, while Ni has many small holes created during the release of oxygen. Such a layer has low mechanical strength after reduction and crumbles when touched; thus, special care was needed with the cell's handling.

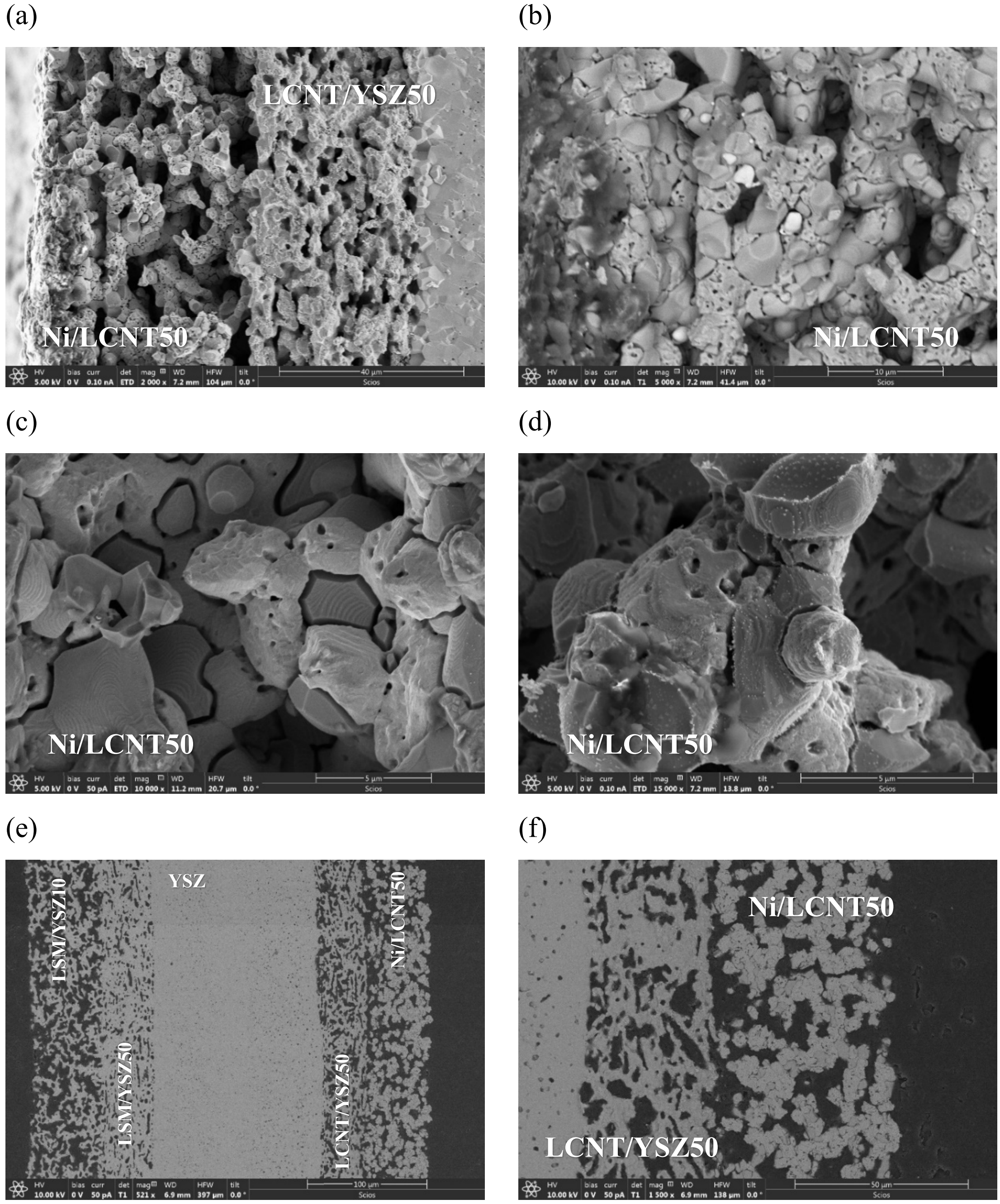

Figure 5-20: SEM analysis of SOFCRoll SRB26P with Ni/LCNT50 current collector and LCNT/YSZ50 active layer. (a) - (d) SEM (SEI) images in various magnifications of the fuel electrode after the test. (e) BSE image of cell's cross-section. (f) BSE image of fuel electrode.

Figure 5-21 a shows a cross-section of the whole SRB26P cell. Cells did not deform during the sintering step and kept the "SOFCRoll shape". The cell showed high OCV, demonstrating a good tightness; however, the defects were still present in the cell's structure (in red in Figure). The delamination primarily developed at the Ni/LCNT50 interface; some cracks also were present in the YSZ electrolyte. The most affected regions are at the end of the main channels, Figure 5-21 b & c. Based on the porosity analysis, Figure 5-22, those parts seem to be under the highest stress, as the inner part of the cell is affected by shrinking the outer layers. In those regions, the cell's structure consists of only a single-layered assembly, not supported by the second one, as in the "Spiral" part, where the number of defects is low; therefore, there are more prone to crack. Also, tapes at the end of the channels are rolled to a higher degree, perhaps bringing additional stress that affects their mechanical strength.

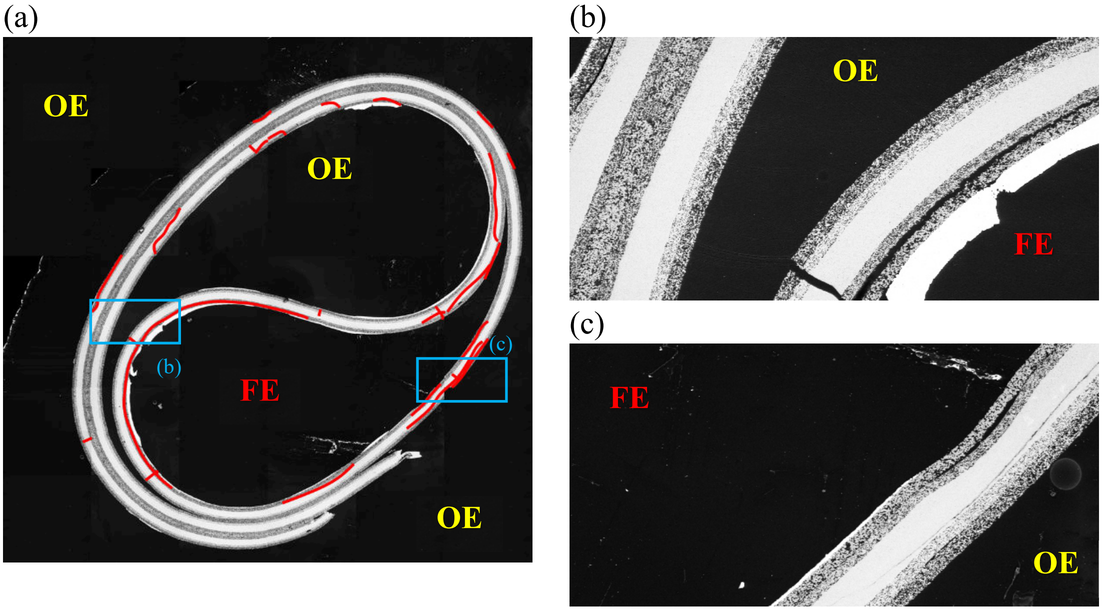

Figure 5-21: SEM (BSE) analysis of cell with Ni/LCNT50 current collector and LCNT/YSZ50 active layer (B26P). (a) The cross-section of the whole cell (defects in red). (b) – (c) Images of the cell's cross-section at indicated locations.

The thickness of the layers and porosity varied across the cell. The active electrodes have a thickness of between 30 and 40 µm, while the YSZ thickness electrolyte was between 120 and 140 µm. The thickness of the current collector layers varies between 50 and 60 µm on both sides. The thickness of the green tape from the one casting may change; the amount of slurry in the container decreases during tape casting, extracting lower pressure on the doctor blade gap; thus, the tape becomes thinner. However, differences in the thickness of the given layer are expected between various cells than in the single one.

The variations in the thickness are likely related to changes in stress distribution at various locations in the cell, which better illustrates the porosity measurement Figure 5-22.

Higher stress causes a decrease in the porosity and thickness of sintered layers. The porosity of the LSM/YSZ10 current collector OE varied between 45% and 72%; the 27% difference is very high for homogeneous tape, illustrating significant variation in stress/ shrinking across the cell, Figure 5-22 a.

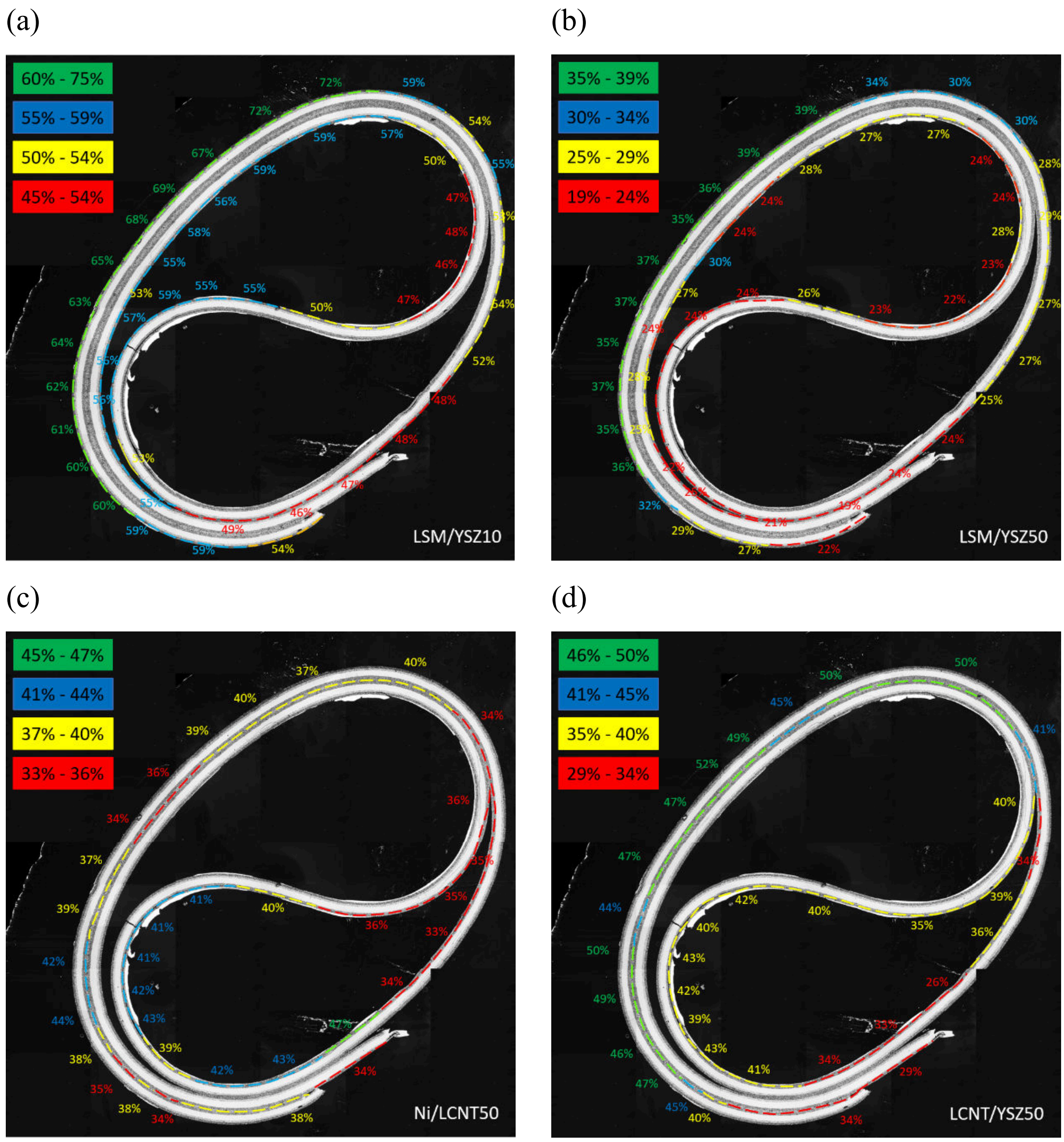

Figure 5-22: The porosity measurement at various locations in SOFCRoll SRB26P. (a) The current collector OE, LSM/YSZ10. (b) The active OE, LSM/YSZ50. (c) The current collector FE, Ni/LCNT50. (d) The active FE, LCNT/YSZ50.

The differences in porosity in LSM/YSZ10 are the highest among all tapes, supposedly because it is the softest material; however, the other tapes also show significant variations exceeding 20%. At the outer layer, on top of the cell, where the cell's structure is made of two adjacent layered assemblies, the porosity is the highest for all tapes, except Ni/LCNT50 current collector FE; which likely is because Ni/LCNT50 is sandwiched from both sides by other layers. The lowest porosity values were measured at the main channels, especially where channels go into a spiral; the measurement coincides with the location of the cracks, which are more likely to be present where the cell is subjected to higher stress.

Figure 5-23: The SEM (BSE) images of small cells with Ni/LCNT50 current collector and LCNT/YSZ active (SRB30P) fuel electrode (FE) layers; and LSM/YSZ50 active oxygen electrode (OE).

Next, the tapes were shortened (Table 5-8), and the small cells were manufactured, Figure 5-23; such modification was aimed to decrease the size of the "Spiral" part. The area of tapes used for small cell preparation was reduced by more than double, but it allowed for more effective surface area utilisation, and stress in the cell was significantly reduced. The small SOFCRoll cells had an "exposed oxygen electrode" design; tapes were shortened to the point that the whole surface area of the oxygen electrode was exposed to the atmospheric air. Therefore, the current collector layer made of pure LSM was not needed; only LSM/YSZ50 active electrode was used, which was entirely covered with the silver paste, to fully utilise its surface area. The stress was reduced as the fewer layers were co-sintered; the LSM layer shrank the most in the previous design, putting the highest pressure on other layers. Also, before the cell interior was entirely encircled by a spiral, which resulted in higher stress on the inner part, Figure 5-22.

Two types of SRB30P cells were produced (SRB30P1 and SRB30P2). The active fuel electrode LCNT/YSZ50 was used with a Ni/LCNT50 current collector layer, the same as in SRB26P. The spiral part on the fuel side was lowered to 1 cm, reducing the current collector and diffusion path for H_2. The SRB30P1 was a smaller analogue of SRB26P, whereas, in the B30P2 type, the additional porous YSZ layer (P-YSZ) with 90% porosity was used in the spiral part of the fuel electrode to study if the cell could achieve better and more stable performance when decreasing diffusion losses at the fuel electrode side in the spiral.

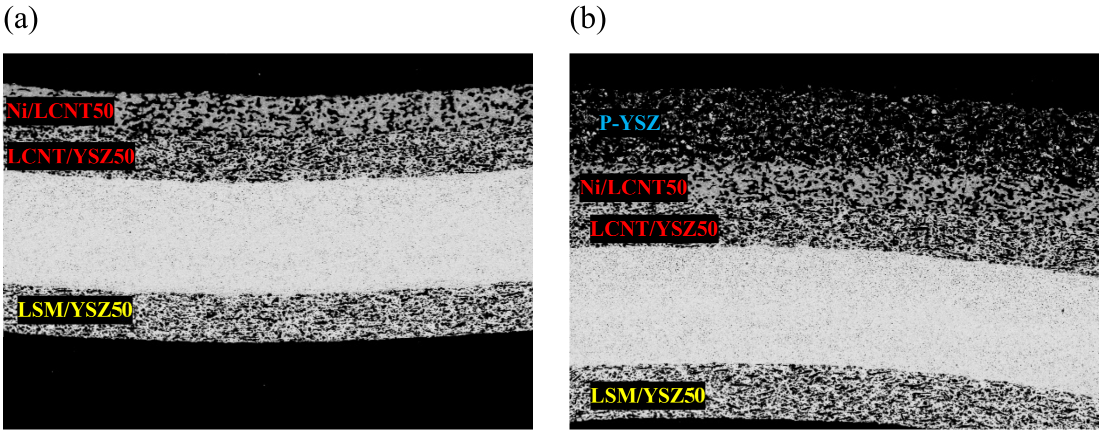

Figure 5-24: BSE analysis of B30P's cross-section (x350 mag). (a) The B30P1 cell. (b) The B30P2 cell with porous YSZ layer (P-YSZ).

No single crack or delamination was discovered in the first type of the cell without porous YSZ; in the second type, some small cracks were found in the middle part of the electrolyte. Likely, the porous YSZ layer added more internal stress during sintering, and the electrolyte cracked in its weakest part (at the area between the two electrolyte layers).

Due to the weak mechanical properties of Ni/LCNT50, the pure Ni or high Ni content (up to 90% by vol. in Ni/YSZ composite) layers were revised to use as the fuel electrode's current collector. Those would have much better mechanical properties, be cheaper, and have much better conductivity. However, it was challenging to use it with LCNT/YSZ50 active FE, as layers showed significant delamination that eventually destroyed the cell's interior, Figure 5-25 a & b.

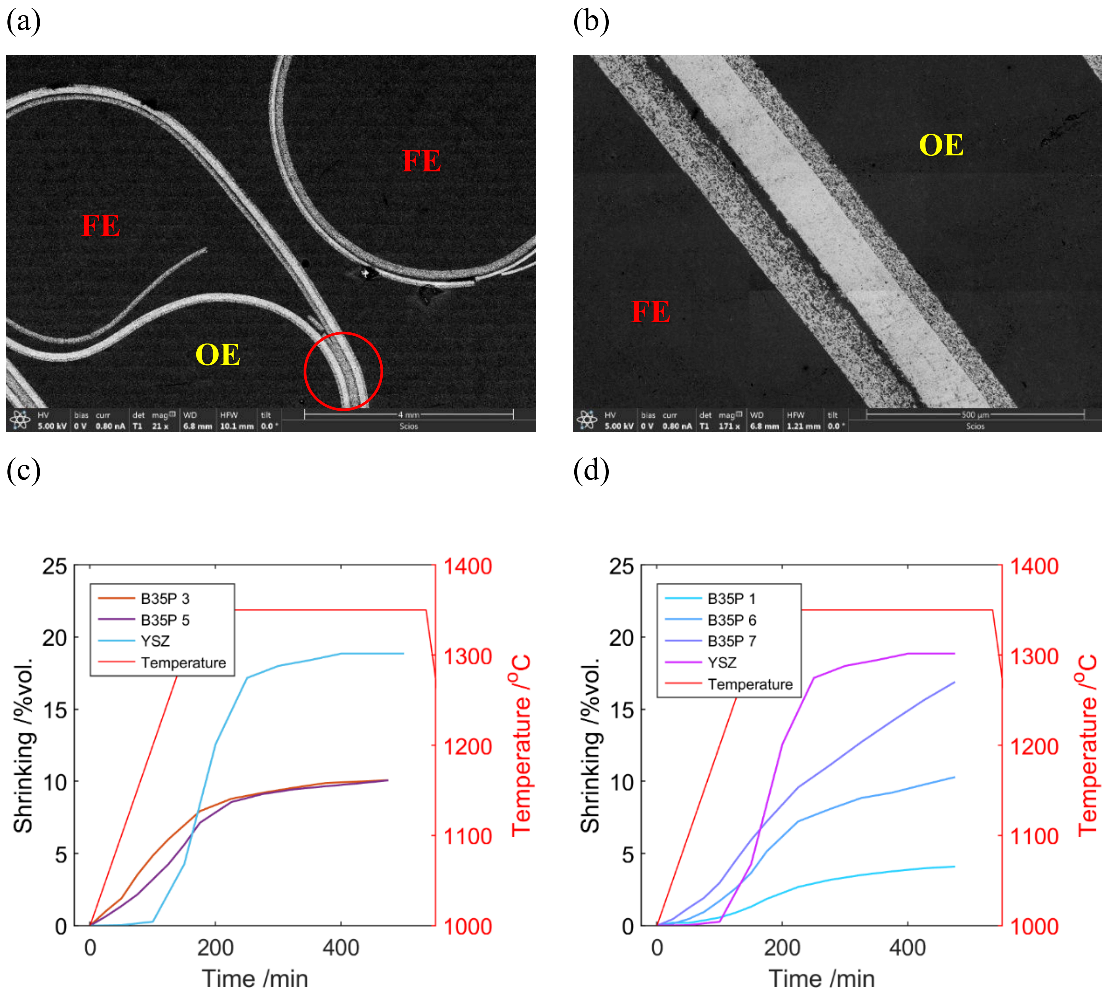

Figure 5-25: Development of Ni-based current collector layers. (a) – (b) The SOFCRoll with Ni current collector on LCNT/YSZ50 active FE. (c) Shrinking profile of Ni current collector layers. (d) Shrinking profile of Ni/YSZ10 current collector layers.

First, the pure NiO layer was considered. The shrinking profile of two NiO layers was tested with 1.43 and 0.64 μm particle size; both had the same pore former concentration of 50% by volume. The measurement showed almost no dependence on particle size and very low shrinking in general. Such behaviour suggests rather coarsening than densification, where evaporation-condensation and surface diffusion are the two most frequent mechanisms [278]. Therefore, the layer NiO was unsuitable due to the significant differences in shrinking between active and current collector layers. Next, the NiO/YSZ10 composite was investigated for the current collector purpose; the material was pre-sintered first then ball milled to the required size. The addition of YSZ did not modify the shrinking profiles. The Ni/YSZ10 layer with a similar particle size to the Ni layer had almost the same shrinking; the layer had 10% more pore formers by volume, but as explained already, the addition of pore former at this concentration has a low dependency on shrinking.

Table 5-9: The characteristic of NiO and NiO/YSZ10 pre-sintered composite used for tapes production, milled with LB – large balls (at 400 rpm), SB –small balls (at 800 rpm); and maximum shrinking and porosity of selected tapes.

Material	Tape no.	Milling time/ h	D50/ µm	Max Shr./ %	Pore former./ %	Porosity/ %
NiO	SRB35P 3	0	1.434	10.07	50	Not used
NiO	SRB35P 5	4 (LB)	0.64	10.06	50	35%
NiO/YSZ10	SRB35P 1	0.5 (LB); 0.1 (SB)	2.3	4	50	Not used
NiO/YSZ10	SRB35P 6	1 (LB); 1 (SB)	0.614	10.29	60	42%
NiO/YSZ10	SRB35P 7	1 (LB); 1 (SB)	0.614	16.88	70	32%

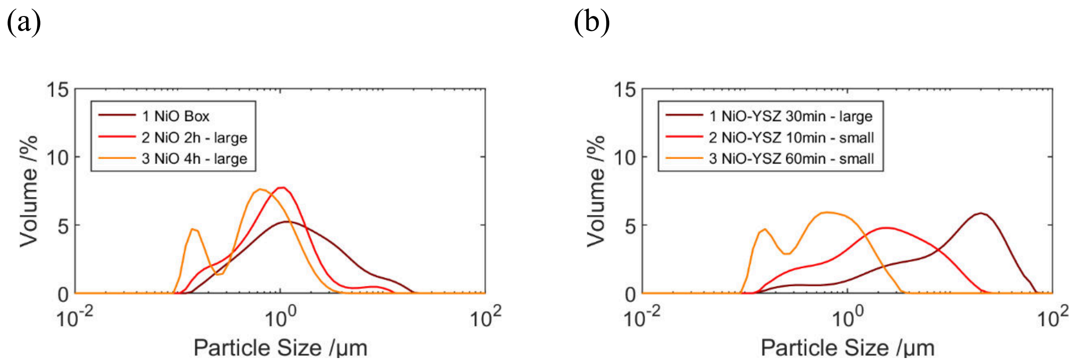

Figure 5-26: The PSA analysis of NiO and NiO/YSZ10 pre-sintered composite used for tapes production, milled with LB – large balls (at 400 rpm), SB –small balls (at 800 rpm);

The layer caused significant damage to the cell's structure, but a valuable detail was noticed. The layers delaminated to a lesser extent in the spiral part when sandwiched between other layers than in the main channel, red circle in Figure 5-25 a. Thus, the sandwiched layers form a more compact structure, with much lower deformation of adjacent layers. This behaviour has been exploited in further experiments. The idea was to sinter Ni-based current collector just in the spiral part; as in the channel, this function is met by the silver current collector. Moreover, such a solution further decreases the amount of used material for cell preparation, reducing its cost and weight.

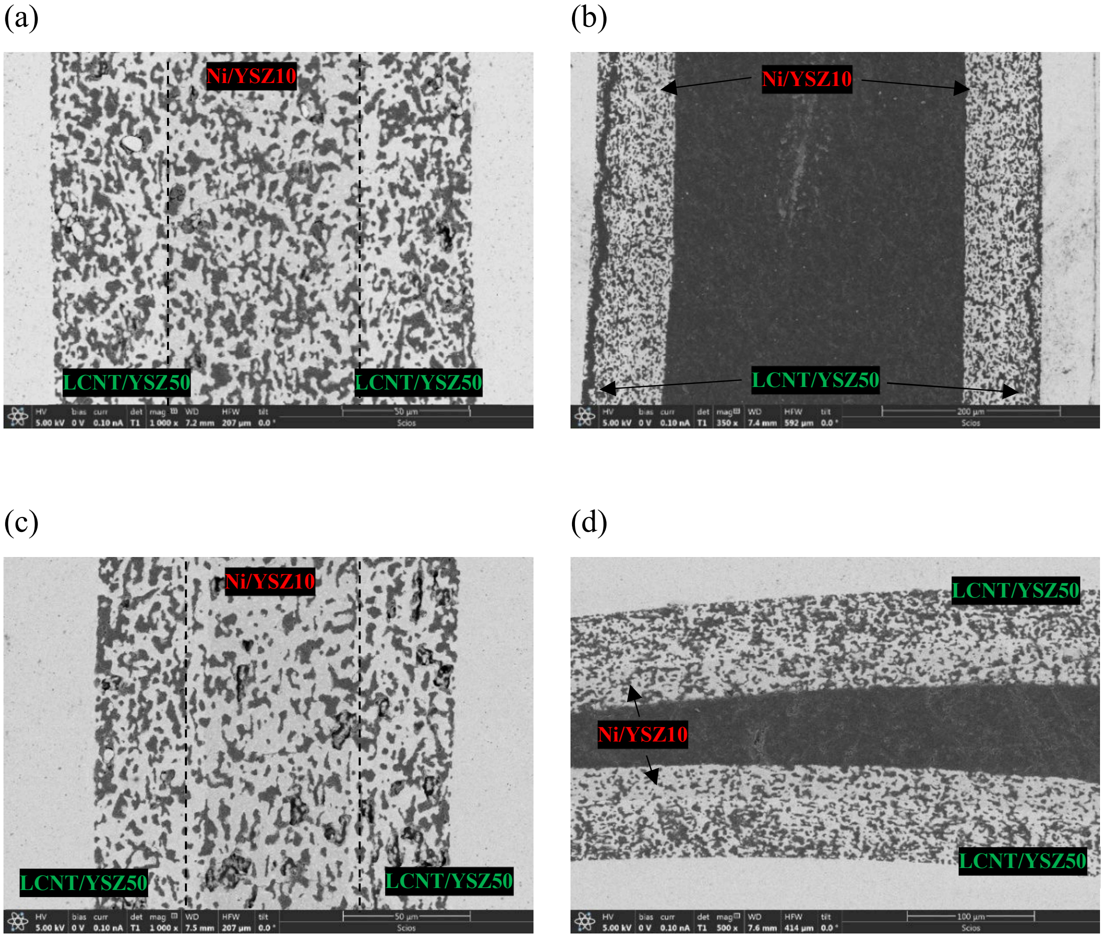

Figure 5-27: SOFCRoll with Ni/YSZ10 current collector on LCNT/YSZ50 active FE in the spiral part of SOFCRoll. (a) – (b) SRB35P 6, with 60% of pore-former by volume. (c) – (d) SRB35P 7, with 70% pore former by volume.

Even with the low shrinking of around 10% placed in the spiral part, the current collector Ni/YSZ10 did not delaminate when in contact with other layers on both sides, Figure 5-27 a; but, in areas where the layers were not in contact, they still seem to separate, Figure 5-27 b. The Ni/YSZ10 layer was further modified, very high concentration of pore formers was added, up to 70%, Table 5-9. Such a significant addition of pore-former increased the shrinking and perhaps made layer more flexible, and finally, no delamination of the Ni-based current collector layer was detected in the spiral part, either where layers were touching each other or in areas where they were not in contact, Figure 5-27 c & d.

5.5 Electrochemical performance of SOFCRoll with LCNT/YSZ50 active fuel electrode

5.5.1 Model for H_2 oxidation on perovskite surface

The oxidation of H_2 to water on the perovskite surface can be clarified on the basis of the model proposed on the Ni/YSZ fuel electrode [119], except that H_2 would dissociate and absorb directly on the perovskite surface instead of on the nickel [142]. Assuming that perovskite has sufficient oxygen ion conductivity, such a mechanism would involve H_2 gas, lattice oxygen (O_O^X) and B-site cation (B_B^X). The products of the reaction are H_2O, oxygen vacancies ($V_O^{\cdot\cdot}$) and electrons associated with B-site cation (B_B'), the reaction can be written in Kröger-Vink notation:

$$\mathbf{H_2(g) + O_O^X + 2B_B^X = H_2O(g) + V_{\ddot{O}} + 2B_B'} \qquad \textbf{Equation 5-1}$$

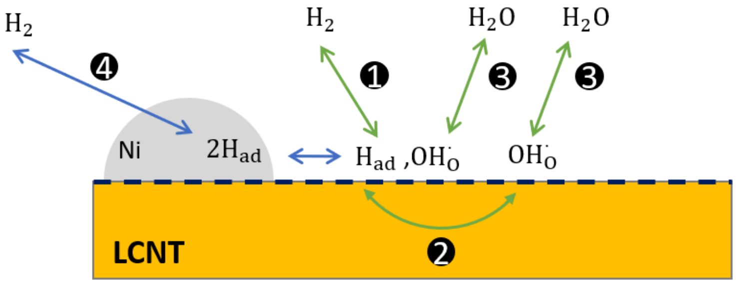

Figure 5-28: The H2 oxidation/ H2O reduction mechanism on LCNT surface.

This reaction will not proceed instantly but consists of multiple steps, starting with the diffusion of gases into the vicinity of active material, followed by the dissociative adsorption and transport of intermediate species for charge transfer reaction [142].

Each of these steps has its own kinetic, which, apart from operational conditions (e.g. temperature, type and concentration of reactants, pressure, overpotential), also depends on the properties and structure of the ceramic layers used in the cell (e.g. catalytic activity of electrodes, the electronic and ionic conductivity of materials, their thickness and microstructure), [57]. The absorption/dissociation process is often considered the slowest step on oxide fuel electrodes (RDS) [142] by many authors working both on perovskites [139], [140], [303], and doped ceria electrodes [304].

Before exsolution, only the MIEC surface takes part in the adsorption (step 1 in Figure 5-28). Hydrogen would chemisorb on the MIEC absorption vacant site, which depends on the concentration of oxygen-terminated surface sites, as during chemisorption, hydrogen bonds with oxygen [142], [305]. Likely, the process involves the two-step oxidative hydrogen dissociation to surface hydroxyl [142], [183], [306], [307]. And water formation and desorption in the last step (3 in Figure 5-28) [308]. Assuming that only Ti cation takes part in charge transfer reaction; the elementary steps on perovskite surface, without metal catalyst, would look as follows:

$\mathbf{H_2(g) + O_O^X + Ti_{Ti}^X = OH_O^{\cdot} + H_{ad}(LCNT) + Ti_{Ti}'}$ **Equation 5-2**

$\mathbf{H_{ad}(LCNT) + O_O^X + Ti_{Ti}^X = OH_O^{\cdot} + Ti_{Ti}'}$ **Equation 5-3**

$\mathbf{2OH_O^{\cdot} = O_O^X + H_2O(g) + V_O^{\cdot\cdot}}$ **Equation 5-4**

The perovskite, particularly oxygen-deficient and with low ionic conductivity, may have low availability of sites for reaction; hence step one could become RDS. Electrodes with Ni catalyst on the surface show improved performance, most likely due to Ni activity towards H_2 adsorption and dissociation [141]. In such a system, hydrogen will also absorb and dissociate to hydrogen species on the Ni and diffuse to the LCNT surface, bypassing the step described by Equation 5-2 (1 in Figure 5-28) [183], [309], [310].

$\mathbf{H_2(g) = 2H_{ad}(Ni)}$ **Equation 5-5**

For the titanates perovskite, oxygen ion conductivity may be too low to supply oxygen ions from the bulk of the material to the reaction site, either to equation 5-2 or 5-3 [311]. Therefore, the surface path should be considered in the composite LCNT/YSZ electrode (in Figure 5-28 for simplicity, only the bulk path is presented). YSZ would improve material functionality in such a system by providing a conduction path for oxygen ions. The oxygen ions could diffuse through the surface to the vacant site on MIEC or/ and H species to the oxygen site on 3PB. In such a mechanism, the reaction would occur in the vicinity of 3PB; therefore, it should be optimized for best performance.

5.5.2 Exsolution and LCNT defect chemistry

Defect stoichiometry in the $La_{0.43}Ca_{0.37}Ni_{0.06}Ti_{0.94}O_{3-\gamma}$ (LCNT) fuel electrode plays an essential role in its activity and should be considered when investigating its kinetics during SOC operation. For the electrode functionality, the charge disproportionation reaction (eq. 5-6) is in equilibrium with the partial pressure of oxygen, pO_2, and affects the concentration of Ti^{4+}/Ti^{3+} and the number of oxygen vacancies. The doping of higher valency La^{3+} into a Ca^{2+} position introduces A-site vacancies for charge neutrality. The large number of A-site vacancies pushing eq. 5-7 left and reducing the number of $V_O^{\bullet\bullet}$, for a given pO_2 to opposite the change eq. 5-6 shifts right, generating $V_O^{\bullet\bullet}$ and Ti^{3+} [96]. The oxygen vacancies make a diffusion path for oxygen ions, thus increasing oxygen ion conductivity in the material, while the generation of Ti^{3+} increases its electronic conductivity.

$$\mathbf{O_O^x + 2Ti_{Ti}^x \leftrightarrow V_O^{\bullet\bullet} + 2Ti_{Ti}' + \frac{1}{2}O_2} \qquad \textbf{Equation 5-6}$$

$$\mathbf{O_O^x + 4Ca_{Ca}^x + La_2O_3 \leftrightarrow V_O^{\bullet\bullet} + 4CaO + 2V_{Ca}'' + 2La_{Ca}^x} \qquad \textbf{Equation 5-7}$$

Assuming that only oxygen vacancies concentration contributes to charge carrier concentration, the concentration of Ti^{3+} is equal [311]:

$$[\boldsymbol{B_B'}] = \mathbf{2}[\mathbf{V_O^{\bullet\bullet}}] \qquad \textbf{Equation 5-8}$$

According to eq. 1-33, the conductivity of LCNT, besides $[\mathbf{B_B'}]$ will depend only on charge carrier mobility, which is temperature-dependent.

The mass-action law for the eq. 5-6 can be written as:

$$[\mathbf{V_O^{\bullet\bullet}}][\boldsymbol{B_B'}]^2(\boldsymbol{pO_2})^{1/2} = \boldsymbol{K}_{\mathbf{V_O^{\bullet\bullet}}}(\boldsymbol{T}) \qquad \textbf{Equation 5-9}$$

Where $\boldsymbol{K}_{\mathbf{V_O^{\bullet\bullet}}}(\boldsymbol{T})$ is a temperature-dependent constant related to the formation of oxygen vacancies, the concentration of oxygen sites $[\mathbf{O_O^x}]$ is large; thus assumed to be constant.

Therefore, according to the equation, conductivity should have a $(\boldsymbol{pO_2})^{-1/4}$ dependence for bulk governed mechanism [311].

The partial substitution of Ti^{4+} by Ni^{2+} increases the concentration of oxygen ion vacancies, eq. 5-10; hence, B-site doping is expected to facilitate the oxygen ion conduction.

$$\mathbf{O_O^x + Ti_{Ti}^x + NiO \leftrightarrow V_O^{\bullet\bullet} + Ni_{Ti}'' + TiO_2} \qquad \textbf{Equation 5-10}$$

In reducing atmosphere, either driven by gas or applied overpotential, the Ni cations would be released on the perovskite surface, eq. 5-11. The process would be facilitated in A-site deficient electrodes [147]–[149], where deficiency may minimize the formulation of A-site rich islands on the surface, which is known to suppress exsolution [149]. Moreover, A-site deficiency could enhance a B-site cation diffusion in perovskite bulk by lowering the activation energy of the migration process, which is likely to occur between B-sites along a curved trajectory in the (110) planes [149], [312].

$$\mathbf{O_O^x + Ni_{Ti}'' \leftrightarrow V_O^{\bullet\bullet} + V_{Ti}'''' + + Ni(ex) + \frac{1}{2} O_2} \qquad \textbf{Equation 5-11}$$

The driving force for exsolution is the difference in oxygen chemical potential between bulk and surface, leading to the reduction of perovskite lattice [147], [149], [174]. In the chemical exsolution process, pO_2 is controlled by gas composition and temperature. During switching, the process is triggered by applying a high cathodic polarisation to the fuel electrode in electrolysis mode [148], [153], [182]. The low value of pO_2 at electrode moves eq. 5-6 and 5-11 to the right. In the first reaction, oxygen is stripped from the perovskite lattice, leaving oxygen vacancies and reduced Ti cations (Ti^{3+}). In the second reaction, the Ni^{2+} is reduced to metal and stripped together with oxygen from the perovskite lattice, leaving oxygen vacancies and an empty B-site. The Ni metal diffuses to the surface due to the elastic energy of the system [177]. In exsolution triggered by applied potential, the driving force for the reaction is overpotential on the fuel electrode (working electrode), $\boldsymbol{\eta_{WE}}$, which causes defect chemical polarisation of the perovskite phase [183]. The η_{WE} is proportional to the applied voltage U_{DC}, generated current I_{DC} and resistance from electrolyte and equipment and overpotential on a counter electrode:

$$\eta_{WE} = U_{DC} - I_{DC}(R_{rig} + R_{YSZ}) - \eta_{CE}$$ **Equation 5-12**

The overpotential at the electrode changes the chemical oxygen potential in the bulk of the electrode, eq. 5-13. The higher overpotential in EC mode (η_{WE} takes a negative value) lowers the effective pO_2 at the fuel electrode, $(pO_2)_{FE}$, from the pO_2 induced by the gas atmosphere, $(pO_2)_{atm}$. The $(pO_2)_{atm}$ could be calculated from the Nernst equation for a specific OCV value.

$$\eta_{WE} = \frac{RT}{nF} \ln \left(\frac{(pO_2)_{FE}}{(pO_2)_{atm}}\right)$$ **Equation 5-13**

The capability of the cation to be reduced depends on its Gibbs energy for the reaction:

$$M_xO_y = xM + \frac{y}{2}O_2$$ **Equation 5-14**

The low value of Gibbs free energy for reaction leads to Ni reduction and exsolution [171], [173], [147], [313]. On the other side, the stability of the LCNT/YSZ electrode in operating conditions and during switching comes from the large value of Gibbs free energy for other cations (Table 5-10).

Table 5-10: The change of Gibbs free energy for M/MO reaction at 800°C [55], [314].

M/MO	La/La_2O_3	Ca/CaO	Ni/NiO	Ti/TiO_2	Zr/ZrO_2	Y/Y_2O_3
ΔG [kJ/mol]	-887.1	-1038.4	-286.507	-750.45	-894.938	-1063.546

The pO_2 at which the metal cations, M, in the perovskite lattice will be reduced, among others [313], depends on the equilibrium partial pressure of oxygen $(pO_2)_{Eq}$, for the eq. 5-16. Both $(pO_2)_{Eq}$ and ΔG could be deducted from the Ellingham diagram [314], which shows their change with temperature. The pO_2 and ΔG are connected through the equation:

$$\Delta G = RT\ln(p(O_2))$$ **Equation 5-15**

The equilibrium overpotential for eq. 5-14, $\eta_{M/MO}$, could be calculated from eq. 5-16 for all metal cations in LCNT/YSZ electrode (Table 5-11).

$$\mathbf{n}_{\mathbf{M/MO}} = \frac{\mathbf{RT}}{\mathbf{nF}} \mathbf{ln}\ (\frac{\mathbf{p(O_2)_{Eq}}}{\mathbf{p(O_2)_{atm}}}) \quad \textbf{Equation 5-16}$$

Table 5-11: The equilibrium overpotential for M/MO reaction at 1.0867 V open-circuit voltage. The minus sign is related to cathodic polarisation.

M/MO	La/La$_2$O$_3$	Ca/CaO	Ni/NiO	Ti/TiO$_2$	ZrO$_2$	Y/Y$_2$O$_3$
η_{EQ} [V]	-1.53	-1.55	0.375	-1.2	-1.27	-1.14

After electrochemical switching, when voltage is lowered for the cell operation, the potential change will affect both the defect chemistry of LCNT and the oxidation state of exsolved Ni. The generation of Ti^{3+} cations will be partially reversible, as the lower overpotential will shift eq. 5-6 to the left, thus lowering conductivity. At standard fuel cell operating conditions, pO$_2$ is below ***(pO$_2$)$_{Eq}$*** for Ni oxidation; Ni will retain on the perovskite surface in reduced form.

5.5.3 Electrochemical testing of planar cells

The SOFCRoll is an inhomogeneous system, and it is challenging to recognise what processes affect their performance; therefore, a set of planar cells with known surface area and more homogeneous gas conditions was tested to better understand their functionality.

5.5.3.1 YSZ sample and silver electrode

To investigate the ohmic contribution from YSZ electrolyte sintered at 1350 °C planar YSZ sample was tested. For the sample preparation, two layers of YSZ electrolyte tapes were laminated and cut into a circular shape with a diameter of 2.5 cm and sintered under 1350 °C for 5 h. The electrolyte sample was produced with a diameter of 1.85 cm (Figure 5-29 a) and an average thickness of 110 µm. The tape was sintered sandwiched between two porous alumina plates; the porosity of the alumina plates ensured that gas from the burning of organics would be released, while its weight prevented the sample from bending during the heat treatment. The produced sample had a slightly irregular surface; the higher weight could improve the cell's regularity; however, the excessive weight would prevent micromovements of material during sintering, thus could cause the formation of cracks. Also, a higher weight makes the sample thinner; hence, more fragile and more difficult to handle. The silver paste used for the current collector was painted directly on the YSZ electrolyte and took the function of symmetrical silver electrodes. The surface area of 1.4 cm^2 was normalised to 1 cm^2. The YSZ sample was heated with a 1 °C/min rate, and an impedance test was made at the temperature range 700-800 °C at 50 °C temperature step, in a frequency range of 0.1 MHz – 0.5 Hz and the amplitude of excitation voltage 20 mV under atmospheric air.

The EIS measurement shows a semi-circle shape, which illustrates the polarisation resistance of the silver electrode, which is relatively low, as silver is known to have high activity for oxygen incorporation/ evolution reaction [57]. After extracting the inductance and rig's ohmic resistance (Rs) values, the Rs of YSZ were calculated. From Rs of YSZ, the conductivity and activation energy which is 0.023 S/cm at 800 °C and 0.7 eV, respectively, were determined; as shown on the Arrhenius graph, Figure 5-29 d, the slope and conductivity of experimentally measured YSZ electrolyte is lower than the expected theoretical value [86], [87]. Performance loss may be due to the lower sintering temperature of the prepared electrolyte and different dwelling times.

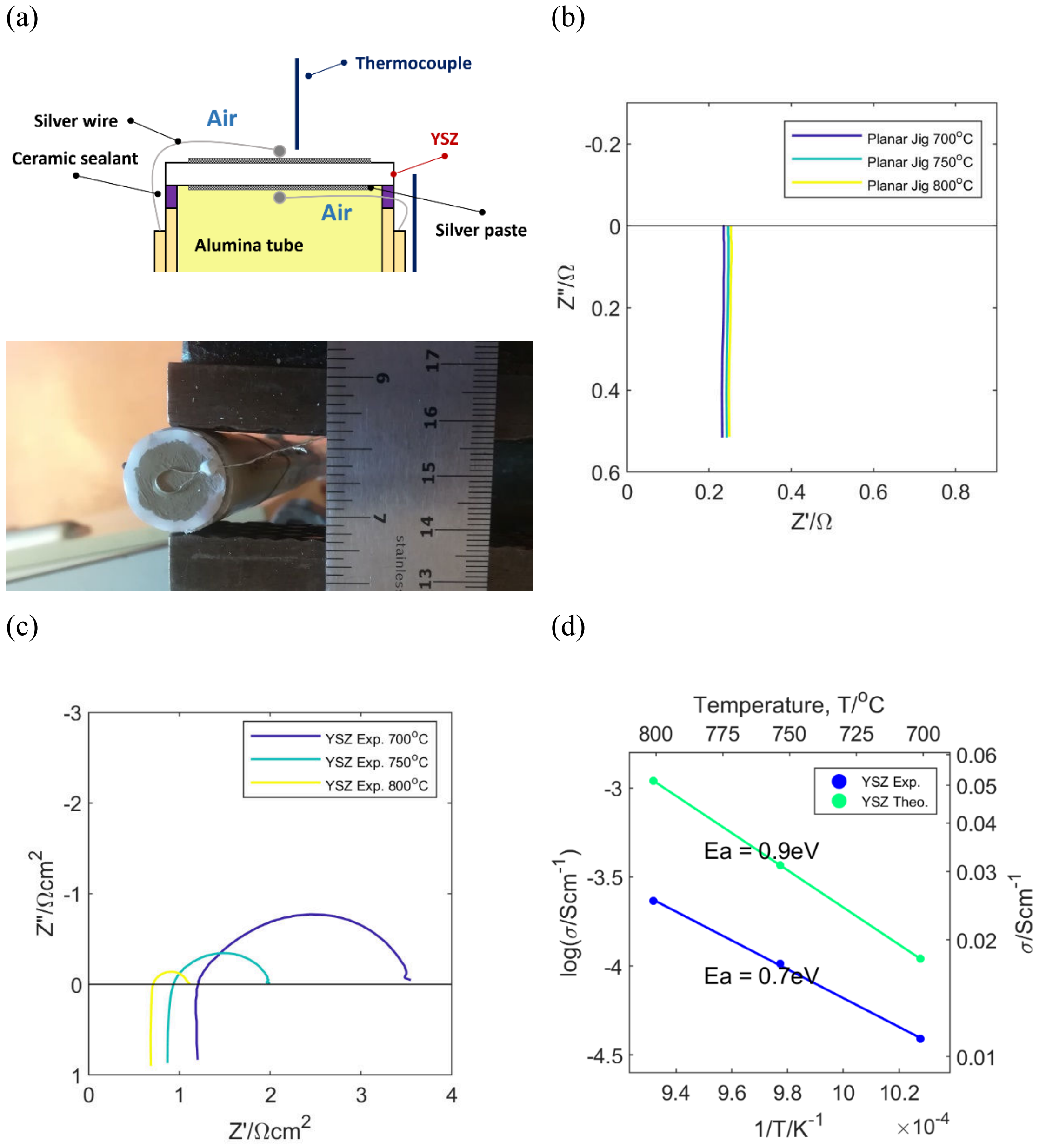

Figure 5-29: Impedance test of YSZ electrolyte with silver electrodes in the temperature range 700-800 °C and atmospheric air. (a) A testing set-up and YSZ sample. (b) Rig's EIS at short circuit. (c) EIS of YSZ electrolyte with silver electrodes in air. (d) Theoretical and experimental conductivity of YSZ [87].

5.5.3.2 LSM/YSZ50 Composite

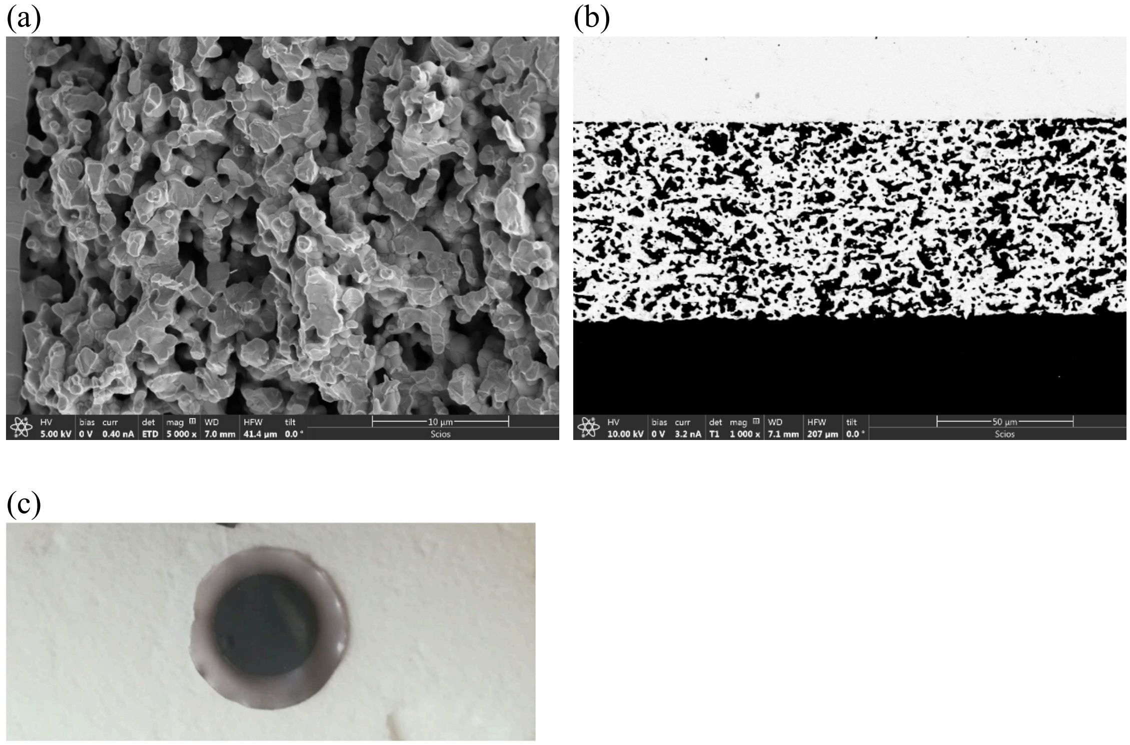

Figure 5-30: LSM/YSZ50 symmetrical cell. (a) SEM (SEI) of the co-sintered electrode. (b) SEM (BSE) of electrode and interface with electrolyte. (c) Image of planar LSM/YSZ50 symmetrical cell.

The symmetrical planar cell with LSM/YSZ50 composite electrode was tested to investigate polarisation's characteristic frequency and behaviour from the oxygen electrode. LSM/YSZ50 composite cells were prepared with two single LSM/YSZ50 electrode layers on both sides and a double YSZ electrode tape. The SEM image of produced composite LSM/YSZ50 oxygen electrode shows in Figure 5-30. The analysis of the BSE image gives 75 µm of electrodes and 40% porosity, and 110 µm electrolyte; no delamination or cracks were detected. The co-sintered cell shows the change in the colour of the YSZ electrolyte on the cell's edges (Figure 5-30 c), indicating possible diffusion of Mn ions into the YSZ electrolyte [293].

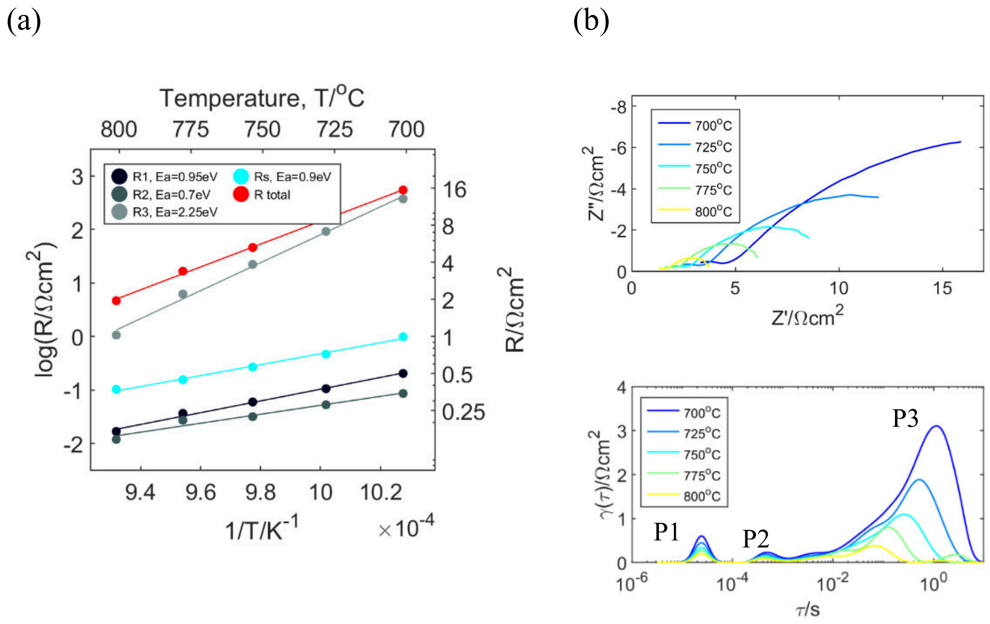

Figure 5-31: Impedance analysis of planar, symmetrical, co-sintered cells with LSM/YSZ50 oxygen electrode in the temperature range 700-800 °C and atmospheric air. (a) Arrhenius plot of ohmic and polarisation resistance of the LSM/YSZ50 (one layer). (b) EIS of the symmetrical cell and DRT of the single LSM/YSZ50 layer.

The DRT, constructed for a single LSM/YSZ50 layer, reveals at least three polarisation processes, with the most significant process at low frequency (P3). The initial resistance of the P1, P2, P3 processes was found through the method shown in Figure 4-17. The equivalent circuit was made of ohmic resistance (Rs), and three semicircles made of resistance (R) and contact phase element (CPE) connected parallel (R/CPE). In the first stage of equivalent circuit development, the calculated resistance from DRT at 700 °C was "fixed" while other parameters were "open". The fitting with such a circuit gave the parameters of the constant phase elements. In the second fitting, the calculated "n" of CPE elements (defining the shape of semicircles) calculated in the first fitting ($n1 = 0.85$ for P1, $n2 = 0.7$ for P2) were fixed, while all other parameters were open. The calculated polarisation resistance (which in this case was an "open" parameter) was close to the value calculated from the DRT pattern, proving the accuracy of the circuit. A developed equivalent circuit with n-parameters fixed was used for the whole temperature range.

The surface area of the symmetrical cell, 1.4 $cm^{2,}$ was normalised to 1 cm^2. Figure 5-31 a shows the Arrhenius Plot of ohmic and polarisation resistance of a single LSM/YSZ50 composite layer, calculated from the equivalent circuit. All elements follow Arrhenius dependence, meaning they are thermally activated; thus, the activation energy ***E_a*** could be calculated from the slope of the lines. The total polarisation resistance of the single 75 µm LSM/YSZ50 layer was between 14 – 1.35 Ω/cm^2 at 700-800°C under atmospheric air. The ***Rs*** of the YSZ electrolyte (calculated in 5.5.3.1) were extracted from the data. The ohmic resistance of the LSM/YSZ50 layer was between 1 – 0.4 Ω/cm^2 at 700-800°C and had an ***Ea*** of 0.9 eV. The activation energy of 0.9 eV is much higher than LSM, which is about 0.1 eV [191]. Also, the values of resistance were close to the resistance of 75 µm YSZ layer in this temperature range when calculated from data obtained for YSZ conductivity; indicating that the YSZ phase could control the conductivity of the electrode; therefore, there could be no sufficient percolation in the LSM/YSZ50 composite between LSM grains.

Table 5-12: The overview of processes delivered from symmetrical LSM/YSZ50 cell impedance.

No.	Char. Freq./ Hz at 700-800°C	Ea/ eV 700 - 800°C	Capacitance/ F at 700-800°C
Rs	-	0.93	-
P1	22500 - 17500	0.95	$1\times10^{-7} – 3\times10^{-5}$
P2	900 - 500	0.7	$4\times10^{-4} – 1\times10^{-3}$
P3	0.15 – 2.4	2.25	$5\times10^{-2} – 7\times10^{-2}$

The recognised polarisation processes correspond to one in SOFCRoll with a Ni/YSZ based electrode (Table 4-6). Measurement, in addition, made visible a small polarisation process at medium frequency P2, which previously merged with the more extensive charge transfer process from Ni/YSZ fuel electrode. Characteristic frequencies of the primary peak P3, 0.15 – 1.5 Hz at the 700-800°C temperature range, were designated from the equivalent circuit. As explained already, the process could be associated with oxygen adsorption/ dissociation and transport of intermediates to 3PB [294]. The process was found to be a rate-limiting in LSM/YSZ composite [295] and shows pO_2 dependency. As in this case, the process is known to have large activation energy, and its maximum frequency decreases at a lower temperature [294], [296]. The P1 and P2 processes are known to be linked to oxygen ion transport through the interface and the YSZ of the composite. The value of activation energy of P1 corresponds to the reported 1 eV value [294], [296].

5.5.3.3 LCNT/YSZ50 sample

The impedance of planar cell with silver oxygen electrode and LCNT/YSZ50 fuel electrode was tested after gas reduction and electrochemical switching at 2.1V for 2 min. The produced impedance spectra were used to determine polarisation on LCNT/YSZ50 fuel electrode, thanks to the low contribution of the silver electrode. After applying high potential, there were concerns about silver instability, which could bring significant error into impedance analysis after switching. Therefore the polarisation of symmetrical cells with silver electrodes (the same design as the cell discussed in Chapter 5.5.3.1) was tested before and after applying 1V of overpotential in the air atmosphere (Figure 5-32).

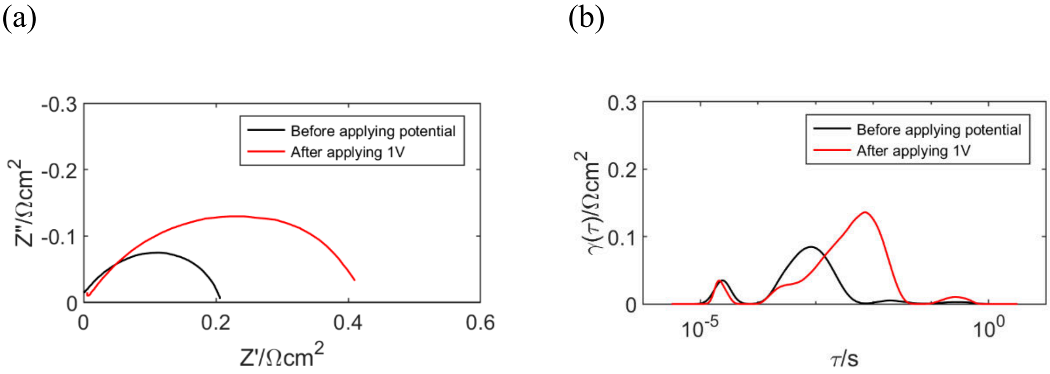

Figure 5-32: The impedance analysis of symmetrical cells with silver electrodes before and after applying 1V of overpotential in an air atmosphere at 800 °C. (a) EIS. (b) DRT is calculated from impedance data.

Impedance measurement shows the impedance of the single layer of the silver electrode after extraction of the ohmic resistance. After applying overpotential, the polarisation resistance increased two times; however, in both cases, polarisation is relatively small and would not bring a significant error to the measurement; especially since the size of the active area of the silver electrode was enlarged in relation to the surface area of the fuel electrode, which was 2.4 cm^2 for the silver electrode and 1.4 cm^2 for LCNT/YSZ50, which after normalisation to 1cm^2 would give about 0.12 Ω before and 0.24 Ω after poling with voltage at 800 °C. The DRT shows two peaks; the high-frequency peak is most likely related to the charge transfer process with a characteristic frequency of ~ 8 kHz before and ~ 7 kHz after applying voltage; it does not significantly change. The low-frequency peak is related to the surface process, and its frequency decreased from ~ 200 Hz to ~ 20 Hz; its enlargement is the reason for the increase of resistance after applying voltage.

Figure 5-33 shows impedance analysis of the LCNT/YSZ50 electrode at 700-800 °C temperature range, under the 50 ml/min of wet H_2 in FE and atmospheric air in OE. The total polarisation resistance of the 50 µm LCNT/YSZ50 electrode was between 29.6 - 9.4 Ω/ cm^2 before switching and 16.6 - 5 Ω/ cm^2 after switching at 800 °C. The ohmic resistance of a single layer before switching was between 2.5 – 1.4 Ω/ cm^2 and 1.7 – 0.65 Ω/ cm^2 after switching.

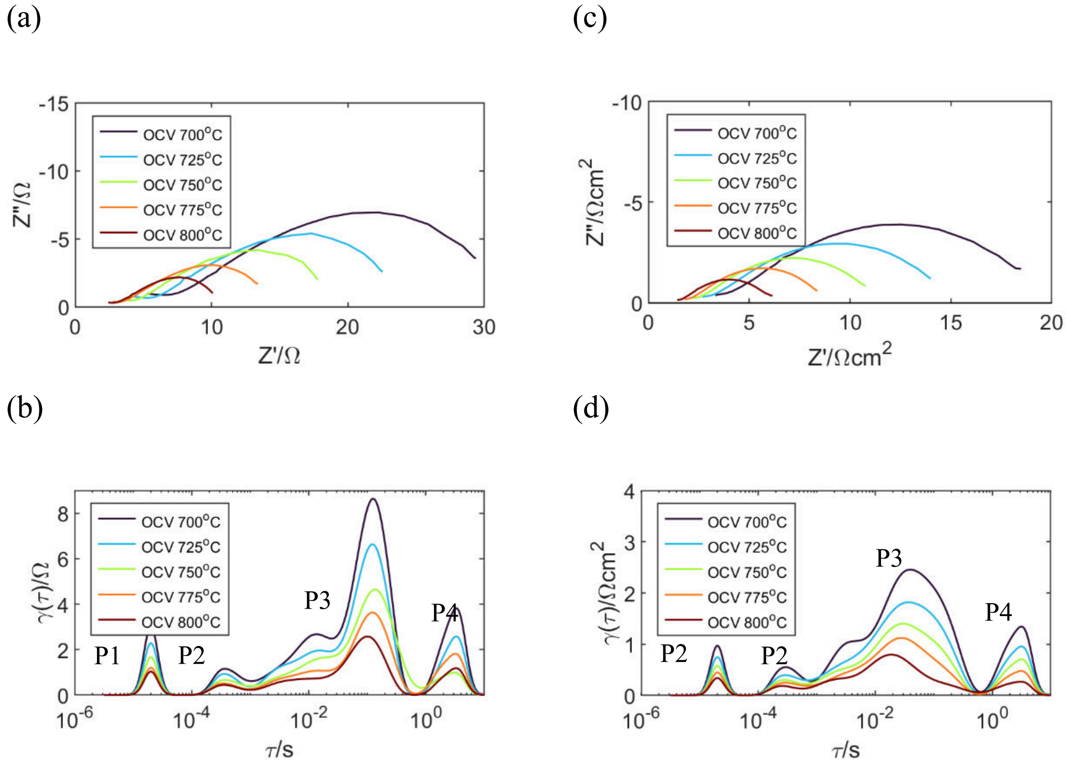

Figure 5-33: Impedance analysis of planar cell, with co-sintered LCNT/YSZ50 fuel electrode tested at the 700-800 °C and the 50 ml/min of wet H_2 in FE and atmospheric air in OE. (a)-(b) After reduction with H_2. (c)-(d) After switching at 2.1V for 2 min.

The DRT analysis of the LCNT/YSZ50 sample reveals at least four processes with the highest contribution at the medium frequency. As in an oxygen electrode, two high-frequency P1 and P2 processes are likely related to the charge transfer and transfer of oxygen ions through an interface, similar to the perovskite oxygen electrode; they give two separate arcs with different capacitance ranges and characteristic frequencies. Here they are modelled by R and CPE connected parallel. One of the processes could represent the oxygen ion transfer at YSZ/LCNT interface, and the second could be related to charge transfer at the grain boundaries or through the MIEC. However, with those data is not possible to assign them precisely. They could depend on either oxygen ion conduction or electronic conductivity; therefore, they will be proportional to the concentration of Ti^{4+}/Ti^{3+} and oxygen vacancies.

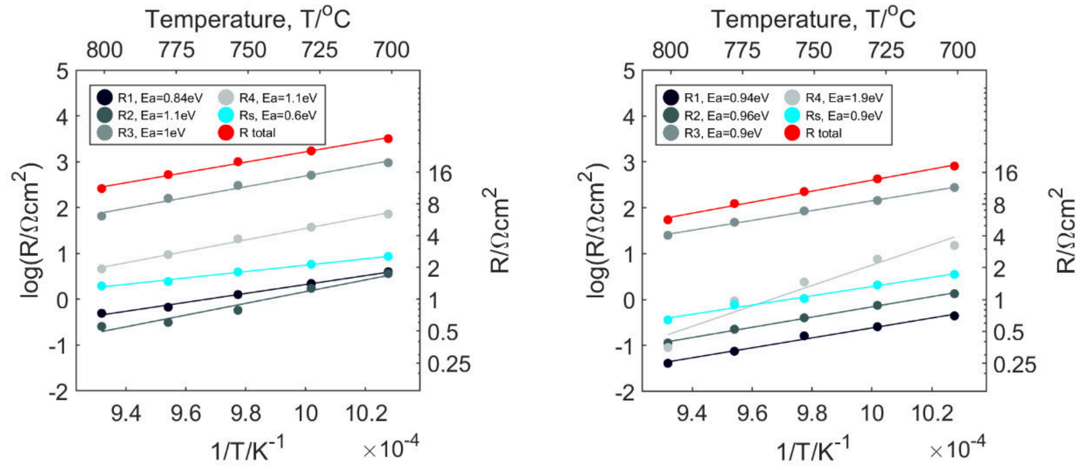
(c) (c)

Figure 5-34: Impedance analysis of planar cell, with co-sintered LCNT/YSZ50 fuel electrode, tested in the 700-800 °C and the 50 ml/min of wet H_2 in FE and atmospheric air in OE. EIS, DRT and Arrhenius plot of ohmic and polarisation resistance from the equivalent circuit. (a)-(c) After reduction with H_2. (d)-(f) After switching at 2.1V for 2 min.

Table 5-13: The overview of processes delivered from LCNT/YSZ50 fuel electrode impedance before (R) and after electrochemical switching (S).

No.	Reduced/ Switched	Char. Freq./ Hz at 700-800°C	Ea/ eV 700 - 800°C	Capacitance/ F at 700-800°C
Rs	R/ S	-	0.6/ 0.9	-
P1	R/ S	103300 - 88700/ 40000 - 50000	0.84/ 0.95	1×10^{-6} - 3×10^{-6}/ 8×10^{-6} - 2×10^{-5}/
P2	R/ S	6622 - 2387/ 900 - 1000	1.1/ 1.1	2×10^{-5} - 2×10^{-4}/ 2×10^{-4} - 5×10^{-4}
P3	R/ S	0.21 - 3.66/ ~0.05	1/ 1	5×10^{-2} - 6×10^{-3}/ 3×10^{-3} - 7×10^{-3}
P4	R/ S	0.65 - 1.73/ ~0.05	1.1/ 2	5×10^{-2} - 7×10^{-2}/ 4×10^{-2} - 6×10^{-2}

Both EIS and DRT spectra indicate a non-standard shape of the spectra of the P3 process at low frequency, and DRT shows a minor P4 process at ultra-low frequency. As mentioned already, the interpretation of processes on very high and low frequency (border processes) by DRT could have an error as function estimates data beyond the measuring range; however, further tests on the very high overpotential made on tubular cells reveal the presence of the P4 process (Chapter 6.5.2.2), which can not be ignored. Several processes could be related to the low-frequency spectra, including dissociative adsorption of H_2/ H_2O, surface transport of hydrogen species and the reaction of adsorbed species with lattice oxygen either on perovskite surface or 3PB, diffusion/ transport of oxygen ion to the reaction site (either through the bulk or surface).

Due to the non-standard shape of P3, the process is considered to be coupled with chemical diffusion, which could be modelled either by finite-length Warburg (FWL) or Gerischer element, most likely in its fractal form due to the complexity of porous MIEC electrode. The use of the fractal element could be compared to the using constant phase element instead of capacitance in the Cole element [315], [316].

Boukamp [315] used the expression of the Finite Length Warburg (FLW) to model oxygen ion diffusion (or the diffusion of mobile cation) through the mixed electronic conductor (MIEC), assuming that electronic conduction is sufficiently large to be ignored. Both FWL and Gerischer are derived from Fick's laws of diffusion, but Gerischer includes the reaction term, which changes the activity of these species [317].

A good fit was produced for impedance at 700 °C with the use of the fractal FLW (f-FLW) with n equal to 0.4; unfortunately, Z-View software used for evaluation of impedance data does not offer fitting with fractal Gerischer. Therefore, due to challenges to fit impedance on the whole temperature range, the simplified equivalent circuit of semicircles was used to calculate resistance and activation energy (Figure 5-34). The equivalent circuit consisting of the Gerischer element was used in the further part of the project to analyse the impedance of tubular cells. Moreover, as in the cells with composite electrodes, the impedance of the oxygen electrode merges with the impedance of the fuel electrode almost at the whole frequency range; in those cells, fitting with R/CPE is more sensible Gerisher would not present any specific process, which involves diffusion.

Therefore, composite fuel cells and planar symmetrical cells were fitted with simple semicircles to compare the cell's performance.

The resistance was calculated directly from DRT (Figure 4-17) and fitted to a simplified equivalent circuit, where a semi-circle modelled the P3 process with n equal to 0.5; the CPE with n=0.5 is considered to be a special type of Warburg [318]. The dispersion with n between 0.5 and 1 is mainly capacitive; below this value, the process is related to distributed diffusion [318], [319]. Calculated resistance was plotted on the Arrhenius plots, which were used to calculate the activation energy of the individual processes, which are summarised in Table 5-13.

The P4 process could be linked to the dissociative/ adsorption of H_2 (concentration polarisation), which appears at a low frequency in oxide-based fuel electrodes [318], [319], n for the P4 process approach "1", indicating distributive capacitive behaviour.

On the MIEC electrodes, the so-called chemical capacitance should also be considered, which influences impedance on low frequency [142], [319]–[321]. The chemical capacitance is related to the bulk process, which expresses the capability of the material (MX) to store chemical energy, e.g. change of chemical potential of X species due to variation in stoichiometry [322]. Such capacitance could approach the value of many Farads, where the large area of the electrode is active. The bulk properties of perovskite, such as the concentration of oxygen vacancies, will be directly related to pO_2, either controlled by the gas atmosphere or applied potential. Also, concentration polarisation will be sensitive to the gas concentration.

The measurement on tubular cells (Chapter 6.5.2.2), when tested on the wide overpotential range between electrolysis and fuel cell mode, showed that P1, P2 and P3 increase their kinetics at higher cathodic polarisation. In light of the above consideration, the improvement could be explained by an increase in the concentration of oxygen vacancies in the material; hence oxygen ion transfer either through the interface or bulk of the electrode improve. The P4 process significantly decreased at a higher overpotential when tested in fuel cell mode, which could be related to improved kinetics for the H_2 adsorption/ dissociation process, due to the generation of adsorption sides at a higher anodic overpotential. The process also improved its kinetics after switching, which could be related either to the generation of Ni or adsorption sides directly on the perovskite surface, which would take part in the adsorption/ dissociation process as explained in Chapter 5.5.1.

5.5.3.4 Planar fuel cell with composite electrodes

Co-sintered planar fuel cells were made with standard single layer LCNT/YSZ50 and LSM/YSZ/50 composite active layers. Figure 5-35 shows the SEM image of the cell‘s cross-section. No delamination or cracks were visible; the electrode has a well-sintered interface with electrolyte layers. The electrolyte thickness was 113 µm, while the thickness of both electrodes was about 50 µm. The YSZ electrolyte is nearly dense with a small fraction of closed porosity, while the microstructure of electrodes is porous to assure gases exchange with the active region.

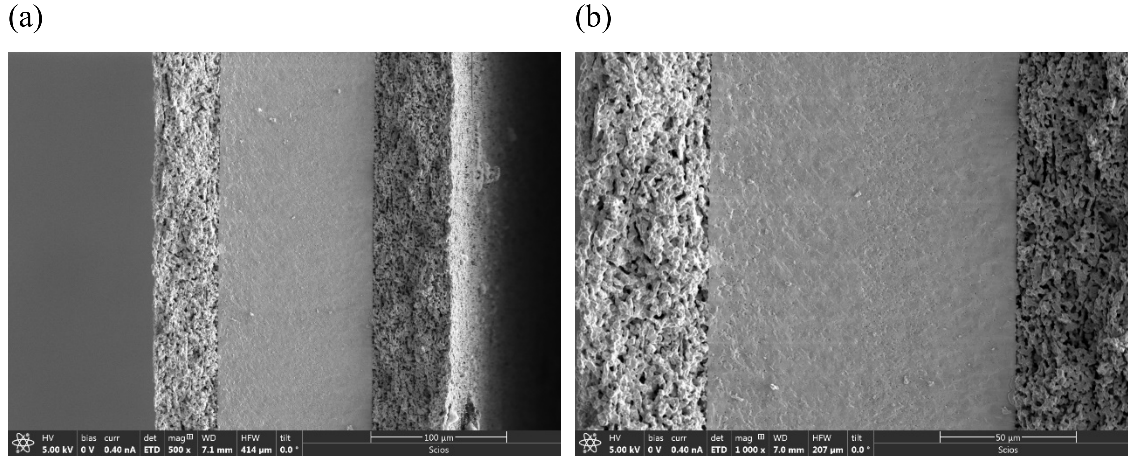

Figure 5-35: The SEM image of the planar fuel cell (a)-(b) cross-section, from left to right LCNT/YSZ50 active anode, YSZ electrolyte, LSM/YSZ50 cathode.

Due to the very high convergence of the characteristic frequency of LSM/YSZ50 and LCNT/YSZ50 composite electrodes, the separation of individual contributions either through DRT or equivalent circuit analysis was not possible. Therefore, the equivalent was made of four elements representing processes on a specific frequency range from both electrodes. The DRT spectra show a dominant process at low-frequency P3 and a smaller peak at low-frequency P4; both coincide with the LCNT/YSZ50 fuel electrode peaks discussed in the previous chapter; however, they are most likely affected by the low polarisation process at LSM/YSZ50 electrode. Also, P1 and P2 processes on both electrodes are located at a close frequency range and merge into single arcs in the Nyquist plot. In general, the LSM/YSZ50 has lower polarisation but much higher activation energy than the reduced fuel electrode. Therefore more significant contribution from LSM/YSZ50 could be expected at 700 °C, which basing on the analysis of cells with a single type of electrodes, is around half of the LCNT/YSZ50. Whereas at 800 °C, the polarisation resistance of LCNT/YSZ50 is about seven times larger.

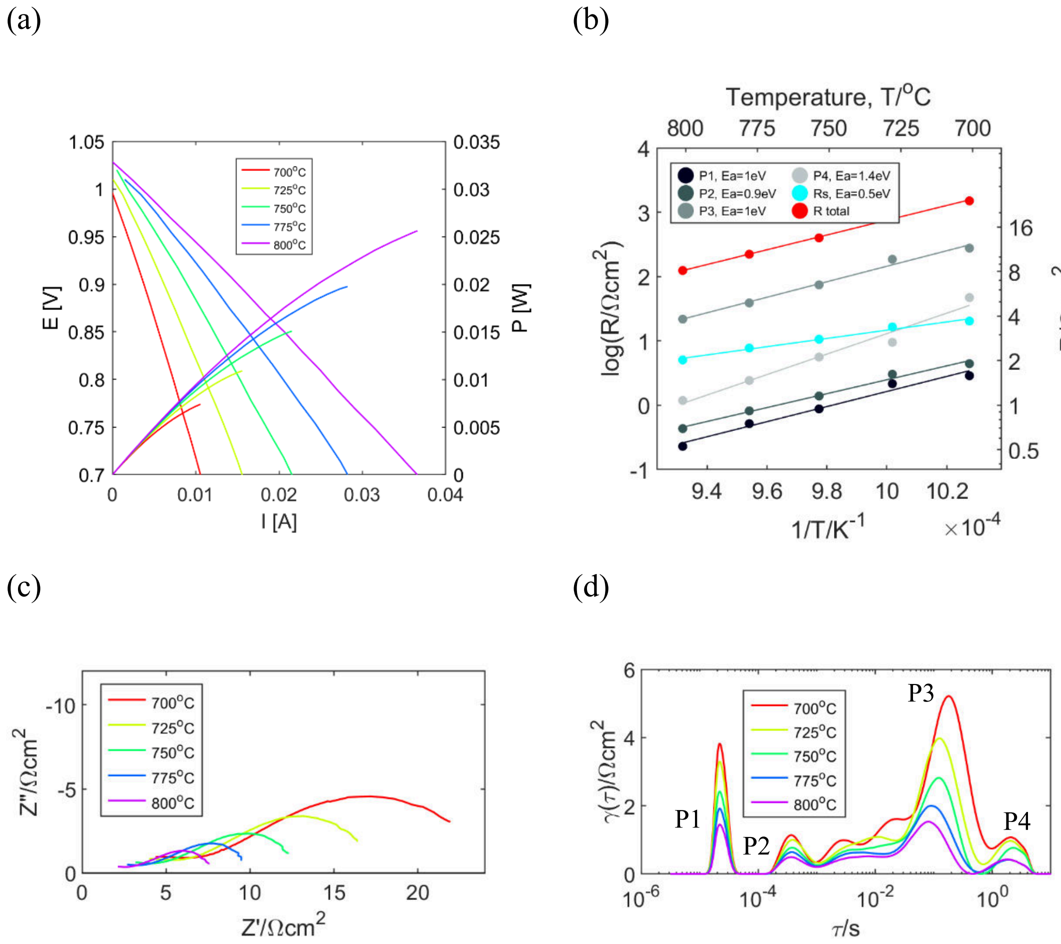

Figure 5-36: The electrochemical performance of the planar fuel cell before switching tested in the 700-800 °C and the 50 ml/min of wet H_2 in FE and atmospheric air in OE. (a) I-V curve of cell operating in fuel cell mode. (b) Arrhenius plot of ohmic and polarisation resistance. (c) – (d) EIS and DRT analysis of impedance data at OCV conditions.

The test was done at 700-800 °C, and the 50 ml/min of wet H_2 in FE and atmospheric air in OE. The cell's total polarisation resistance after gas reduction, which includes polarisation from both electrodes, is between 20.6 – 6 Ω/cm^2 at 700 – 800 °C, and the total ohmic resistance is between 3.8 – 2 Ω/cm^2. The polarisation resistance is lower than expected based on the analysis of symmetrical LSM/YSZ50 symmetrical cell and cell with LCNT/YSZ50, indicating that direct comparison with the previous measurement where the electrodes were measured separately is not entirely possible.

Table 5-14: The overview of processes delivered from the impedance of planar fuel cell with LCNT/YSZ50 FE and LSM/YSZ50 OE after 2 h of gas reduction in H_2.

No.	Char. Freq./ Hz at 700-800°C	Ea/ eV 700 - 800°C	Capacitance/ F at 700-800°C
Rs	-	0.5	-
P1	17000 - 13000	1	$8\times10^{-6} – 3\times10^{-5}$
P2	200	0.9	$5\times10^{-4} – 1\times10^{-3}$
P3	0.4 – 2	1	$5\times10^{-2}– 3\times10^{-2}$
P4	~ 0.08	1.4	$5\times10^{-2}– 1\times10^{-1}$

The calculated activation energy of dominant process P3 is 1 eV in the measured temperature range (Table 5-14); the activation energy, peak position and shape is similar to that detected on LCNT/YSZ50 electrode. The modelling of the P4 process with equivalent circuits gave slightly higher magnitude and activation energy values than DRT indicated. DRT could bring errors at a very high and very low frequency as this data is extrapolated. The activation energy is higher than in the LCNT/YSZ50 composite, which could be due to the polarisation of the LSM/YSZ50 electrode.

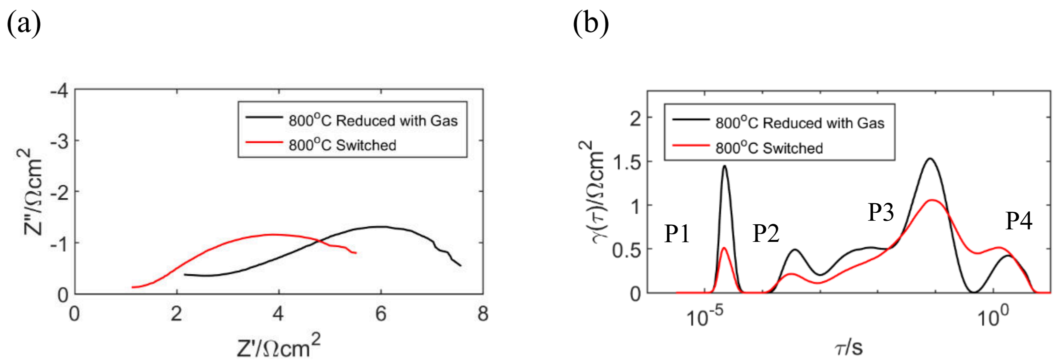

Figure 5-37: Impedance analysis of planar fuel cell, before and after switching at 2.1V for 2 min at 800 °C and the 50 ml/min of wet H_2 in FE and atmospheric air in OE. (a) EIS at the OCV. (b) DRT calculated from impedance data.

The cell was heated up to 800 °C and reduced for 2 hours in 50 ml/min of 3% H_2O/H_2 and atmospheric air. Next, the switching was performed by applying 2.1V in the electrolysis mode. After electrochemical switching, all processes seem to be reduced. The reduction of ohmic resistance is due to an increase in electrodes conductivity. Assuming that the electronic path is dominant, this will be due to the generation of Ti^{3+} on the fuel electrode; similarly, on the oxygen site, processes could be improved. LSM/YSZ is a p-type conductor; high anodic polarisation has likely doped holes into locations associated with the B-site improving its electronic conductivity. P1 and P2 attributed to charge transfer and oxygen ion transfer on an interface could be reduced on the fuel electrode side due to the generation of oxygen vacancies and Ti^{3+} in MIEC, increasing both ionic and electronic conductivity, which would improve the kinetics of these processes. The kinetics of P3 and P4 improve after switching in most cases; however, improvement seems not to be significant in this particular example. As explained already, improvement of P3 and P4 process on fuel electrode side after switching is expected due to generation of vacancies, which would increase oxygen ion diffusion, but also the generation of mobile oxygen sites for H_2 adsorption on perovskite surface and exsolution of Ni, which would support H_2 oxidation according to explain the mechanism in Chapter 5.5.1. Moreover, if the electronic conductivity is rate-determining, e.g. for H_2 dissociation, electronic conductivity improvement will also affect low polarisation processes. Also, low-frequency polarisation on the LSM/YSZ50 would be reduced after the switching procedure. It is well known that LSM could become activated by a high anodic polarisation, and its performance could improve [57], [44], [301]. As the LSM/YSZ50 significantly contributes to composite-based cell ohmic and polarisation resistance, such activation undoubtedly changes the cell's performance after switching.

Figure 5-38 shows SEM (SEI) of LCNT/YSZ50 electrode before and after electrochemical switching. The co-sintered electrode, before reduction, shows the well-homogenised structure of LCNT and YSZ grains; LCNT could be easily distinguished due to the terrace-like structure. Upon switching, the perovskite structure become rougher, and terraces fade. Also, some porosity developed in the perovskite material, visible in Figure 5-38 d. Exsolved metallic particles have various sizes between several and dozen nanometres. Besides metallic particles, larger islands exsolved from the perovskite, which are believed to be TiO_2, observed already after reduction in A-site deficient titanates [156]; in many locations, islands are located under exsolved metallic particles.

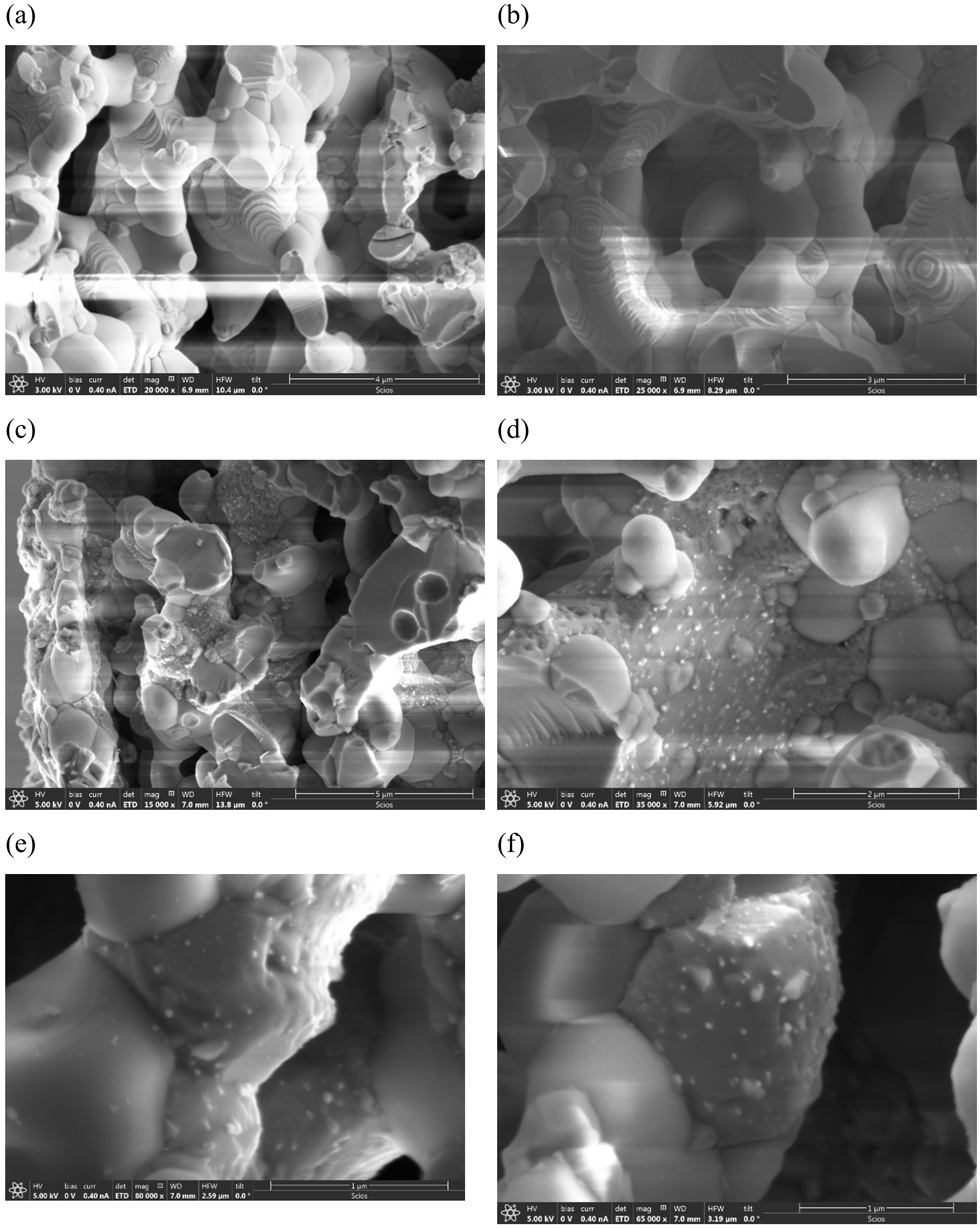

Figure 5-38: SEM (SEI) of LCNT/YSZ50 layer in a planar cell at various magnifications. (a)-(b) Unreduced. (c)-(f) After electrochemical switching at 2.1V for 2 min. at 800 °C

5.5.4 *The large SOFCRoll with LCNT based fuel electrode (SRB25P & SRB26P)*

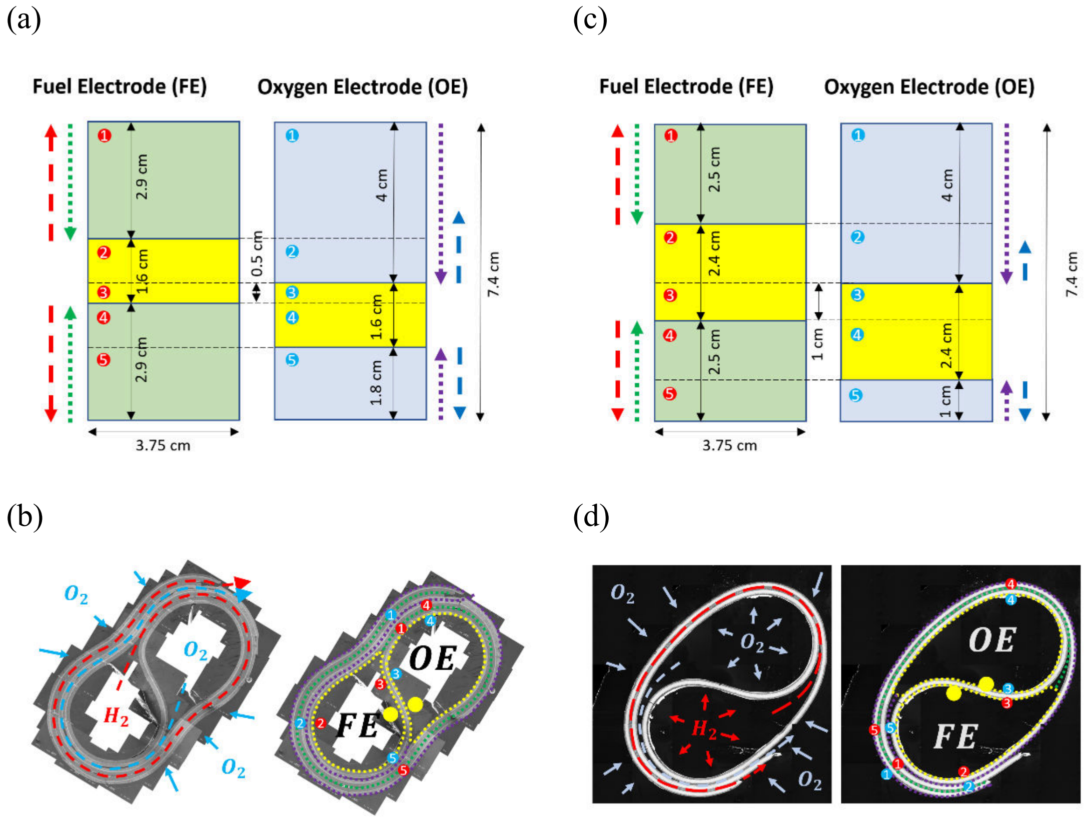

Figure 5-39: The length of current and diffusion paths in various regions of SOFCRoll. (a) – (b) The original design, with silver paste applied on the whole channel area. (c) – (d) SRB25P & SRB26P with LCNT based FE and enlarged inlet channels; Yellow – silver CC, Green – conductivity path FE, Purple - conductivity path OE. Red – diffusion path FE. Blue – diffusion path OE.

In LCNT based SOFCRoll, the whole area in the "Channel" was covered with silver paste to amplify the efficiency of current collecting in this region, Figure 5-39 c. Moreover, the structure of SOFCRoll was modified due to the concerns about the insufficient conductivity of the LSM current collector and developed Ni/LCNT50 current collector on the fuel side to conduct electrons through the whole "Spiral" and about diffusion losses on both sides. Figure 5-39 shows the various areas of activity for SOFCRolls cells made of 5 x 9 cm electrode green tapes, with various size of inlet channels. In the SRB25P and SRB26P cells, stainless steel tubes with a higher diameter were used to roll the green tapes. The "Channel" area was enlarged, and the length of the "Spiral" was reduced; therefore, both diffusion and current collector distance decreased. After sintering, the total surface area of the fuel electrode was about 27.75 cm^2; however, gas conditions and the current collector efficiency vary between parts of the cell; hence, not the same level of activity could be expected at the whole interface (Table 5-15).

Table 5-15: Dimensions and maximum diffusion and current collector distance in various activity regions in SOFCRoll SRB25P and SRB26P (Figure 5-37). L is the thickness of the electrode

Region no.	**1**	**2**	**3**	**4**	**5**
Surface area [cm^2]	9.375	5.25	3.75	5.25	3.75
Diffusion distance H_2 [cm]	2.5 + L	L	L	1.4 + L	2.5 + L
Diffusion distance O_2 [cm]	L	1 + L	L	L	1 + L
Current distance FE [cm]	2.5 + L	L	L	1.4 + L	2.5 + L
Current distance OE [cm]	4	1.4 + L	L	L	1 + L

The most active region in SOFCRoll is between the main channels in the cell centre, (3) in Figure 5-39. The gases from both sides can freely diffuse to this region; hence, the diffusion distance to the interface is limited only by the thickness of the electrodes; it is also entirely covered with silver paste. Region (2) is located in the main channels on the FE side, covered with silver and available for H_2 gas; on the OE side, the gas concentration will be limited by diffusion in the OE spiral (the short part is open to the atmospheric air, which is omitted here for simplicity), while the charge transfer by the conductivity of LSM layer. Whereas region (4) is located in the main channels on the OE side, covered with silver and available for O_2 gas; but on the FE side, the gas concentration will be limited by diffusion of fuel in the FE spiral, while the charge transfer by its conductivity. Region (1) is inside the spiral at the FE side, limited by its conductivity and gas diffusion. Whereas the OE side is the outer layer of the cell exposed to atmospheric air; thus, diffusion distance is limited only by the electrode thickness, but the current collector path is long as the charge must travel through the whole length of an outer layer and the spiral part to silver current inside a cell. Region (5) has the highest limitation for both sides, as both gases and charge transfer are provided through the spirals. If the conductivity and porosity in the “Spiral” are insufficient to manage the required gas exchange and charge transfer, the cell’s activity in the specific areas will decrease with a higher distance.

The SRB25P and SRB26P were the first SOFCRoll with LCNT based fuel electrodes with high OCV and stable operation. Better performance partially resulted from the fully matched shrinking profiles between all layers and the co-casting method detailed in the previous section; since not many defects were present in their structure.

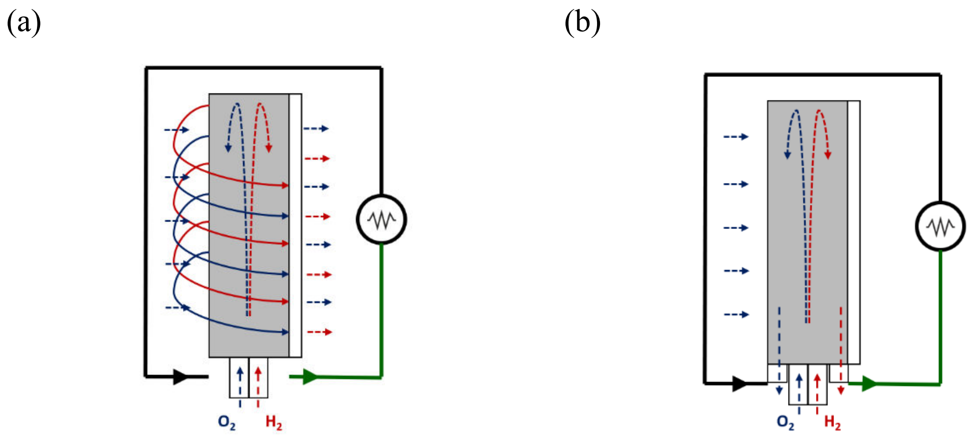

Figure 5-40: Principle of SOFCRoll operation, (a) with a central outlet at the cell's side (b) with outlets on the bottom.

Another reason was the application of the gas outlet at the bottom of the cell. In the original design, the gases were introduced through the "Channel" and diffused through the "Spiral" outside to the outlet alongside the cell, Figure 5-40 a. The modified cells had the outlets at the bottom (basically cell was not entirely sealed) (Figure 5-40 b). Such alteration stabilised OCV and allowed it to operate on higher gas flow (before voltage decreased with the higher flow of H_2). In the new design, excess gases do not diffuse through the whole spiral outside to the large outlet on the side of the cell; instead, they diffuse to the spiral part as much as diffusion restriction allows for that, but the gas excess is discharged from the bottom. The drop in OCV was considered to originate from the microcracks in the spiral part. However, a further evaluation showed that the OCV also was stabilised by decreasing the size of the outlet alongside the cell, indicating that the counter diffusion of the air into a fuel outlet could be responsible.

Cells with LCNT/YSZ50 active electrode primary were tested with the wet H_2. Often cells could not achieve sufficient OCV when reduced with 5% H_2 (either SOFCRoll or further developed tubular cells with composite FE), implying that the activity of the electrode under those conditions could be not sufficient to achieve potential differences with the other side of the cell. Another reason could be the low value of oxygen partial pressure for bulk reduction of the LCNT/YSZ50; usually, the 5% H_2 is sufficient to reduce perovskite material. Perhaps, gases still counter diffuse from the outlet; for a pure H_2 at a low extent of counter diffusion, this may not have a significant impact, but for 5% H_2/N_2, it could affect pO_2 to a much larger degree.

5.5.4.1 The SRB25P SOFCRoll with LCNT/YSZ50 electrode

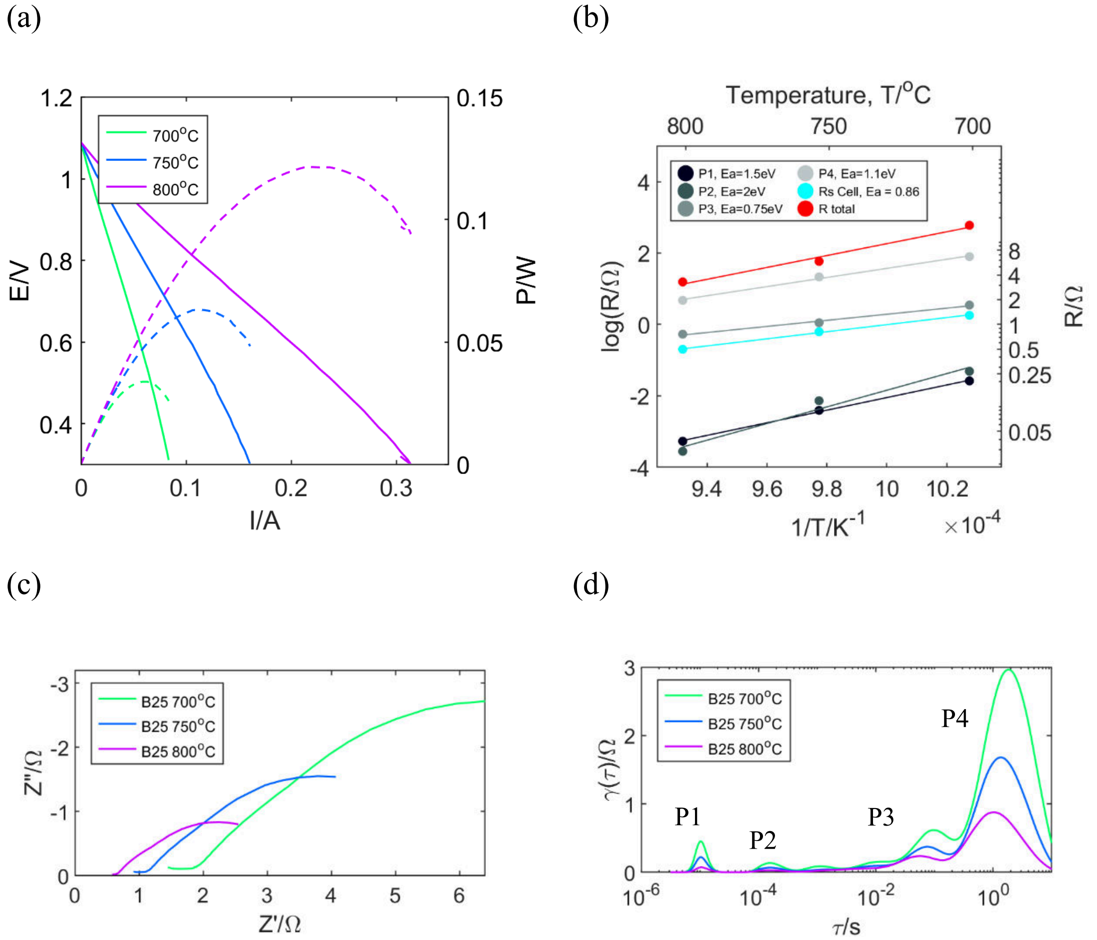

Figure 5-41: The electrochemical performance of the SRB25P SOFCRoll cell before switching in the 700-800 °C and the 50 ml/min of wet H_2 in FE and 100 ml/min of air in OE. (a) I-V curve of cell operating in fuel cell mode. (b) Arrhenius plot of ohmic and polarisation resistance. (c) – (d) EIS and DRT analysis of impedance data at OCV conditions.

The SRB25P was tested with 50 ml/min of wet H_2 in FE and 100 ml/min of air in OE. The open-circuit voltage was above 1.09 V at a temperature range from 700 – 800 °C and increased slightly to 1.1 V after applying the switching method at 2.3 V for 10 min at 800 °C. The high OCV value confirms that the YSZ is dense, and the cell was uncracked during testing. Before switching, the cell's maximum power density was equal to 33.8, 68 and 121.5 mW at 700, 750, 800°C, respectively.

The DRT was created from the imaginatory part of impedance (Figure 5-41 d), indicating at least four processes. The equivalent circuit was constructed with the number of elements known, consisting of ohmic resistance (Rs) and four semi-circles. The initial resistance of the P1, P2, P3, P4 processes was found through the method shown in Figure 4-17, which were 0.26, 0.26, 1.6, 6.65 Ω at 700 °C, respectively. In the first fitting, the calculated resistance from DRT for P1, P2, and P4 was "fixed" while other parameters were "open". The fitting with such a circuit gave the parameters of CPE. In the second fitting, the approximated "n" of CPE elements calculated in the first fitting (n1 = 0.85 for P1, n2 = 0.7 for P2, n3 = 0.62 for P3, n4 = 0.82) were fixed, while all other parameters were open. Such an equivalent circuit was stable and could be used for the whole temperature range. The resistance of the P1, P2, P3, P4 processes calculated at the "second run" were 0.21, 0.27, 1.7, 6.7 Ω at 700 °C, respectively. The calculated polarisation resistance (which in this case was an "open" parameter) was close to the values calculated from the DRT pattern at the whole temperature range, proving the accuracy of the circuit.

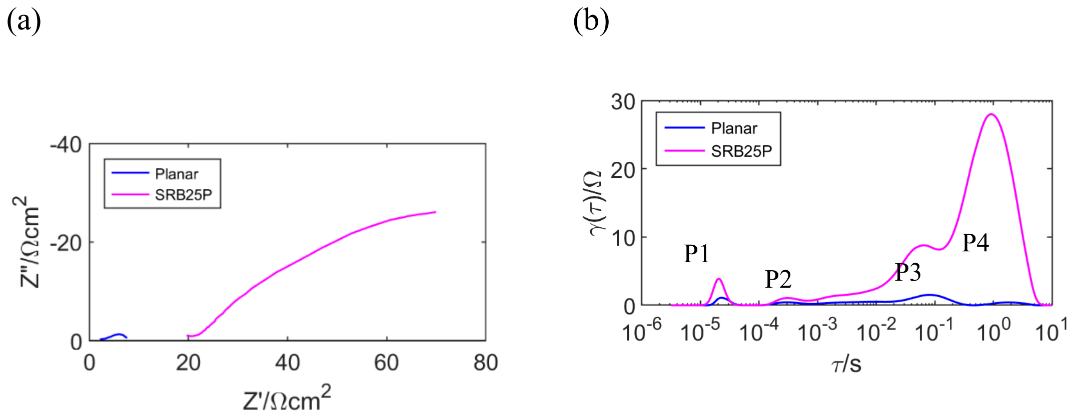

Figure 5-42: The comparison of the planar cell and SOFCRoll B25P (normalised to cm^2) at 800 °C and 50 ml/min of wet H_2 in FE and air in OE (a) EIS analysis. (b) DRT calculated from impedance data.

The ohmic and polarisation resistance should scale with the utilised surface area in the homogeneous system; however, comparing the SOFCRoll with other configurations could be challenging due to changing conditions inside a cell and differences in the microstructure. The DRT analysis shows that the polarisation process of SRB25P does not scale proportionally to the planar configuration, implying the influence of microstructure, design and gas condition on the cell's operation (Figure 5-42 b). The comparison shows an enlargement of P4 while the other contribution decreased considerably; especially P1 and P2 decreased, which are known to be highly dependent on microstructure. The polarisation distribution is different from the planar cell, where P4 was relatively small and P3 was dominant. As explained, the P4 process is sensitive to gas concentration; likely, the process is enlarged in the SOFCRoll configuration due to more significant diffusion losses on one of the electrodes.

The current generated from SRB25P indicates that not much more than 4 cm^2 of the electrode's surface area is utilised effectively. Comparing the SRB25P cell directly to the planar cell, at 0.7 V at 800 °C before switching, about three times more current was generated in SOFCRoll, which was 0.15A and 0.055 A/ cm^{2,} respectively; the increase is low, taking into account the size of SOFCRoll electrodes. The ohmic resistance was reduced about four times (2 Ω in planar cell and 0.5 Ω in SRB25P) while total polarisation resistance by a factor of two (5.9 Ω in planar cell and 2.8 Ω in SRB25P).

The total surface area of the electrodes was 27.75 cm^2, consisting of the spiral part, about 18.75 cm^2, and the channel region of about 9 cm^2, which was entirely covered with silver paste (Figure 5-39). The SRB25P cell was produced with LCNT/YSZ50 only. This configuration most likely did not give an optimal use of cells surface area, as the 25 mm in the distance of LCNT/YSZ50 sandwiched between other layers does not have any current collector, and as indicated (Figure 5-18 a) and in the analysis of planar cell (Chapter 5.5.3.3), the conductivity of the LCNT/YSZ50 material is low. In the best case, assuming that LSM current collector can conduct electrons for a distance of 10 mm, the cell's active area would be equal to the area of the fuel channel, which is about 9 cm^2. However, as already explained, the most active region is where the cell is covered with silver from both sides, between the oxygen and fuel channels, region (3) in Figure 5-39, which is 3.75 cm^2. Region (3) also has the lowest diffusion losses. The remaining area of the channel at the FE side (5.25 cm^2), region (2), is covered with silver; however, on the OE side, the area is inside the channel; therefore, the current distribution is dependent on LSM current collector layer, and the concentration of oxygen gas will be lower further into a spiral due to diffusion loses. The impedance in SOFCRoll will be affected by the inhomogeneity of the system, e.g. local impedance at region (3) will be different from the region (2), which will be more altered by oxygen diffusion and lower efficiency of current collecting.

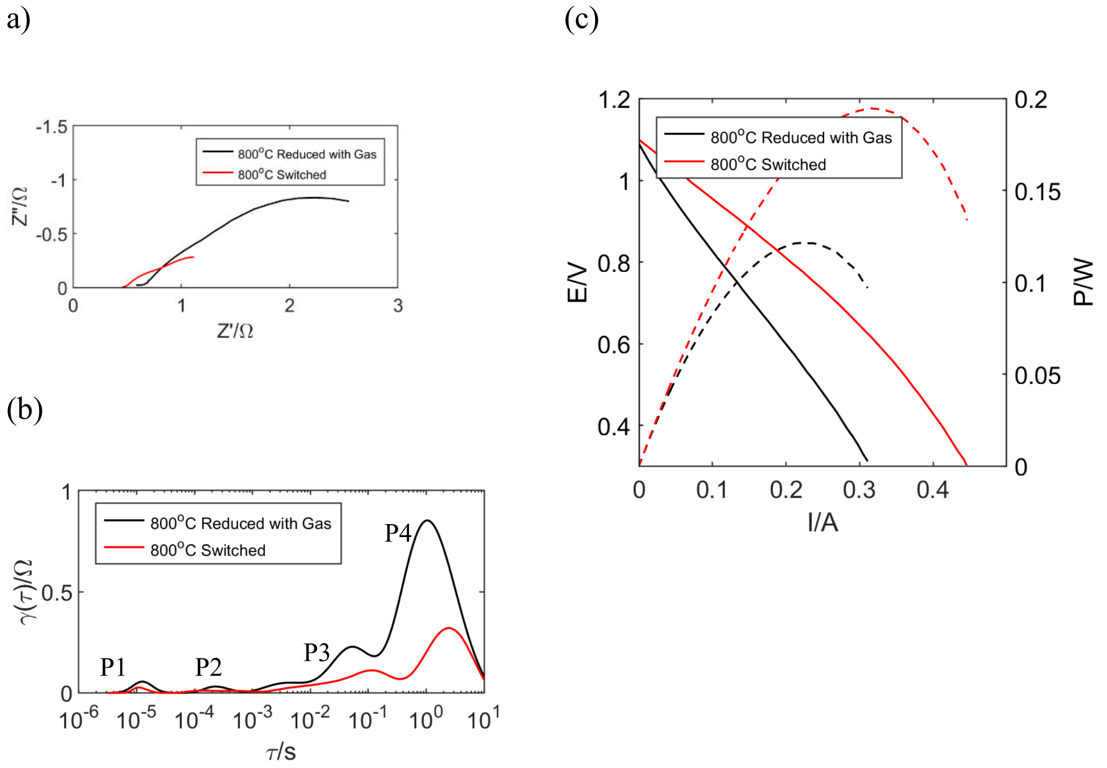

Figure 5-43: Electrochemical analysis of SRB25P, before and after switching at 2.3V for 10 min at 800 °C and 50 ml/min of wet H_2 in FE and 100 ml/min of air in OE (a) EIS at the OCV. (b) DRT calculated from impedance data. (c) IV characteristic.

Figure 5-43 a-b shows the impedance analysis at OCV of the cell before and after the switching procedure; all resistive contribution seems to be reduced and moved to the lower frequency; the equivalent circuit indicates an increase of their capacitance. The behaviour is different from planar cells, where all processes move to a higher frequency. Also, in SRB25P, the P4 process seems to be reduced to a much greater extent than any previously described process in planar cells.

Figure 5-43 c shows the I-V characteristic of the cell after the gas reduction and switching procedure, tested at 700-800 °C and 50 ml/min of wet H_2 in FE and 100 ml/min of air in OE. After applying electrochemical poling at 2.3V for 10 min, the power density increased from 121.5 mW to 195 mW at 800 °C. The linear slope of I-V curves changes below 0.75V, indicating concentration losses at a higher current or decrease of electrode activity, e.g. due to higher oxygen partial pressure. The switching potential was changed from 2.3V to 2.1V in the following tests, as SEM analysis indicated possible decomposition of material under high overpotential and mentioned the already “rough” surface of perovskite, which may be detrimental to the electrode’s functionality (Figure 5-44). Initially, the switching procedure was changed from 2.3V for 10 min to 2.1V; then switching time was further reduced to 2 min. Some tests were conducted to compare those conditions, and not much difference in performance was observed. The cells switched at 2.3V had slightly higher performance, caused by a higher reduction of ohmic resistance.

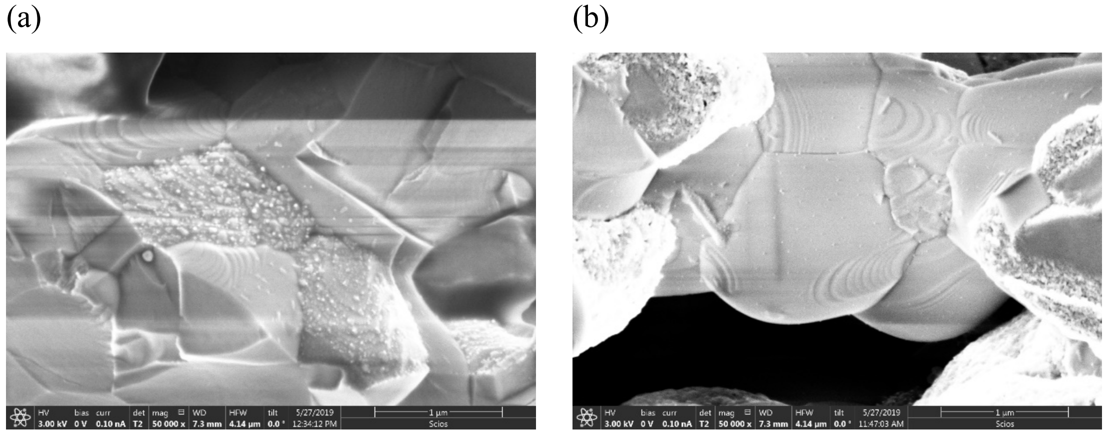

Figure 5-44: (a)-(b) SEM (SEI) of LCNT/YSZ50 layer in a SOFCRoll SRB25P after electrochemical switching at 2.3V for 10 min at 800 °C.

5.5.4.2 The SRB26P SOFCRoll with Ni/LCNT50 fuel electrode current collector.

SOFCRoll SRB26P was made with the same tapes and dimensions, but additionally, a current collector Ni/LCNT50 layer was sintered on top of the fuel electrode; also, SRB26P had a thinner electrolyte (140 against 180 µm).

The use of Ni/LCNT50 current collector layer on top of LCNT/YSZ50 aimed to increase the working cells are to the spiral region of the cell, e.g. regions (1), (4) and (5) in Figures 5-39 c-d. It is commonly considered that the active cell area does not exceed 20 µm from YSZ/electrode interface [99]. However, the possibility that the performance of the active electrode would be affected by co-sintering with a layer of high Ni content cannot be ruled out [323]; this could be related to the diffusion of Ni from the current collector layer to the active region.

The SRB26P was tested at 700-800 °C and 50 ml/min of wet H_2 in FE and 100 ml/min of air in OE. After gas reduction, the cell generated 0.36 A at 0.7 V at 800°C, more than six times more than the planar cell (0.055A/ cm2) and two times more than the SOFCRoll SRB25P (0.15A).

As previously, the total surface area of the electrodes was 27.75 cm^2, consisting of the spiral part, about 18.75 cm^2, and the channel region of about 9 cm^2, which was entirely covered with silver paste (Figure 5-39). The SRB26P cell was produced with Ni/LCNT/50 current collector layer where the 25 mm in its distance was sandwiched between other layers; it is the maximum distance for gas diffusion and conductivity at the fuel electrode side. The oxygen site has the same configuration as in SRB25P, with the LSM current collector layers in (1), (2), (5) and additionally covered with silver paste in the region (3) and (4). As previously, region (3) with a surface area of 3.75 cm^2 is considered the most active and, according to the model cell, has the same activity level as SRB25P. Similarly, region (2) with 5.25 cm^2 will have the same activity level, as in both cases, this part of the cell was covered with a current collector on the fuel site and had LSM current collector on the OE side. The activity region will likely be extended into the area (4), which also has 5.25 cm2; in SRB25P, due to the lack of a current collector on the FE side, the region was considered entirely inactive even though the OE side is covered with silver paste. The regions (1) and (5) could also become active; however, as already explained, even if the cell did not have any internal defects, the long diffusion and current collector paths can significantly affect their performance.

Figure 5-45 a-b shows the impedance analysis at OCV of the cell before and after the switching procedure; as previously, all resistive contribution seems to be reduced. Before switching, the maximum power density of SRB26P at 800 °C was equal to 290 mW at 800 °C and increased to 450 mW after applying the switching method at 2.1V for 10 min. In the first experiment, SRB26P was switched at 2.3V for 10 min as SRB25P; however, subsequent tests with tubular cells and other tests made on SRB26P showed no higher performance gain when switching at 2.3V compared to 2.1V. Therefore, the switching voltage was decreased as it could be less damaging to the cell structure. The SEM analysis of the LCNT/YSZ50 layer in SRB26P after electrochemical switching shows in Figure 5-46. The perovskite seems to retain its terrace-like microstructure, and metallic particles are more homogeneous in shape and size; however, there are areas on LCNT/YSZ50 on which the particles have not emerged; likely indicating the various distribution of overpotential within the fuel electrode; which is considered to be a driving force for exsolution.

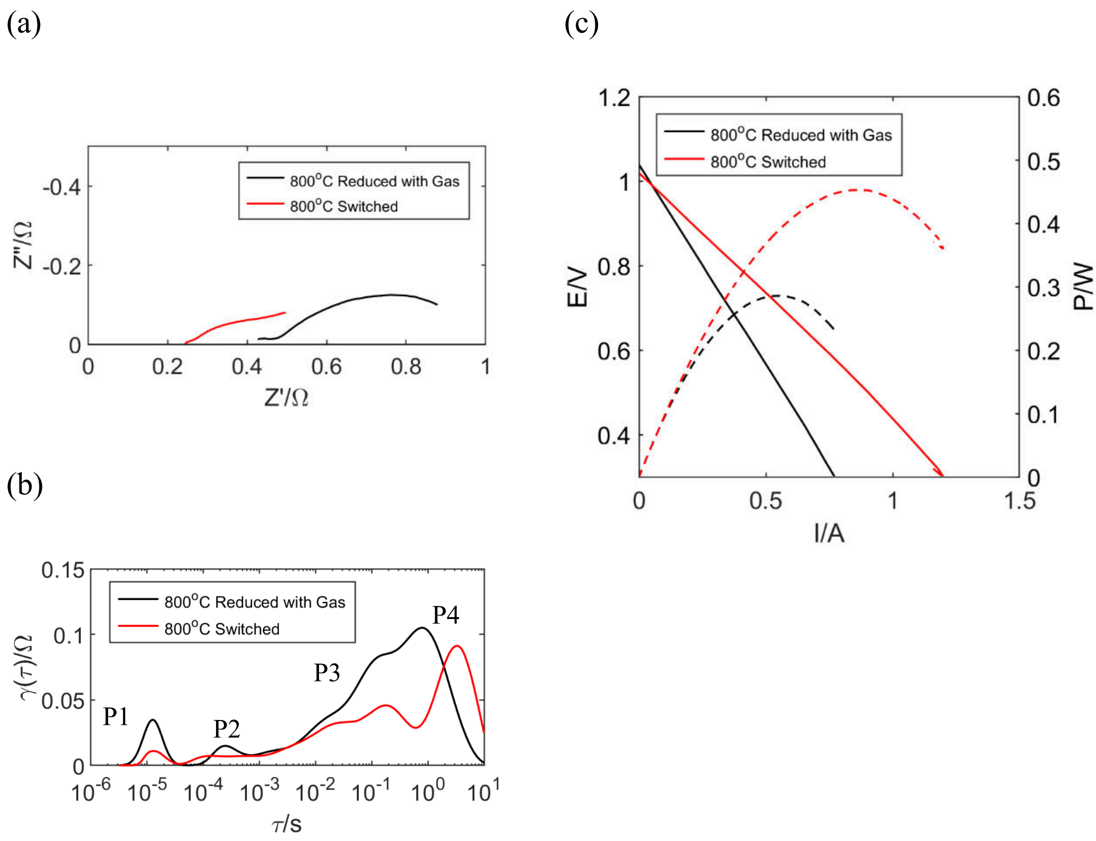

Figure 5-45: Impedance analysis of SRB26P, before and after switching at 2.1V for 10 min at 800 °C and 50 ml/min of wet H_2 in FE and 100 ml/min of air in OE. (a) EIS at the OCV. (b) DRT calculated from impedance data. (c) IV characteristic.

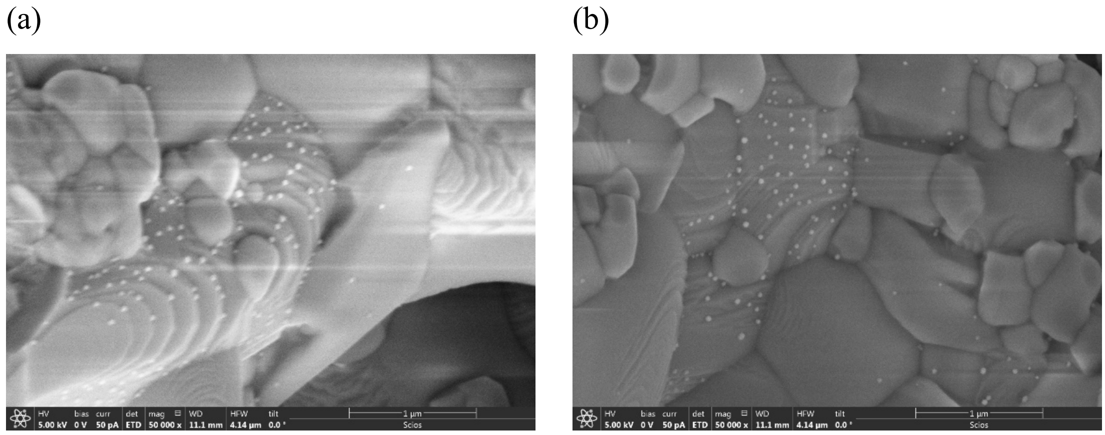

Figure 5-46: (a)-(b) SEM (SEI) of LCNT/YSZ50 layer in a SOFCRoll SRB26P after electrochemical switching at 2.1V for 10 min.

Figure 5-47 shows a comparison between a planar cell (normalised to cm^2) and both discussed types of SOFCRoll after gas reduction. Compared to the planar cell, the ohmic resistance in SRB26P was reduced 4.3 times, while the polarisation resistance 12.7. Comparing the SRB26P and a planar cell, the P4 is enlarged in relation to P3, similarly like in SRB25P; however, not to such an extent.

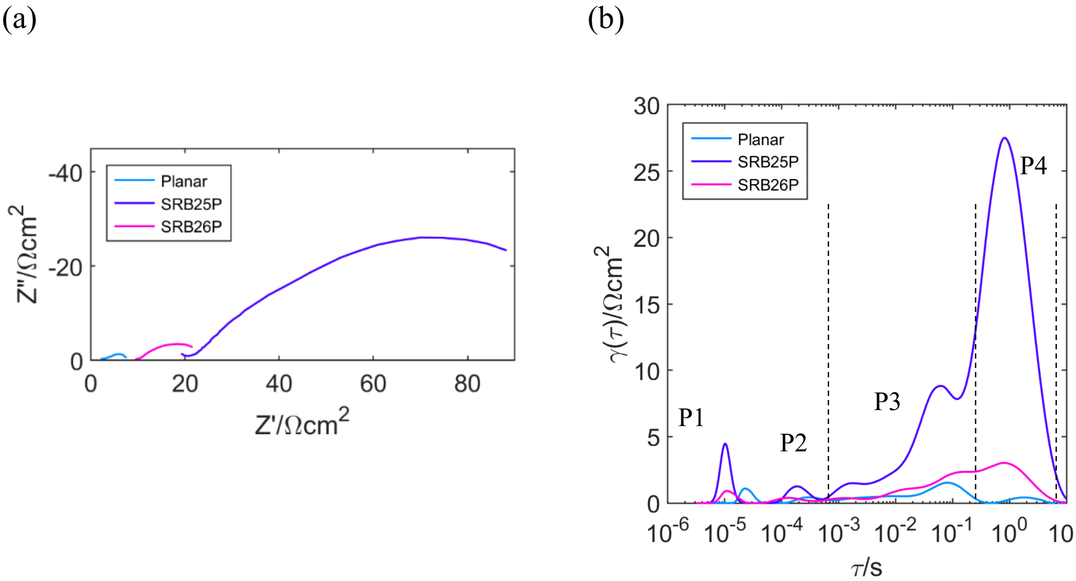

Figure 5-47: The comparison of the planar cell, SOFCRoll SRB25P and SRB26P (normalised to cm^2), at 800 °C and 50 ml/min of wet H_2 in FE and air in OE. (a) EIS. (b) DRT calculated from impedance data.

Figure 5-48 shows the electrochemical performance of the SRB26P SOFCRoll cell at a temperature range from 700 – 800 °C and 50 ml/min of wet H_2 in FE and 100 ml/min of air in OE; after switching at 2.1V for 10 min at 800 °C. The open-circuit voltage of SRB26P was above 1V at the whole temperature range, confirming a good tightness. After switching, the cell's maximum power density was equal to 208, 302 and 450 mW at 700, 750, 800 °C, respectively.

The DRT was constructed from imaginatory part of impedance (Figure 5-48 d), where all four processes are indicated. A similar equivalent circuit was used as in SRB25P, but P1 and P2 were fitted as a single semicircle; they were too small to fit separately. The accuracy of the fitting was confirmed by calculating the resistance of polarisation processes directly from DRT. Figure 5-48 b shows the Arrhenius Plot of ohmic resistance of cell's polarisation resistance, calculated from the equivalent circuit. After the rig's resistance was extracted, the cell's ohmic resistance was in the range of 0.15 - 0.31 at 800

– 700 °C. The total polarisation resistance at OCV increases from 0.39 Ω at 800 °C to 0.88 Ω at 700 °C. P3 and P4 contribute similarly to the polarisation resistance with a very close value of about 0.15 Ω each at 800 °C and activation energy of 0.7 eV. The activation of the P3 and P4 processes seems to be lower than in the planar cell, while the activation energy of ohmic resistance slightly increased.

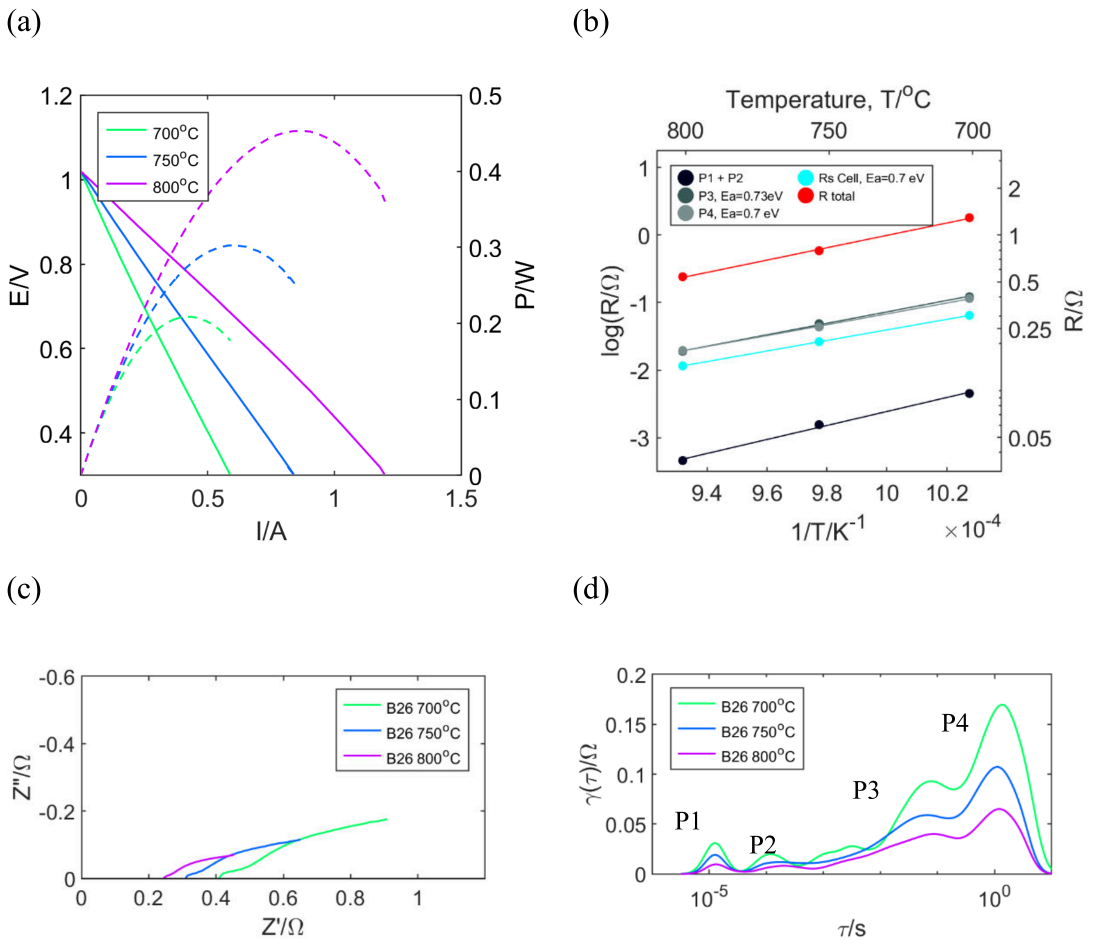

Figure 5-48: The electrochemical performance of the SRB26P SOFCRoll cell at a temperature range from 700 – 800 °C and 50 ml/min of wet H_2 in FE and 100 ml/min of air in OE; after switching at 2.1V for 10 min at 800 °C. (a) I-V curve of cell operating in fuel cell mode. (b) Arrhenius plot of ohmic and polarisation resistance. (c) – (d) EIS and DRT analysis of impedance data at OCV conditions.

5.5.5 The small SOFCRoll with LCNT based fuel electrode (SRB30P & SRB36P)

5.5.5.1 The small SRB30P SOFCRoll with implemented Ni/LCNT50 current collector.

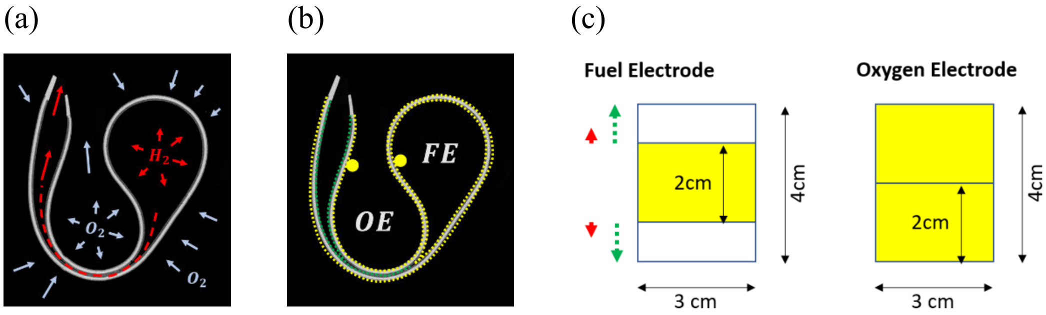

Figure 5-49: Small SOFCRoll cell (a) – (b) The current and diffusion paths in small SOFCRoll; Yellow – silver CC, Green – conductivity path FE, Red – diffusion path FE. Blue – diffusion path OE. (c) Electrode dimension, diffusion and charge paths and location of the silver current collector in small cells.

In the SRB30P cell, the total surface area of the electrodes is 12 cm^2, about 2.3 times lower than in SRB25P and SRB26P. The small SOFCRoll cells had an "exposed oxygen electrode" design; tapes were shortened to the point that the whole surface area of the oxygen electrode was exposed to the atmospheric air. Therefore, the current collector layer made of pure LSM was not needed; only LSM/YSZ50 active electrode was used, which was entirely covered with the silver paste, allowing for full utilisation of its surface area. The whole area of the LSM/YSZ50 was exposed to atmospheric air, which was used for the cell operation; additionally, the air was blown through the main channel from the bottom of the cell to assure faster oxygen exchange with the atmosphere, the main channel at the OE side was not sealed; hence the pumped air outlet was on the top of the cell (Figure 5-50 a & c). SRB30P cell had the active fuel electrode LCNT/YSZ50 and a Ni/LCNT50 current collector layer, the same as in SRB26P. The spiral part on the fuel side was lowered to 1 cm; hence, it reduced the current collector distance. The diffusion path of H_2 through the porous layer of the current collector was even lower than 1 cm as electrode layers are not adjacent near the outlet (Figure 5-49 a). The area of the "Spiral" was about 6 cm^{2,} and an equal area was in the "Channel." SRB30P had almost the same electrolyte thickness as SRB26P (between 130 and 140 µm).

As mentioned earlier, cell performance and OCV were improved when tested with channels at the bottom; this issue was further investigated. The comparison of SRB30P cells with various configurations of the outlet channel illustrate in the figure below.

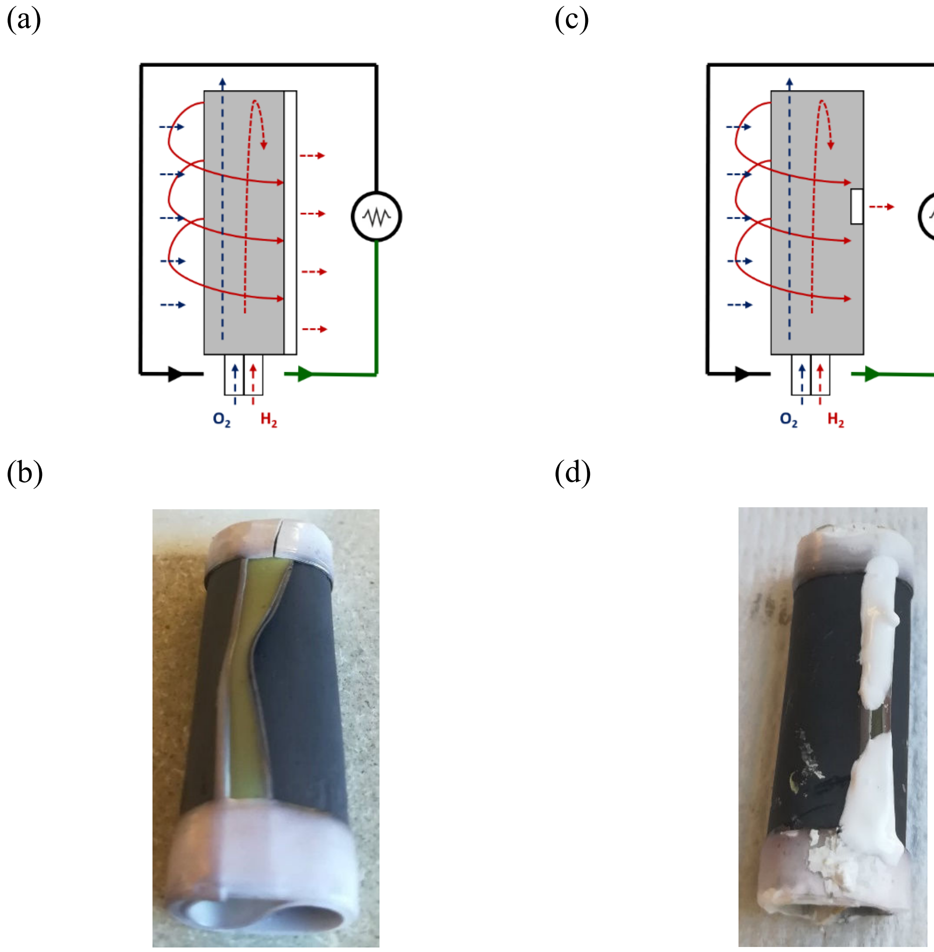

Figure 5-50: (a)-(b) Principle of operation and image of the cell with the large gas outlet. (c)-(d) Principle of operation and image of the cell with the small outlet.

The cell's performance with the large outlet at the side, where the H_2 gas was directed to the spiral part and outside through the outlet at the middle cell's area ("B30 – large channel" in Figure 5-51 a), was multiple times lower than when channels were at the bottom ("B30 – bottom channels" in Figure 5-51 a) or when the size of the channel was decreased ("B30 – small channel" in Figure 5-51 a).

Also, when testing the cell with a large channel at higher H_2 flow, the cell's OCV decreased; in the shown case (Figure 5-51 b), the highest OCV was achieved for an H_2 flow rate much below 50 ml/min in FE. First, the drop in OCV originated from the microcracks in the spiral part. Therefore, a tentative explanation for higher OCV at lower flow was that the spiral part is “less pressurised” by the gasses; hence they do not leak via the microcracks. Similarly, the performance improvement could be explained in the bottom channel design; the spiral part is under lower gas pressure hence does not leak.

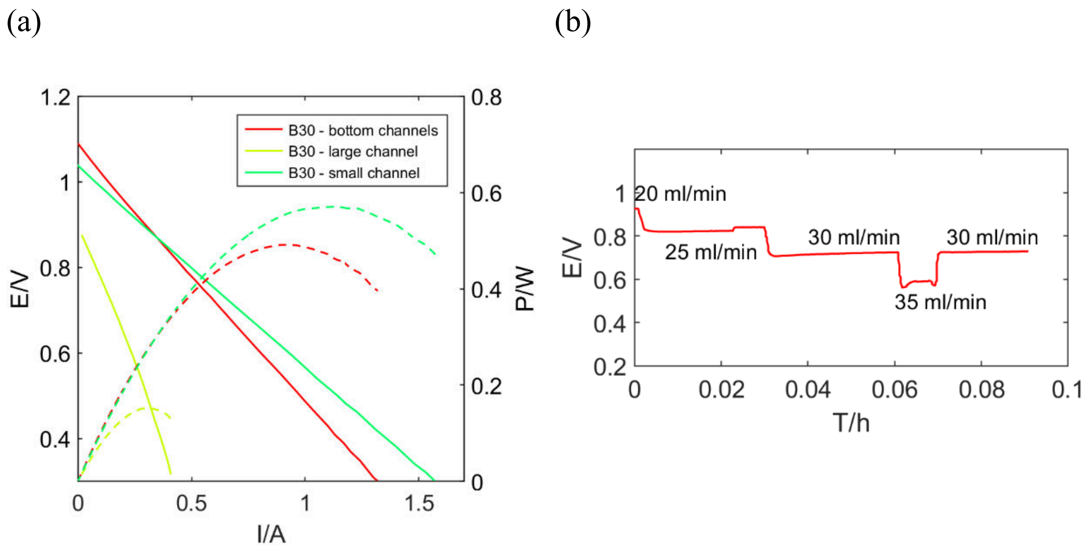

Figure 5-51: (a) Comparison of SRB30P cells I-V with the various design of the gas outlet. (b) OCV of cell with the large gas outlet at the cell’s central area at the various flow of wet H_2 in FE and atmospheric air in OE.

However, in the SRB30P cells, not many defects were detected; therefore, this explanation did not entirely work out. A breakthrough has come with using a smaller gas outlet at the cell’s outer area (most of the outlet was sealed, as shown in Figure 5-50 d). By decreasing its size, a much higher OCV value was achieved with a higher flow of H_2, and the amount of generated current increased several times (“B30 – small channel” in Figure 5-51 a). The improved performance suggests that not only the internal defects were responsible for lower performance but also the size of the outlet, indicating that the counter diffusion of the air into a cell through an outlet channel may be a reason.

Further on, the possibility of co-sintering the outlet channel into the cell’s structure was studied (Figure 5-52). The outlet channel made of YSZ tape was successfully implemented into the design. For the preparation, a piece of YSZ tape was rolled into a small tube and sealed with a YSZ slurry on the end of the cell’s spiral; the outlet along the cell was entirely sealed. The presented cell successfully operated at high OCV (1V at 800°C) and high H_2 flow up to 40 ml/min. The maximum power at 800°C was 0.26W.

However, the part of the tested cell seems to show a similar problem as in the original design. Most likely, the size of the co-sintered outlet channel was too large; hence diffusion from outside still was an issue.

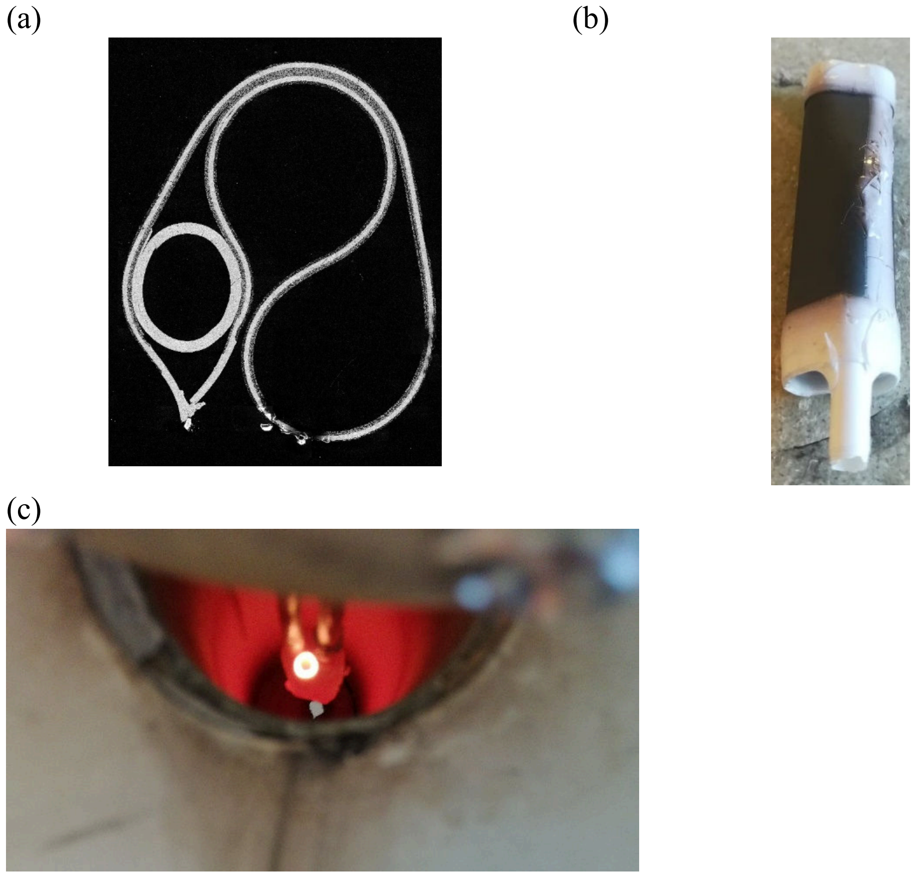

Figure 5-52: Cell design with co-sintered outlet channel. (a) Cross-section of the cell. (b) Cell's Image. (c) The image of the cell's operation.

In Figure 5-52 c, it could be seen that all exhausted gasses are directed outside through a co-sintered outlet, actually providing the first proof ever that gases in SOFCRoll could diffuse through a spiral to the outlet. Perhaps such a design opens a new possibility of using SOFCRoll cells, e.g., in an application where gas collection is required, like an electrolysis cell.

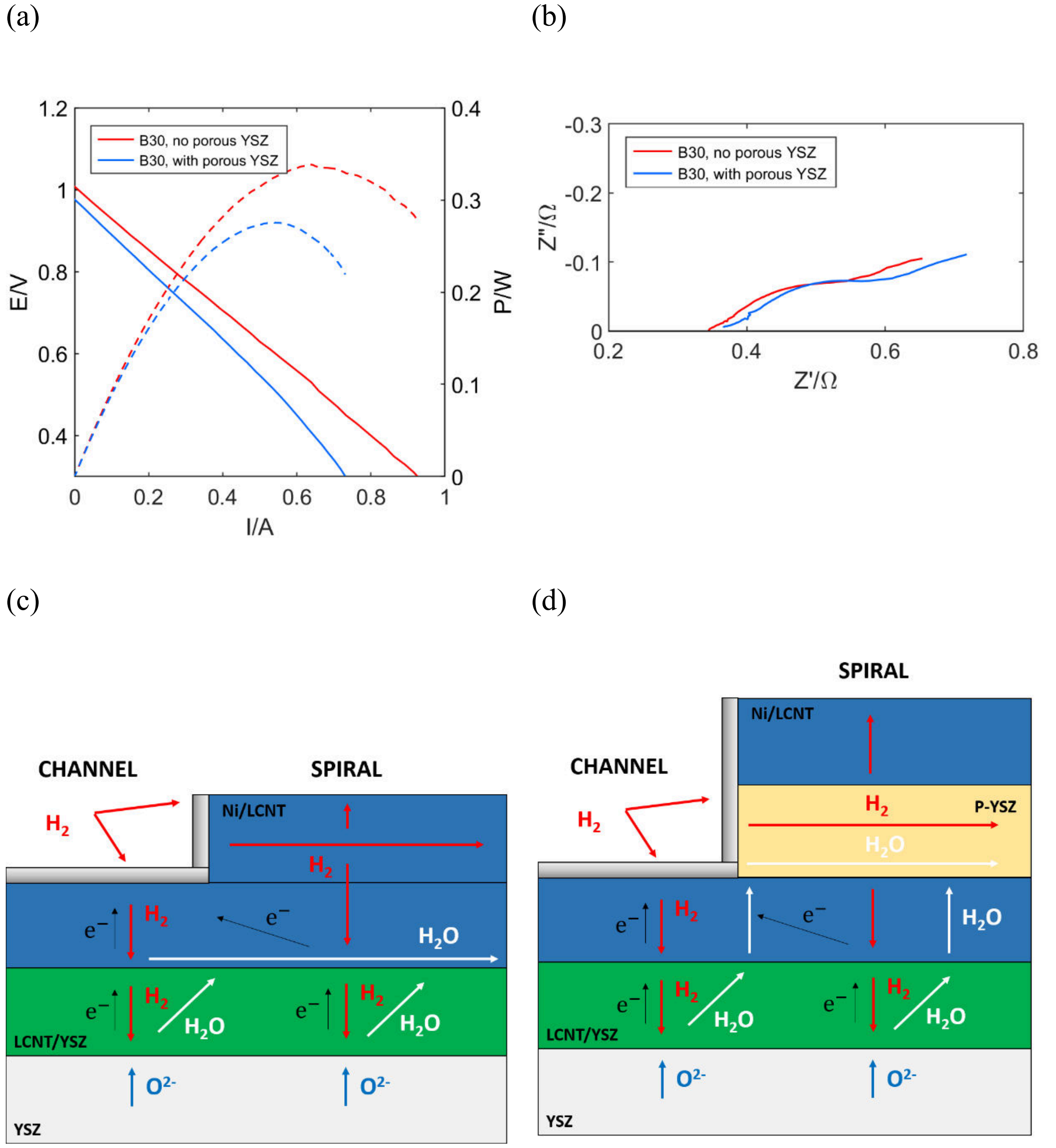

Figure 5-53: Comparison of cells performance, with and without porous (P-YSZ) layer at 800 °C and 25 ml/min of wet H_2 in FE and atmospheric air in OE; after switching at 2.1V for 10 min at 800 °C. (a) I-V characteristic. (b) EIS analysis. Patch for gas/ charge transfer (c) in the cell without a porous layer. (d) in the cell with a porous layer.

Two types of SRB30P cells were produced (SRB30P1 and SRB30P2). In the SRB30P2, the additional porous YSZ layer (P-YSZ) with 90% porosity was used in the spiral part of the fuel electrode to study if the cell could achieve better and more stable performance when decreasing diffusion losses at the fuel electrode side in the spiral. Both cells were sealed at the bottom and had a small outlet at the central part (Figure 5-50 d).

The addition of a porous layer did not improve the cell's functionality; in fact, the cell with P-YSZ had about 30% lower maximum power (0.39W in SRB30P1 and 0.26W in SRB30P2) at 800°C and 25 ml/min of wet H_2 in FE and atmospheric air in OE; after switching at 2.1V for 10 min at 800 °C. The I-V curve of SRB30P2 seems to have a slightly higher slope than SRB30P1, indicating higher ASR. Also, SRB30P2 had a lower OCV value; this may be due to cracks inside a cell, which are more likely to form in the cell with P-YSZ due to higher stress (Chapter 5.4). The lower value of OCV could also result from a variation in the size of the outlet, made by ceramic sealant applied by hand.

The I-V curve of SRB30P2 also shows some possible concentration losses at higher potential, contrary o expectations as the porous layer should improve gas diffusion into a spiral. Possibly P-YSZ worsened diffusion to the active layer or due to the cracks gases from both compartments mixed hence lower concentration. The EIS curves are very similar in shape and magnitude at OCV. The impedance was fitted with an equivalent circuit made of three semicircles. A closer investigation reveals the increase of all polarisation processes in SRB30P2, indicating that the leading cause of the lower performance in this cell is the reduction of utilized surface area. Perhaps, a crack in the cell or counter diffusion of air made a small part of the cell inactive.

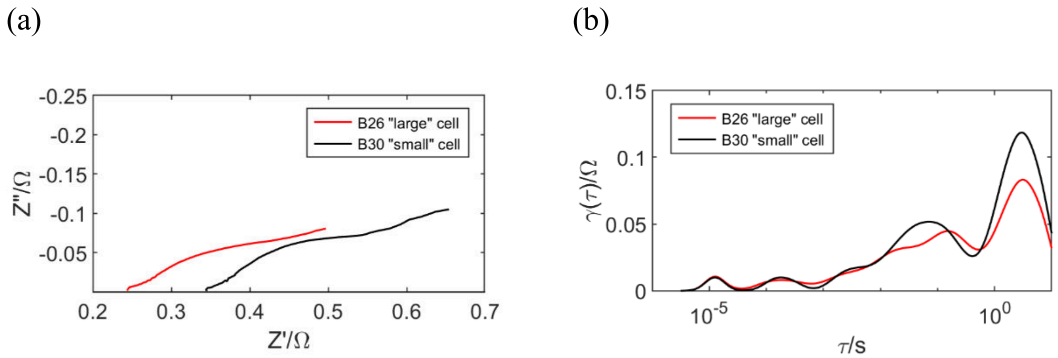

Figure 5-54: Comparison of cells performance from the bath SRB26P (the large cell) and SRB30P (the small cell) at 800°C after electrochemical switching (SRB26P at 2.1V for 10min, SRB30P at 2.1V for 2.5 min), tested with wet H_2 in FE and air in OE. (a) EIS. (b) DRT from impedance data.

Figure 5-54 compares the electrochemical measurements of the SRB30P1 and previously described SRB26P. The SRB30P1 did not have an additional porous layer, and essentially it is the smaller version of SRB26P. The cell was switched at the same potential, 2.1V, but for a shorter time – only 2.5 min. Conducted analysis on the same cells indicated almost no difference in performance when switching for 2.5 min or 10 min at the same voltage and temperature; thus, conditions were changed.

After switching, the maximum generated power at 800 °C was 0.35W for SRB30P and 0.45 W for SRB26P. The relatively low difference in generated power reveals that a large part of SRB26P had a low activity or was not active at all (the total surface area was 27.75 cm^2 in SRB26P and 12 cm^2 in SRB30P). Following the previous consideration, the most likely is that regions (2), (3), (4) which would give 14.25 cm^2 of surface area, are the most active regions in SRB26P, and the most of outer regions are not active; from the other side, this assessment indicates that most of the small cell's surface area is electrochemically active.

Comparison of impedance data reveals the same processes in both cells varying in magnitude. The ohmic resistance of the SRB30P was 0.24 Ω against 0.15 Ω in SRB26P (after extraction of 0.1 Ω of rig's resistance), which gives a ratio of about 1.6. The total polarisation resistance of the SRB30P was 0.4 Ω against 0.3 Ω in SRB26P, which gives a ratio of about 1.3.

The temperature dependence of the SRB30P1 shows in Figure 5-55. The cell was tested with 25 ml/min of gas flow with wet H_2. The open-circuit voltage was around 1V at a temperature range from 700 – 800 °C. Before switching, the cell's power density was equal to 150 mW at 800 °C and increased to 340 mW after applying the switching method at 2.1V for 2.5 min. The same equivalent circuit was used as four SRB26P, with P1 and P2 fitted as the single semicircle. Figure 5-55 b shows the Arrhenius Plot of ohmic resistance of cell's polarisation resistance, calculated from the equivalent circuit. After extraction of the rig's resistance, the cell's ohmic resistance was 0.24 - 0.46 Ω at 800 – 700 °C, while the total polarisation resistance at OCV was between 0.42 and 1.11 Ω. The P3 had an activation energy of 0.95 eV, slightly larger than 0.73 eV in SRB26P, the characteristic frequency of the process was 2.75 Hz at 800 °C in both cells. The P4 has an activation energy of 0.65 eV and a characteristic frequency of 0.15 Hz at 800 °C.

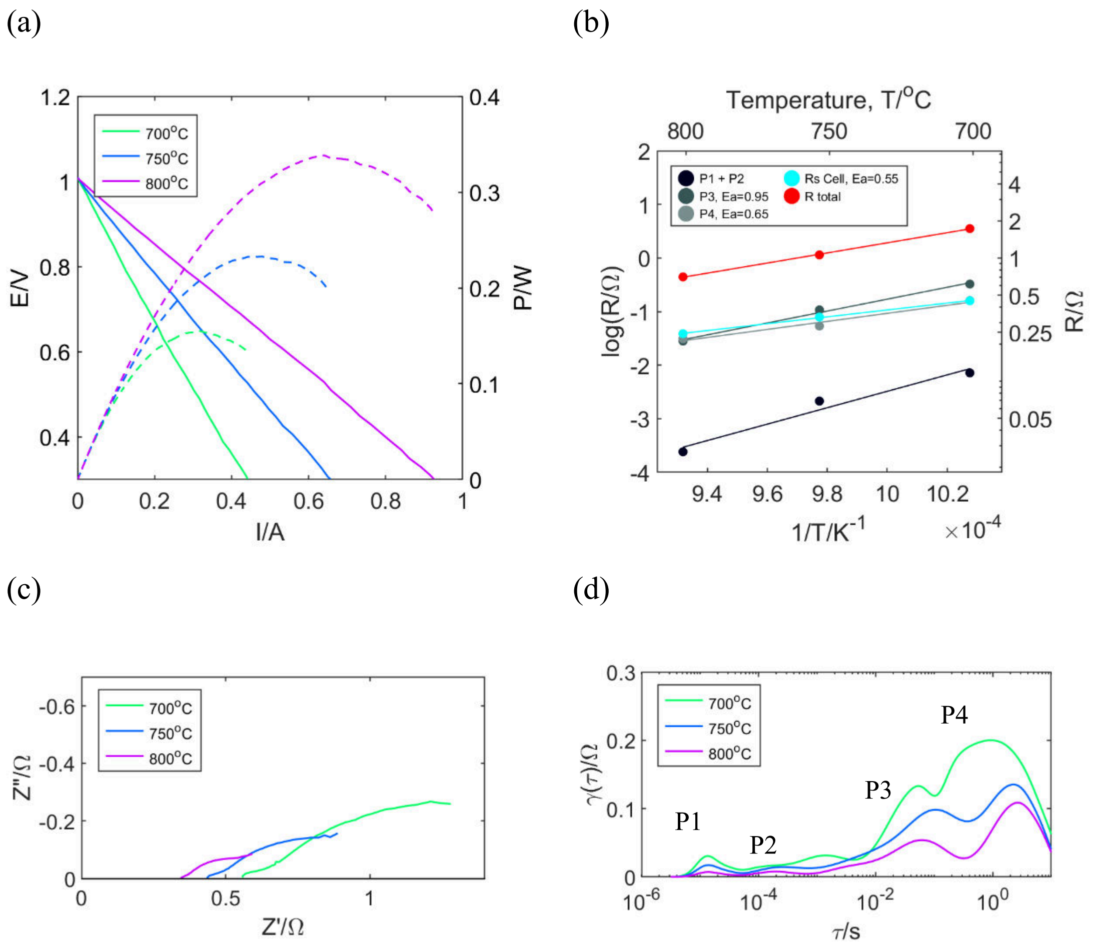

Figure 5-55: The electrochemical performance of the SRB30P1 SOFCRoll cell at a temperature range from 700 – 800 °C and 25 ml/min of wet H_2 in FE and atmospheric air in OE; after switching at 2.1V for 2.5 min at 800 °C.. (a) I-V curve of cell operating in fuel cell mode. (b) Arrhenius plot of ohmic and polarisation resistance. (c) – (d) EIS and DRT analysis of impedance data at OCV conditions.

Figure 5-56 shows SEM (SEI) of LCNT/YSZ50 electrode after electrochemical switching. The co-sintered electrode robustly interfaces with the YSZ electrolyte without cracks or delamination, Figure 5-56 a. The lower magnification (Figure 5-56 b) reveals a structure made of particles with a large size distribution, where very small LCNT particles could be visible, produced with long ball-milling times. Exsolved metallic particles have are between several and few nanometres; very small particles could be visible in Figure 5-56 c. As previously mentioned, larger islands exsolved from the perovskite in some locations, which are believed to be TiO_2 (Figure 5-56 d).

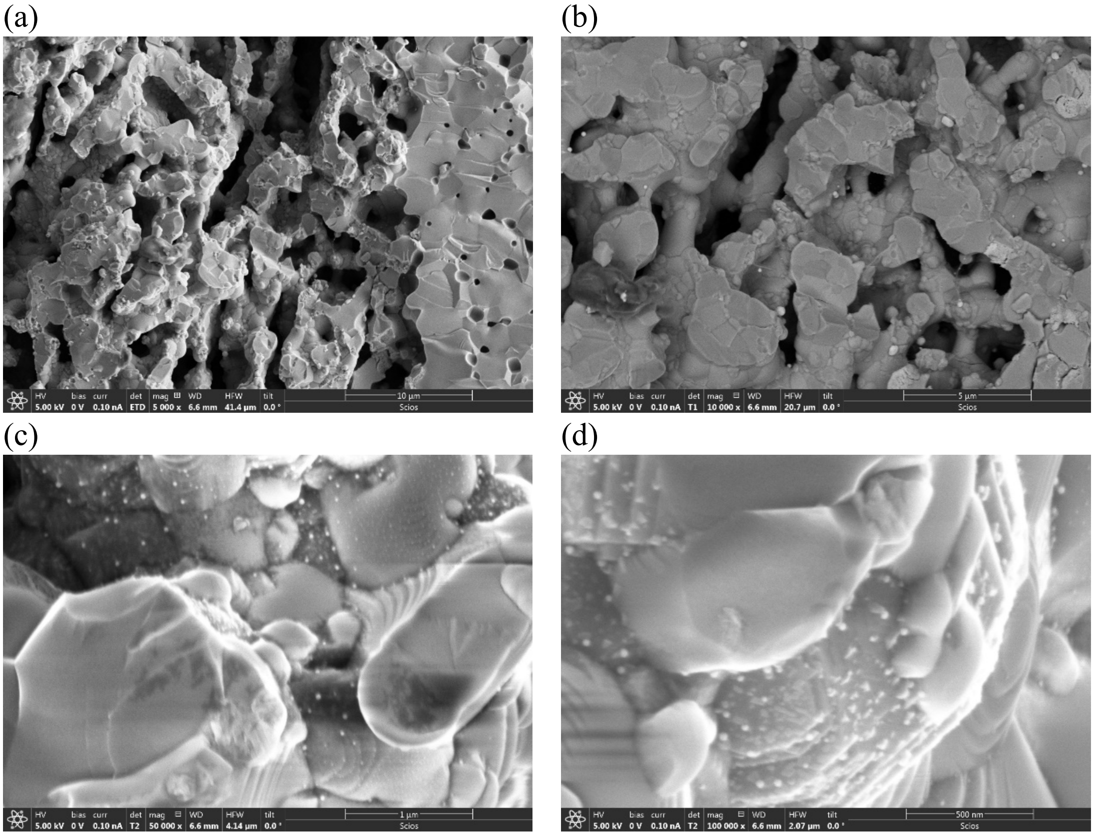

Figure 5-56: SEM (SEI) analysis of LCNT/YSZ50 layer in a SOFCRoll SRB30P after electrochemical switching at 2.1V for 2.5 min. (a) The interface of active FE with YSZ electrolyte. (b) Image of the active FE layer in ×10k magnification. (c) Image of the active FE layer in ×50k magnification. (d) Image of the active FE layer in ×100k magnification.

5.5.5.2 The small SRB36P SOFCRoll with Ni/YSZ10fuel electrode current collector.

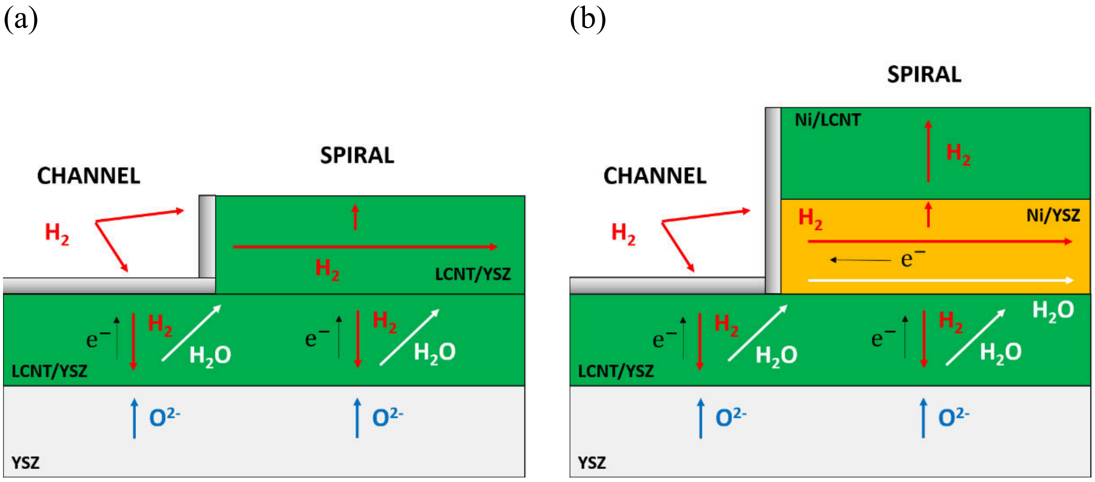

Figure 5-57: The principle of operation of the SRB36 SOFCRoll Cell. (a) With the active LCNT/YSZ50 active FE layer (SRB36P1). (b) With the active LCNT/YSZ50 layer and Ni/YSZ10 current collector (SRB36P2).

Like SRB30P, the SRB36P cells had 12 cm^2 of total surface area in an “exposed oxygen electrode” design (Figure 5-49), where the LSM/YSZ50 active layer was used, entirely covered with a current silver collector and exposed to atmospheric air. The first type of SRB36 (SRB36P1) did not have any current collector layer on the fuel side, only an LCNT/YSZ50 active electrode (Figure 5-57 a). Therefore, only the area covered with silver paste was likely active, up to 6 cm^2 in the “Channel”. The second type of SRB36 (SRB36P2) had a Ni/YSZ10 current collector layer in the spiral part of the cell only (Figure 5-57 b). The cells comparison can reveal if the spiral part is active.

As explained in Chapter 5.4, co-sintering of the Ni/YSZ10 layer on the entire LCNT/YSZ50 active layer area was impossible due to delamination, which eventually destroyed the cell’s internal, when Ni/YSZ10 was co-sintered only in the spiral part, sandwiched between other layers was less prone to delamination. The current collector layer is not required at the central area of the fuel electrode, as this is available for the current collector, which could be applied before cell’s testing, e.g. silver paste. In SRB36P2, the function of the Ni/YSZ10 current collector layer is to collect the current from the spiral part and transport it to the main channel of the cell to the silver current collector. The cells were sealed at the bottom, and the size of the H_2 gas outlet at the cell’s middle area was decreased with ceramic sealant.

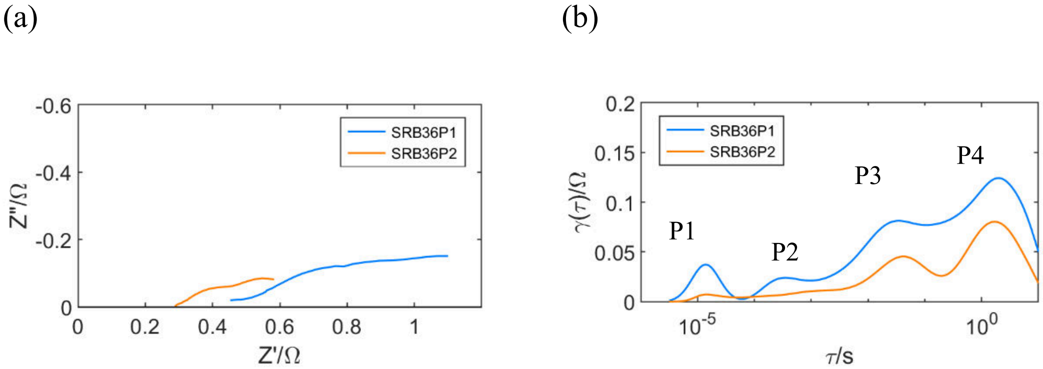

Figure 5-58: Comparison of cells impedance at OCV and 800°C from the bath SRB36P, without the current collector (SRB36P1) and with the Ni/YSZ10 current collector (SRB36P2) at an 800 °C and 25 ml/min of wet H_2 in FE and atmospheric air in OE; after switching at 2.1V for 2.5 min at 800 °C.. (a) EIS measurement. (b) DRT analysis.

Figure 5-58 compares the electrochemical measurements of the SRB36P1 without a co-sintered current collector and SRB36P2 with a co-sintered Ni/YSZ10 current collector in the spiral part, revealing the same processes in both cells varying in magnitude, indicating the differences in active surface area. The ohmic resistance of the SRB36P1 was 0.26 Ω against 0.18 Ω in SRB36P2 (after extraction of 0.1 Ω of rig's resistance), which gives a ratio of about 1.5. The total polarisation resistance of the SRB36P1 was 0.82 Ω against 0.35 Ω in SRB36P2, which gives a ratio of about 2.3. Similarly, before switching, the ohmic and polarisation resistance ratio is about 1.5. Much higher performance in SRB36P2 than in SRB36P1 proves that the spiral part of the fuel cell is active.

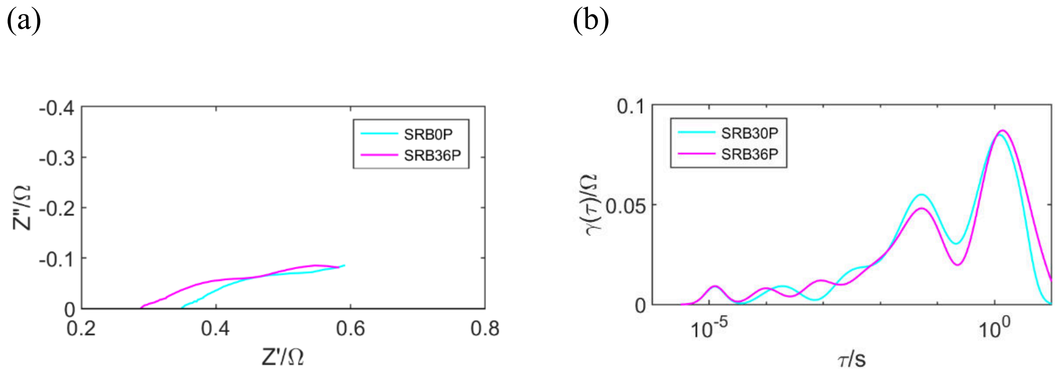

Figure 5-59: Comparison of cells impedance at OCV and 800 °C from the bath SRB30P with the Ni/LCNT50 co-sintered current collector and SRB36P with the Ni/YSZ10 co-sintered current collector at a temperature range from 700 – 800 °C and 25 ml/min of wet H_2 in FE and atmospheric air in OE; after switching at 2.1V for 2.5 min at 800 °C.. a) EIS measurement. (b) DRT analysis.

Before switching, the maximum power density of the SRB36P2 cell with a co-sintered Ni/YSZ10 current collector was equal to 120 mW at 800°C and increased to 320 mW after applying the switching method at 2.1V for 2.5 min. A very similar performance was obtained when compared to SRB30P2. Cells had the same dimensions and active electrodes; the only difference was the current collector layer on the fuel side. In SRB30P2, the whole area of the LCNT/YSZ50 active layer was covered with Ni/LCNT50 current collector, while in the SRB36P2, the Ni/YSZ10 current collector layer was used only in the spiral part. The comparison of impedance data reveals a very close magnitude of polarisation processes (Figure 5-59 b) and a slightly higher ohmic resistance in SRB30P, possibly due to the lower conductivity of the Ni/LCNT50 current collector layer than Ni/YSZ10, with much higher Ni content. Similar performance and impedance spectra indicate that both current collector layers mainly perform the function of the current collector, enlarging the utilised surface area and not participating in the overall reaction of H_2 oxidation.

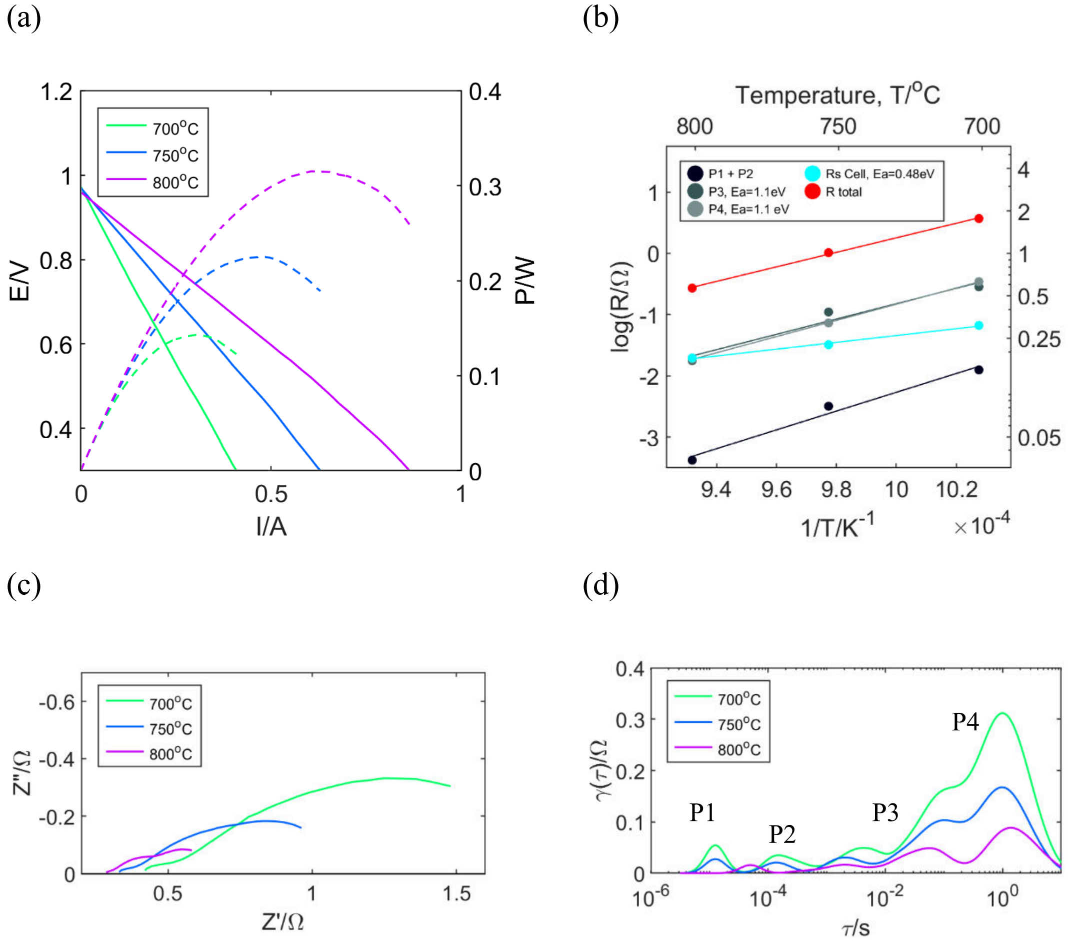

Figure 5-60: The electrochemical performance of the SRB36P2 SOFCRoll cell at a temperature range from 700 – 800 °C and 20 ml/min of wet H_2 in FE and atmospheric air in OE; after switching at 2.1V for 2.5 min at 800 °C. (a) I-V curve of cell operating in fuel cell mode. (b) Arrhenius plot of ohmic and polarisation resistance. (c) – (d) EIS and DRT analysis of impedance data at OCV conditions.

The SRB36P2 was entirely sealed for the performance test, with a small outlet on the front (Figure 5-50 d). The cell was tested with 20 ml/min of gas flow with wet H_2. The open-circuit voltage was below 1V at a temperature range from 700 – 800 °C; the lower OCV could come either from cracks or diffusion from outside through the outlet (perhaps the outlet was still too large).

The same equivalent circuit was used as four SRB30P, with P1 and P2 fitted as the single semicircle. Figure 5-60 b shows the Arrhenius Plot of ohmic resistance of cell's polarisation resistance, calculated from the equivalent circuit. After extraction of the rig's resistance, the cell's ohmic resistance was in the range of 0.18 - 0.3 Ω at 800 - 700°C, lower than in SRB30P but with a very similar activation energy of ~0.5 eV. The total polarisation resistance at OCV was between 0.38 and 1.36 Ω. The P3 had an activation energy of 1.1 eV, slightly larger than 0.95 eV in SRB30P, the characteristic frequency of the process was 3.55 Hz at 800°C. The P4 has an activation energy of 1.1 eV, larger than 0.65 eV in SRB30P, and the same characteristic frequency of 0.15 Hz at 800°C.

5.6 Summary

During the evolution of the new SOFCRoll, the electrode's shrinking profile and microstructure were controlled by the particle size and a pore former concentration. The method was very challenging because of several reasons. Firstly, when changing the particle size or concentration of pore former, both shrinking and microstructure were affected, which required controlling two parameters simultaneously. In addition, both shrinking profile and microstructure were influenced by other layers in cells assembly; thus, they behaved not the same way when analysed outside SOFCRoll's structure. In addition, changing the concentration of ceramic materials or pore former or their surface area required adjusting the organic content in the slurry. Therefore, a special procedure must be developed to prepare layers with exact shrinking and microstructure for co-sintering purposes. Finally, the procedure was developed for LCNT/YSZ material, including specific steps. In addition, for softer materials, like LSM used for the oxygen electrode, the pre-sintering as a composite with YSZ has proven to be an effective method in controlling its shrinking.

Surprisingly, the SOFCRoll could not achieve a sufficient OCV to be tested even with a matched shrinking profile. The turning point was a modification of the cell's outlet. The cells achieved a high OCV and reasonable performance. The cells were switched, which means that a high cathodic polarisation was applied on the fuel electrode to facilitate reduction and exsolution. Switching resulted in a higher current, and both ohmic resistance and polarisation on the whole frequency range were reduced. The Ni/LCNT current collector seems to extend a cell's surface area into the spiral network; however, presumably, not much more than 25% of the total 27.75 cm^2 cell's area was active; it is believed that the leading cause of low surface area utilisation was an insufficient current collection and inhomogeneous gas conditions in the long spiral part. For this reason, a

SOFCRoll design was changed entirely, and the long tapes were replaced by a shorter ones, making a total surface area equal to 12 cm^2. The silver current collector was applied to the whole area of the oxygen electrode; thus, LSM pure layer was not required, while on the fuel side, the Ni/YSZ10 current collector was co-sintered in the spiral part; such solution resulted almost in uncracked cells, and presumably, the most of the area in the cell's spiral part was active.

6 Development of tubular cells with LCNT based fuel electrode

6.1 Introduction

The final chapter of the thesis covers developing and analysing the small tubular cells with an LCNT based fuel electrode. The cell was fuel electrode supported, with LCNT/YSZ50 fuel electrode and LSM/YSZ50 oxygen electrode. The cells also were prepared by the tape casting technique; first, the lamination method was used, then co-cast, and cells were co-sintered. The same tapes were used for the first generation of tubular cells as for SOFCRoll, but without current collector layers, as in the tubular cells, the surface area was more easily accessible.

Next, the possibility of co-sintering of porous YSZ backbone and impregnating with functional materials were investigated to improve the electrode activity. First, the LSM/YSZ50 composite was replaced by impregnated LSF electrode; then LCNT/YSZ50 electrode by impregnated LCNT. With a new casting method, the thickness of the YSZ electrolyte was decreased to about 20 µm. The thickness of the electrodes was about 100 µm each. The LSF impregnated oxygen electrode developed a network of LSF nanoparticles formed on the YSZ surface. On the other side, the impregnated LCNT perovskite created a dense layer of small grains covering the whole YSZ surface.

The advantage of the second design was the possibility of co-sintering at a higher temperature than 1350 °C, producing a better-densified electrolyte. At the same time, the functional materials could be introduced at a much lower temperature. Also, it gave much higher flexibility in the selection of materials. With the method, the new electrode could be introduced without shrinking analysis and matching.

6.2 Tubular cells with LCNT/YSZ50 and LSM/YSZ50 composite electrodes

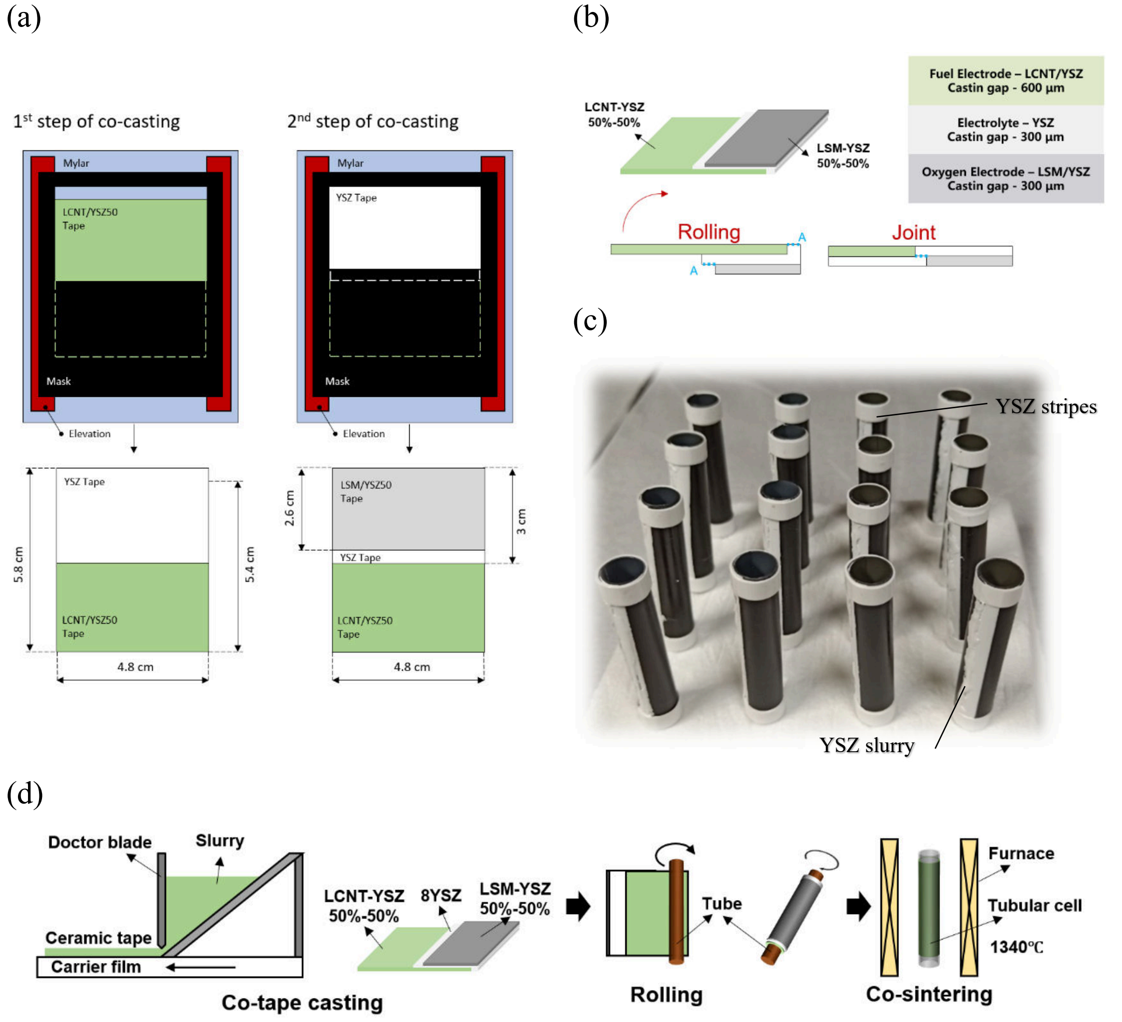

Figure 6-1: The production of small tubular cells with composite electrodes. (a) Green tapes and mask assembly for co-casting. (b) Rolling of tape's assembly, A – point of contact. (c) Photo of the tubular cells before sintering. (d) The manufacturing steps for tubular cells production, [324].

The small tubular cells with composite electrodes were produced with active layers developed for SOFCRoll. The tubular design offers a much simpler design, with more homogeneous gas conditions and more surface area available for the current collection. The tubular cells did not have co-sintered current collector layers, and tapes were not folded multiple times as in SOFCRoll; hence, the stress in the cells was significantly reduced. The standard LSM/YSZ50 was used as an oxygen electrode, LCNT/YSZ50 as the fuel electrode and YSZ electrolyte. The tape's dimensions are lower than for

SOFCRoll, which gives up to 7 cm^2 of surface area after sintering. In the tubular cells, the whole surface area of electrodes is covered with silver paint and gas diffusion is only limited by the layer's thickness. As the cells do not have a "Spiral", which in SOFCRoll took the role of support, the thickness of the fuel electrode was enlarged to provide mechanical strength to the cell.

For cell production, the thick layer of LCNT/YSZ50 was cast first with a c gap equal to 600 µm; the gap was two times higher than for layers presented so far. Also, the rolled assembly had a double layer of LCNT/YSZ50, Figure 6-1 b, which gave about 170 µm thickness after sintering and porosity of ~40%. Such thick LCNT/YSZ50 support enlarged ohmic resistance as LCNT/YSZ50 has very low electronic conductivity. There were trials to produce a tubular cell with a thin LCNT/YSZ50 and Ni/LCNT50 supporting layer, but they were unsuccessful as Ni/LCNT50 tended to delaminate. It seems that stress inside the SOFCRoll channels and the spiral prevented Ni/LCNT50 from delamination.

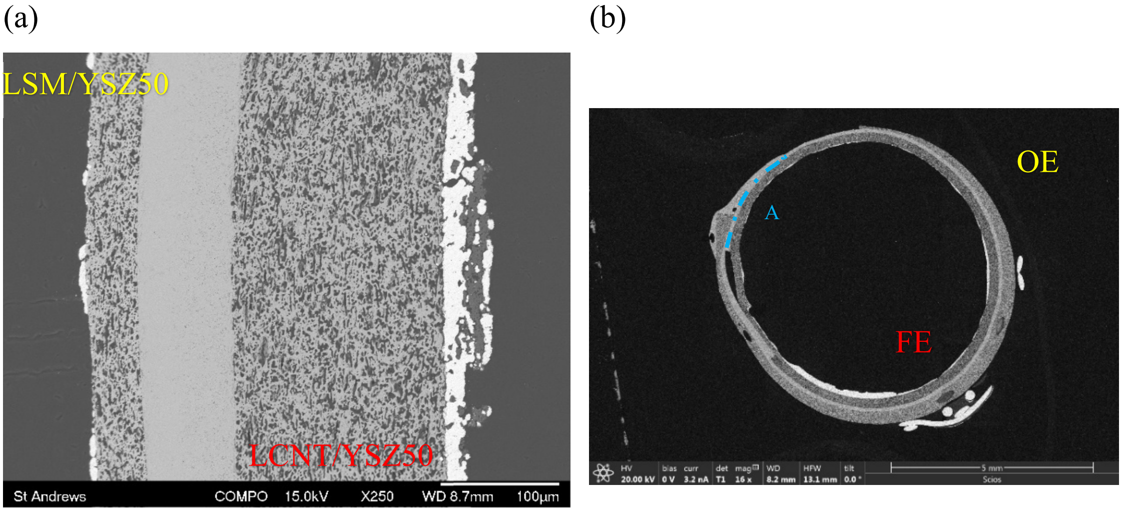

Figure 6-2: (a) – (b) SEM (BSE) images of small tubular cells with composite electrodes. A – the point of contact of tapes on opposite sides.

For the cell's preparation, LCNT/YSZ50 tape was cast first, dried and masked, and a single layer of YSZ was cast over it with a standard 300 µm casting gap, plus 70 µm from the Mylar mask, Figure 6-1 a. When dried, the assembly was masked again, and a single layer of LSM/YSZ50 oxygen electrode was cast with a standard 300 µm casting gap, producing a 40 µm thick layer with 30% porosity. The casting assembly was ended with YSZ electrolyte attached to its other side after rolling (surface A on Figure 6-1 b and

Figure 6-2 b); such joining is required to prevent a gas crossover between both sides of the cell. As seen in the SEM image, Figure 6-2 b, the part where the two ends of the tape come together is not entirely covered by electrodes from both sides. Also, tapes in this location often tend to delaminate during production or sintering, so YSZ slurry could be applied to strengthen the structure, Figure 6-1 c; the connection point at the YSZ is the weakest point of the cell.

After sintering, the YSZ electrolyte had a thickness of about 80 μm, a thinner electrolyte than in the case of SOFCRoll did not result in its damage; cells had almost no internal defects and gave a high value of open-circuit voltage.

6.3 Tubular cells with composite LCNT/YSZ50 and impregnated LSF/P-YSZ electrodes

The cells described so far were produced by co-sintering of multiple layers. Those must be able to sinter well to each other, create a good interface, and have an optimised microstructure; also, the rate of this sintering must be close; otherwise, the created stress would destroy a fragile ceramic structure. The control of co-sintering was possible through the size of particles and the composition; however, the method is limited by material selection and requires high-temperature sintering. Therefore, the development of ceramic tapes for co-sintering purposes is often very time consuming and problematic, which does not always bring anticipated results. For example, a failed attempt to co-sinter pure LCNT layer with YSZ electrolyte (Chapter 5.2). Whereas developed co-sintered electrodes used in the project have relatively poor performance due to the requirement of high-temperature sintering (Chapter 5.5.3).

The impregnation method involves the saturation of ceramic backbone, usually made of the same material as the electrolyte, with a solution that will decompose to the required material after calcination, creating a functional layer. Using this technique in co-sintered cells simplifies manufacturing and makes a broader range of materials available. After the porous backbone is made, any chosen active material could be impregnated; there is no requirement to measure the shrinking profile whenever a new electrode is tested. It could be sintered at an optimal temperature to maximise its performance and avoid unfavourable reactions.

The development of a porous backbone is much simpler than the composite electrode. The differences in shrinking profile between porous YSZ and YSZ arise only from the presence of pore-former in porous YSZ slurry, not from different properties of materials; these differences could be much easier maintained; also, the interface between porous YSZ and YSZ should be better than in composite electrode.

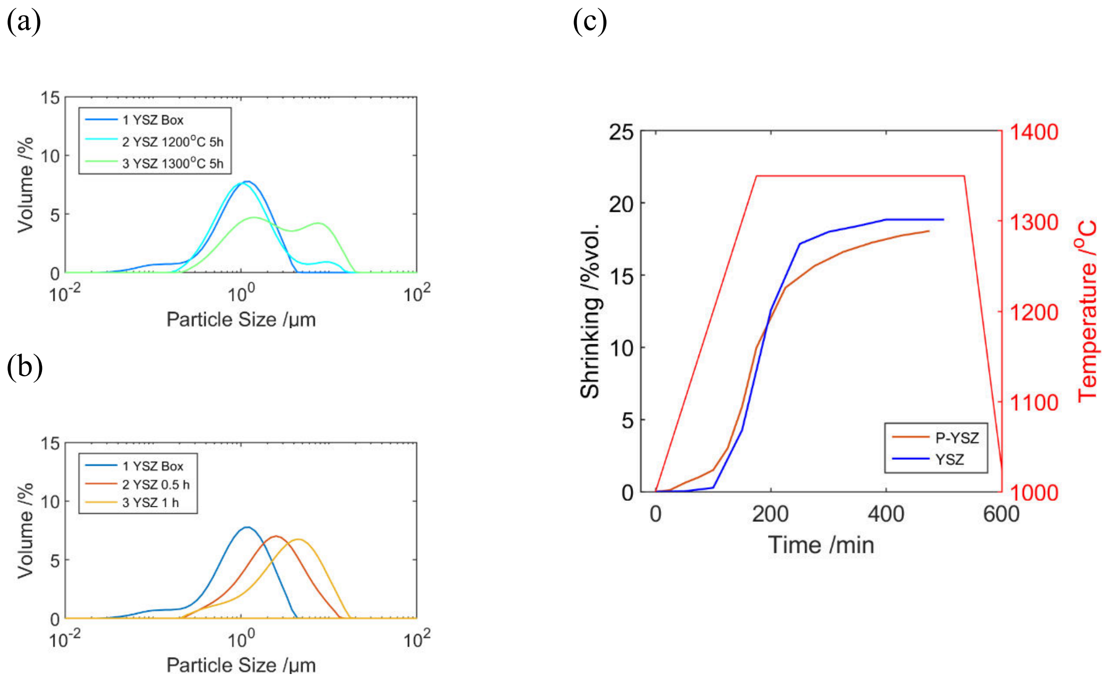

Figure 6-3: (a) Particle size analysis of pre-sintered YSZ for 5 h at various temperatures. (b) Particle size analysis of pre-sintered and ball-milled YSZ and commercial powder. (c) Shrinking profile of P-YSZ made for co-sintering at 1350°C.

For the porous YSZ (P-YSZ) production, the ceramic powders were mixed with pore-formers (graphite and starch from rice) to provide a well-developed porous structure. The pore former's addition into porous backbone slurry also could create differences in the shrinking profile between the electrolyte and electrodes during the cell's sintering, which leads to the delamination and formation of other defects in the cell.

As previously, the shrinking profile and microstructure of the porous electrode were optimized by adjusting the size of ceramic particles and pore former concentration in the slurry. For the ceramic backbone preparation, a mixture of the large and small sizes of

YSZ particles was used, where the large particle size of ~ 3.5 µm was achieved by ball milling of the sintered YSZ pellets (1350 °C for 5 h) at 400rpm for 1 h while the small particles ~ 1 µm comes from untreated YSZ powder (PI-KEM Limited). Presenting YSZ pellets and ball milling them to the required particle size was advantageous over presenting YSZ powder, giving homogeneous particles without a trace of large agglomerations (Figure 6-3 a & b).

Table 6-1: The analysis of YSZ particle size, pre-sintered at various temperatures and times.

Material	Temperature/°C	Time/h	D10/µm	D50/µm	D90/µm	SSA/m^{2}g
YSZ	As provided	-	0.337	1.109	2.482	10.2
YSZ	1200	5	0.472	1.151	3.394	6.43
YSZ	1300	5	0.694	2.545	10.608	3.67

Table 6-2: The analysis of YSZ particle size, pre-sintered as pellets at 1350°C, crushed and ball milled for various times with mixed milling balls.

Material	Time/h	D10/µm	D50/µm	D90/µm	SSA/m^{2}g
YSZ	0.5	0.967	3.846	9.552	2.76
YSZ	1	0.810	2.456	6.233	3.54

The slurry contained 75% pore former by volume (mixture of starch and graphite 1:1 by vol.). The standard concentration of organics was used (Table 4-2), with the solid/ organics volume ratio equal to 3.37. The measurement showed that additions of such a large amount of pore former into a YSZ slurry enlarge its high-temperature shrinking by about 10% without any particle size modification. The P-YSZ was cast with a gap of 300 µm, giving a porous layer of about 60 µm after sintering with about 80% porosity.

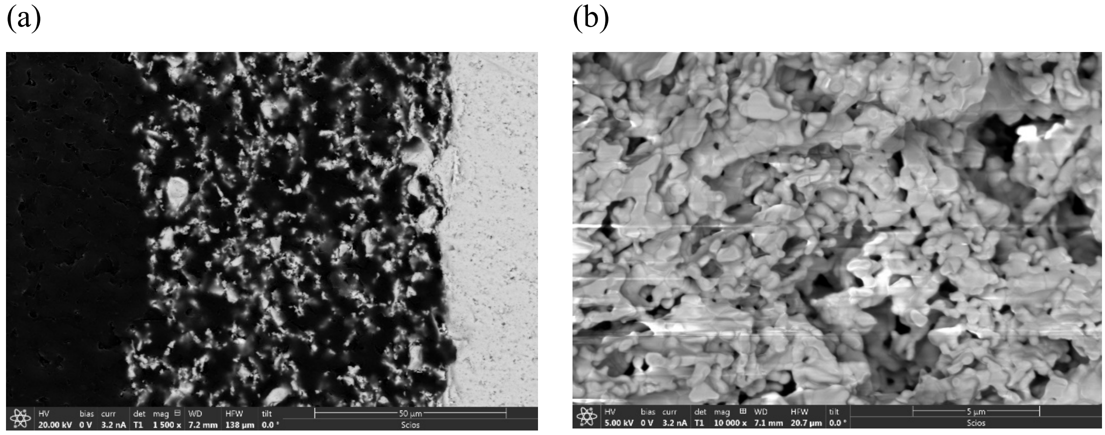

Figure 6-4: The SEM analysis of porous YSZ layer developed for the co-sintering purpose, sintered at 1350°C. (a) SEM (BSE) analysis. (b) SEM (SEI) analysis of the layer.

A standard LCNT/YSZ50 composite electrode was adapted on the fuel side as a supporting layer. The same method of layer assembly was employed as in fully composite tubular cells, but LSM/YSZ50 co-cast at the last step was replaced with the P-YSZ, Figure 6-1. The cells were sintered at 1350 °C. The LSF solution was impregnated onto the porous YSZ backbone on the outer layer by a micro-pipette to a final amount of ~ 30 vol%, and the final calcination temperature was 850 °C for 5h. After every impregnation cycle, the cells were placed in a furnace at 700 °C to de-compose precursors. The LSF was chosen to replace LSM due to much better oxygen incorporation and transport kinetics than LSM. The material has lower reactivity with YSZ than other well-performing oxygen electrode LSCF and does not contain carcinogenic cobalt [76]. For this purpose, a developed porous YSZ layer (P-YSZ) was used to replace LSM/YSZ50 composite material, impregnated with nitrate LSF solution, and synthesised at 850 °C (Chapter 3.7). It has been reported that LSF synthesised at 850 °C has much higher activity than its analogue sintered at a higher temperature due to higher surface area [76].

Figure 6-5 shows the analysis of the cell's microstructure. The thickness of impregnated oxygen electrode was ~70 µm, the YSZ electrolyte was ~100 µm, and the supporting LCNT/YSZ50 fuel electrode had a thickness of ~200 µm. The total porosity of impregnated electrode was about 58%; however, the LSF seems to agglomerate closer to the electrode's surface; hence, the porosity distribution was less homogeneous than in the composite layer (up to 10% variation between the outer and inner part of the electrode). In comparison, the porosity of the composite was homogeneous and about 42% by volume. The cell did not show cracks or delamination. During the assembly, the ends of the tapes must be adjacent and sintered during a thermal step; otherwise, the cell could deform, and gas could crossover between channels, resulting in a drop in OCV. The joining method is shown in Figure 6-1 b depends only on 4 mm in the length of YSZ and may lead to such a defect (Figure 6-5 b,c); therefore, the method was modified as explained next.

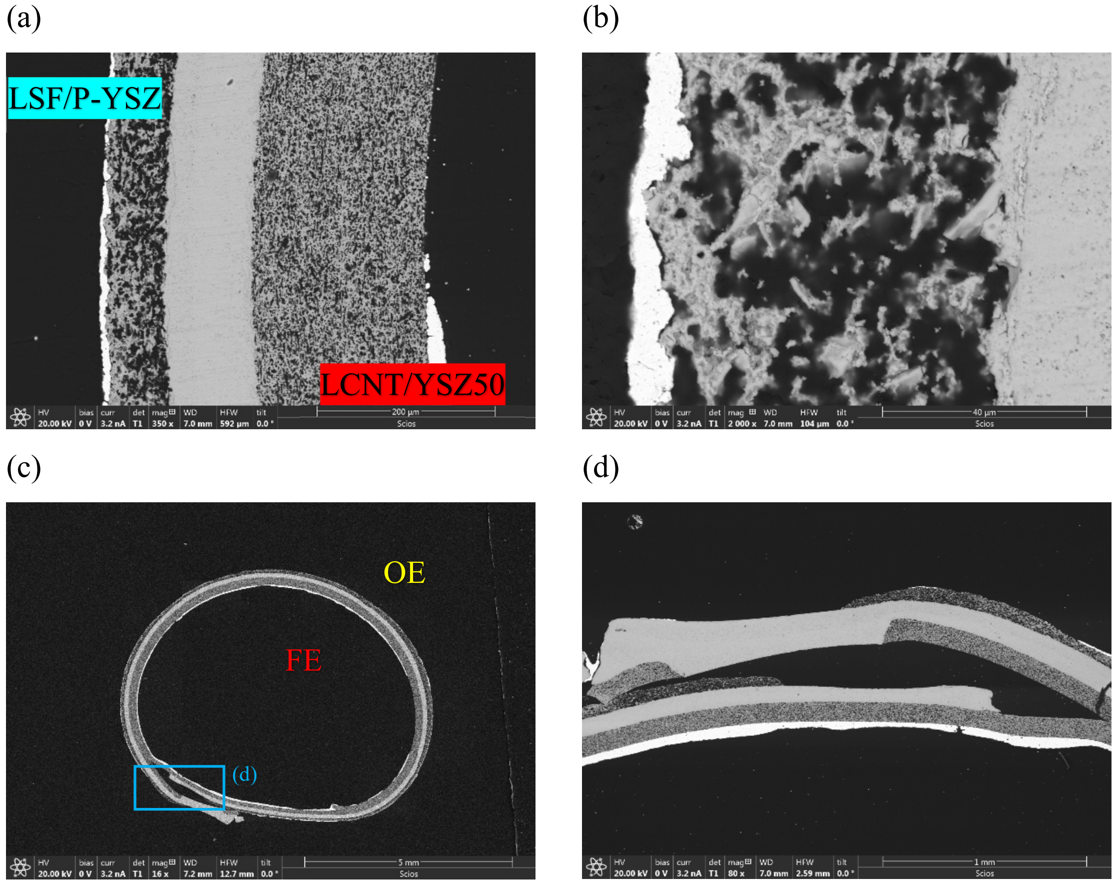

Figure 6-5: SEM (BSE) images of a tubular cell with LCNT/YSZ50 composite FE and impregnated LSF/P-YSZ OE. (a) A cross-section of a fuel cell. (b) LSF impregnated electrode. (c) Full image of the cell. (d) Point of contact between the cell's ends.

6.4 Tubular cells with LCNT/P-YSZ and LSF/P-YSZ impregnated electrodes

Eventually, fully impregnated tubular cells were developed, where composite LCNT/YSZ50 composite electrode was replaced with LCNT impregnated fuel electrode. However, before that, the possibility of quick impregnation was investigated, as the impregnation method is relatively slow and requires multiple steps to achieve the required catalyst loading [325]. As explained in Chapter 6.5.1.3, tubular cells showed extraordinary durability to withstand rapid temperature changes; cells did not crack when inserted directly into the furnace at 700 °C; hence in the employed method, after saturation of the porous backbone with solution, the cell was placed almost instantly into a furnace heated to 700 °C for calcination step. The technique significantly shortened the time required for catalyst deposition, enabling the electrode preparation in one working day.

The technique was investigated first on the symmetrical tubular cell with LSF electrodes, and analyses were done to investigate their microstructure. Those cells were made by the lamination method, and both sides used one layer of electrolyte and one layer of thick porous YSZ (P-YSZ). A new assembly method was used; instead of using a thick 200 µm supporting layer inside a cell, a cell was made with the same electrode's thickness of about 100 µm and 60 µm electrolyte. All layers were cast separately for the cell assembly, P-YSZ with a casting gap of 600 µm, while YSZ electrolyte with a gap of 300 µm.

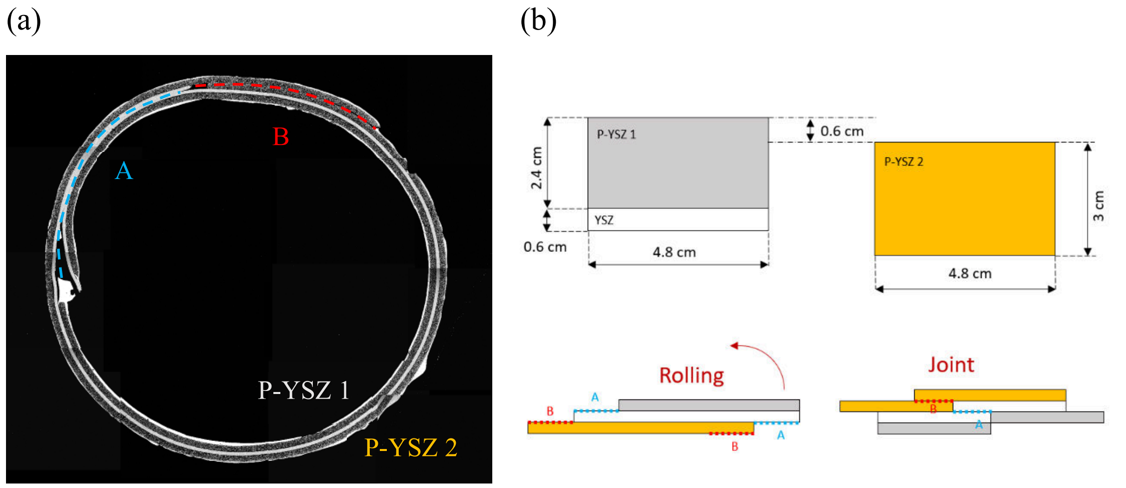

Figure 6-6: (a) Full image of the cell made by lamination with double supported electrodes (sintered at 1400 °C). (b) Green tapes assembly for lamination, rolling of tape's assembly, A – point of contact of YSZ layer, B – point of contact of P-YSZ 2 layer. P-YSZ 1 – inner electrode, P -YSZ 2 – outer electrode.

A new assembly method was needed for such a design, Figure 6-6. The inner electrode tape was shortened to the level that, after being rolled, creates a single layer of the functional electrode. The inner tape was 6 mm shorter than the electrolyte, while the outer layer had the same dimension but was shifted 6 mm down. Such assembly creates two long points of contact (A and B in Figure 6-6), strengthening the connection and protecting the structure against deformation and delamination.

The sintering temperature was 1350 or 1400 °C. The cell was impregnated by dipping in LSF 0.5 mol solution, drying at 80 °C for a few minutes, inserted directly into the furnace at 850 °C for 10 minutes and then taken out to the room. The cycle was repeated seven times, the whole process was finished in one day, and cells were sintered at 850 °C overnight. A single impregnation cycle requires several hours; the cell is usually placed in the furnace and heated overnight. Therefore, a new approach shortened preparation time for at least one week. From the measurement of weight and with the assumption of the constant mass of P-YSZ, in every cycle, about 2-2.5% of the material was impregnated by weight (up to 2.2% by vol.).

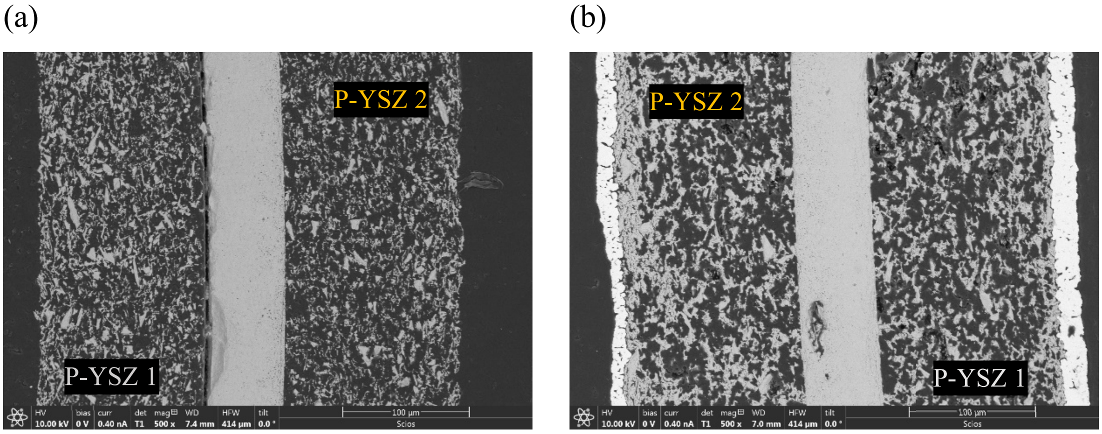

Figure 6-7: SEM of the tubular cell with porous YSZ electrode layers sintered at 1350 °C. (a) Before impregnation. (b) After seven cycles of a rapid impregnation experiment, impregnated with LSF.

Figure 6-7 shows the backscattering analysis of the cell sintered at 1350 °C before and after impregnation. The porosity of the outside, not impregnated layer is about 75%, while the inside layer is 70%. The difference in porosity likely comes from higher stress exerted on the inner part of the cell, similarly as the measurement of SOFCRoll indicated, Figure 5-22. After impregnation, the porosity of the outside layer is about 66.5%, while the inside layer is 61.5%. The same difference in porosity (5%) between the outer and inner layer indicates the same amount of impregnated solution. As previously, there is some un-homogeneity in impregnated material through the electrode; a denser material is created closer to the surface.

After seven impregnation cycles and after the electrochemical test (where the cell was also directly placed in the furnace), the cell did not show any cracks or other defects, showing great thermal shock resistance ability. The YSZ electrolyte had only about 60 µm and did not crack in such harsh conditions.

The manufacturing method and layers assembly were modified at the next stage. First, a P-YSZ backbone was co-cast with a thin layer of YSZ electrolyte over it, and another layer of P-YSZ was laminated or co-cast on the whole assembly. Then, after rolling in tubular shape and co-sintering, the porous backbone was impregnated with functional perovskite materials, the LCNT for the fuel side and the LSF for the air electrode.

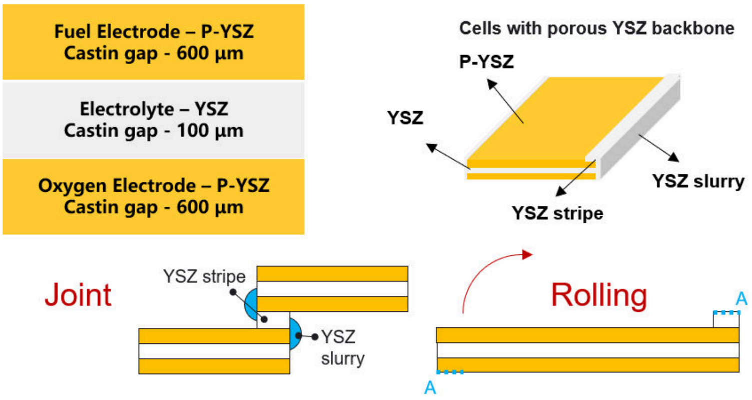

Figure 6-8: Green tapes assembly for co-casting method, rolling of tape's assembly, A – point of contact.

In the new assembly method, Figure 6-8, the co-casting method was simplified and improved, producing a thin 20 µm YSZ electrolyte. The P-YSZ layer was cast first with the doctor blade gap equal to 600 µm. After drying overnight, the YSZ was cast directly on the P-YSZ tape with the doctor blade gap equal to 100 µm. After drying overnight, another layer of the porous backbone was cast directly on the electrolyte tape with the doctor blade gap equal to 600 µm, or previously cast tape was laminated. The doctor's blade was elevated to prevent the destruction of tapes underneath. The slurries were cast on the whole area of the green tapes below; in the method, the mask was not required, as additional YSZ stripes were laminated at the end of cells assembly to connect its opposite sides after rolling, and YSZ slurry was applied to prevent gas crossover. Such assembly was cut into 30 mm×48 mm rectangles, rolled on an 8 mm steel bar to a tubular geometry and tied with electrolyte stripes. The cell's ends were covered with a YSZ slurry to avoid leaking of impregnating solution between electrodes. The cell's sintering contained two stages, low-temperature calcination at 1000 °C for 5 h and high-temperature sintering for 5 h, which was increased to 1450 °C.

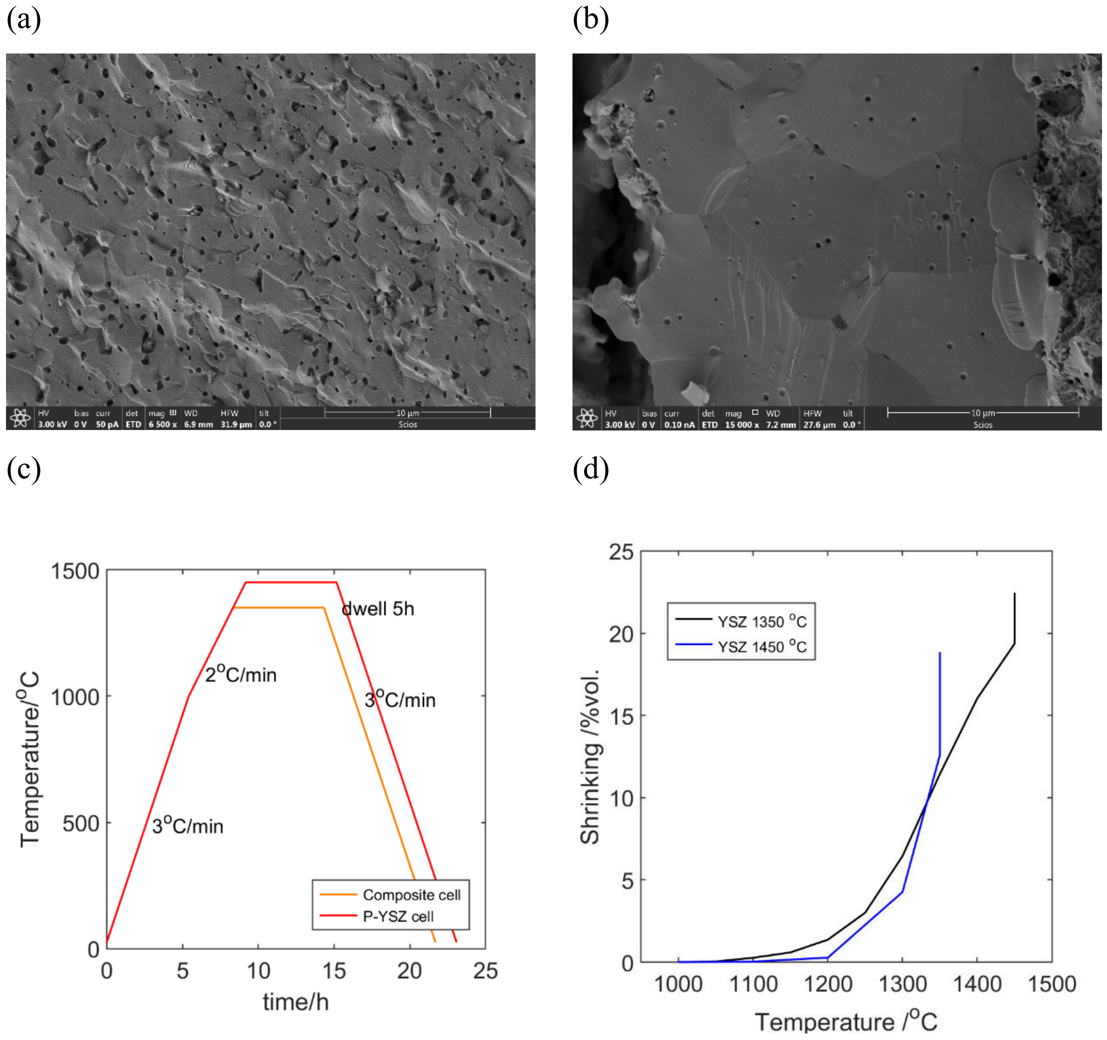

Figure 6-9: SEM (SEI) of YSZ electrolyte sintered (a) at 1350°C for 5 h; (b) at 1450°C for 5 h. (c) Temperature profile of high-temperature sintering step. (d) YSZ shrinking profile at various temperatures.

For the development of previous cells, the co-sintering of composite materials with YSZ electrolyte, the temperature was limited to 1350 °C to avoid the reaction between the materials; however, low sintering temperature brought concerns about the quality of the YSZ electrolyte, as the SEM analysis showed a number of closed pores in its structure. As the same material with electrolyte was used as the porous scaffold for electrode material, the co-sintering temperature of the cell's backbone was increased to 1450 °C, ensuring much better densification of electrolyte. The shrinking profile of YSZ electrolyte showed almost 3.6% further densification, which is the volume of closed porosity that got reduced, Figure 6-9 d. The SEM analysis of the cell's crosssection shows dens YSZ electrolyte, and only sparse closed pinholes inside large grains are visible, Figure 6-9 b.

The electrodes had good adhesion with YSZ electrolyte; no crack or delamination was visible in the cell's structure. The cell was double electrode supported, with an electrode thickness of about 100 µm and porosity of about 62%; the use of a 100 µm casting gap reduced the thickness of the YSZ electrolyte to 20 µm.

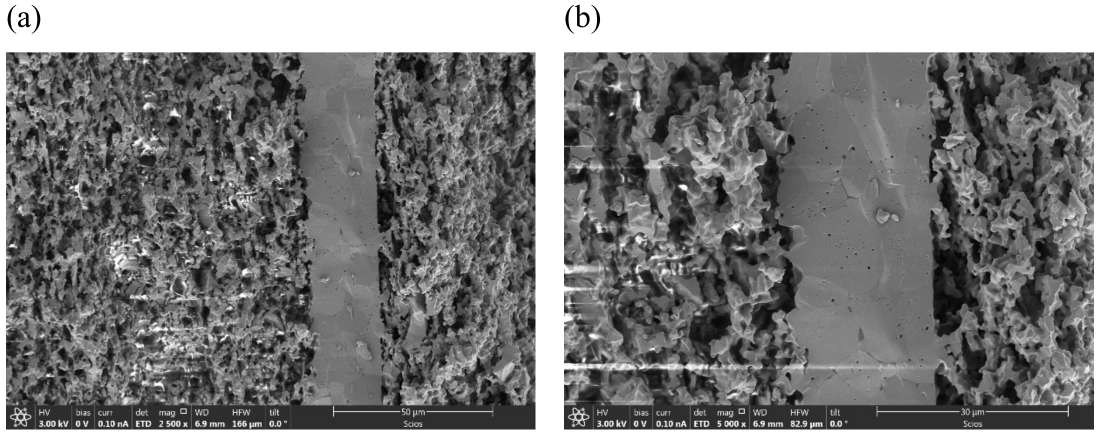

Figure 6-10: (a) – (b) SEM (SEI) of YSZ porous backbone co-sintered with YSZ electrolyte at 1450 °C.

Due to the different calcination temperatures, the fuel and air electrode materials were impregnated separately. Firstly, the LCNT solution was impregnated onto the porous YSZ backbone, inside a cells channel, by pipette until saturation, while the excess of the solution was removed with a cotton pad. After every impregnation cycle, the cells were placed in a furnace at 700°C to de-compose precursors. After achieving 50% by vol. of LCNT material, the cell was calcined at 1100 or 1200 °C dwelled for 5 h. Then, LSF was impregnated onto the outer layer, following the same way as LCNT to a final amount of 30 vol%, and the final calcination temperature was 850 °C for 5 h.

Both impregnated materials were homogeneously distributed through most of a porous backbone structure, Figure 6-11 a & b; however, some agglomeration was created closer to the surface. The measured porosity of the LSF electrode was 45% at the cell's centre and 32% at the surface of the electrode. Similarly, for LCNT, 51% porosity at the centre and 41% closer to the surface. The LSF impregnated oxygen electrode's microstructure is shown in Figure 6-11 c & d, demonstrating the network of LSF nanoparticles formed on the YSZ surface. Such structure could be advantageous in fuel cell operation as it increases the active area of LSF material and its TPB with YSZ [76]. On the other side, in Figure 6-11 e & f, the impregnated LCNT perovskite created a dense layer of small grains covering the whole YSZ surface. After electrochemical testing, the nanoparticles were observed on the LCNT surface, which are believed to be Ni exsolving due to the electrochemical switching.

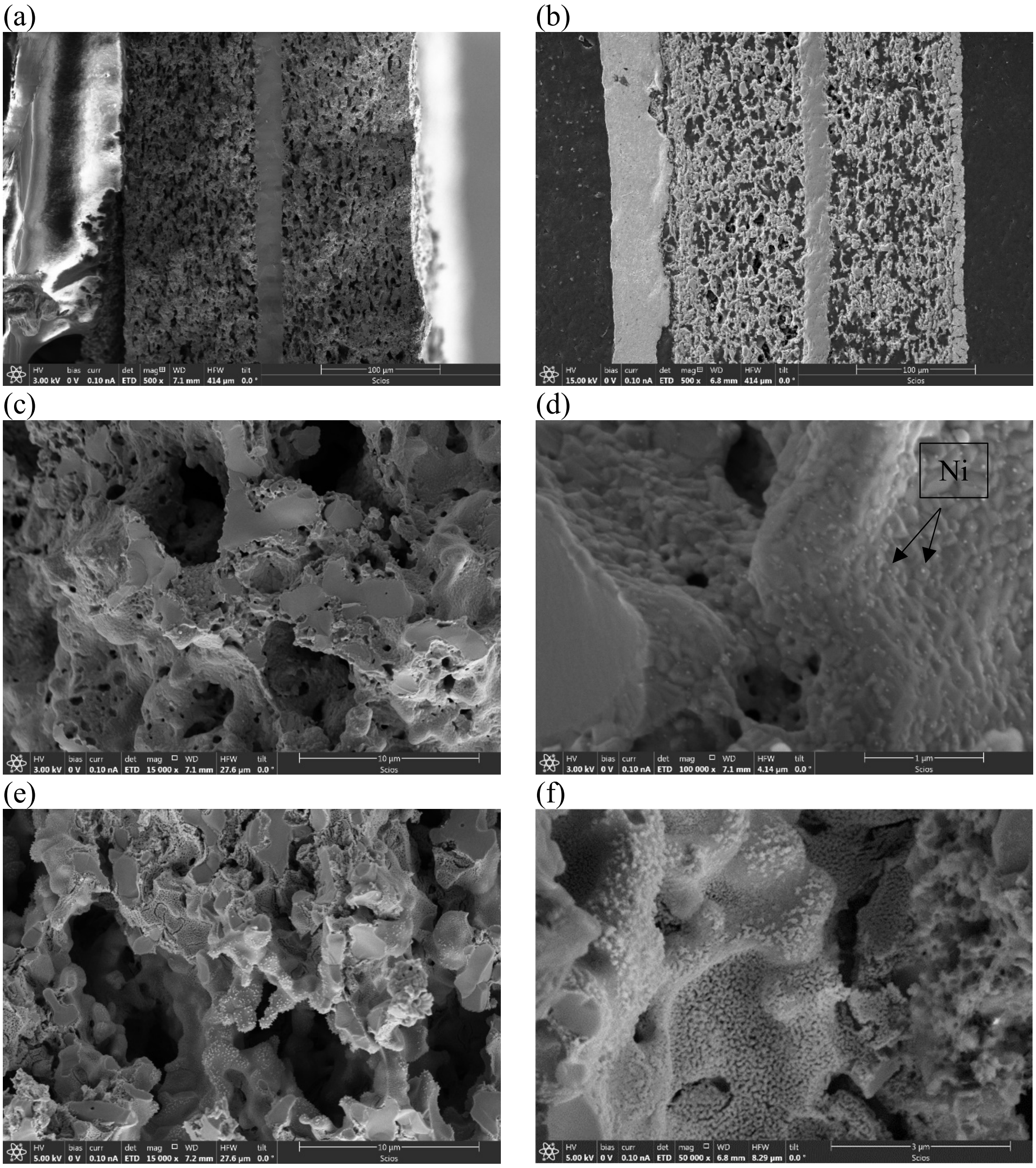

Figure 6-11: SEM analysis of the tubular cell with impregnated perovskite electrodes. (a) SEM (SEI) of cell's crosssection. (b) SEM (BSE) of cell's crosssection. (c) – (d) SEM (SEI) of the LCNT fuel electrode, sintered at 1100 °C, after switching. (e) – (f) SEM (SEI) of the LSF oxygen electrode, sintered at 850 °C.

6.5 Electrochemical test of tubular cells

6.5.1 Tubular cells with composite LCNT/YSZ50 FE and LSM/YSZ50 OE.

6.5.1.1 Gas reduction and switching

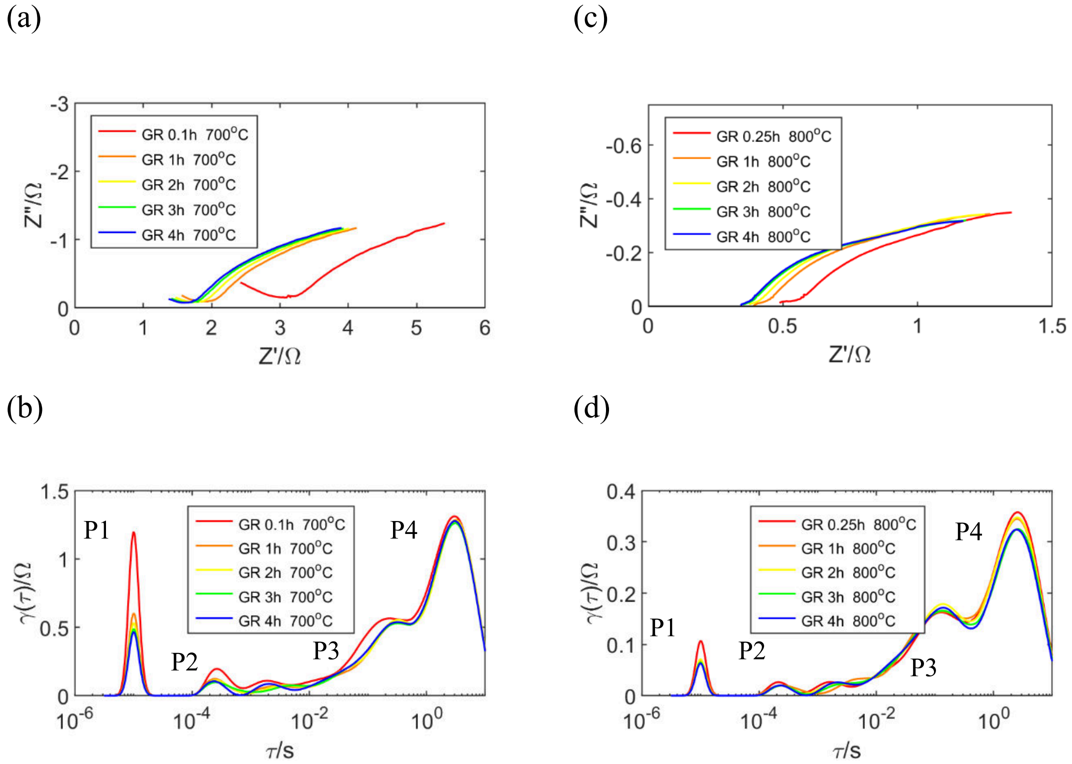

Figure 6-12: Gas reduction of tubular cell with composite electrodes. The EIS taken during gas reduction with 50 ml/min of wet H_2 in FE and atmospheric air in OE and calculated DRT. (a) – (b) at 700°C and (c) – (d) at 800°C.

Figure 6-12 shows the tubular cell's EIS and DRT characteristics during a chemical reduction at OCV. The cell used to analyse how gas reduction and switching affect the cell's performance was first reduced with 50 ml/min 3% H_2O/H_2 at 700°C for 4 h, then heated to 800 °C (in 50 min.) and reduced for further 4 h. The switching was performed in three steps between 2 – 2.1 V, as described next. The gas reduction changes pO_2 only on the fuel electrode side; thus, it is accepted that the impedance change observed during the process is not relevant to the oxygen electrode.

At both temperatures, the ohmic resistance (Rs) decreases during the whole period, mainly in the beginning, then the reduction rate decreases. At 700 °C, when the gas atmosphere was switched to 50 ml/min of wet H_2, the ohmic resistance (Rs) decreased by 28% after the first hour of reduction and about 2% every hour afterwards. At 800 °C as well, the initial drop of Rs was most significant, 24% after the first hour, 5.7% after 2 h, 5.7% after 3 h, and 2.2% after 4 h. Likely, a drop of Rs comes from increased LCNT electronic conductivity, with higher Ti^{3+}/Ti^{4+} pair concentration. The initial period is related to the reduction of the LCNT surface, which becomes the primary path for electronic conductivity, while the further period to the bulk; thus, the process is slower [156].

The polarisation resistance at high frequency (P1, P2) also has the most significant drop in the initial period. The behaviour of the process seems to be controlled by the electronic conductivity of LCNT, indicating that it could be related to a charge transfer, e.g. between LCNT grains. The processes at middle to low frequency are not significantly affected by the gas reduction; their kinetics seems to improve after the initial period at 700 °C and quickly reach equilibrium with the gas atmosphere. The process does not improve after a few hours of gas reduction, even if a large population of nickel nanoparticles has been observed under these conditions (Figure 6-13). If only the presence of Ni contributed to the reduction of low-frequency polarisation through the dissociative/ adsorption of H_2 (Chapter 5.5.1), some change would be visible. Meanwhile, its value remains almost unchanged. Therefore, it becomes evident that the second rate-determining factor is involved.

After several hours of gas reduction, the switching procedure was applied in three steps (Figure 6-14), two times at 2 V in the electrolysis mode for 2 min and once at 2.1 V for 2 min at 800 °C. Apart from further reduction of ohmic and polarisation resistance at high frequency, polarisation at low frequency also decreases, which was not achievable under a gas atmosphere.

The improvement of P3 and P4 kinetics could be explained by a greater extent of Ni exsolution that affects a low-frequency polarisation by increasing the rate of H_2 dissociative adsorption and the generation of oxygen vacancies that controls the exchange of oxygen ions.

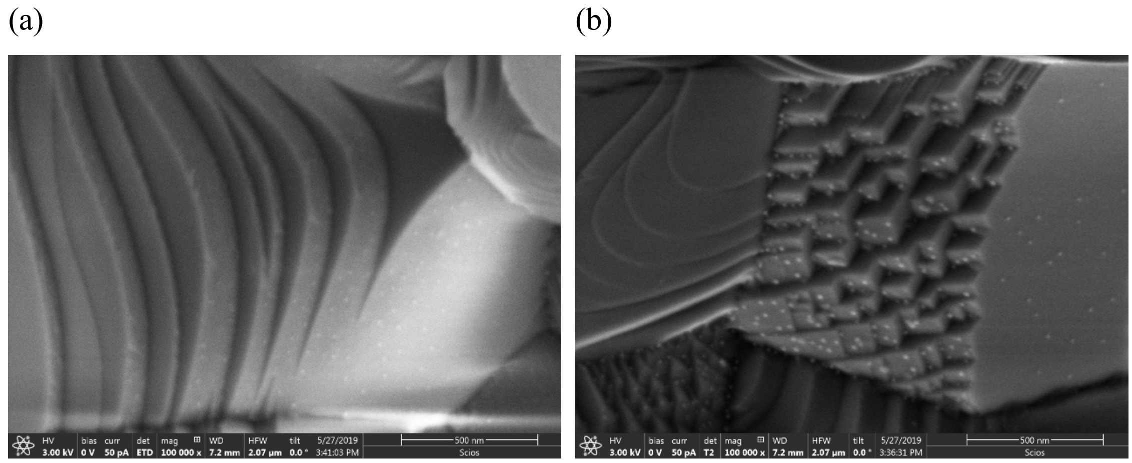

Figure 6-13: LCNT-YSZ anode after gas reduction with wet H_2 at 800°C after 4 h, [324].

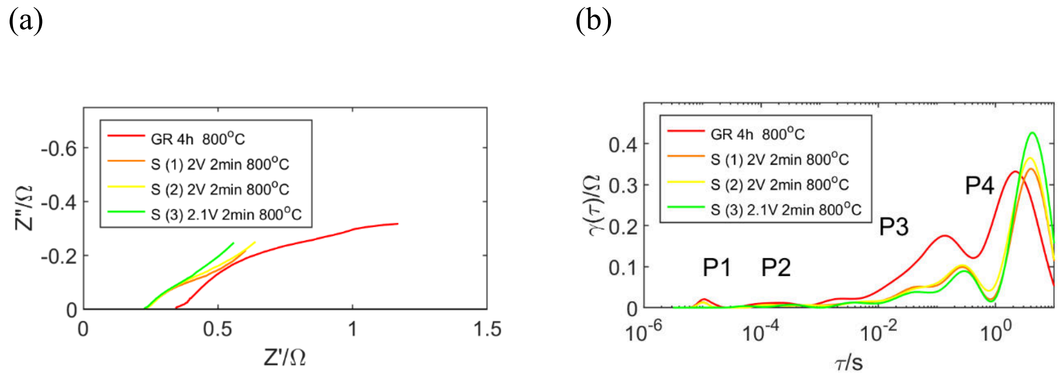

Figure 6-14: Impedance analysis after gas reduction (GR) and switching (S) at indicated conditions with 50 ml/min of wet H_2 in FE and atmospheric air in OE. (a) EIS analysis. (b) Calculated DRT.

The cell was switched three times to observe how the time and value of potential affect impedance data. Second, switching at the same potential did not bring a noticeable change in ohmic resistance. At the same time, Rp has slightly increased, meaning that the 2 min time of the first switch was sufficient for electrodes to achieve equilibrium under created environment, while extending the process may lead to an unbeneficial effect in terms of efficiency. The third switching also lasted 2 minutes, but the potential was increased to 2.1 V. This reduced Rs only slightly (about 2%). At the same time, Rp on low frequency seems to slightly increase, which may be caused by further degradation of the electrode due to applying a high potential.

The current generated from the tubular cell indicates relatively effective surface area utilisation. Assuming that tapes shrink by 25%, the maximum surface area of tubular cells was about 7 cm^2. The cell, after gas reduction, generated 0.31 A at 0.7 V at 800 °C, which is 5.6 times more than in a planar cell normalised to 1 cm^2 (0.055 A/ cm^2, Chapter 5.5.3.4) and 1.35 times smaller than in SOFCRoll with Ni/YSZ10 current collector (SRB36P2) with 12 cm^2, (0.42 A, Chapter 5.5.5.2).

The thickness of the poorly conductive LCNT/YSZ50 layer in the tubular cell is almost three times that of the planar cell; however, the ohmic resistance is not much enlarged. After the gas reduction in the tubular cell, the ohmic resistance was 0.25 Ω at 800°C, which is eight times lower than in the planar cell, normalised to 1 cm^2 at the same temperature after gas reduction.

6.5.1.2 Performance test of tubular cell

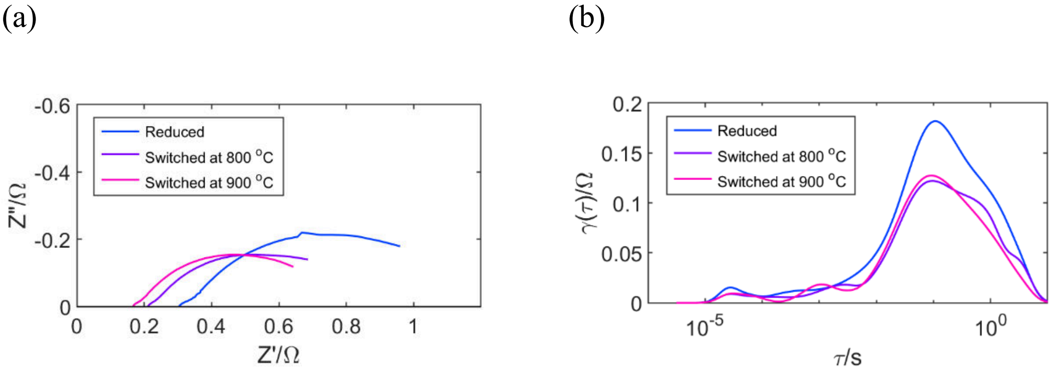

Figure 6-15: The impedance analysis of Tubular cell after 2 h reduction in wet H_2 and switching at 2.1V for 10 min at various temperatures with 50 ml/min of wet H_2 in FE and atmospheric air in OE. (a) EIS analysis. (b) DRT analysis.

Unlike the other tests, the cell used for the performance test was switched at 900 °C in an attempt to maximise switching efficiency. The cell was tested with 50 ml/min of wet H_2 in FE and atmospheric air in OE; the I-V and EIS were measured under cooling-down. The total resistance of the cell after switching at 900 °C was less than 0.1 Ω lower than for the cell switched at 800 °C (Figure 6-15). The error for fitting those impedance data is quite large due to poor separation of individual arcs; thus, the approximate value. Nevertheless, improving switching efficiency due to temperature does not seem significant, and the main difference comes from the reduction of ohmic resistance.

After switching, the electrochemical performance at various temperatures was measured, as shown in Figure 6-16. The measured OCV values were close to theoretical, between 1.05 and 1.02 at the tested temperature range of 700 – 900 °C, indicating good tightness of the cell, sufficiently dense electrolyte and robust structure. The maximum power for a single tubular cell was equal to 760, 530, 350, 210, 110 mW at 900, 850, 800, 750 and 700 °C, respectively.

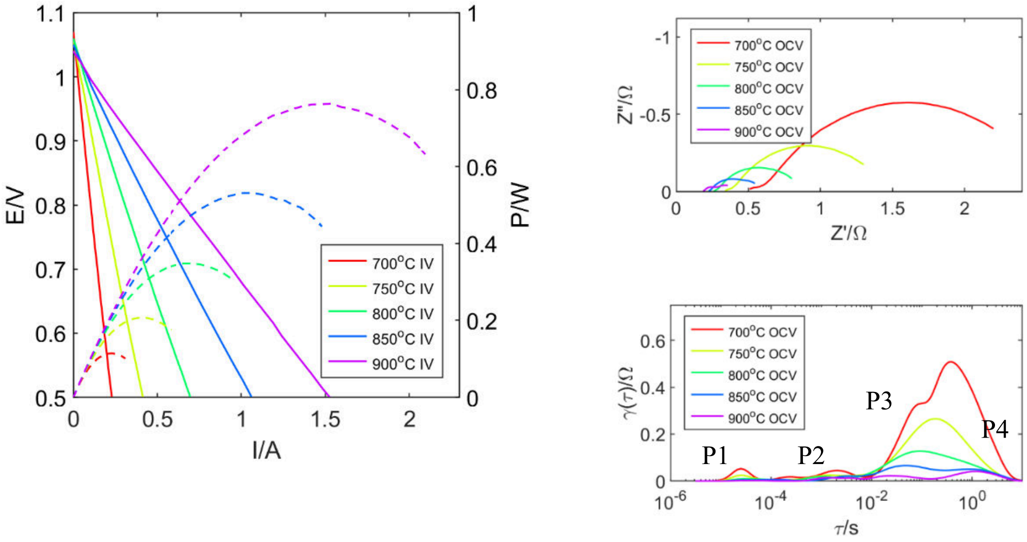
(a) (b)

Figure 6-16: The electrochemical performance of the cell with composite electrodes at various temperatures switched at 900 °C at 2.1 V for 10 min with 50 ml/min of wet H_2 in FE and atmospheric air in OE. (a) I-V analysis. (b) EIS analysis at OCV and calculated DRT.

The DRT was constructed from the imaginatory part of impedance (Figure 6-16 d), where all four processes could be recognised at a higher temperature while at a temperature below 800 °C merging into a single arc. After extraction of the rig's resistance, the cell's ohmic resistance was 0.09 - 0.4 Ω at 900 – 700 °C. The total polarisation resistance at OCV increases from 0.37 Ω at 900 °C to 2.4 Ω at 700 °C; where the low-frequency processes contribute the most, and high-frequency ones are relatively small, similarly as in previous composite cells.

6.5.1.3 Thermal shock resistance

The tubular cells are known for their remarkable ability to withstand temperature changes; thus, a thermal shock resistance test was conducted. Cells used for the thermal shock resistance test, stability test and regeneration were heated up to testing temperature (700 °C) pre-reduced 2 h in wet H_2 and switched at 2.1 V for 10 min; the test was conducted with 50 ml/min of wet H_2 in FE and atmospheric air in OE. During the thermal cycles, the cell was directly taken out from the furnace (700 °C) to room temperature for 5 minutes and then inserted back for the next 5 minutes.

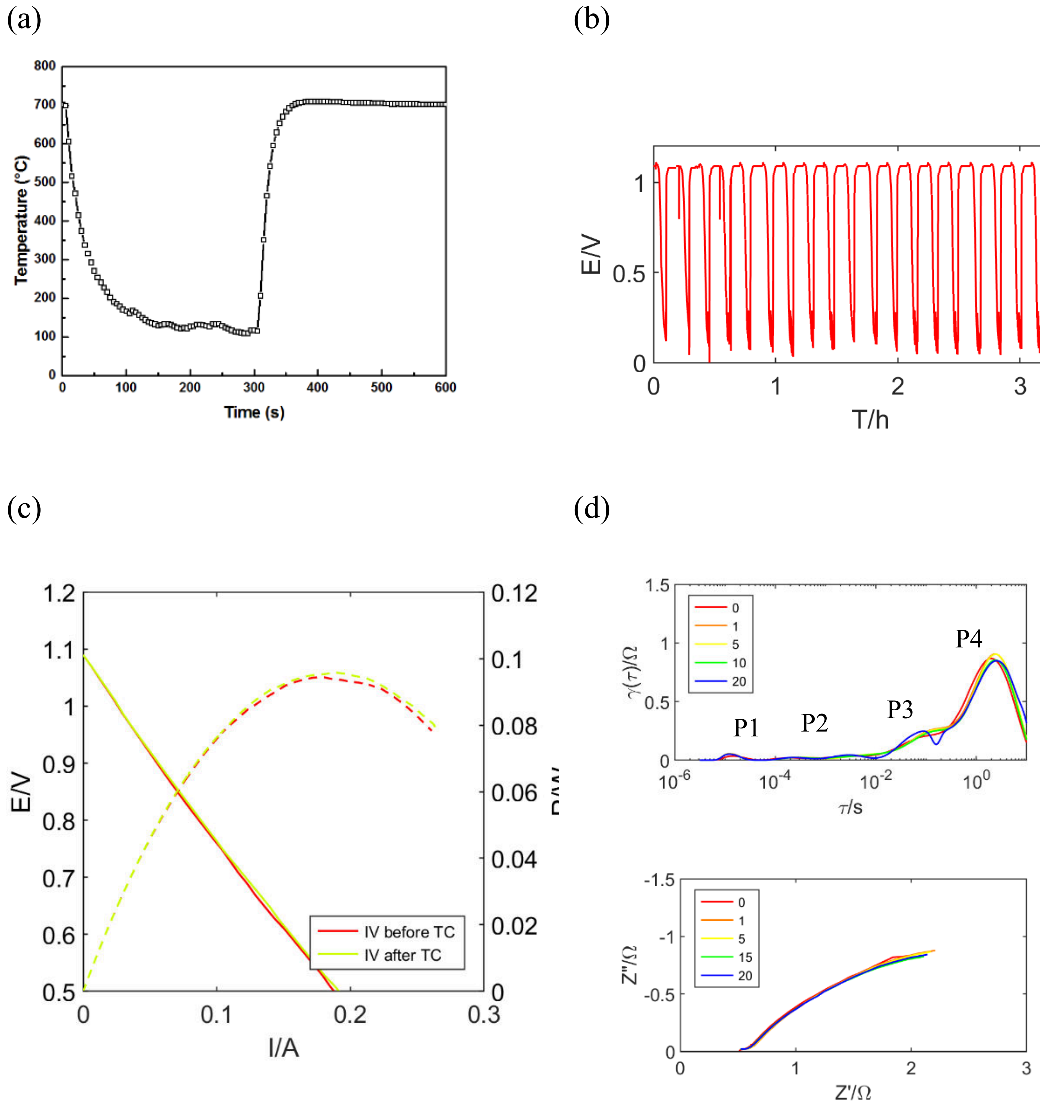

Figure 6-17: Thermal shock resistance test at 700 °C with 50 ml/min of wet H_2 in FE and atmospheric air in OE. (a) Temperature variation inside the cell in a thermal cycling test. (b) OCV variation during 20 thermal cycles. (c) IV curves before and after thermal cycling. (d) The EIS and DRT analysis at OCV between the indicated number of cycles.

Figure 6-17 shows the typical temperature variation inside the tubular cell during a thermal cycling test. After the cell was taken out from the furnace, the temperature inside the cell decreased quickly from 700 °C to less than 200 °C in the first minute and then gradually decreased. During the heating stage, the temperature inside the cell rose rapidly from 115 °C to 629 °C in the first 30 s, then slowly to 700 °C. When the cell was taken out from the furnace during the initial period, the OCV increased, which is likely related to the change of Gibbs free energy of H_2 oxidation at a lower temperature. After about 15 s, the OCV gradually decreased; it probably is related to the cooling of cells, electrodes and electrolyte, thus lowering the ionic conductivity of electrolyte and activity of electrodes and, consequently, drop of potential between the electrodes.

During the thermal cycling, the EIS spectra were taken between cycles. After the temperature stabilised, the OCV of the cell reached almost the same value for every thermal cycle, as shown in Figure 6-17 b. Impedance and current-voltage characteristics since not indicate noticeable degradation from 20 thermal cycles, proving high resistance to temperature changes. The cells were tested basically after a direct insert into a furnace which opens up the possibility for many applications in further development, e.g. portable or transport [45].

6.5.1.4 Cut off fuel delivery

The test was done with a constant voltage of 0.85 V at 700 °C; cycles were done by running the tubular cell with 50 ml/min 3% H_2O/H_2 in FE and atmospheric air in OE, cutting off its supply for 5 minutes and opening it for 5 minutes. The test simulates how the cut-off of the gas supply will affect the functioning of the cell during continuous operation. In cells based on Ni/YSZ fuel electrodes, such cycles could create an oxidising condition on the fuel electrode leading to significant volume change. When Ni forms a large part of the solid framework in the electrode (primarily if a thick anode layer is used as the support), the volume change could damage the shape and microstructure and develop micro cracks and delamination [326]–[328]. In LCNT material, the concentration of Ni is relatively low (only 6%), which does not significantly change the volume of the fuel electrode when Ni is oxidised. Moreover, as the nickel nanoparticles are exsolved at the surface of LCNT, they do not affect the bulk and structure of the composite.

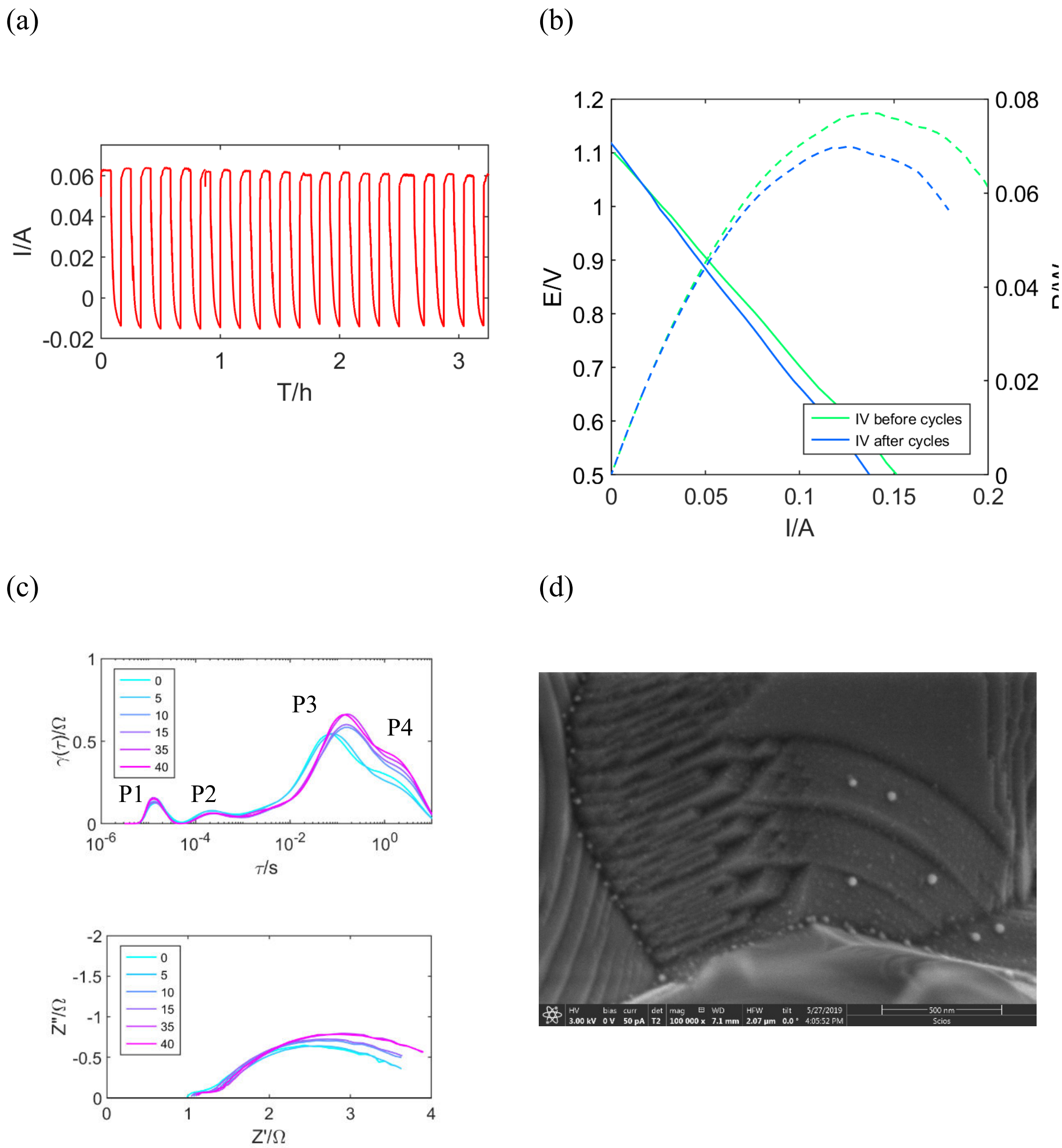

Figure 6-18: Fuel cut-off test with 50 ml/min of wet H_2 in FE and atmospheric air in OE. (a) Discharging curve at 0.85 V for first 20 cycles at 700 °C. (b) IV curves before and after the test. (c) The EIS and DRT analysis at OCV between the indicated number of cycles. (d) SEM image of nickel nanoparticles on the LCNT-YSZ anode after cycling.

In the experiment, the fuel cut-off has dropped of generated current to 0, and eventually below 0. Likely, the cut-off led to the oxygen diffusion into the fuel compartment (through the fuel outlet), increasing pO_2 at the fuel electrode and lowering the potential between electrodes. The appearance of a negative current after it dropped to 0 indicates that the cell switched to electrolysis mode. The current after 40 cycles decreased by about 9.5%. The polarisation resistance is affected at the lower frequency, while the ohmic resistance has increased by about 10%. The increased polarisation resistance at low frequency is likely related to the deterioration of Ni particles due to cycling or perovskite to exchange oxygen ions. The increase of ohmic resistance could be related to the decline of the current collector efficiency (e.g. worsening of contact) or perovskite electronic conductivity.

6.5.1.5 Short term stability tests and regeneration

After the electrochemical switching at 2.1 V for 10 min, cells were discharged at a constant potential at 700 °C with 50 ml/min of wet H_2 in FE and atmospheric air in OE; the first cell for 24 h at 0.7 V and the second one for 20 h at 0.85 V**.**

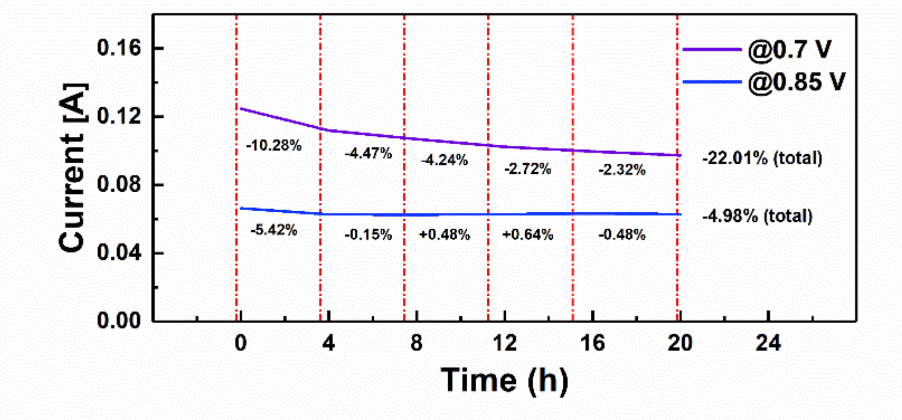

Figure 6-19: First 20h of stability test at 700 °C at 0.7 V and 0.85 V FC potential.

The performance degradation of the cell tested at 0.7 V was 22.01% after 20 h, with very high initial degradation during the first four hours; afterwards, a degradation rate gradually decreased. The cell's current tested at 0.85 V after 4 h fell by 5.42% only and remained almost constant to the end of the test, demonstrating better conditions for fuel cell operation. EIS was measured every four hours, and DRT was calculated to understand better the degradation process during the stability test, as shown in Figure 6-20.

At 0.7 V, the ohmic resistance Rs increased; most in the first four hours, then the degradation rate decreased. P1 and P2 increased at almost the same rate as Rs. The P3 increased considerably in those conditions and is the main reason for performance degradation; P4 increased to a lower degree. An increase in P3 without a noticeable change in P4 may indicate that the degradation of Ni nanoparticles is not responsible but the oxygen ion exchange with adsorbed hydrogen species. At 0 85 V, lower overpotential is applied on the fuel electrode, thus creating a less oxidising environment. The Rs drop only during the first four hours then keep stable even slightly increase; similarly, P1, meaning that they are coupled, both could be related to Ti^{4+}/T^{3+} concentration, which is more stable under less oxidative conditions. The P3 increases to a much lower degree than for higher potential; however, its activity decreases. The P4 is stable under operating conditions.

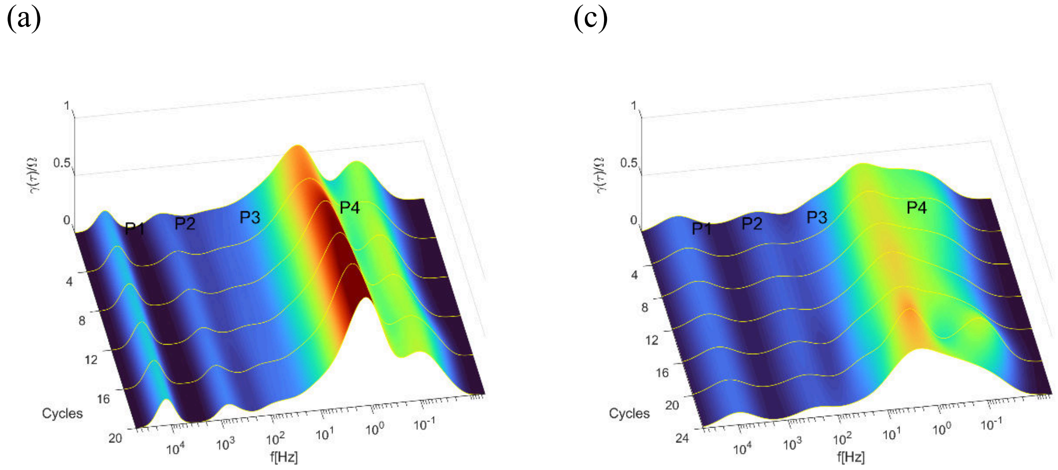

Figure 6-20: Short term stability test with 50 ml/min of wet H_2 in FE and atmospheric air in OE. (a) & (b) DRT and fitting data of impedance spectra taken every 4 h at 0.7 V for 20 hours. (c) & (d) DRT and fitting of impedance spectra taken every 4 h at 0.85 V for 20 hours.

The regeneration test was carried on, on the cell after 20 h stability test, made at 0.7 V (the cell in Figure 6-20 a) and additionally after five redox cycles (cut-off fuel delivery). For regeneration, the same value of potential (2.1 V for 10 min) was applied as for switching to analyse if losses resulting from the cell's operation are reversible.

The change of resistance after every test is summarised in Figure 6-21 a, where a simplified equivalent circuit was used to fit impedance data at OCV (summarised in Figure 6-21 c) made of resistance and two semicircles connected in series, where Rs represents ohmic resistance, Rp1 high-frequency polarisation resistance and Rp2 low-frequency polarisation resistance. The impedance analysis at OCV differs from those carried under the applied voltage discussed in the previous case. When measured under OCV, the P4 process seemed to deteriorate the most after the stability test, while when the cell was under applied voltage, P3 seemed to deteriorate while P4 seemed to be stable (the cell in Figure 6-20 a). It becomes apparent that P4 decreases under applied potential when back in OCV while operating in FC mode degradation does not affect it.

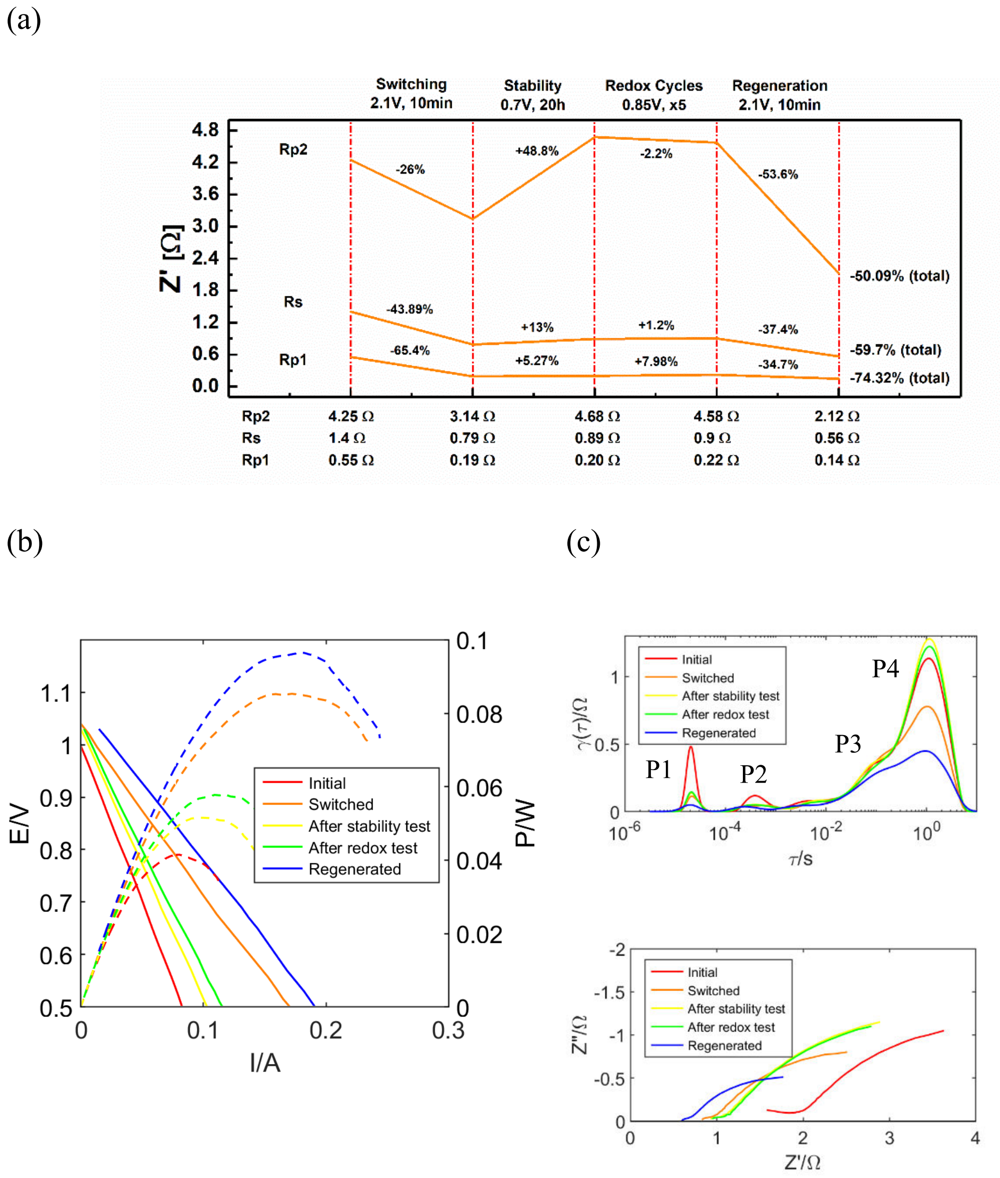

Figure 6-21: Regeneration tests of the cell after 20 h stability test and five redox cycles at 700 °C with 50 ml/min of wet H_2 in FE and atmospheric air in OE. (a) The resistance calculated from impedance data during every step of the test. (b) IV curves after reduction, switching, stability, redox and regeneration tests. (c) DRT and EIS curves after reduction, switching, stability, redox and regeneration tests.

The presented analysis indicates that, at least partially, the degradation process is reversible, as both polarisation and ohmic resistance recovered slightly after the redox cycles and even further improved after applying cathodic polarisation.

There are reports in the literature that help to understand these reversible phenomena. Irvine et al. [103] gave a comprehensive review of mechanisms taking place on 2PB and 3PB and pointed out that they are dynamic interfaces, with continuous irreversible “degradation” and reversible “passivation” changes influencing their electrochemical activity. On Ni/YSZ electrode, the regeneration process was achieved by redox cycles, using high anodic polarisation, followed by reduction, leading to the formation of fresh 3PB and improvement in SOFC performance [329]. Similarly, in the case of the experiment being discussed, discharging the cell at constant voltage and conducting redox cycles could lead to re-oxidation of Ni or/ and MIEC fuel electrode, whereas high cathodic polarisation led to re-arrangement even formulation of fresh 3PB between Ni and MIEC. The exsolved nickel electrode has the advantage in this process, as there is no significant volume change during the cycles. In contrast, in Ni-YSZ anode, if cycles and electrode microstructure are not well controlled, the process threatens irreversible damage of the electrode[329]. Summing up, the possibility of recovering the losses in SOFC devices has a large practical application, significantly increasing their lifetime.

6.5.2 Tubular cells with composite LCNT/YSZ50 FE and impregnated LSF/P-YSZ OE.

6.5.2.1 Temperature dependence, before and after switching. Equivalent circuit with Gerisher element.

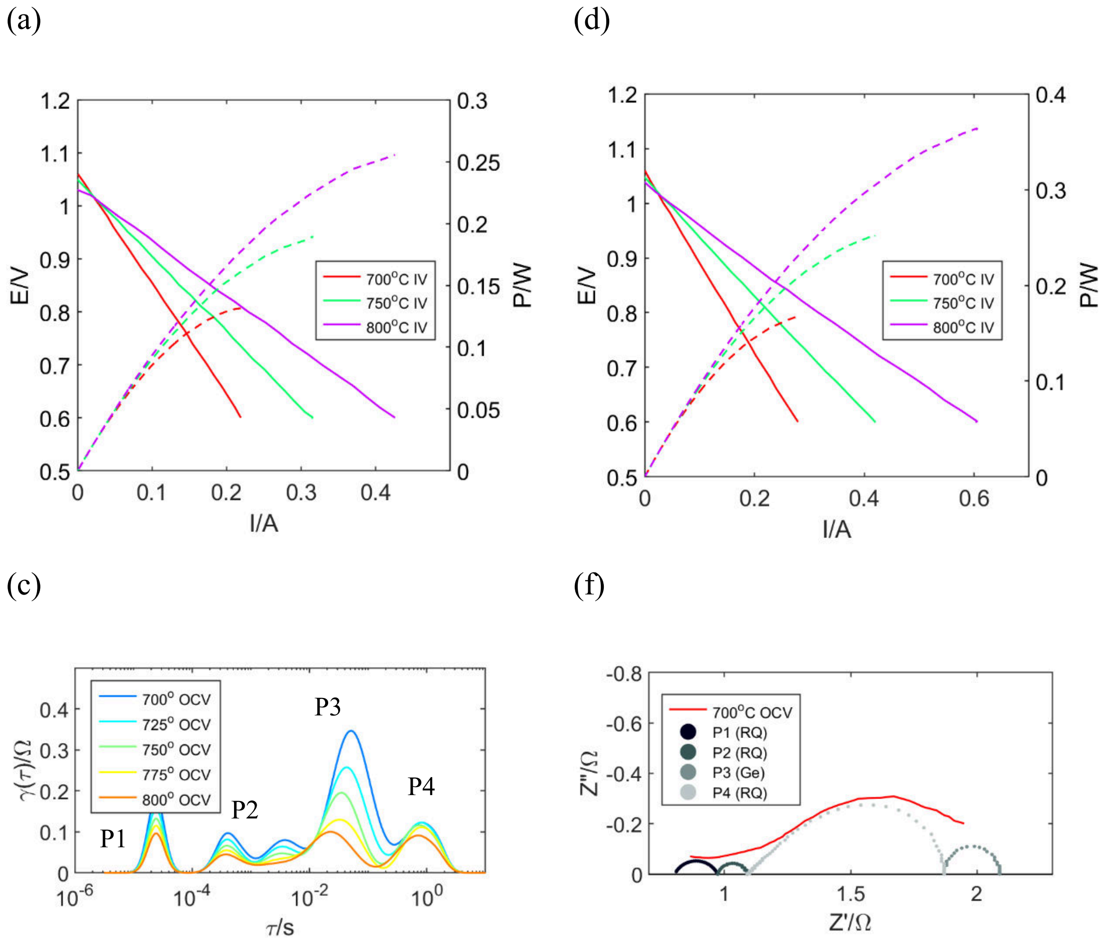

Figure 6-22: I-V curves analysis of the cell operating in FC mode at OCV, at 700 – 800 °C with 50 ml/min of wet H_2 in FE and atmospheric air in OE. (a) before switching, and (b) after switching. (c) DRT before switching. (d) The equivalent circuit used for the analysis.

The cells were tested at 700 – 800 °C with 50 ml/min of wet H_2 in FE and atmospheric air in OE. The DRT of fuel cell operation (Figure 6-22 c) shows at least four distinct processes, already described in Chapter 5.5.3.3. DRT pattern shows the change of the resistive contribution on both electrodes. However, LSF, compared to LCNT, has a low polarisation (around 0.02 Ω at 800 °C) that could be neglected when investigating the fuel electrode kinetics; DRT of LSF has only one peak at a very high frequency, which would merge with much more resistive process P1 on the fuel electrode.

After measuring the resistive contribution of polarisation processes from arc fitting to DRT pattern and their characteristic frequency, it was possible to evaluate them using the CNLS fitting in Z-View software [62]. The equivalent circuit consists of Rs related to ohmic losses in the cell and is modelled by an ohmic resistor, P1 and P2 modelled by two “R/CPE” elements and P3 modelled by a Gerischer element and the low-frequency process P4 also modelled by “R/CPE”.

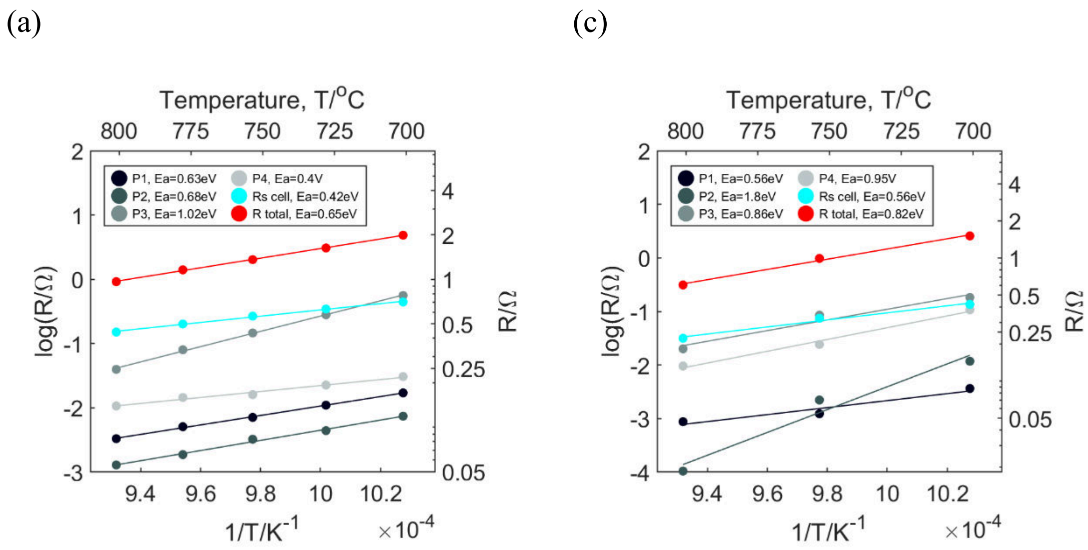

Figure 6-23: Arrhenius plot of ohmic and polarisation resistance (a) After gas reduction. (b) After electrochemical switching at 2.1 V for 2 min at 800 °C.

When analysing cells with composite oxygen electrode, an equivalent circuit made of three semi-circles were used to fit impedance data (Chapter 5.5.3.4). As processes from both electrodes were relatively large on the whole frequency range and had reasonably close characteristic frequencies, the fitted elements represented rather a sum of the responses from electrodes, not any specific process on one of them. In the present cell, the polarisation resistance at low frequency would not merge with the polarisation of the oxygen electrode; therefore, a general semicircle could be replaced with the more fundamental element, such as Gerisher, which, besides resistance or capacitance, describes the kinetics of the specific diffusion process.

The Gerischer or chemical impedance has been frequently observed in MIEC electrodes; it describes a semi-infinite Faradaic diffusion connected with a side reaction that changes their concentration on the diffusion path, e.g., forming electrochemically inactive complexes [317] or migratory species changing into immobile/ inactive species [319]. Adler modelled LSCF oxygen electrode response with Gerischer, where bulk diffusion was coupled with the surface exchange process [198]. Another interpretation by Atangulov et al. [330] can explain a slow adsorption process of H species coupled with surface diffusion, where the reaction term is related to adsorption. Hildenbrand et al. studied the impedance of lanthanum nickelates SOFC cathodes and derived a Gerischer response for the dissociative/ adsorption process coupled with surface diffusion [319]. Hussain et al. used Gerischer to interpret impedance on strontium titanate based SOFC with nano-sized palladium and gadolinium-doped ceria oxide [320]. Blennow et al. [311] also used Gerischer to evaluate the process on strontium titanate based SOFC anode, which according to the Author's mechanism, was also attributed to surface diffusion of oxygen ions in combination with oxygen exchange at the surface and 3PB; or surface diffusion of hydrogen species coupled with hydrogen exchange on the surface. The element was also derived for a surface exchange process on the MIEC electrode, where poor electronic conductivity gave a Gerischer response [318].

It is not simple to assign the element to a specific process. The bulk diffusion of oxygen ions and surface exchange proposed by Adler is not likely, as titanates could have too low ionic conductivity for bulk diffusion to be a dominant process [311]. Instead, following a model proposed by [311], the surface diffusion of oxygen ions or/ and hydrogen species could be the primary mechanism behind dispersion, as defect concentration on the surface is considered higher than in bulk.

The element can be directly derived from Fick's second law by considering a reaction term [317], [331]:

$$\frac{dc(x,t)}{dt} = \widetilde{D}\frac{d^2c(x,t)}{dx^2} - k \times c(x,t) \qquad \textbf{Equation 6-1}$$

where $\boldsymbol{c(x,t)}$ would be excess concentration above the equilibrium constant and $\boldsymbol{k}$ is the reaction rate of the side reaction resulting in concentration change, $\boldsymbol{\tilde{D}}$ is a diffusion coefficient of the mobile species along $\boldsymbol{x}$ coordinate.

The general impedance expression for Gerischer is:

$$Z_{Geri.}(\omega) = \frac{Z_0}{\sqrt{k+j\omega}} \qquad \textbf{Equation 6-2}$$

where $\boldsymbol{k}$ is the reaction rate and $\boldsymbol{Z_0}$ is inversely proportional to the diffusion coefficient and depends on material stoichiometry and surface area [319]. Hildenbrand [319] derived a detailed expression for those parameters by rearranging equations in Adler's model [332]:

$$Z_0 = \frac{RT}{4F^2 c_0 x_v^0 (1-\varepsilon)} \sqrt{\frac{A^0}{D_v(1+2v)}} \qquad [\Omega \times \mathrm{cm}^2 \times \mathrm{s}^{1/2}] \qquad \textbf{Equation 6-3}$$

where $\boldsymbol{c_0}$ and $\boldsymbol{x_0}$ are the molar concentration of oxygen lattice sites, oxygen vacancies at a given temperature, and $\boldsymbol{D_v}$ is the vacancy diffusion coefficient. $\boldsymbol{A_0}$ is the thermodynamic factor that expresses a relation between pO_2 and oxygen non-stoichiometry, $\boldsymbol{\varepsilon}$ is the porosity, and $\boldsymbol{v}$ is the dimensionless ratio between surface diffusion and bulk transport.

$$k = \frac{4A^0 a R_0}{c_0 x_v^0 (1-\varepsilon)} \qquad [\mathrm{s}^{-1}] \qquad \textbf{Equation 6-4}$$

where $\boldsymbol{R_0}$ is the overall surface exchange rate of oxygen atoms in [mol×cm^{-2}×s^{-1}], and $\boldsymbol{a}$ is the surface area.

The Gerischer parameters for temperature dependence measured at OCV were obtained from fitting and plotted on the Arrhenius plot, where $Y_0 = Z_0^{-1}$. Showing enlargement of $\boldsymbol{Y_0}$ with higher temperature and after switching, where according to eq. 6-3 a parameter would illustrate the kinetics of species transport, which could improve due to the generation of oxygen vacancies and increased diffusion coefficient. The parameter $\boldsymbol{k}$ also seems to indicate some degree of thermal activation, as $\boldsymbol{c_0 x_v^0}$ would increase at higher temperatures, its enlargement must be related to increased kinetics of the overall surface exchange rate of oxygen atoms, $\boldsymbol{R_0}$, eq. 6-4.

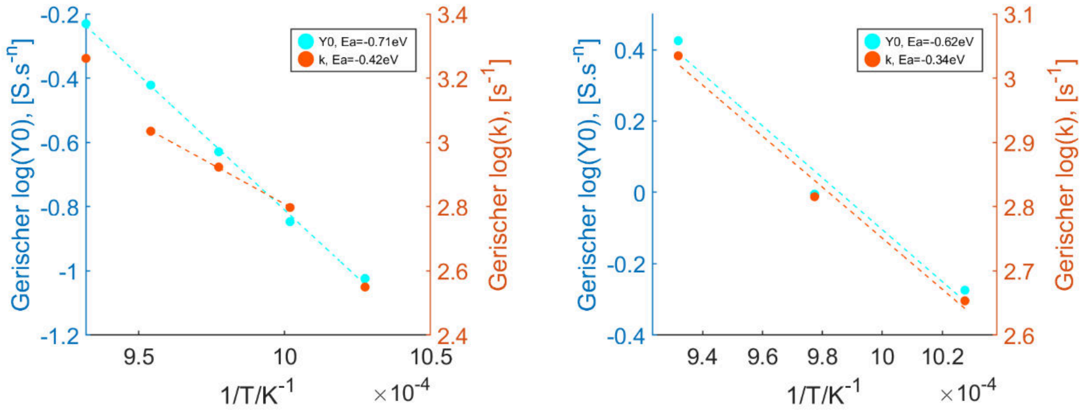
(b)

(d)

Figure 6-24: Gerischer parameters of P3 of the tubular cell with LCNT/YSZ composite electrode and LSF/P-YSZ oxygen electrode. (a) After gas reduction. (c) After electrochemical switching at 2.1 V for 2 min at 800 °C.

6.5.2.2 *Switching characteristics on the wide potential range*

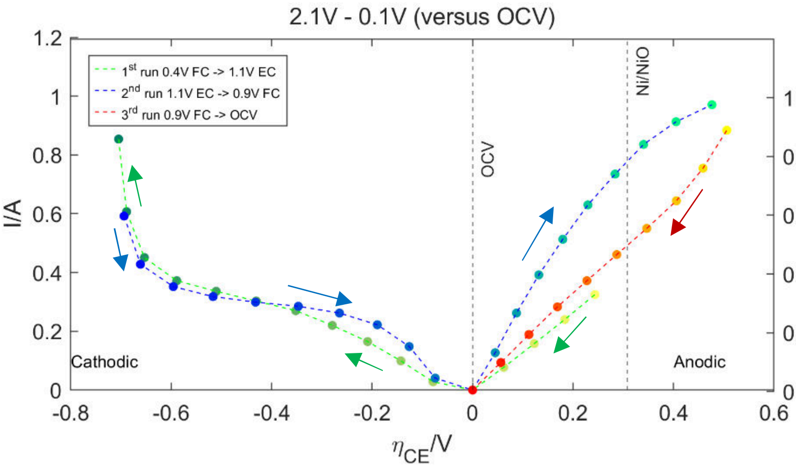

Figure 6-25. The plot of the generated current versus overpotential applied on the fuel electrode at 800 °C with 50 ml/min of 3% H_2O/H_2 in FE and atmospheric air in OE.

The experiment is designed to investigate how switching affects the performance of the redox process in the electrochemical cell. The cell was heated up to 800 °C and reduced for 2 hours at 50 ml/min 3% H_2O/H_2. Afterwards, the cell was measured with EIS and potentiostatic analysis. In the procedure, the potential was applied at 0.1V intervals. At every step, the cell was stabilised for 2 min at potentiostatic, and EIS was taken (which also took just above 2 minutes).

Figure 6-25 shows the dependence of overpotential on the fuel electrode to the generated current during all steps. The potential was applied from 0.4 V voltage bias in a fuel cell (FC) mode up to 1.1 V voltage bias in electrolysis mode (EC) mode at the first run. This measurement showed the cell's performance after gas reduction in FC and EC mode and switching behaviour. At this stage, the reaction is catalysed only by Ni exsolved during gas reduction or at the testing potential. In the second run, the potential was decreased from 1.1 V voltage bias at EC mode down to 0.9 V voltage bias in FC mode, showing changes in EC and FC mode due to switching, e.g. increase of activity due to the exsolved catalyst or improved conductivity when back in FC mode from the high cathodic polarisation. In the third run, the potential was decreased from 0.9 V voltage bias at FC mode back to OCV. The third run was meant to show how oxidative conditions affect the performance of switched LCNT surface. During this step, when an overpotential in FC mode reaches a value above the partial equilibrium pressure for Ni oxidation (about 0.325 V overvoltage in FC mode, Ni will oxidise, lowering activity for fuel oxidation. The equilibrium potential of Ni/NiO was calculated from the equation 5-16 and marked on the plot. It gives a value of overpotential, above which exsolved Ni would be oxidised if present in the system.

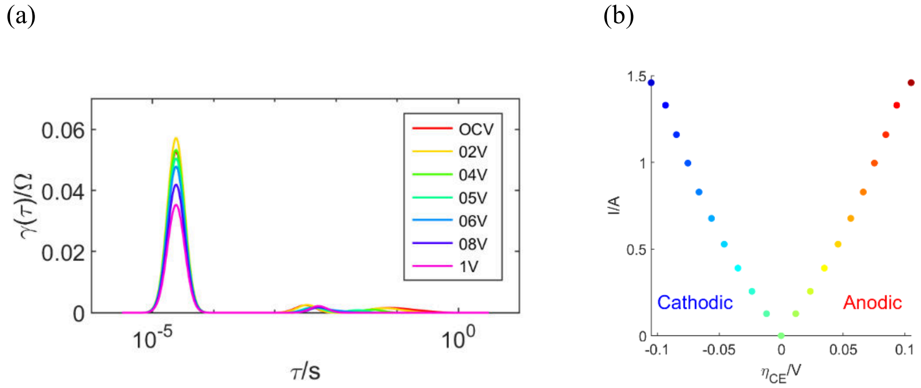

Figure 6-26: (a) DRT of impedance data of symmetrical LSF. (b) Overpotential at LSF. Data is normalized to fuel cell surface area (4 cm^2). Test under the atmospheric air.

The overpotential on the fuel electrode was calculated by the equation 5-12. The polarisation resistance of the LSF electrode was calculated from the experiment on the planar LSF cell, Figure 6-26. The measurement is not entirely accurate for the LSF electrode, as during the operation, the symmetrical cell becomes not symmetrical. Therefore polarisation will consist of both anodic and cathodic contributions, which gives different overpotentials on both sides of the cell [333]. Nevertheless, for the sake of the experiment, it is assumed that both anodic and cathodic overpotentials for LSF are equal at a specific applied DC potential. The overall polarisation on the LSF is small and will not bring significant error to the measurement.

The first run starts below the Ni oxidation point, the slope of the curve decreases exponentially down to -0.46 V of overpotential in EC mode. Likely, due to concentration losses for water electrolysis. Above this point rate of reaction changes, the generated current increases exponentially with applied voltage. The potential was lowered from the switching point at EC mode to FC operational conditions in the second run. When potential decreases, slightly less current is generated at a very high overpotential in EC mode. However, with lower overpotential in EC mode, the electrode activity for H_2O reduction improves. Also, when back in FC mode, more current is generated from H_2 oxidation after switching. The curve changes its slope at a higher overpotential in FC mode, showing a drop in activity for H_2 oxidation. In the third run, the potential is decreased back to OCV. When voltage is decreased, the curve does not follow the previous path. The activity seems to drop almost to the level before switching. Additionally, the curve appears to change its curvature from negative to positive.

To better understand the process on the fuel cell electrode, DRT was constructed from EIS data taken during every run for the whole potential range (Figure 6-27), showing all four processes already discussed in the previous chapter. The P1 and P2 processes behave similarly and seem to follow the behaviour of ohmic resistance. The ohmic resistance, Rs, decreases at higher cathodic polarisation owing to the n-conductivity of LCNT (eq. 1-36). Due to stripping oxygen from the LCNT lattice and increasing Ti^{3+}/Ti^{4+} pair concentration (eq. 5-6), Rs is permanently reduced after reaching very high cathodic polarisation (switching) when potential is decreased.

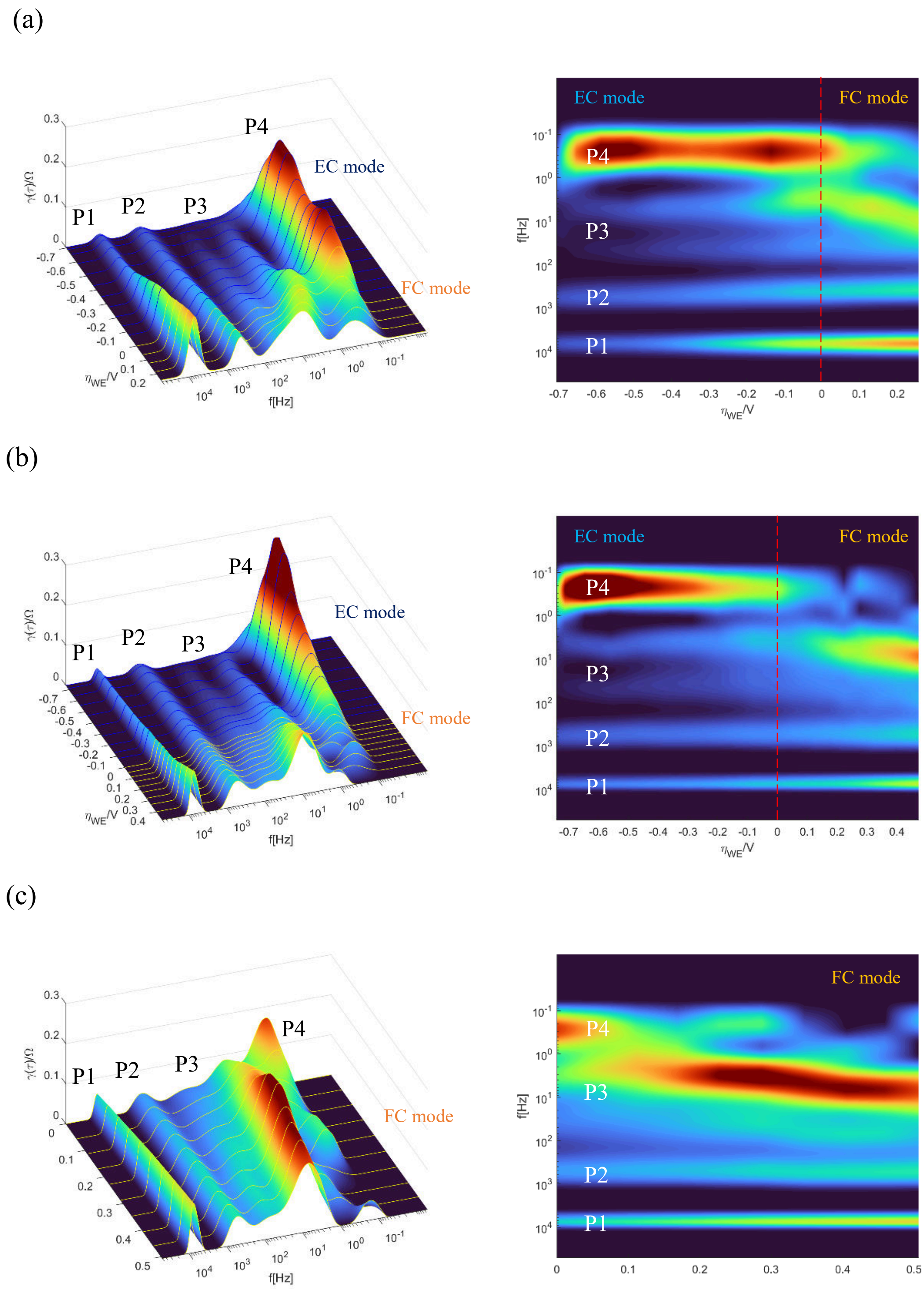

Figure 6-27: DRT of impedance data at 800 °C with 50 ml/min of 3% H_2O/H_2 in FE and atmospheric air in OE. (a) The first run, from 0.4V DC bias at FC mode to the switching potential at 1.1V DC bias in EC mode after 2 h of gas reduction. (b) The second run, from the switching potential at 1.1V DC bias in EC mode down to 0.9V DC bias in FC mode. (c) The third run, from the 0.9V DC bias at FC mode back to OCV.

The fact that P1 and P2 are affected by applied polarisation indicates processes related to defect stochiometry of LCNT. Processes are likely related to the charge transfer, and capacitance is related to double-layer capacitance, similarly as explained by Blennow et al. [311] for strontium titanate fuel electrodes. Author had found $(\boldsymbol{pO_2})^{-1/6}$ dependence, which deviated from mass action law which indicates $(\boldsymbol{pO_2})^{-1/4}$ dependence, eq. 5-9. The deviation was attributed to the surface governed mechanism (rather than the bulk). The surface region would probably be more reducible than the bulk; hence conduction would be governed by the surface process; and associated with the surface defect chemistry.

The kinetics of P3 increase at the cathodic polarisation, Figure 6-27 a. In electrolysis mode, the P3 minimally affects total polarisation resistance, while in FC mode, P3 is the main contribution and increases with higher potential. The P3 improves with the switching and is permanently reduced when back to fuel cell mode, Figure 6-27 b. P3 clearly indicates the diffusion process, with a peak at higher τ-values and a following small peaks for lower τ-values [334], the Gerischer element could fit it. The process is likely related to the surface diffusion of active species, as explained in the previous chapter. The surface transport and species exchange kinetics are controlled by defect stochiometry of LCNT, and oxygen ion diffusion would improve with a higher concentration of oxygen vacancies on the surface. Also, the presence of exsolved particles would improve the kinetics due to the faster rate of H_2 dissociation.

While the P3 likely reflects processes related to surface diffusion and species exchange, the P4 is somewhat sensitive to the gas conditions and seems to reflect the exchange process with the gas phase, where gas composition and rate of dissociative adsorption of H_2/H_2O could affect polarisation. The process increases at the electrolysis mode and is a dominant process, likely due to low H_2O concentration in a gas stream, while at the fuel cell mode when testing at high H_2 concentration, it gives a minimal contribution. After switching, P4 is reduced at working potential in electrolysis mode and fuel cell operation. At very high potential in EC mode height of the peak increase.

After applying the high anodic polarisation, Figure 6-27 c, the kinetics of P3 and P4 substantially decreased, but ohmic resistance, P1 and P2 were only slightly affected.

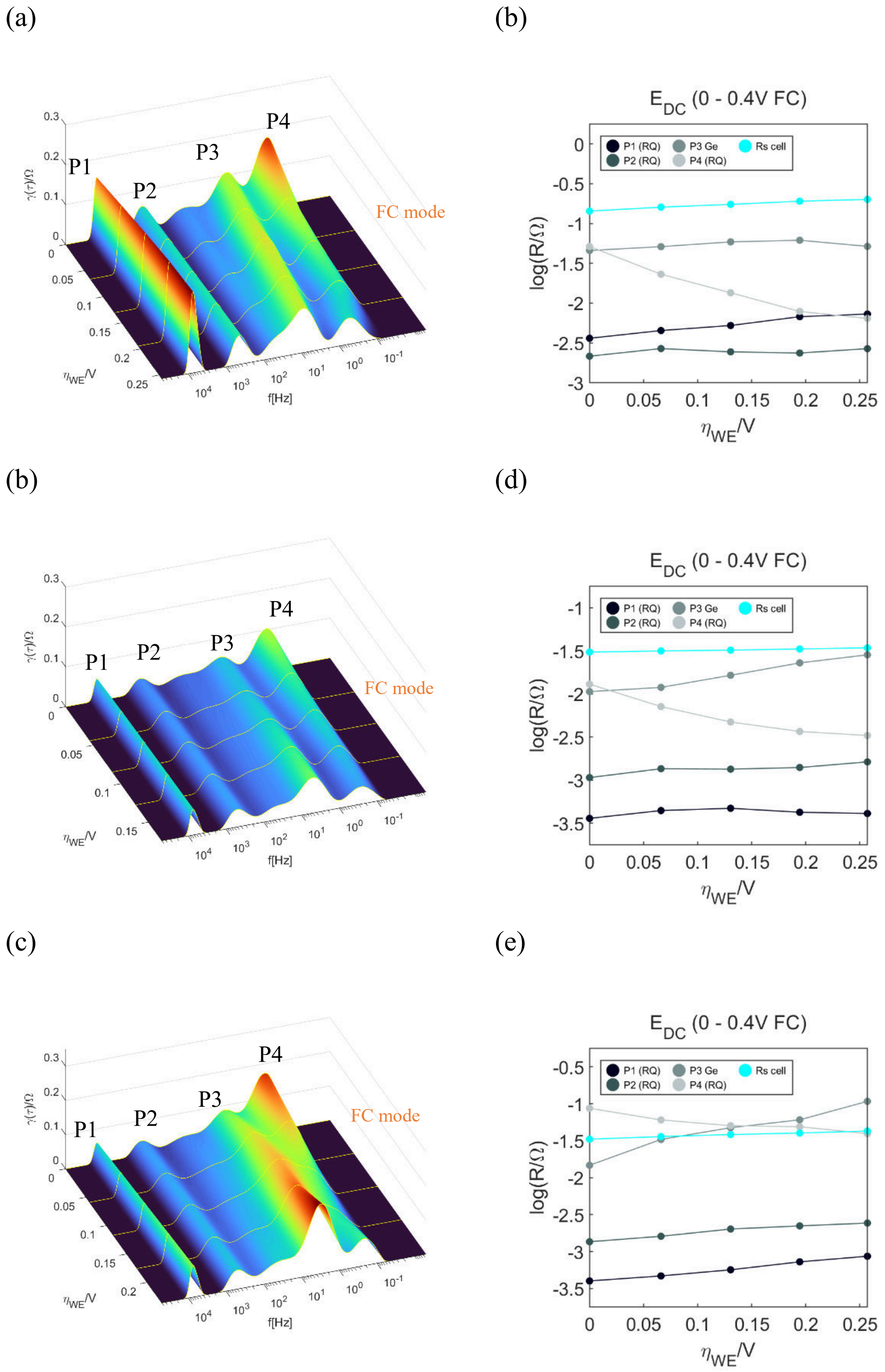

Figure 6-28: DRT analysis and resistive contribution of cell operating at FC mode, from OCV to 0.4 V applied potential, at 800 °C with 50 ml/min of 3% H_2O/H_2 in FE and atmospheric air in OE. (a) – (b) At the 1st run, after 2 h gas reduction. (b) In the second run, after switching at high cathodic polarisation. (c) In the 3rd run, after anodic polarisation.

The DRT of the fuel cell operation up to 0.4 V applied DC voltage bias during all three runs, shown in Figure 6-28, with calculated overpotential on the fuel electrode and ohmic and polarisation resistance calculated from the same equivalent circuit as for temperature dependence (Figure 6-22 f). After the second polarisation run (switching), the kinetics of the P3 and P4 processes increase significantly, and much more DC current is generated. The reduction of P3 and P4 must be attributed to improved kinetics on the LCNT surface, e.g. due to the catalytical activity of exsolved Ni and generation of oxygen vacancies; it may also be affected by the higher ionic and electronic conductivity of LCNT.

According to the adopted mechanism, the P4 is believed to reflect losses from the gas conversion on the perovskite surface. At the fuel cell operation, the P4 will be affected by the dissociative/ adsorption process of H_2 gas on the perovskite surface (or at 3PB with YSZ), eq. 5-2, and dissociation of H_2 gas on exsolved Ni, eq. 5-5. The cell is tested at wet H_2; hence concentration losses due to low gas concentration are not expected; in fact, the P4 process decreases at higher anodic polarisation. The reduction of P4 could be due to the higher availability of adsorption sites for H_2 dissociative adsorption on perovskite oxygen sites or 3PB with YSZ (eq. 5-2). Perhaps, the conversion of absorbed hydrogen to water is sluggish, either due to poor exchange of oxide ions or electrons within the material or slow desorption coefficient, and kinetics improves under applied potential. Also, equation 5-6 shifts left; hence the fuel electrode will have a higher concentration of oxygen ions at the surface. The vacant sites also could be replaced by oxygen ions diffusing through the surface from 3PB [311].

P3 and P4 are somehow related; when P3 increases at a higher potential, P4 decreases almost at the same rate. Perhaps P4 is more favourable at a higher oxidation level of the surface, which improves the exchange rate with the gas phase while surface diffusion coupled with P3 deteriorates.

After the third run (the anodic swept), the low effect on ohmic and high-frequency polarisation resistance indicates that the high anodic polarisation almost did not change the MIEC conductivity. The P3 and P4 processes significantly deteriorate after anodic sweeping, and as the bulk properties seem not to change much with applied overpotential, their enlargement must be related to the surface process. Therefore, the worsening of the kinetics must be related either to the deterioration of the reaction (exchange) rate or surface transport. The oxidation of the NiO would decrease the rate of H_2 dissociation, hence could affect both P3 and P4. However, the nanoparticles should regain their activity after returning to more reductive conditions; meanwhile, the kinetics of both is permanently reduced, suggesting that polarisation could induce other changes affecting the catalytical properties of the material and species diffusion on the surface, than oxidation state of Ni. Figure 6-29 compares low-frequency processes, P3 and P4, during fuel cell operation on every run and Gerischer parameters of the P3 process. The polarisation processes and Gerischer parameters seem to depend on the applied potential, where, as explained in the previous chapter, $\boldsymbol{Y_0}$ is considered to reflect the transport properties of the surface, while $\boldsymbol{k}$ is the rate of exchange.

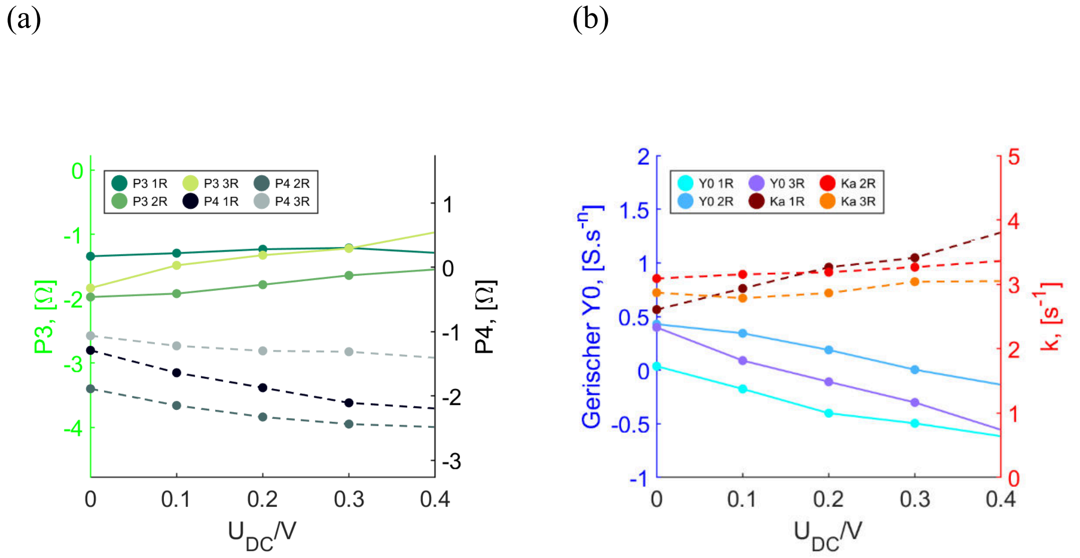

Figure 6-29: (a) The polarisation resistance of P3 & P4. (b) Gerischer parameters of P3 of cell operating at FC mode, from OCV to 0.4 V applied potential at 1st, second and 3rd run (1R, 2R, 3R).

At higher anodic polarisation, $\boldsymbol{Y_0}$ decreases while $\boldsymbol{k}$ increases. Anodic polarisation increases the molar concentration of the oxygen sites $\boldsymbol{c_0}$ and decreases the molar concentration of oxygen vacancies $\boldsymbol{x_0}$ at a given temperature; hence, the change of Gerisher parameter $\boldsymbol{Y_0}$ could be related to the decrease of $\boldsymbol{c_0\ x_0}$ in eq. 6-3, as $\boldsymbol{Y_0 \sim c_0\ x_0}$. Also, assuming that the transport of species processes through oxygen vacancies, the vacancy diffusion coefficient, $\boldsymbol{D_v}$, would decrease due to a lower concentration of $\boldsymbol{x_0}$, and $\boldsymbol{Y_0 \sim \sqrt{Dv}}$. Whereas the Gerisher parameter $\boldsymbol{k}$ would increase due $\boldsymbol{k \sim (c_0 x_0)^{-1}}$ and $\boldsymbol{k \sim R_s}$, eq. 6-4.

Both parameters increase after the switching; however, ***k*** changes its slope; thus, it is lower above 0.2 V of applied DC voltage than before switching. Nevertheless, the polarisation resistance from P3 is reduced due to the improvement of the transport rate of species taking part in the reaction. After applying high anodic polarisation in the third run, perhaps due to a higher concentration of oxygen sites on the surface, $\boldsymbol{Y_0}$ decrease, but not to the level before switching; ***k*** seems to be reduced to the level below the switching and has lower activation; overall, increasing polarisation resistance of P3. Unlike in P3, the polarisation resistance from P4 decreases at the higher anodic polarisation. In FC mode, it is believed that P4 is proportional to the concentration of H_2 gas and the concentration of oxygen ions on the surface and the overall exchange rate. The reduction of P4 polarisation after switching and a significant increase in 3rd run could be due to changes in the exchange rate.

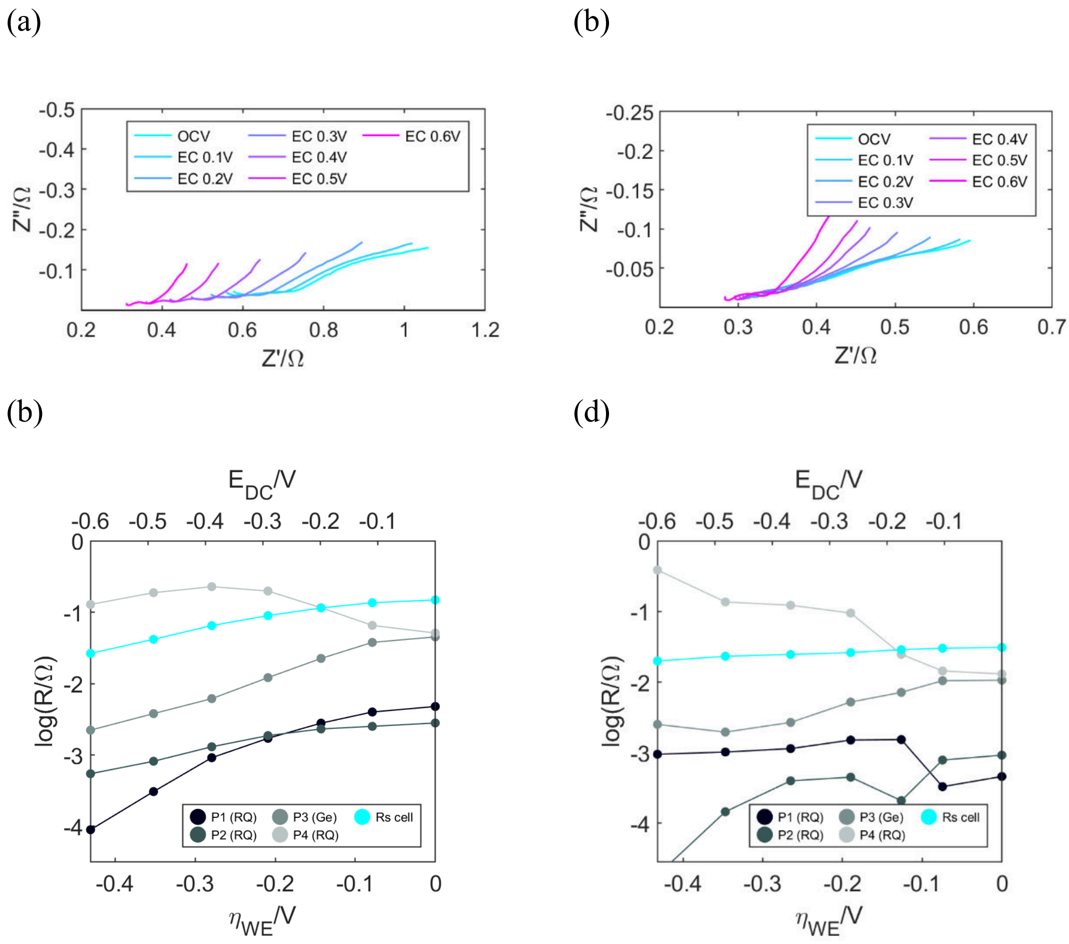

Figure 6-30: EIS analysis and resistive contribution of cell operating at EC mode, from OCV to 0.6 V applied potential at 800 °C with 50 ml/min of $3\%H_2O/H_2$ in FE and atmospheric air in OE. (a) – (b) At the 1st run, after 2 h gas reduction. (c) – (d) At the second run, after switching at high cathodic polarisation.

Figure 6-30 includes EIS of the electrolysis cell operation at a moderate potential between OCV and 0.6 V applied DC voltage bias, before and after switching, with calculated overpotential on the fuel electrode and ohmic and polarisation resistance calculated from the equivalent circuit (Figure 6-22 f). The P4 is the main contribution to water electrolysis at moderate potential and likely comes from a low concentration of H_2O in the fuel stream, which is about 3%, which indicates that P4 is affected by gas concentration. At the electrolysis mode, P4 would be connected to the adsorption of H_2O on perovskite's surface oxygen vacant sites, where both water concentration and availability of oxygen vacancies could become RDS. The large capacitance of the P4 process may also include chemical capacitance (current is stored in chemical energy of electrode); hence capacitance could increase after switching as the material is reduced.

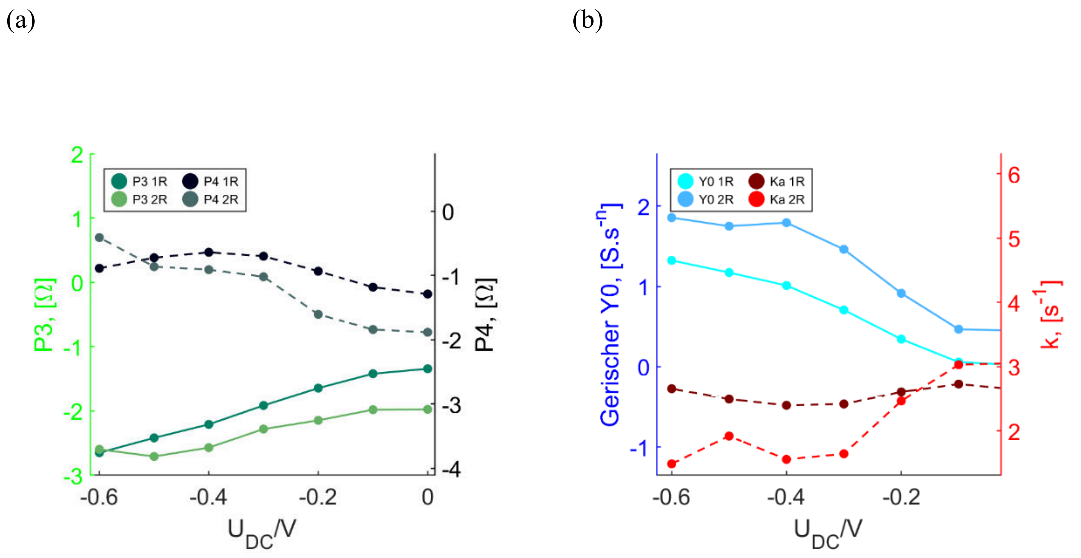

Figure 6-31: (a) The polarisation resistance of P3 & P4. (b) The fitting parameters from Gerischer of cell operating at EC mode, from OCV to 0.6V applied potential at the 1st run, after 2 h gas reduction and at the second run, after switching at high cathodic polarisation.

Figure 6-31 compares low-frequency processes, P3 and P4, and Gerischer parameters of the P3 at the moderate potential before and after switching. After the switching, polarisation resistance decrease in both processes. The Gerischer parameters, Figure 6-31 b, indicate that improvement of P3 is related to faster diffusion of species, likely due to a greater extent of surface reduction, even though the rate of species exchange decreased. The improvement of P4 after switching could be related to the generation of oxygen vacancies at the surface, hence more adsorption sites for H_2O from the gas phase.

Figure 6-32 shows the EIS of the electrolysis cell operation at a very high potential between 0.6 V and 1 V applied DC voltage bias before and after switching, the kinetics of P4 seems to change, and P4 is getting reduced; the change is quite remarkable as P4 from dominant process reduces to a very low value, especially on the switching potential where P4 is almost entirely, reduced.

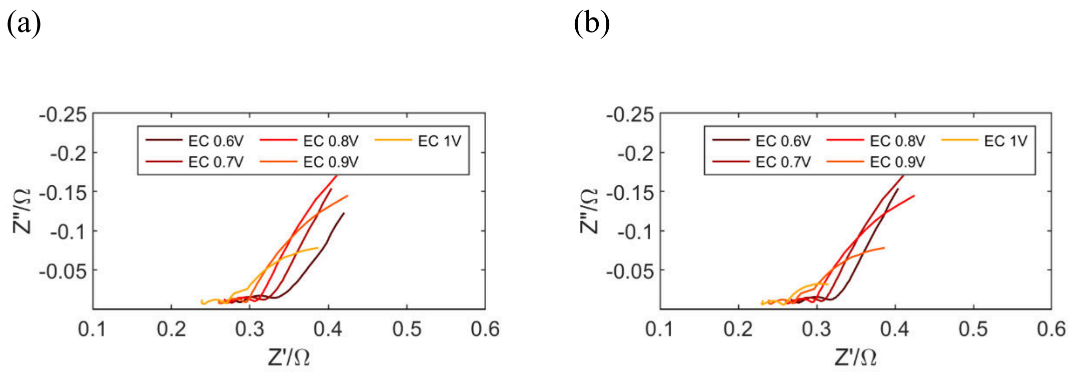

Figure 6-32: Impedance analysis of cell operation at EC mode, from 0.6 V to 2.1 V applied potential (switching) at 800 °C with 50 ml/min of 3%H_2O/H_2 in FE and atmospheric air in OE. (a) At the 1st run, after 2 h gas reduction. (b) In the second run, after switching.

6.5.3 Tubular cells with impregnated LCNT/P-YSZ FE and impregnated LSF/P-YSZ OE.

6.5.3.1 Evaluation of cell performance with fully impregnated electrodes.

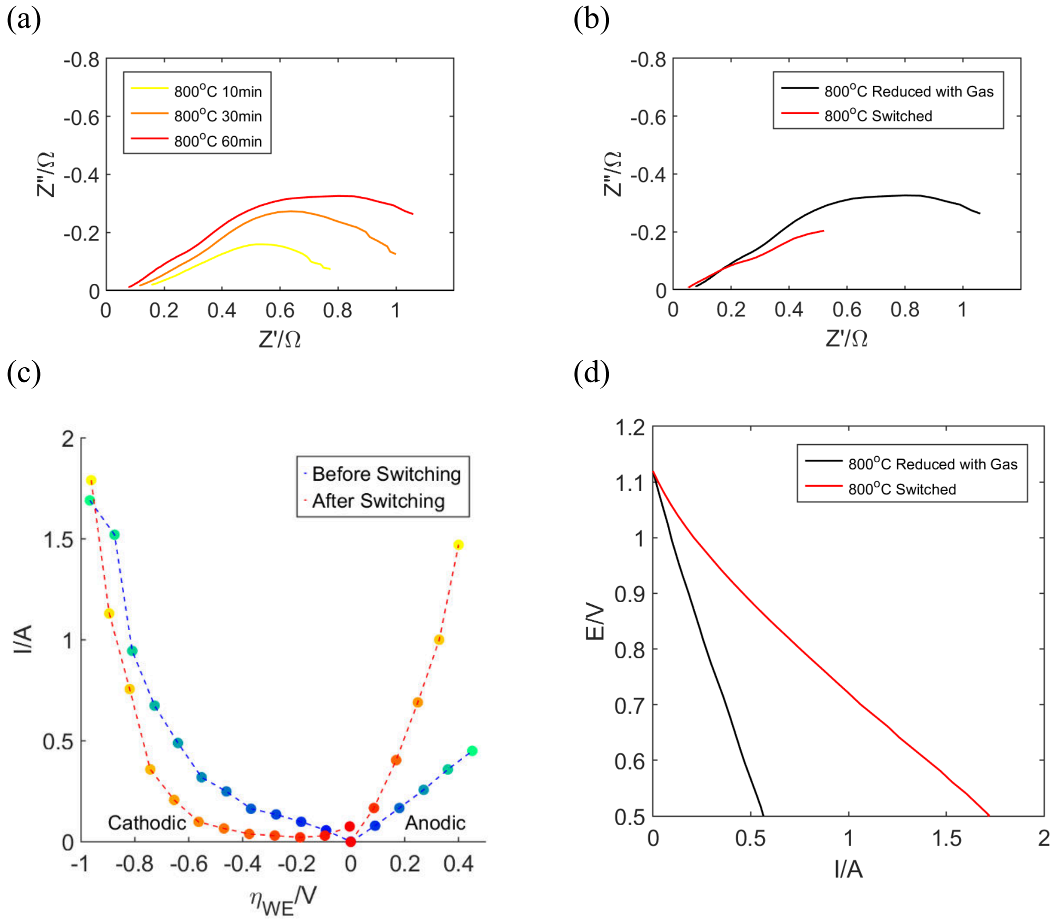

Figure 6-33: Electrochemical test of the tubular cell with LCNT/P-YSZ FE sintered at 1100 °C, tested at 800 °C in 50 ml/min 3% H2O/H2 in FE and atmospheric air in OE. (a) EIS analysis at OCV during a chemical reduction. (b) EIS analysis at OCV after a chemical reduction and switching. (c) The generated current versus overpotential on the fuel electrode during the switching. (d) I-V characteristic of the cell after a chemical reduction and switching.

For the cell preparation, the porous YSZ (P-YSZ) was impregnated with LSF at the oxygen side and LCNT for the fuel electrode, as explained in Chapter 3.7. At the last step, LSF was calcinated at 850 °C, while LCNT was at 1100 °C. For a fuel cell operation, wet hydrogen (3% H_2O/H_2) was used as the fuel with a 50 ml/min flow rate and ambient air was used as the gas for the oxygen electrode. Before electrochemical switching, the fuel electrode was reduced in a wet hydrogen atmosphere at 800 °C for 1 h. Then, the switching was applied at 800 °C in a three-step process: (1) The stair-step up to 2.1 V from the open-circuit voltage (OCV) with 40 mV/5sec potential step. (2) Electrochemical polling at 2.1 V for 2 min. (3) The stair-step down to OCV from 2.1 V with 40 mV/5-sec potential steps. Figure 6-33 a shows the tubular cell's EIS characteristic during a chemical reduction in wet H_2 (3% H_2O/H_2). After the reduction for about one hour, the EIS stabilized and presumably, the electrode material was in equilibrium, or close to, with the gas atmosphere. The ohmic and high-frequency polarisation resistance decreases during the process, while, contemporary to expectations, P3 and especially P4 increased. It seems that the chemical reduction gave rise to the passivation phenomenon that changes the perovskite surface properties, lowering activity for gas conversion. At least, the OCV conditions suggest that. During the process, the absorption sites on the oxygen sites would be gradually filled by hydrogen. Perhaps, if the conversion of absorbed hydrogen to water is sluggish, either due to poor exchange of oxide ions or electrons within the material or slow desorption coefficient, part of the adsorption sites would be blocked by the hydroxyl ions itself; thus, polarisation resistance will increase, as it is in this case.

Figure 6-33 b shows the EIS analysis at OCV of the cell after the switching procedure. All resistive contributions seem to be reduced; however, low polarisation processes decreased, unlike after chemical reduction. Figure 6-34 d shows the I-V characteristic of the cell after gas reduction and switching procedure. After switching, three times more current is generated at 0.5 V in fuel cell mode. Both curves seem to decrease their slope at a higher current, but the switched cell to a higher degree.

Figure 6-33 c shows the dependence of the generated current versus overpotential applied on the fuel electrode during the switching at 800 °C. The overpotential on the fuel electrode (η_{WE}) was calculated from dependence: $\eta_{WE=}U_{DC}-I_{DC}(R_{rig}+R_{YSZ})-\eta_{WE}$, where U_{DC} is applied voltage bias, I_{DC} generated current, R_{rig} is rig's ohmic resistance, R_{YSZ} is theoretical YSZ ohmic resistance, and η_{CE} is the overpotential on LSF oxygen electrode calculated from the test on planar cell; with the assumption of 6cm^2 of tubular's cell surface area. The behaviour is very different from the composite cell (Figure 6-25), especially in EC mode after switching. In the cell with co-sintered composite LCNT/YSZ50 fuel electrode, current after switching increased at the moderate potential in the electrolysis mode, while here decreased, showing the worst electrode kinetics for water electrolysis after electrochemical poling. As shown next, similar processes could be recognised on the impregnated electrode as in composite cell; perhaps the worst kinetics could be due to a decrease of Gerisher parameter ***k*** of the P3 process, where species exchange is coupled with surface diffusion. In the composite cell, ***k*** decreased; however, $\boldsymbol{Y_0}$ increased significantly, hence overall improvement; perhaps on the impregnated electrode change of ***k*** determinates polarisation, decreasing overall activity. According to the mechanism shown in Chapter 5.5.1, a lower activation level could be related to a lower oxidation level of perovskite surface for sorption of hydrogen species from water dissociation in eq. 5-4 after switching. The differences in fuel electrode microstructure likely changed the mechanism of gas conversion; thus, differences in functionality of impregnated and composite electrodes; the impedance data were not taken at electrolysis mode; therefore, the exact reason is not known. As Figure 6-11 shows, LCNT creates a thin coating on the whole YSZ scaffold; therefore, the reaction zone must be on the LCNT surface rather than on 3PB. Also, the oxygen ion transport in fuel cell operation to the reaction zone from the YSZ electrolyte must involve bulk, as this is the only possible path. Perhaps, the deficiency of oxygen sites in an impregnated electrode on the LCNT surface becomes determining (in contrast to the composite electrode where oxygen ions are provided from 3PB).

The tubular cell's open-circuit voltage (OCV) after switching at 700-800 °C was above 1.1V at the whole temperature range, suggesting a good tightness (Figure 6-34 a). The I-V curve slope decreases at a higher potential, indicating improved electrode kinetics. The maximum power density decreased from 0.87 W at 800 °C at 0.6 V to 0.35 W at 700 °C. Compared to the cell with a composite LCNT/YSZ50 electrode shown in Chapter 6.5.1, more than two times of maximum power is generated after electrochemical switching at 800 °C. It is accepted here that the cell's polarisation mainly comes from the LCNT impregnated fuel electrode. As explained in the previous chapter, the symmetrical planar cell with oxygen electrodes was analyzed separately (Figure 6-26). The calculation indicates that one oxygen electrode layer showed a value of polarisation resistance not higher than 0.02 Ω at 800 °C, located at a very high frequency. The same equivalent circuit was adopted as in composite cell, containing two semicircles to model P1 and P2, Gerischer reflecting polarisation of the P3 process and P4 modelled by a semicircle.

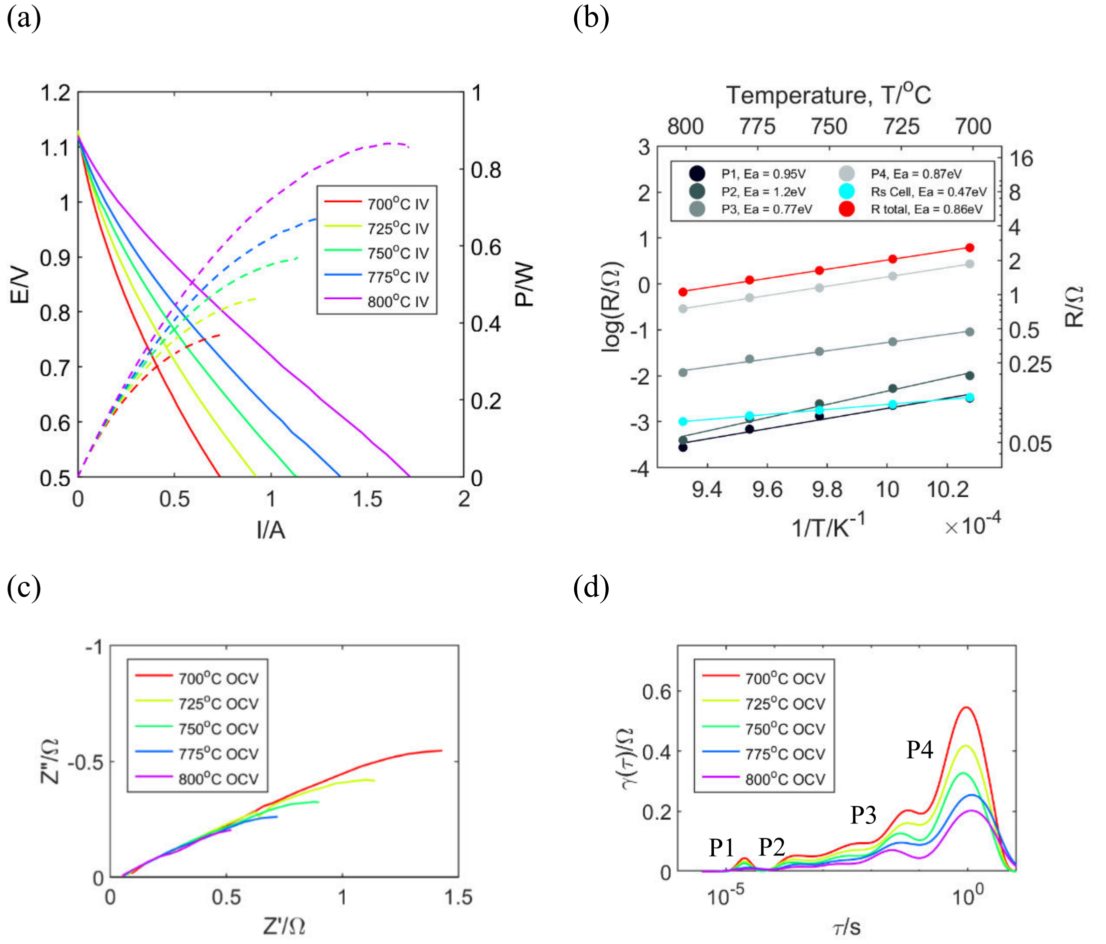

Figure 6-34: Electrochemical test of the tubular cell after switching at 800°C, tested at 700-800 °C with 50 ml/min 3% H2O/H2 in FE and atmospheric air in OE. (a) I-V curve of cell operating in fuel cell mode at various temperatures. (b) Arrhenius plot of cell's resistance at OCV. (c) EIS analysis at OCV. (d) DRT calculated from EIS.

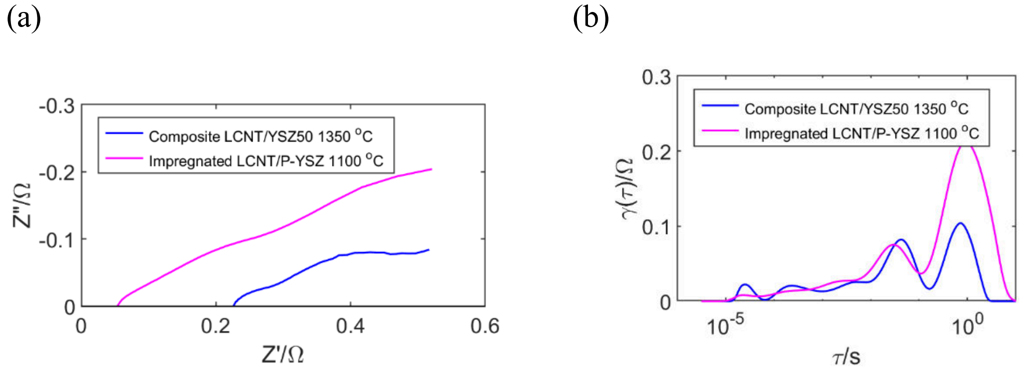

Figure 6-35: Comparision of impedance analysis of tubular cell with co-sintered LCNT/YSZ50 FE and with impregnated LCNT/ P-YSZ FE after switching at 2.1 V for 2 min, with 50 ml/min 3% H2O/H2 in FE and atmospheric air in OE. (a) EIS analysis at OCV. (b) DRT analysis at OCV.

Figure 6-34 b shows the Arrhenius Plot of the cell's ohmic and polarisation resistance, calculated from the equivalent circuit. The cell's ohmic resistance (Rs) calculated from the equivalent circuit increases from 0.05 Ω at 800 °C to 0.085 Ω at 700 °C. Rs is the sum of electrolyte resistance and both electrodes after extraction of rig's resistance which is about 0.1 Ω. The cell's ohmic resistance comes from two thick 100 µm electrode layers rather than the 20 µm electrolyte. The Rs minimally contribute to the total resistance; its low value indicates a good conductivity of functional materials. The total polarisation resistance at OCV increases from 0.79 Ω at 800 °C to 2.12 Ω at 700 °C. The P1 and P2 are also very low and likely reflect the same processes as the composite electrode. The P1 and P2 have a low value of 0.03 Ω at 800 °C, respectively. The P4 is the main contribution to the polarisation resistance at OCV with a value of 0.58 Ω at 800 °C and a characteristic frequency of 0.25 Hz; however, as shown later at the fuel cell's operating conditions, when testing on high hydrogen concentration, it is almost entirely reduced. The P3 process modelled by Gerischer has a resistance of about 0.14 Ω.

Figure 6-36 shows the EIS analysis of the tubular cell operating at the various potential in fuel cell mode after the switching procedure. The impedance data of switched cell was fitted according to the proposed equivalent circuit. However, due to fitting difficulties at higher voltage, two semicircles at higher frequency were replaced by a single semicircle (P1+P2), the calculated ohmic and polarisation resistance were plotted against the applied potential. The figure also contains the Gerischer parameters of P3.

There are some differences in the behaviour of individual processes, but there are also similarities in comparison to a composite LCNT/YSZ50 fuel electrode. The ohmic resistance increases minimally at anodic polarisation from 0.0475 to 0.056 Ω, and as previously, this enlargement could be attributed to LCNT defect stochiometry. In composite electrodes, high-frequency processes seem to follow ohmic resistance, increasing polarisation resistance at anodic polarisation. Similarly, in the cell with impregnated electrodes, after gas reduction. High-frequency processes increase with applied potential in FC mode; this is visible on DRT in Figure 6-36 a.

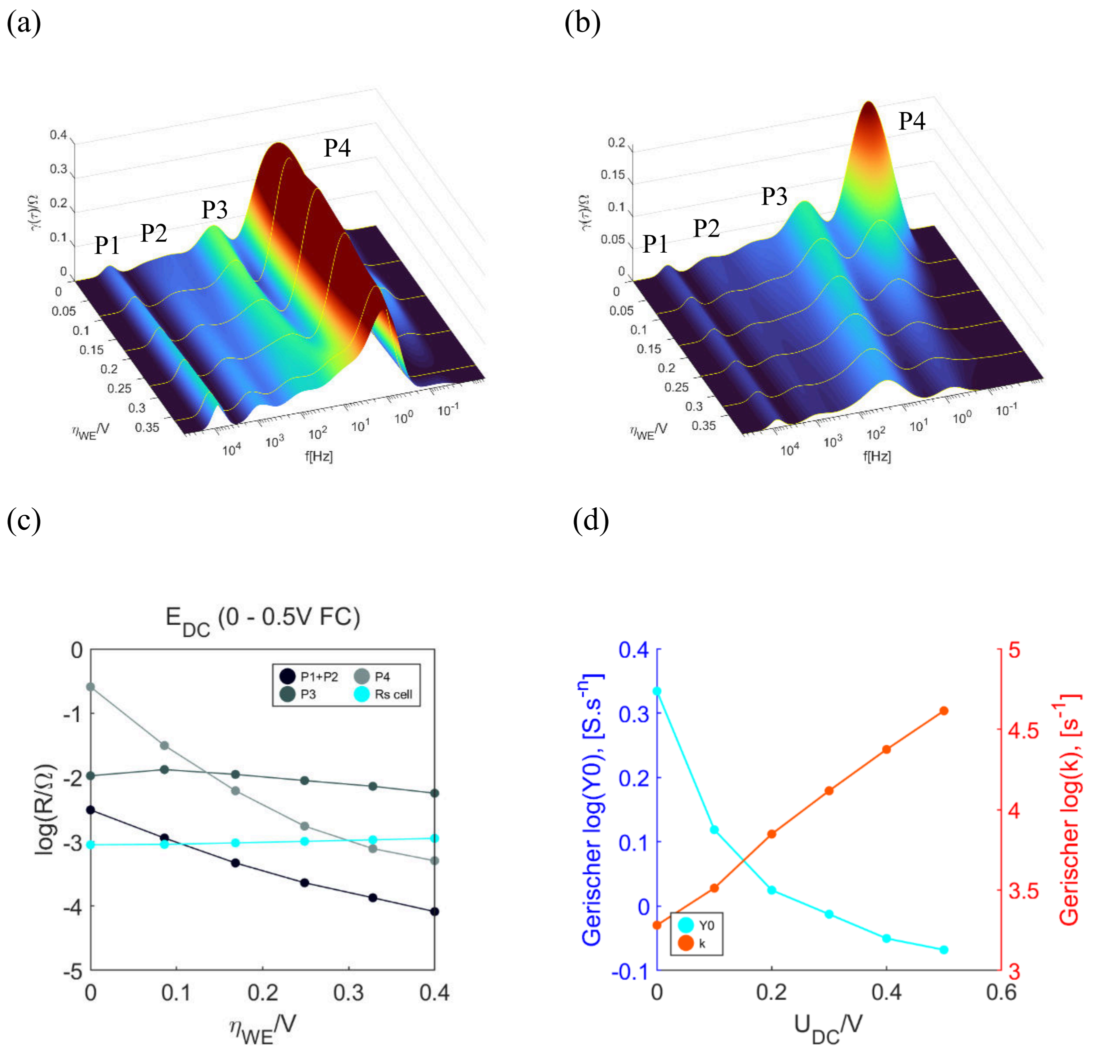

Figure 6-36: Voltage dependence. DRT at 800 °C from OCV to 0.5 V DC applied potential in FC mode of the cell, tested with 50 ml/min 3% H2O/H2 in FE and atmospheric air in OE (a) after gas reduction, (b) after switching at 2.1 V. (notice difference in scale). (c) Polarisation and ohmic resistance calculated from the equivalent circuit after switching, (d) fitted Gerischer parameters of P3 after switching.

After switching, the high-frequency processes seem to decrease. Both DRT and EIS indicate that; however, their low value may bring errors in evaluation. Perhaps a change of behaviour is related to better conductivity of electrode, e.g. change of RDS. Also, due to the reduction of overall polarisation, the processes on the LSF electrode could become visible, which is expected to affect polarisation at high frequency. P4 process is the main contribution after gas reduction and slightly decreases at the applied potential (Figure 6-36 a). After switching, the kinetics of the process improves. When potential is applied, the process is substantially reduced. The behaviour of the process after switching is similar to a composite electrode (Figure 6-28). The P3 is reduced at a higher potential, indicating different behaviour than in composite cells where P3 seems to increase. As previously ***Y0***, proportional to the diffusion coefficient decreases, while the reaction rate ***k*** increases; however, overall polarisation resistance decreases due to the much higher value of ***k*** in the impregnated electrode. As all polarisation resistance decreases at higher overpotential, the change of the I-V slope (Figure 6-34 a) is simple to explain.

Figure 6-37 shows a comparison of the low-frequency process and Gerisher parameters of P3 at FC operation. P4 behaves similarly, decreasing on the whole frequency range; its resistive contribution in an impregnated electrode exceeds that in composite at OCV condition, which is also visible in Figure 6-35; but the rate of its reduction at potential is higher and eventually above 0.2V DC bias in FC mode P4 is lower than in composite electrode. The behaviour of P3 under the applied potential shows some differences in both types. It gives almost the same resistive contribution at OCV conditions, but, contemporary to composite cell, the P3 decreases at the higher potential in FC mode.

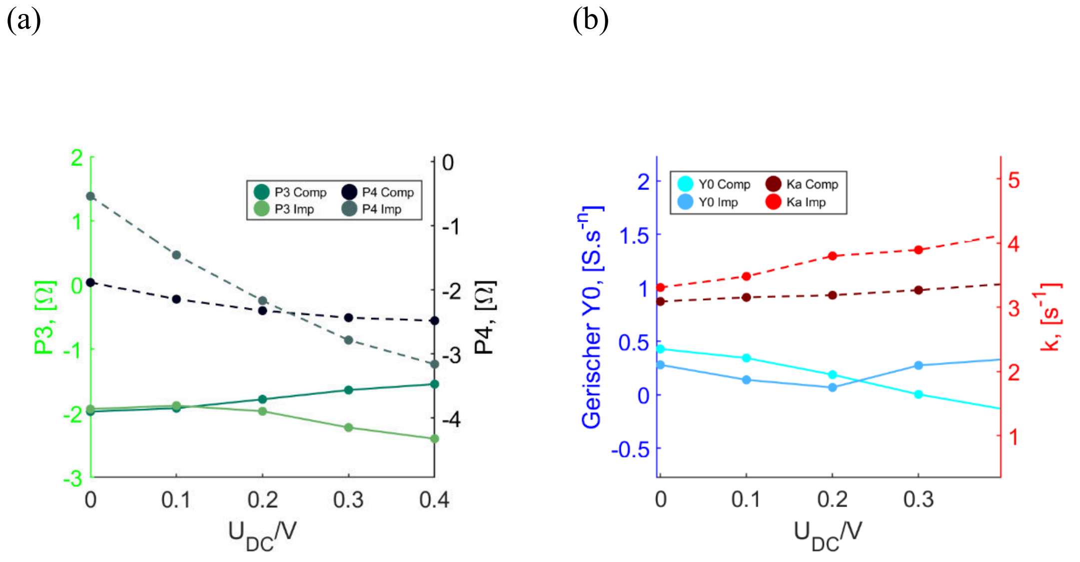

Figure 6-37: Comparision of impedance analysis of tubular cell at the applied potential in FC mode, with co-sintered LCNT/YSZ50 FE and with impregnated LCNT/ P-YSZ FE after switching at 2.1V for 2 min at 800 °C, tested with 50 ml/min 3% H_2O/H_2 in FE and atmospheric air in OE. (a) Comparison of P3 and P4's polarisation resistance. (b) Comparison of Gerisher elements.

The parameter ***k*** has a comparable value at OCV for both electrodes; however, under applied overpotential of 0.4V DC voltage bias in FC mode, ***k*** in the impregnated electrode is more than two times higher. A higher reaction rate in an impregnated electrode could be related to the higher surface area of active material, ***a*** in eq. 6-4. The LCNT coats the whole surface of porous YSZ (P-YSZ), while a maximum of 50% of the area is active in the composite electrode. Also, other parameters could have contributed to the improvement of reaction rate, such as the thickness of LCNT or the size of LCNT grains could affect material “reduce-ability”; hence the concentration of oxygen ions/ vacant sites may differ. Moreover, most likely, the various routes of material preparation would affect Ni exsolution. The parameter ***Y0*** in the impregnated electrode is lower at OCV conditions and up to 0.2 DC bias in FC mode, indicating the worst transport properties of spices to the reaction site; this could be due to different transport mechanisms, e.g. in impregnated electrode, only the bulk transport of oxygen ions is possible through a thin LCNT coating. While in the composite electrode, oxygen ions could be transported from 3PB through the surface to depleted oxygen sites, or hydrogen species could be transported to 3PB, where the reaction occurs. Above 0.2V, DC bias in FC mode parameter ***Y0*** increases; the reason for such behaviour is not apparent; it likely is related to improved kinetics under higher oxidation levels of LCNT material.

6.5.3.2 The performance at fuel with a low concentration of hydrogen (5% H_2) and switching evaluation at the increasing potential.

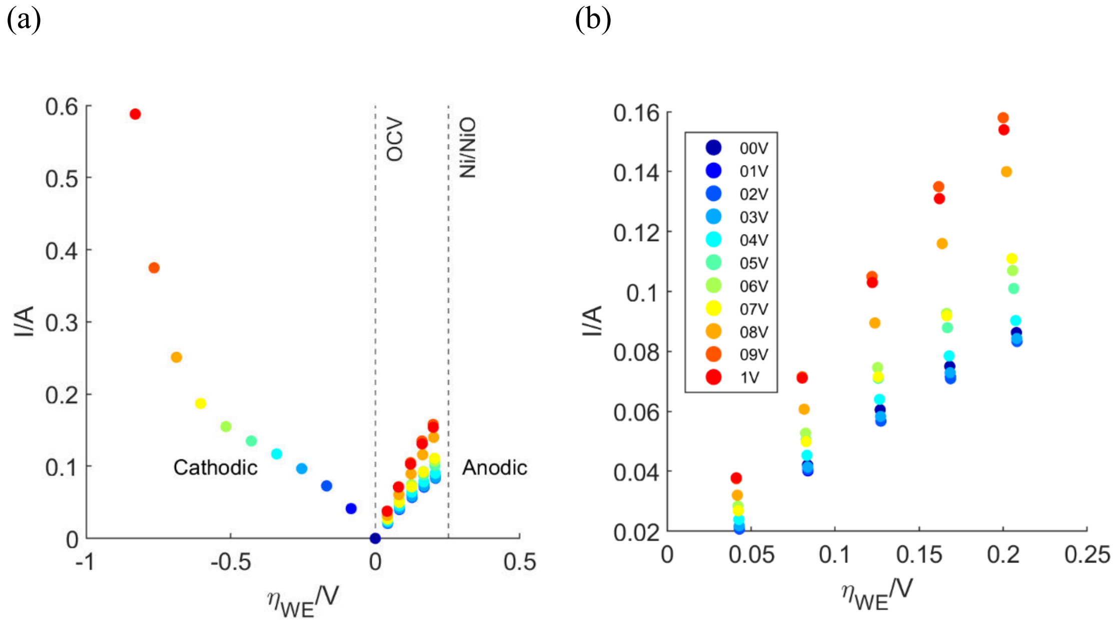

Figure 6-38: (a) Plot of the generated current versus overpotential applied on fuel electrode. (b) Current versus overpotential, in FC mode. After every step of the switching process, between 0-1V of applied potential in EC mode. Test at 800 °C, with 100 ml/min wet 5% H_2/N_2 in FE and atmospheric air in OE.

For the cell preparation, the porous YSZ (P-YSZ) was impregnated with LSF at the oxygen side and LCNT for the fuel electrode, as explained in Chapter 3.7. At the last step, LSF was calcinated at 850 °C, while LCNT was at 1200 °C. Cell achieved high OCV up to 0.95 V and was tested at 100 ml/min flow of the 5% H_2/N_2 in FE directed through a bubbler and atmospheric air in OE. Unlike previous cells with composite electrodes, a newly developed, fully impregnated tubular cell could be tested under fuel with a low concentration of H_2, likely due to the higher activity of electrodes. The advantage of testing with diluted fuel is much higher fuel utilization. For impedance analysis in FC mode, it creates the possibility of recognizing how low fuel concentration affects individual processes; thus, it brings more information about their nature and behaviour. Previously, there were no concentration losses at FC mode as the cell was tested in pure wet H_2. The experiment reveals how specific voltage applied in EC mode affects the performance of the FC operation. The cell was heated up to 800 °C and reduced for 2 hours in wet 5%H_2/ N_2. The potential was applied at 0.05 V intervals up to 0.25 V DC bias in FC mode at the first run. At every potential, the cell was stabilised for 20 s at potentiostatic, and EIS was taken between 50000 and 2.5 Hz. The first run reveals how reducing conditions influence cell's performance. In the second run, the 0.1 V voltage bias was applied in EC mode for 1 minute, and the cell was switched to FC mode and tested with the same program as in the first step. Such a treatment revealed how 0.1 V DC voltage bias applied in EC mode affects the performance of the FC operation. At every subsequent step, voltage bias applied in EC mode was 0.1 V higher; 11 steps were conducted up to 1 V of DC bias applied in EC mode. The procedure allowed to recognise what potential applied in EC mode gives the most pronounced changes on FC operation, either due to Ni exsolution or increased material conductivity and number of oxygen vacancies. As the changes induced by cathodic overpotential on cell's operation is the main point of interest; and as the previous measurement showed the high anodic overpotential could significantly decrease cell's performance (Chapter 6.5.2.2), in the conducted experiment, the maximum applied potential in FC mode was below the Ni oxidation point (Figure 6-38). The potentiostatic measurement in FC mode shows almost no change in the amount of generated power after up to 0.4 V DC bias is applied in the EC mode (Figure 6-38). The current in FC mode increase eventually after applying 0.5 V DC bias in EC mode, and not much change is visible until the ninth run (0.8 V DC bias in EC mode), where activity in FC mode increase significantly. A tenth step (0.9 V DC bias in EC mode) also improves fuel cell performance; however, the cell starts to deteriorate after 1 V DC bias was applied in EC mode at the eleventh run. One more step was applied at 1.1 V DC bias in EC mode, which led to fatal failure and cell dropped voltage in OCV operation. Likely a very high switching potential resulted in cell rupture. The breakage highlights the need for careful control of the switching potential; the optimal voltage must be applied to ensure maximum performance on the one hand, but at the same time do not damage the cell's microstructure. The behaviour of the potentiostatic curve in EC mode somehow coincides with changes in FC mode. The curve has negative curvature up to 0.4 V DC bias in EC mode; then, it changes its curvature to positive, and the generated current increases exponentially.

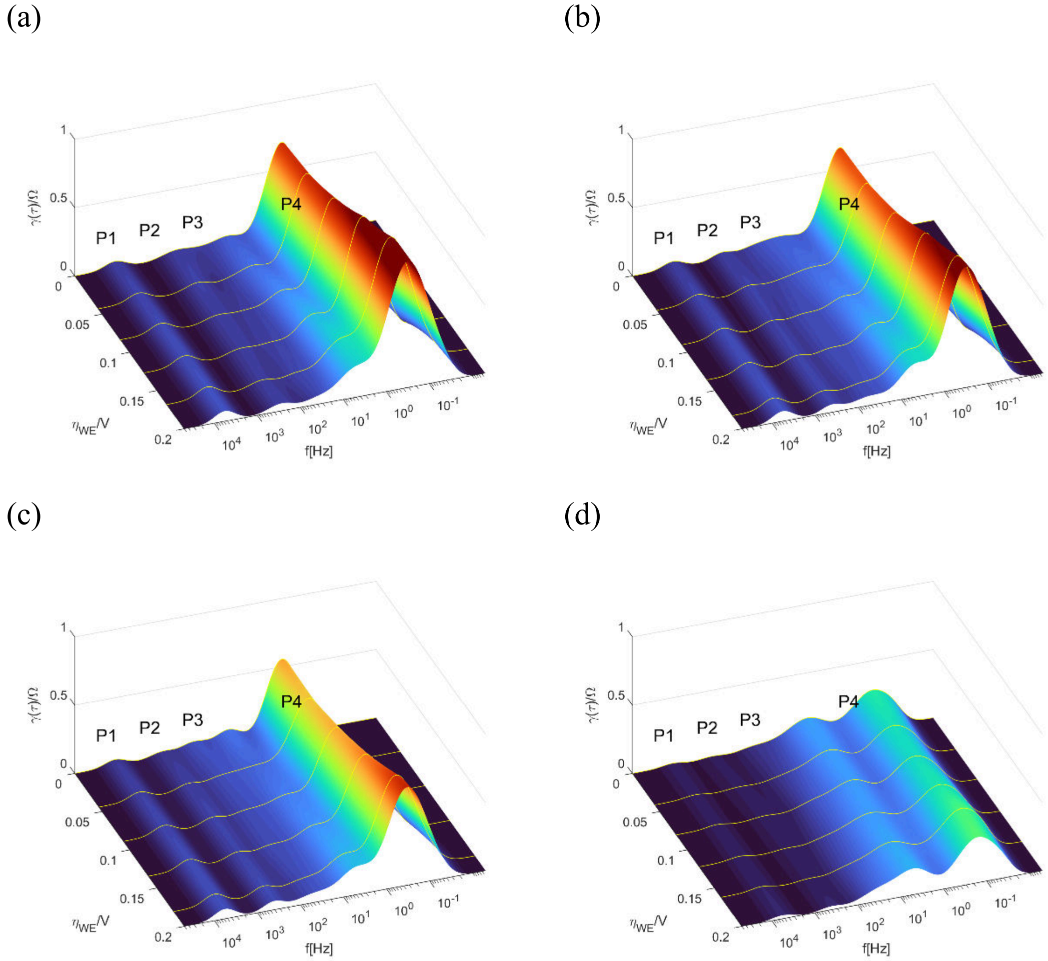

Figure 6-39: DRT of impedance data taken in FC mode up to 0.25V DC bias, at 800 °C, with 100 ml/min wet 5% H2/N2 in FE and atmospheric air in OE. (a) Before the switching procedure after gas reduction. (b) After switching at 0.4V DC bias in EC mode. (c) After switching at 0.5V DC bias in EC mode. (d) After switching at 1V DC bias in EC mode.

To better understand the process on the fuel cell electrode, DRT was constructed from EIS data taken during every run for the FC operation for potential range (Figure 6-39), showing all four processes already recognized in previous chapters. Not much change could be visible before switching above 0.4 V DC bias in EC mode (Figure 6-39 a&b); after applying 0.5 V DC bias in EC mode, the primary P4 process seems to be reduced (Figure 6-39 c) and further decreased to maximum switching potential (Figure 6-39 d). However, DRT taken after switching at 1 V DC bias in EC mode indicates worsening P3 kinetics.

In line with the observations, the P4 process is sensitive to the gas atmosphere; this is shown when testing in electrolysis mode where the cell was tested on low H_2O

concentration (~3%), under moderate potential, P4 increased considerably (Figure 6-27). However, the cell was tested with almost pure H_2; therefore, at the higher potential in FC mode, P4 did not show any concentration losses. Therefore the assumption that the kinetics of the P4 was also connected to the H_2 gas concentration was rather intuitive.

During the testing with fuel with 5% H_2 (Figure 6-39), at the potential range from OCV up to 0.1V, DC bias was applied in FC mode, the P4 decreases, similarly to previous analyses, representing improved P4 kinetics under anodic bias. However, P4 increases at the higher potential, above 0.1 V DC bias in FC mode, indicating concentration losses due to low concentration of H_2 gas.

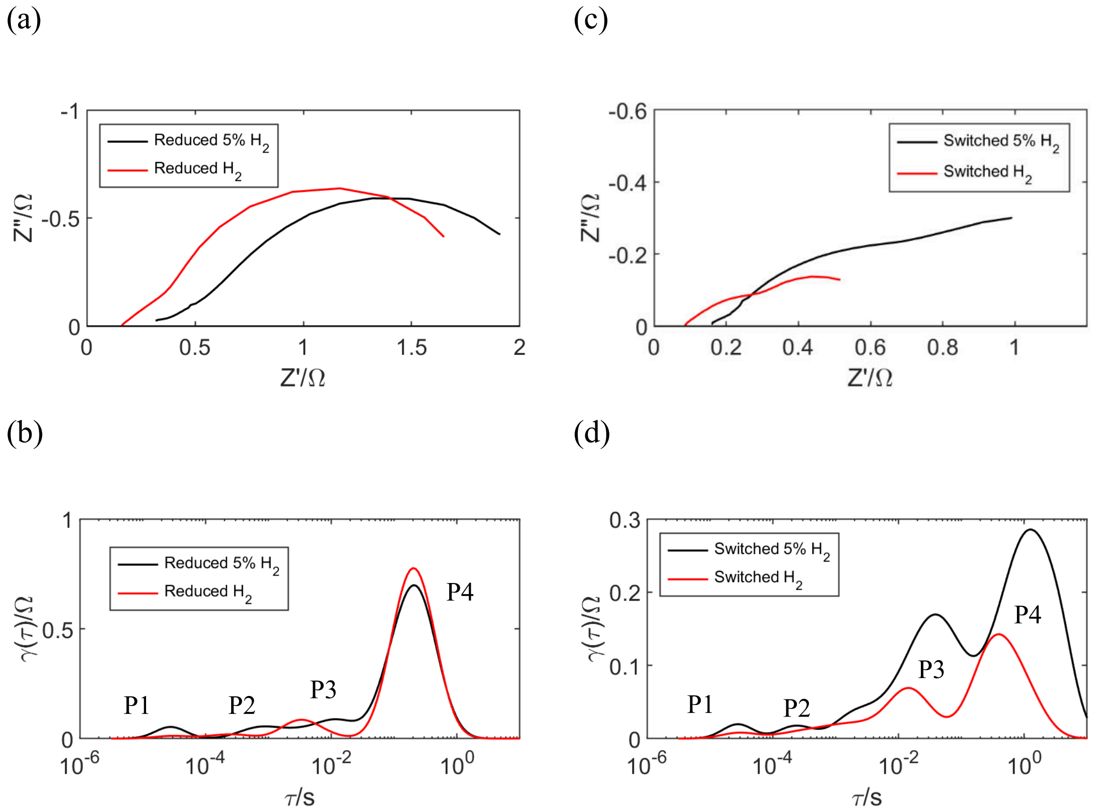

Figure 6-40: Nyquist and DRT plots of impedance data of tubular cell with impregnated LCNT electrode sintered at 1200°C tested on 100 ml/min 5%H_2/N_2, or 50 ml/min of H_2 in FE, and atmospheric air in OE. (a) – (b) After gas reduction. (c) – (d) After switching.

Compared to the cell tested with pure wet H_2 after chemical reduction (Figure 6-40 a-b), the gas atmosphere seems to most influence the ohmic resistance and high-frequency processes; this would be related to a more considerable extent of reduction under H_2, which would improve LCNT conductivity and processes related to the charge transfer. Not much difference could be recognised at low frequency; P4 has almost the same magnitude in both cases. Considering the P4 as the processes illustrating kinetics of H_2 gas adsorption/ dissociation on perovskite surface, such behaviour indicating not much of an increase in the surface activity for those processes under the higher gas concentration after chemical reduction; it also indicates that not a gas concentration becomes determining, but rather the ability of the surface to accept H_2 molecules. After electrochemical switching (Figure 6-40 c-d), not only ohmic resistance and high-frequency processes seems to be reduced in pure H_2 atmosphere concerning 5% H_2, but also low-frequency processes, the P3 and P4.

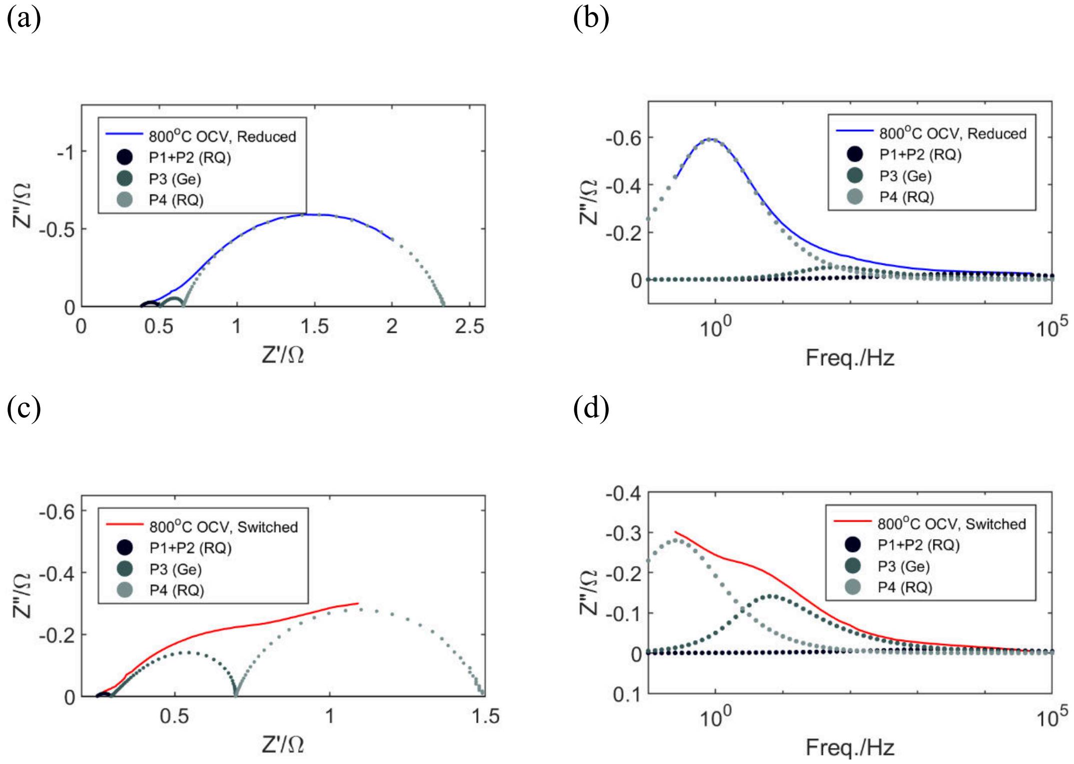

Figure 6-41: Equivalent circuit used for impedance analysis, Nyquist and Bode plot with fitted elements. (a)-(b) Reduced sample. (c)-(d) After switching at 1V DC bias in EC mode.

The equivalent circuit used for the impedance analysis consists of Rs related to ohmic losses in the cell and is modelled by an ohmic resistor, P1 and P2 modelled by single “R/CPE” elements and P3 modelled by a Gerischer element and the low-frequency process P4 also modelled by “R/CPE”, Figure 6-41.

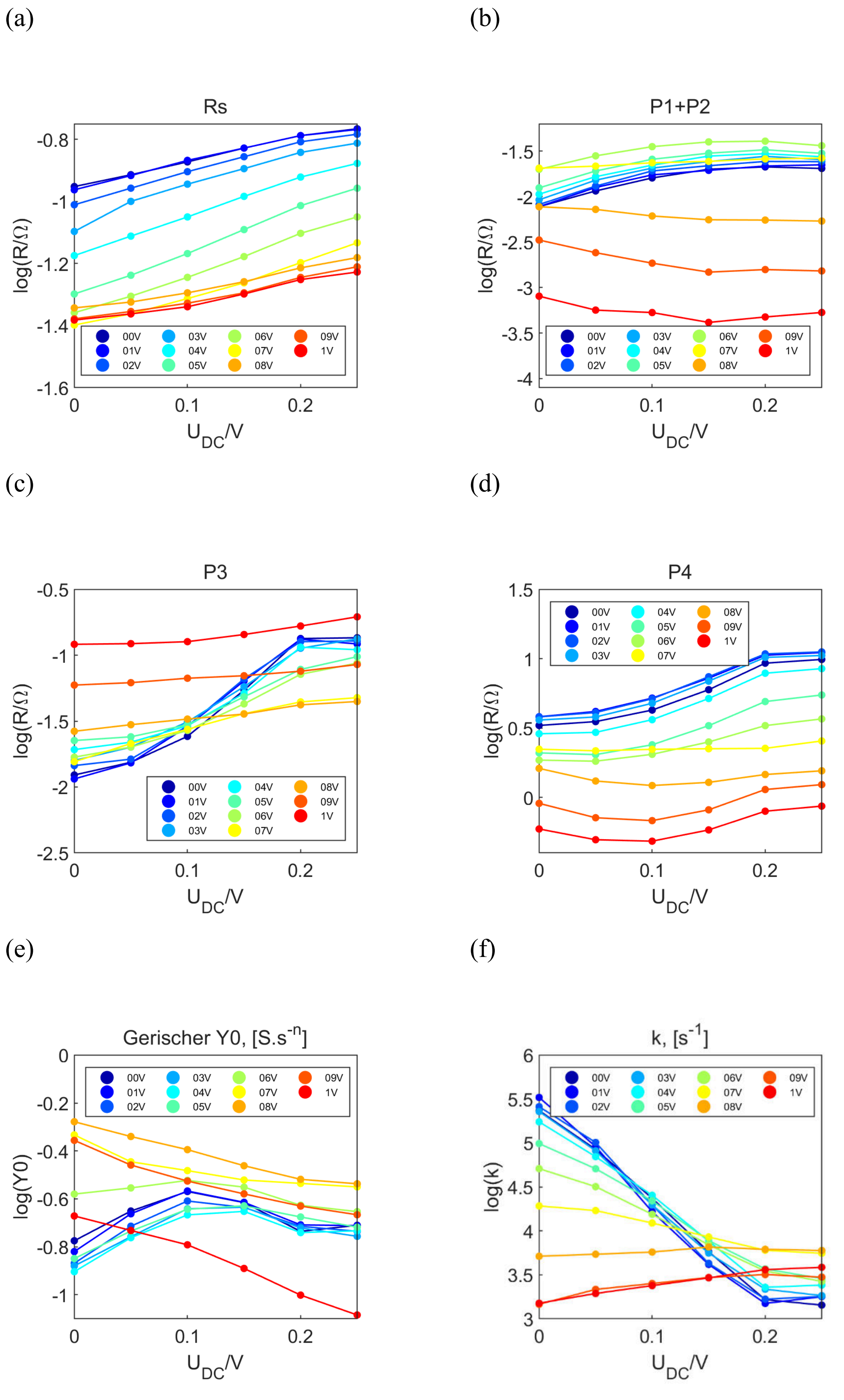

Figure 6-42: Impedance analysis of cell operation at FC mode from the fitting in the equivalent circuit. (a)-(d) Ohmic and polarisation resistance of individual processes. (e)-(f) Gerisher parameters of P3.

The impedance data of the tubular cell operating at the various potential in fuel cell mode after every step of the switching procedure was fitted according to the proposed equivalent circuit, and ohmic and polarisation resistance was summarised in Figure 6-42. Due to fitting difficulties at higher voltage, two semicircles at higher frequency were replaced by a single semicircle (P1+P2), the calculated ohmic and polarisation resistance were plotted against the applied potential. The figure also contains the Gerischer parameters of P3, where ***Y0*** is proportional to the diffusion coefficient of species taking part in H_2 oxidation while ***k*** to surface exchange rate, eq. 6.3 & 6.4.

The ohmic resistance Rs is already reduced after the 3rd run (0.2V DC bias in EC mode) and is reduced until the 10th step; applying 1V DC bias in EC mode in the last run almost did not influence ohmic resistance. The extent of Rs reduction increases up to 0.5V DC bias applied and slows down afterwards. The ohmic resistance increases at anodic polarisation due to a drop in electronic conductivity with oxidation of Ti^{3+} to Ti^{4+}. The most pronounced influence of anodic polarisation on Rs could be seen after switching at moderate potentials (0.4-0.6V DC bias); this coincides with the “speed” of Rs reduction due to applied potential, showing that, after switching at moderate potential, perovskite conductivity (thus defect stochiometry) is most susceptible to polarisation changes. After the last run, ohmic resistance equals 0.25 Ω, while when testing at pure wet H_2, the Rs were equal to 0.05 Ω. The difference is due to changes in stochiometry due to gas conditions with which LCNT is in equilibrium and perhaps some differences in surface area and thickness of electrolyte/ electrodes. Less likely due to switching at higher pO_2 due to gas conditions, as the last run showed that material could not be further reduced already at 5% H_2 after 0.9V DC bias in EC mode.

The kinetics of high-frequency processes (P1+P2) seemed to follow changes in ohmic resistance in a cell with a composite fuel electrode (Figure 6-28); however, in fully impregnated cells, their kinetics seems not to be related to changes in LCNT conductivity. In fact, their overall polarisation resistance increases until switching at 0.6V DC bias and decreases substantially after the switching at every next step. Perhaps, an oxygen electrode influences the polarisation of high-frequency processes to a greater extent in impregnated electrodes than in composite due to the overall lower polarisation of the first one; therefore, the changes on an oxygen electrode are more pronounced.

There is a substantial difference in kinetics of P3 and P4 in impregnated LCNT in comparison to a composite LCNT/YSZ50 electrode (Figure 6-29), where P3 and P4 seem to be somehow competitive; when P4 decreased at higher anodic overpotential, presumably due to better electrode activity for H_2 adsorption/ dissociation, the P3, associated with surface diffusion of species and change of their activity due to reaction, increased. The worst P3 kinetics was related to a decrease in the efficiency of surface transport, which governed the behaviour of the process; however, the reaction part improved. Perhaps, the P4 kinetics could be coupled with surface exchange rate $\boldsymbol{R_0}$, which is included in Gerisher parameter ***k***, which would explain the improved kinetics of P4 at the higher potential in composite cells. In impregnated electrode, tested at pure H_2 (Figure 6-36), the kinetics of the P4 process decreased at higher anodic overpotential, similarly to composite cells. Also, the ***Y0*** parameter decreased at higher potential and ***k*** increased; however, opposite in composite electrode, the overall kinetics of P3 improved at anodic polarisation due to a much higher value of ***k*** and change of ***Y0*** kinetics at higher anodic overpotential, Figure 6-37.

In impregnated electrode, tested at 5% H_2, the trend indicates worst kinetics at anodic polarisation in both low-frequency processes P3 and P4; implying that both are sensitive to some extent to gas concentration; presumably through the exchange rate. P4 shows a minimal change until 0.4 V applied DC bias in the EC mode and seems to increase at the whole potential range in FC mode. After the 4th step, a process starts to be reduced at every following step up to maximum switching potential. The improvement kinetics of P4 at higher anodic bias becomes visible after switching at 0.8 V, where the P4 improves up to 0.1 V in FC mode, and then kinetics decreases due to low gas concentration. P3 also shows a small change until 0.4 V applied DC bias in the electrolysis mode, and its polarisation resistance increased at anodic overpotential. After the 4th step, P3 increases at lower anodic overpotential; however, its sensitivity to polarisation decreases, and at its higher value, resistance is lower than before switching, which is beneficial if operating at a higher bias in fuel cell operation. The last two steps are deteriorating for kinetics of P3 on the whole range in FC mode to such an extent that it becomes the main contributor to cell resistance.

Before the switching procedure, both Gerisher parameters behave differently from composite cell or impregnated cells tested on pure wet H_2, where parameters follow the same trend before and after the switching. The ***Y0*** parameter decreases at higher anodic polarisation while ***k*** improves. When testing at 5% H_2 in the cell with impregnated fuel cell electrode, ***Y0*** increases at anodic overpotential up to 0.1 V DC bias and decreases afterwards. Such a trend continues to switching at 0.4 V, and every run seems to be slightly deteriorating and starts to improve in the following steps, to a greater extent at lower anodic bias. The switching at 0.8 V is most beneficial for its value, and its behaviour starts to show similarities with previously mentioned cells, having optimal value at OCV conditions and decreasing at a whole range of fuel cell operation. Two last step results in a large drop in its value, which is why the significant increase in P3 resistance. Before switching, ***k*** decreases on the whole range of fuel cell operation; the influence of polarisation becomes less steep with higher switching potential. After switching at 0.8V DC bias in EC mode, the parameter increases at higher anodic polarisation; thus, behaviour shows similarity with the cell is tested at pure wet H_2. The decrease of ***k*** with anodic polarisation before switching at 0.8 V could indicate that ***k*** is dependent on gas concentration. More than one parameter could be determinantal on its behaviour when anodic polarisation is applied, which could stand behind the changing trend during the switching procedure. For example, after switching at 0.8 V, the activity of the surface increases, improving kinetics for gas dissociation; thus, lowering concentration losses to such an extent that improved kinetics due to higher oxidation levels at fuel cell operation becomes more pronounced.

6.6 Summary

The tubular cell made of composite materials achieved high OCV, was close to theoretical and showed remarkable thermal shock resistance; the cell withstood many thermal cycles when taken directly from the furnace at 700 °C to room temperature and inserted back. The stability test at 0.7 V in fuel cell mode showed a much higher degradation rate than the test carried out at 0.85 V. The loss of performance was related to increasing the polarisation resistance at low frequency. The regeneration experiment showed that the cell's performance could be recovered by re-applying high potential. The composite tubular cells showed relatively high Ohmic resistance due to the poorly conductive LCNT/YSZ support. Moreover, the analysis clearly showed that the low-frequency polarisation processes limit the cell's performance, coming from both the oxygen and fuel electrode side, likely due to slow gas conversion on the surface of the electrodes.

Compared to the cell with composite electrodes, the generated power in tubular cells with impregnated electrodes was almost two times higher. The cell had low ohmic resistance due to applying the very thin YSZ electrolyte and higher conductivity of impregnated electrodes than composite ones. Test on planar LSF cell showed minimal polarisation resistance. Hence, the polarisation showed by impedance data was believed to come mainly from LCNT impregnated fuel electrodes. Especially at low frequency, which still limits cells performance.

The impedance analysis showed that the same equivalent circuit could be used to both composite and impregnated fuel electrodes; consisting of high-frequency contribution likely related to oxygen ion transfer on interface, middle frequency process coupled with chemical diffusion of species takin part in the reaction and low-frequency process, coupled with adsorption and dissociation from the gas phase on the electrode's surface. The data were interpreted using a simple model of electrode functionality. As in the case of the previous cells, the switching procedure resulted in the reduction of ohmic and polarisation resistance on the whole frequency range, which was related to electronic conductivity, the exsolution of Ni catalyst and the generation of oxygen vacancies.

In contrast to the composite cell, the cell with impregnated fuel electrode showed worse performance in electrolysis mode after switching, indicating differences in the mechanism of H_2O electrolysis in both types of cells, suggesting that longer TPB with YSZ could be advantageous, likely due to the availability of oxygen ions.

Particular attention should be paid to the test conducted on the wide frequency range on the cell with the composite electrode. The cell's performance sharply deteriorated after applying very high anodic polarisation (oxidising conditions); the DRT analysis suggests changes related to the fuel electrode's surface.

Summary of the development of the cells

Developing a well-performing SOFCRoll with a Ni/YSZ based fuel electrode is an attractive perspective despite Ni/YSZ composite stability problems. Thanks to its excellent performance, high electronic conductivity, good mechanical properties and relatively low cost, this electrode is still the most widely used solution.

The main direction of their improvement should be focused on defects minimisation in the SOFCRoll structure. As shown in the following chapters, on the example of alternative fuel electrode material, through the appropriate modification of the input materials, slurry composition, manufacturing method and cells design, it is possible to produce a defect-free cell, which allows the optimisation of cells performance.

The tests made on large SOFCRoll with alternative an LCNT/YSZ50 fuel electrode indicate a not much higher activity level than the small cells. The analysis showed that the modification of SOFCRoll construction allowed to utilise of a large part of surface area (12 cm^2) in a developed small SOFCRoll design with the co-sintered current collector on the fuel electrode side. Theoretically, the improvement of large SOFCRoll and extension of the active region into the spiral part is possible. However, the biggest obstacle is ensuring effective current collection through the spiral. The co-sintering of the Ni/YSZ10 current collector layer on the fuel side seems to be an effective solution, but an extension of the spiral part would require a similar solution on the oxygen electrode, which is much more challenging in terms of material selection. The test on the large cell in Chapter 5.5.4 showed that LSM could have too low electronic conductivity to assure good current collector distribution on the oxygen electrode for such a long distance. Moreover, as shown in Figure 5-22, the internal defects are more prone to develop in large SOFCRoll, even though all the ceramic layers have matched shrinking profile. Defects are a consequence of higher stress created due to the LSM current collector layer and a higher number of folded layers, which stress the middle part.

On the other side, active electrodes for the co-sintered LCNT/YSZ50 and LSM/YSZ50 active oxygen electrodes show relatively low activity; therefore, further development of SOFCRoll should focus on their optimisation. Both the ohmic and polarisation resistance should be reduced for the fuel electrode. Probably the higher content of LCNT would be beneficial; however, the poor sinter-ability between YSZ and LCNT makes it challenging to achieve in SOFCRoll design. Possibly, a closer investigation of the sintering mechanism between those materials would allow the implementation of the electrode with higher content of active perovskite, either by changing the conditions of the sintering process (e.g. gas atmosphere, heating rate, temperature) or the material's stoichiometry. Also, the activity of the material should be improved by better control of the exsolution mechanism. Although improvement of electrode kinetics was visible after applying the switching procedure, the electrode still seems to have sizable polarisation resistance. Perhaps, the extent of exsolution could be improved by creating a higher overpotential on the fuel electrode site, e.g. by changing gas conditions for the switching procedure. Different materials could also be investigated in material selection for a fuel electrode. Besides activity for H_2 dissociation/ adsorption offered by exsolved metal, the ideal fuel electrode should have sufficient electronic and ionic activity to assure fast kinetics for fuel conversion. The selection of such materials and processing techniques is challenging for SOFCRoll, as the activity of the material must be retained after co-sintering at high temperatures.

Similarly, the oxygen electrode shows a relatively large resistance. The experiment on planar cells shows quite significant ohmic resistance, likely due to the low percolation of LSM. The ohmic resistance could be reduced by adding the higher LSM content; this may increase polarisation resistance due to a decrease of 3PB with YSZ; therefore, more work needs to be done to find the optimal proportion of both materials.

The composite based tubular cell produced in the project offers a much simpler solution than SOFCRoll; the silver current collector could be applied directly; thus, co-sintering of current collector layers is not required. If the co-sintering of all functional materials is chosen for their further development, the activity of the active layer should be improved, as already explained for SOFCRoll design.

The co-sintering of porous YSZ backbone and impregnation with functional perovskites seems to be an effective solution. The method avoids the difficulties resulting from high-temperature sintering, thus, increasing activity and material selection. The impregnated cell had a very low ohmic resistance, proving that coating a porous YSZ layer with perovskites is an effective method to produce well conductive electrodes. The cell's polarisation resistance mainly comes from the fuel electrode. Although impregnated electrode's functionality is much better than composite, their electrochemical activity still seems to be too low to assure an efficient fuel utilization. The cell's functionality should be optimized by further investigating the kinetics of the exsolution process material and microstructure modification.

A final recommendation is to try to scale up tubular cells further. Developed methods, slurries, and materials could be used to produce a large tubular SOFC with several dozen square centimetres of surface area. Also, other manufacturing methods should be investigated, such as extrusion and dip coating.

References

[1] NASA/GISS, “GISS Surface Temperature Analysis,” 2016. http://data.giss.nasa.gov/gistemp/.

[2] US EPA, “Overview of Greenhouse Gases,” 2020. [Online]. Available: https://19january2021snapshot.epa.gov/ghgemissions/overview-greenhouse-gases_.html.

[3] WMO, *State of the Global Climate 2020*, no. 1264. 2021.

[4] IPCC, “Climate Change and Land: an IPCC special report,” *Clim. Chang. L. an IPCC Spec. Rep. Clim. Chang. Desertif. L. Degrad. Sustain. L. Manag. food Secur. Greenh. gas fluxes Terr. Ecosyst.*, pp. 1–864, 2019, [Online]. Available: https://www.ipcc.ch/srccl/.

[5] IPCC, “IPCC Special Report on the Ocean and Cryosphere in a Changing Climate,” *Intergov. Panel Clim. Chang.*, p. undefined, 2019, [Online]. Available: https://www.ipcc.ch/srocc/chapter/summary-for-policymakers/.

[6] USGCRP, “Climate Science Special Report: Fourth National Climate Assessment, Volume I,” U.S. Global Change Research Program, Washington, DC, USA, 2017. doi: 10.7930/J0J964J6.

[7] V. Masson-Delmotte *et al.*, “2018: Summary for Policymakers,” 2018. [Online]. Available: https://www.ipcc.ch/site/assets/uploads/sites/2/2019/05/SR15_SPM_version_report_LR.pdf.

[8] R. Lindsey and L. A. Dahlman, “Climate Change: Global Temperature,” 2020. [Online]. Available: https://www.climate.gov/author/rebecca-lindsey-and-luann-dahlman.

[9] “Climate Change,” *Wikipedia*, 2020. https://en.wikipedia.org/wiki/Climate_change (accessed Oct. 11, 2021).

[10] New Climate Institute, “WARMING PROJECTIONS GLOBAL UPDATE,”

2019. [Online]. Available: https://climateactiontracker.org/publications/governments-still-not-acting-on-climate-crisis/.

[11] IPCC, "Assessment Report 6 Climate Change 2021: The Physical Science Basis," 2021, [Online]. Available: https://www.ipcc.ch/report/ar6/wg1/.

[12] Efbrazil, "Global Temperature And Forces," 2021. https://creativecommons.org/licenses/by-sa/4.0/legalcode.

[13] P. Friedlingstein *et al.*, "Global Carbon Budget 2019," *Earth Syst. Sci. Data*, vol. 0, pp. 1783–1838, 2019, doi: https://doi.org/10.5194/essd-11-1783-201.

[14] Efbrazil, "CO2 Emissions by Source Since 1880," 2020. https://creativecommons.org/licenses/by-sa/4.0/legalcode (accessed Oct. 11, 2021).

[15] J. S. Apte, J. D. Marshall, A. J. Cohen, and M. Brauer, "Addressing Global Mortality from Ambient PM2.5," *Environ. Sci. Technol.*, vol. 49, no. 13, pp. 8057–8066, 2015, doi: 10.1021/acs.est.5b01236.

[16] A. Vodonos Zilberg, J. D. Schwartz, E. Marais, M. Sulprizio, Payer, and L. Mickley, "Global Mortality from Outdoor Fine Particle Pollution Generated by Fossil Fuel Combustion," *ISEE Conf. Abstr.*, vol. 2018, no. 1, pp. 1–30, 2018, doi: 10.1289/isesisee.2018.p03.2000.

[17] International Renewable Energy Agency (IRENA), "Renewable Capacity 2019," no. March, p. 3, 2019, [Online]. Available: www.irena.org/publications.

[18] O. Ellabban, H. Abu-Rub, and F. Blaabjerg, "Renewable energy resources: Current status, future prospects and their enabling technology," *Renew. Sustain. Energy Rev.*, vol. 39, pp. 748–764, 2014, doi: 10.1016/j.rser.2014.07.113.

[19] C. Graves, S. D. Ebbesen, M. Mogensen, and K. S. Lackner, "Sustainable hydrocarbon fuels by recycling CO2 and H 2O with renewable or nuclear energy," *Renew. Sustain. Energy Rev.*, vol. 15, no. 1, pp. 1–23, 2011, doi: 10.1016/j.rser.2010.07.014.

[20] European Commission, “A hydrogen strategy for a climate-neutral Europe,” 2020. doi: 10.1017/CBO9781107415324.004.

[21] F. G. I. Dodds P. E., Velazquez Abad A., McDowall W., “Opportunities for hydrogen and fuel cell technologies to contribute to clean growth in the UK,” London,UK, 2020.

[22] IEA, “Hydrogen report,” 2019.

[23] R. Moss *et al.*, “Critical Metals in the Path towards the Decarbonisation of the EU Energy Sector: Assessing Rare Metals as Supply-Chain Bottlenecks in Low-Carbon Energy Technologies,” 2013. doi: 10.2790/46338.

[24] European Commission, “Europe’s moment: Repair and Prepare for the Next Generation - COM(2020) 456,” vol. COM(2020), pp. 1–18, 2020.

[25] M. W. Menezes, D. R. Simmons, S. Winberg, R. Baranwal, P. Hoffman, and S. L. Genatowski, “U.S. Department of Energy Hydrogen Program Plan,” 2020.

[26] Government of Canada, “Seizing the Opportunities for Hydrogen,” 2020.

[27] COAG Energy Council Hydrogen Working Group, “National Hydrogen,” 2019. [Online]. Available: https://www.industry.gov.au/sites/default/files/2019-11/australias-national-hydrogen-strategy.pdf.

[28] UK Goverment, “UK hydrogen strategy,” London,UK, 2021.

[29] The Scottish Government, *Climate Change (Emissions Reduction Targets) (Scotland) Act 2019*. 2019.

[30] The Scottish Government, “Scottish Government Community Energy Policy Statement,” 2020.

[31] N.Q. Minh, T. Takahashi, *Science and Technology of Ceramic Fuel Cells*. 1995.

[32] I. EG&G Technical Services, “Fuel Cell Handbook,” *Fuel Cell*, 2004, doi: 10.1002/zaac.200300050.

[33] R. Konar, J. Mukhopadhyay, A. Das Sharma, and R. N. Basu, “Synthesis of Cu-YSZ and Ni-Cu-YSZ cermets by a novel electroless technique for use as solid

oxide fuel cell anode: Application potentiality towards fuel flexibility in biogas atmosphere," *Int. J. Hydrogen Energy*, vol. 41, no. 2, pp. 1151–1160, 2016, doi: 10.1016/j.ijhydene.2015.10.003.

[34] W. R. Grove, "On a new Voltaic Combination and On Voltaic Series and the Combination of Gases by Platinum," *Philos. Mag.*, vol. 14, pp. 127–130, 1839.

[35] I. Rhys, Morus, *Grove, Sir William Robert (1811–1896)*. Oxford University Press, 2005.

[36] M. Warshay and P. Prokopius, "The fuel cell in space: yesterday, today and tomorrow," *J. Power Sources*, vol. 29, pp. 193–200, 1990.

[37] K. Kendall, M. Kendall, and S. B. Adler, *High-Temperature Solid Oxide Fuel Cells for the 21st Century*. 2016.

[38] Hydrogen and Fuel Cell Technologies Office, "Types of Fuel Cells," 2016. https://www.energy.gov/eere/fuelcells/types-fuel-cells (accessed Jul. 28, 2021).

[39] K. Wipke, S. Sprik, J. Kurtz, T. Ramsden, C. Ainscough, and G. Saur, "All Composite Data Products: National FCEV Learning Demonstration With Updates Through Jan 18, 2012," no. January, pp. 1–101, 2012, [Online]. Available: http://www.osti.gov/bridge.

[40] L. Tokyo Gas Co. and P. Corporation, "Launch of New 'Ene-Farm' Home Fuel Cell Product More Affordable and Easier to Install," 2013. https://news.panasonic.com/global/press/data/2013/01/en130117-5/en130117-5.html.

[41] G. Mulder, P. Coenen, A. Martens, and J. Spaepen, "Market-ready Stationary 6 kW Generator with Alkaline Fuel Cells," *ECS Trans.*, vol. 12, no. 1, pp. 743–753, 2019, doi: 10.1149/1.2921601.

[42] N. Q. Minh, T. Takahashi, and N.Q. Minh, T. Takahashi, *Science and technology of ceramic fuel cells*. Elsevier Ltd, 1995.

[43] B. C. H. Steele, P. H. Middleton, and R. A. Rudkin, "Material science aspects of SOFC technology with special reference to anode development," *Solid State*

Ionics, vol. 40–41, pp. 388–393, 1990.

[44] S. B. Adler, “Factors governing oxygen reduction in solid oxide fuel cell cathodes,” *Chem. Rev.*, vol. 104, no. 10, pp. 4791–4843, 2004, doi: 10.1021/cr020724o.

[45] K. Kendall, *Portable Early Market SOFCs*, 2nd ed. Elsevier Ltd., 2016.

[46] M. Mogensen and K. Kammer, “Conversion of Hydrocarbons in Solid Oxide Fuel Cells,” *Annu. Rev. Mater. Res.*, vol. 33, no. 1, pp. 321–331, 2003, doi: 10.1146/annurev.matsci.33.022802.092713.

[47] S. McIntosh and R. J. Gorte, “Direct hydrocarbon solid oxide fuel cells,” *Chem. Rev.*, vol. 104, no. 10, pp. 4845–4865, 2004, doi: 10.1021/cr020725g.

[48] Y. Jiang and A. V. Virkar, “Fuel Composition and Diluent Effect on Gas Transport and Performance of Anode-Supported SOFCs,” *J. Electrochem. Soc.*, vol. 150, no. 7, p. A942, 2003, doi: 10.1149/1.1579480.

[49] A. D. Bonaccorso and J. T. Irvine, “Development of tubular hybrid direct carbon fuel cell,” *Int. J. Hydrogen Energy*, vol. 37, no. 24, pp. 19337–19344, 2012, doi: 10.1016/j.ijhydene.2012.02.104.

[50] F. S. Baumann, J. Fleig, H. U. Habermeier, and J. Maier, “Impedance spectroscopic study on well-defined (La,Sr)(Co,Fe)O3-δ model electrodes,” *Solid State Ionics*, vol. 177, no. 11–12, pp. 1071–1081, 2006, doi: 10.1016/j.ssi.2006.02.045.

[51] S. C. Singhal and K. Kendall, *High-temperature Solid Oxide Fuel Cells: Fundamentals, Design and Applications*. 2003.

[52] R. A. George, “Status of tubular SOFC field unit demonstrations,” *J. Power Sources*, vol. 86, no. 1, pp. 134–139, 2000, doi: 10.1016/S0378-7753(99)00413-9.

[53] J. W. Gibbs, “On the Equilibrium of Heterogeneous Substances,” *Trans. Connect. Acad. Arts Sci.*, 1876.

[54] L. Q. Chen, “Chemical potential and Gibbs free energy,” *MRS Bull.*, vol. 44, no.

7, pp. 520–523, 2019, doi: 10.1557/mrs.2019.162.

[55] R. V. Kumar, J. Chivall, D. Brook, B. Barber, and L. Sallows, “Ellingham Diagram.” https://www.doitpoms.ac.uk/tlplib/ellingham_diagrams/credits.php (accessed Sep. 09, 2020).

[56] J. Jamnik and J. Maier, “Generalised equivalent circuits for mass and charge transport: Chemical capacitance and its implications,” *Phys. Chem. Chem. Phys.*, vol. 3, no. 9, pp. 1668–1678, 2001, doi: 10.1039/b100180i.

[57] F. S. Baumann, “Oxygen reduction kinetics on mixed conducting SOFC model cathodes,” *Arbeit*, vol. 135, p. 2001, 2006.

[58] H. Rickert, *Electrochemistry of Solids*. Berlin: Springer-Verlag, 1982.

[59] Bauerle, J., E., “Study of solid electrolyte polarization by a complex admittance method,” *J. Phys. Chem. Solids*, vol. 30, no. 12, pp. 2657–2670, 1969.

[60] J. T. S. S. Irvine, D. C. Sinclair, and A. R. West, “Electroceramics: Characterization by Impedance Spectroscopy,” *Adv. Mater.*, vol. 2, no. 3, pp. 132–138, 1990, doi: 10.1002/adma.19900020304.

[61] A. Lasia, *Electrochemical Impedance Spectroscopy and its Applications*. Springer, 2014.

[62] P. Johnson, “ZPlot, ZView Electrochemical Impedance Software”.” Scribner Associates Inc., 2000.

[63] K. S. Cole and R. H. Cole, “Dispersion and Absorption in Dielectrics I . Alternating Current Characteristics Published by the AIP Publishing Articles you may be interested in Alternating current conductivity and dielectric dispersion in copper-silica nanocomposites synthesized by Di,” vol. 341, no. 1941, 1998, doi: 10.1063/1.1750906.

[64] H. Schichlein, A. C. Müller, M. Voigts, A. Krügel, and E. Ivers-Tiffée, “Deconvolution of electrochemical impedance spectra for the identification of electrode reaction mechanisms in solid oxide fuel cells,” *J. Appl. Electrochem.*, vol. 32, no. 8, pp. 875–882, 2002, doi: 10.1023/A:1020599525160.

[65] A. Leonide, “SOFC Modelling and Parameter Identificationby means of Impedance Spectroscopy,” Karlsruher Institut für Technologie (KIT), 2010.

[66] B. A. Boukamp, “A Nonlinear Least Squares Fit Procedure for Analysis of Immitance Data Of Electrochemical Systems,” *Sol. State. Ion.*, vol. 20, pp. 31–44, 1986, doi: 10.1016/0167-2738(86)90031-7.

[67] R. M. Fuoss and J. G. Kirkwood, “Electrical Properties of Solids. VIII. Dipole Moments in Polyvinyl Chloride-Diphenyl Systems,” *J. Am. Chem. Soc.*, vol. 63, no. 2, pp. 385–394, 1941, doi: 10.1021/ja01847a013.

[68] B. A. Boukamp and J. R. Macdonald, “Alternatives to Kronig-Kramers transformation and testing, and estimation of distributions,” *Solid State Ionics*, vol. 74, no. 1–2, pp. 85–101, 1994.

[69] B. A. Boukamp, “A Linear Kronig-Kramers Transform Test for Immittance Data Validation,” no. 6, 1995.

[70] J.-C. Njodzefon, “Electrode Kinetics and Gas Conversion in Solid Oxide Cells,” Technical University of Denmark, 2015.

[71] D. L. Misell, P. A. Childs, A. F. Jones, D. L. Misell, P. A. Childs, and D. L. Misell, “The application of deconvolution techniques to dielectric data,” 1973.

[72] T. H. Wan, M. Saccoccio, C. Chen, and F. Ciucci, “Influence of the Discretization Methods on the Distribution of Relaxation Times Deconvolution: Implementing Radial Basis Functions with DRTtools,” *Electrochim. Acta*, vol. 184, pp. 483–499, 2015, doi: 10.1016/j.electacta.2015.09.097.

[73] F. Ciucci, “Personal communication,” 2022.

[74] B. Zeimetz *et al.*, “Using the Distribution of Relaxation Times for analyzing the Kramers-Kronig Relations in Electrochemical Impedance Spectroscopy To cite this version : HAL Id : hal-01692003,” *Electrochim. Acta*, vol. 1, pp. 1–18, 2018.

[75] V. V. Kharton, F. M. B. Marques, and A. Atkinson, “Transport properties of solid oxide electrolyte ceramics: A brief review,” *Solid State Ionics*, vol. 174, no. 1–4, pp. 135–149, 2004, doi: 10.1016/j.ssi.2004.06.015.

[76] J. M. Vohs and R. J. Gorte, “High-performance SOFC cathodes prepared by infiltration,” *Adv. Mater.*, vol. 21, no. 9, pp. 943–956, 2009, doi: 10.1002/adma.200802428.

[77] K. R. Sridhar and B. T. Vaniman, “Oxygen production on Mars using solid oxide electrolysis,” *Solid State Ionics*, vol. 93, no. 3–4, pp. 321–328, 1997, doi: 10.1016/s0167-2738(96)00513-9.

[78] D. T. Chin and C. Y. Cheng, *Techniques of Electroorganic Synthesis, Part III.* New York: Wiley, 1995.

[79] M. Ni, M. K. H. Leung, and D. Y. C. Leung, “A modeling study on concentration overpotentials of a reversible solid oxide fuel cell,” vol. 163, pp. 460–466, 2006, doi: 10.1016/j.jpowsour.2006.09.024.

[80] C. Petot *et al.*, “Microstructure and ionic conductivity of freeze-dried yttria-doped zirconia,” *J. Eur. Ceram. Soc.*, vol. 18, no. 10, pp. 1419–1428, 1998, doi: 10.1016/s0955-2219(98)00024-7.

[81] T. H. Etsell and S. N. Flengas, “The Electrical Properties Of Solid Oxide Electrolytes,” *Chem. Rev.*, vol. 70, p. 339, 1969.

[82] V. V. Kharton, E. N. Naumovich, and A. A. Vecher, “Research on the electrochemistry of oxygen ion conductors in the former Soviet Union. I. ZrO2-based ceramic materials,” *J. Solid State Electrochem.*, vol. 3, no. 2, pp. 61–81, 1999, doi: 10.1007/s100080050131.

[83] M. S. Khan, S. B. Lee, R. H. Song, J. W. Lee, T. H. Lim, and S. J. Park, “Fundamental mechanisms involved in the degradation of nickel–yttria stabilized zirconia (Ni–YSZ) anode during solid oxide fuel cells operation: A review,” *Ceram. Int.*, vol. 42, no. 1, pp. 35–48, 2016, doi: 10.1016/j.ceramint.2015.09.006.

[84] S. P. S. Badwal, F. T. Ciacchi, and D. Milosevic, “Scandia-zirconia electrolytes for intermediate temperature solid oxide fuel cell operation,” *Solid State Ionics*, vol. 136–137, pp. 91–99, 2000, doi: 10.1016/S0167-2738(00)00356-8.

[85] University of Cambridge, “DoITPoMS,” 2016. http://www.doitpoms.ac.uk/tlplib/fuel-cells/sofc_electrolyte.php?printable=1.

[86] J. H. Kim and G. M. Choi, "Mixed ionic and electronic conductivity of [(ZrO2)0.92(Y2O3)0.08]1-y ·(MnO1.5)y," *Solid State Ionics*, vol. 130, no. 1, pp. 157–168, 2000, doi: 10.1016/S0167-2738(00)00539-7.

[87] C. C. Appel, N. Bonanos, A. Horsewell, and S. Linderoth, "Ageing behaviour of zirconia stabilised by yttria and manganese oxide," *J. Mater. Sci.*, vol. 36, no. 18, pp. 4493–4501, 2001, doi: 10.1023/A:1017938904673.

[88] B. C. H. Steele, "Appraisal of Ce 1 2 y Gd y O 2 2 y / 2 electrolytes for IT-SOFC operation at 500 8 C," vol. 129, pp. 95–110, 2000.

[89] T. Ishihara, H. Matsuda, and Y. Takita, "Doped LaGaO3 Perovskite Type Oxide as a New Oxide Ionic Conductor," *J. Am. Chem. Soc.*, vol. 116, no. 9, pp. 3801–3803, 1994, doi: 10.1021/ja00088a016.

[90] M. Mogensen, N. M. Sammes, and G. A. Tompsett, "Physical , chemical and electrochemical properties of pure and doped ceria," vol. 129, pp. 63–94, 2000.

[91] N. P. Brandon, "Materials Engineering for Solid Oxide Fuel Cell Technology," in *Materials Science Forum*, 2007, pp. 20–27.

[92] B. C. H. Steele, "Materials for IT-SOFC stacks - 35 years R&D: The inevitability of gradualness?," *Solid State Ionics*, vol. 134, no. 1–2, pp. 3–20, 2000, doi: 10.1016/S0167-2738(00)00709-8.

[93] L. Robert, B. N. Peter, D. Athol, E. Karim, and S. Martin, "A method and apparatus for operating an intermediate-temperature solid-oxide fuel cell stack," GB2411043(A), 2005.

[94] R. Leah, M. Lankin, R. Pierce, and A. Bone, "Metal Supported Solid Oxide Fuel Cell," US20150064597A1, 2015.

[95] P. . Slater, J. T. S. Irvine, T. Ishihara, and Y. Takita, "High-Temperature Powder Neutron Diffraction Study," *J. Solid State Chem.*, vol. 143, no. 139, pp. 135–143, 1998.

[96] J. T. S. Irvine, "Perovskite Oxide Anodes for SOFCs," in *Perovskite Oxide for Solid Oxide Fuel Cells*, T. Ishihara, Ed. Springer, 2009, pp. 167–182.

[97] X. Zhang, S. Ohara, H. Okawa, R. Maric, and T. Fukui, “Interactions of a La Sr Ga Mg O electrolyte with Fe O,” *Solid State Ionics*, vol. 139, pp. 145–152, 2001, [Online]. Available: www.elsevier.com.

[98] J. H. Lee, K. N. Kim, J. W. S. J. Kim, B. K. Kim, H. W. Lee, and J. Moon, “An investigation of the interfacial stability between the anode and electrolyte layer of LSGM-based SOFCs,” *J. Mater. Sci.*, vol. 42, no. 6, pp. 1866–1871, 2007, doi: 10.1007/s10853-006-1315-x.

[99] A. Atkinson *et al.*, “Advanced anodes for high-temperature fuel cells,” *Nature Materials*, vol. 3, no. 1. pp. 17–27, 2004, doi: 10.1038/nmat1040.

[100] H. S. Spacil, “Electrical device including nickel-containing stabilized zirconia electrode.,” 3558360, 1970.

[101] P. R. Slater, D. P. Fagg, and J. T. S. Irvine, “Synthesis and electrical characterisation of doped perovskite titanates as potential anode materials for solid oxide fuel cells,” *J. Mater. Chem.*, vol. 7, no. 12, pp. 2495–2498, 1997, doi: 10.1039/a702865b.

[102] R. J. Gorte and J. M. Vohs, “Nanostructured anodes for solid oxide fuel cells,” *Curr. Opin. Colloid Interface Sci.*, vol. 14, no. 4, pp. 236–244, 2009, doi: 10.1016/j.cocis.2009.04.006.

[103] J. T. S. Irvine, D. Neagu, M. C. Verbraeken, C. Chatzichristodoulou, C. Graves, and M. B. Mogensen, “Evolution of the electrochemical interface in high-temperature fuel cells and electrolysers,” *Nature Energy*, vol. 1, no. 1. 2016, doi: 10.1038/nenergy.2015.14.

[104] W. Z. Zhu and S. C. Deevi, “A review on the status of anode materials for solid oxide fuel cells,” vol. 362, no. July, pp. 228–239, 2003, doi: 10.1016/S0921-5093(03)00620-8.

[105] Y. Matsuzaki, “The poisoning effect of sulfur-containing impurity gas on a SOFC anode: Part I. Dependence on temperature, time, and impurity concentration,” *Solid State Ionics*, vol. 132, no. 3–4, pp. 261–269, 2000, doi: 10.1016/S0167-2738(00)00653-6.

[106] B. C. H. Steele, I. Kelly, H. Middleton, and R. Rudkin, "Oxidation of methane in solid state electrochemical reactors," *Solid State Ionics*, vol. 28–30, pp. 1547–1552, 1988.

[107] D. J. L. Brett, A. Atkinson, P. Brandon, S. J. Skinner, A. Atkinson, and D. J. L. Brett, "Intermediate temperature solid oxide fuel cells," pp. 1568–1578, 2008, doi: 10.1039/b612060c.

[108] T. Takeguchi *et al.*, "Study on steam reforming of CH4 and C2 hydrocarbons and carbon deposition on Ni-YSZ cermets," *J. Power Sources*, vol. 112, no. 2, pp. 588–595, 2002, doi: 10.1016/S0378-7753(02)00471-8.

[109] M. Mori, T. Yamamoto, and H. Itoh, "Thermal Expansion of Nickel - Zirconia Anodes in Solid Oxide Fuel Cells during Fabrication and Operation Thermal Expansion of Nickel-Zirconia Anodes in Solid Oxide Fuel Cells during Fabrication and Operation," 1998.

[110] F. Tietz, "Thermal Expansion of SOFC Materials," *Ionics (Kiel).*, vol. 5, pp. 129–139, 1999.

[111] A. Hauch, P. S. Jørgensen, K. Brodersen, and M. Mogensen, "Ni/YSZ anode - Effect of pre-treatments on cell degradation and microstructures," *J. Power Sources*, vol. 196, no. 21, pp. 8931–8941, 2011, doi: 10.1016/j.jpowsour.2011.01.009.

[112] A. Gubner, H. Landes, J. Metzger, H. Seeg, and R. Stübner, "Investigation into the degradation of the cerment anode in solix oxide fuel cell," in *SOFC V*, 1997, p. 844.

[113] Primdahl Søren, *Nickel/yttria-stabilised zirconia cermet anodes for solid oxide fuel cells*, vol. PhD. 1999.

[114] C. M. Dikwal, W. Bujalski, and K. Kendall, "The effect of temperature gradients on thermal cycling and isothermal ageing of micro-tubular solid oxide fuel cells," *J. Power Sources*, vol. 193, no. 1, pp. 241–248, 2009, doi: 10.1016/j.jpowsour.2009.01.097.

[115] K. Kendall, "Progress in microtubular solid oxide fuel cells," *Int. J. Appl. Ceram.*

Technol., 2010, doi: 10.1111/j.1744-7402.2008.02350.x.

[116] T. Iwata, “Characterization of Ni-YSZ Anode Degradation for Substrate-Type Solid Oxide Fuel Cells,” *J. Electrochem. Soc.*, 1996, doi: 10.1149/1.1836673.

[117] H. He and J. M. Hill, “Carbon deposition on Ni/YSZ composites exposed to humidified methane,” *Appl. Catal. A Gen.*, vol. 317, no. 2, pp. 284–292, 2007, doi: 10.1016/j.apcata.2006.10.040.

[118] M. B. Mogensen *et al.*, “Comprehensive Hypotheses for Degradation Mechanisms in Ni-Stabilized Zirconia Electrodes,” *ECS Trans.*, vol. 91, no. 1, pp. 613–620, 2019, doi: 10.1149/09101.0613ecst.

[119] H. Zhu, R. J. Kee, V. M. Janardhanan, O. Deutschmann, and D. G. Goodwin, “Modeling Elementary Heterogeneous Chemistry and Electrochemistry in Solid-Oxide Fuel Cells,” *J. Electrochem. Soc.*, vol. 152, no. 12, p. A2427, 2005, doi: 10.1149/1.2116607.

[120] M. Mogensen, J. Høgh, K. V. Hansen, and T. Jacobsen, “A Critical Review of Models of the H2/H2O/Ni/SZ Electrode Kinetics,” *ECS Trans.*, vol. 7, no. 1, pp. 1329–1338, 2007, doi: 10.1149/1.2729236.

[121] S. Skaarup, B. Zachau-Christiansen, and T. Jacobsen, “No Title,” in *17th Risø Internat. Symp. Mat. Science*, 1996, p. 423.

[122] M. Mogensen and S. Skaarup, “Kinetic and geometric aspects of solid oxide fuel cell electrodes,” *Solid State Ionics*, vol. 86–88, no. PART 2, pp. 1151–1160, 1996, doi: 10.1016/0167-2738(96)00280-9.

[123] E. S. Putna, J. Stubenrauch, J. M. Vohs, and R. J. Gorte, “Ceria-Based Anodes for the Direct Oxidation of Methane in Solid Oxide Fuel Cells,” *Langmuir*, vol. 11, no. 12, pp. 4832–4837, 1995, doi: 10.1021/la00012a040.

[124] K. Eguchi, T. Setoguchi, T. Inoue, and H. Arai, “Electrical properties of ceria-based oxides and their application to solid oxide fuel cells,” *Solid State Ionics*, vol. 52, pp. 165–172, 1992.

[125] O. A. Marina, C. Bagger, S. Primdahl, and M. Mogensen, “A solid oxide fuel cell

with a gadolinia-doped ceria anode: Preparation and performance," *Solid State Ionics*, vol. 123, no. 1–4, pp. 199–208, 1999, doi: 10.1016/s0167-2738(99)00111-3.

[126] S. Tao and J. T. S. Irvine, "Discovery and characterization of novel oxide anodes for solid oxide fuel cells," *Chemical Record*. 2004, doi: 10.1002/tcr.20003.

[127] C. D. Savaniu and J. T. S. Irvine, "Reduction studies and evaluation of surface modified A-site deficient La-doped SrTiO3 as anode material for IT-SOFCs," *J. Mater. Chem.*, vol. 19, no. 43, pp. 8119–8128, 2009, doi: 10.1039/b912305a.

[128] T. Ishihara, "Structure and Properties of Perovskite Oxides," in *Perovskite Oxide for Solid Oxide Fuel Cells*, T. Ishihara, Ed. Springer, 2009, pp. 1–16.

[129] J. T. S. Irvine, "New Electrodes for Improved Oxidation of Hydrocarbons in High Temperature Fuel Cells," *Fuel Cells*, vol. 1, pp. 205–210, 2001, doi: 10.1002/chin.200211244.

[130] S. Tao and J. T. S. Irvine, "A redox-stable efficient anode for solid-oxide fuel cells," *Nat. Mater.*, vol. 2, no. 5, pp. 320–323, 2003, doi: 10.1038/nmat871.

[131] H. Yokokawa, N. Sakai, T. Kawada, and M. Dokiya, "Thermodynamic stabilities of perovskite oxides for electrodes and other electrochemical materials," *Solid State Ionics*, vol. 52, pp. 43–56, 1992.

[132] J. Sfeir *et al.*, "Lanthanum chromite based catalysts for oxidation of methane directly on SOFC anodes," *J. Catal.*, vol. 202, no. 2, pp. 229–244, 2001, doi: 10.1006/jcat.2001.3286.

[133] J. B. Goodenough and Y. H. Huang, "Alternative anode materials for solid oxide fuel cells," *J. Power Sources*, vol. 173, no. 1, pp. 1–10, 2007, doi: 10.1016/j.jpowsour.2007.08.011.

[134] J. Canales-Vázquez, S. W. Tao, and J. T. S. Irvine, "Electrical properties in La2Sr4Ti6O19-δ: A potential anode for high temperature fuel cells," *Solid State Ionics*, vol. 159, no. 1–2, pp. 159–165, 2003, doi: 10.1016/S0167-2738(03)00002-X.

[135] O. A. Marina, N. L. Canfield, and J. W. Stevenson, “Thermal, electrical, and electrocatalytical properties of lanthanum-doped strontium titanate,” *Solid State Ionics*, vol. 149, no. 1–2, pp. 21–28, 2002, doi: 10.1016/S0167-2738(02)00140-6.

[136] V. Vashook, L. Vasylechko, M. Knapp, H. Ullmann, and U. Guth, “Lanthanum doped calcium titanates: Synthesis, crystal structure, thermal expansion and transport properties,” *J. Alloys Compd.*, vol. 354, no. 1–2, pp. 13–23, 2003, doi: 10.1016/S0925-8388(02)01345-2.

[137] V. Vashook *et al.*, “A-site deficient perovskite-type compounds in the ternary CaTiO3-LaCrO3-La2/3TiO3 system,” *J. Alloys Compd.*, vol. 419, no. 1–2, pp. 271–280, 2006, doi: 10.1016/j.jallcom.2005.09.063.

[138] J. C. Ruiz-Morales, J. Canales-Vázquez, C. Savaniu, D. Marrero-López, W. Zhou, and J. T. S. Irvine, “Disruption of extended defects in solid oxide fuel cell anodes for methane oxidation,” *Nature*, vol. 439, no. 7076, pp. 568–571, 2006, doi: 10.1038/nature04438.

[139] Q. X. Fu, F. Tietz, and D. Stöver, “La[sub 0.4]Sr[sub 0.6]Ti[sub 1−x]Mn[sub x]O[sub 3−δ] Perovskites as Anode Materials for Solid Oxide Fuel Cells,” *J. Electrochem. Soc.*, vol. 153, no. 4, p. D74, 2006, doi: 10.1149/1.2170585.

[140] S. Primdahl, J. R. Hansen, L. Grahl-Madsen, and P. H. Larsen, “Sr-Doped LaCrO[sub 3] Anode for Solid Oxide Fuel Cells,” *J. Electrochem. Soc.*, vol. 148, no. 1, p. A74, 2001, doi: 10.1149/1.1344519.

[141] S. Primdahl and M. Mogensen, “Mixed conductor anodes: Ni as electrocatalyst for hydrogen conversion,” *Solid State Ionics*, vol. 152–153, pp. 597–608, 2002, doi: 10.1016/S0167-2738(02)00393-4.

[142] T. Zhu, D. E. Fowler, K. R. Poeppelmeier, M. Han, and S. A. Barnett, “Hydrogen Oxidation Mechanisms on Perovskite Solid Oxide Fuel Cell Anodes,” *J. Electrochem. Soc.*, vol. 163, no. 8, pp. F952–F961, 2016, doi: 10.1149/2.1321608jes.

[143] Y. Nishihata *et al.*, “Self-regeneration of a Pd-perovskite catalyst for automotive emissions control,” *Nature*, vol. 418, no. 6894, pp. 164–167, 2002, doi:

10.1038/nature00893.

[144] C. Yang, Z. Yang, C. Jin, G. Xiao, F. Chen, and M. Han, “Sulfur-tolerant redox-reversible anode material for direct hydrocarbon solid oxide fuel cells,” *Adv. Mater.*, vol. 24, no. 11, pp. 1439–1443, 2012, doi: 10.1002/adma.201104852.

[145] T. H. Shin, Y. Okamoto, S. Ida, and T. Ishihara, “Self-recovery of pd nanoparticles that were dispersed over La(Sr)Fe(Mn)O 3 for intelligent oxide anodes of solid-oxide fuel cells,” *Chem. - A Eur. J.*, vol. 18, no. 37, pp. 11695–11702, 2012, doi: 10.1002/chem.201200536.

[146] B. H. Park and G. M. Choi, “Ex-solution of Ni nanoparticles in a La0.2Sr 0.8Ti1 - XNixO3 - δ alternative anode for solid oxide fuel cell,” *Solid State Ionics*, vol. 262, pp. 345–348, 2014, doi: 10.1016/j.ssi.2013.10.016.

[147] D. Neagu, G. Tsekouras, D. N. Miller, H. Ménard, and J. T. S. Irvine, “In situ growth of nanoparticles through control of non-stoichiometry,” *Nat. Chem.*, vol. 5, no. 11, pp. 916–923, 2013, doi: 10.1038/nchem.1773.

[148] G. Tsekouras, D. Neagu, and J. T. S. S. Irvine, “Step-change in high temperature steam electrolysis performance of perovskite oxide cathodes with exsolution of B-site dopants,” *Energy Environ. Sci.*, vol. 6, no. 1, pp. 256–266, 2013, doi: 10.1039/c2ee22547f.

[149] D. Neagu *et al.*, “Nano-socketed nickel particles with enhanced coking resistance grown in situ by redox exsolution,” *Nat. Commun.*, vol. 6, 2015, doi: 10.1038/ncomms9120.

[150] Y. Sun *et al.*, “A-site deficient perovskite: The parent for in situ exsolution of highly active, regenerable nano-particles as SOFC anodes,” *J. Mater. Chem. A*, vol. 3, no. 20, pp. 11048–11056, 2015, doi: 10.1039/c5ta01733e.

[151] D. Papargyriou and J. T. S. Irvine, “Nickel nanocatalyst exsolution from (La,Sr)(Cr,M,Ni)O3 (M=Mn,Fe) perovskites for the fuel oxidation layer of Oxygen Transport Membranes,” *Solid State Ionics*, vol. 288, pp. 120–123, 2016, doi: 10.1016/j.ssi.2015.11.007.

[152] D. Neagu *et al.*, “In Situ Observation of Nanoparticle Exsolution Mechanistic

Insight to Nanostructure Tailoring," 2019, doi: 10.1021/acsnano.9b05652.

[153] J. H. Myung, D. Neagu, D. N. Miller, and J. T. S. Irvine, "Switching on electrocatalytic activity in solid oxide cells," *Nature*, vol. 537, no. 7621, pp. 528–531, 2016, doi: 10.1038/nature19090.

[154] S. C. P. Ltd, "Perovskites: The next PV revolution?," 2014. http://www.solarchoice.net.au/blog/news/perovskites-the-next-solar-pv-revolution-240714.

[155] G. Trolliard, N. Ténèze, P. Boullay, and D. Mercurio, "TEM study of cation-deficient-perovskite related AnB n-1O3n compounds: The twin-shift option," *J. Solid State Chem.*, vol. 177, no. 4–5, pp. 1188–1196, 2004, doi: 10.1016/j.jssc.2003.10.024.

[156] D. Neagu, "Materials and Microstructures for High Temperature Electrochemical Devices through Control of Perovskite Defect Chemistry," no. December, pp. 1–257, 2012.

[157] H. Arai, T. Yamada, K. Eguchi, and T. Seiyama, "Catalytic combustion of methane over various perovskite-type oxides," *Appl. Catal.*, vol. 26, pp. 265–276, 1986.

[158] R. D. Shannon, "Revised Effective Ionic Radii and Systematic Studies of Interatomie Distances in Halides and Chaleogenides," *Acta Cryst.*, vol. A 32, p. 751, 1976.

[159] T. D. McColm and J. T. S. Irvine, "B site doped strontium titanate as a potential SOFC substrate," *Ionics (Kiel).*, vol. 7, no. 1–2, pp. 116–121, 2001, doi: 10.1007/BF02375477.

[160] H. Iwahara, "Ionic Conduction in Perovskite-Type Compounds," in *Perovskite Oxide for Solid Oxide Fuel Cells (Hardback)*, 2009.

[161] R. N. Blumenthal and R. K. Sharma, "Electronic Conductivity in Nonstoichiometric Cerium Dioxide *," vol. 364, pp. 360–364, 1975.

[162] H. L. Tuller and A. S. Nowick, "Small polaron electron transport in reduced

CeO2 single crystals," *J. Phys. Chem. Solids*, vol. 38, no. 8, pp. 859–867, 1977.

[163] F. A. Groger, *The Chemistry of Imperfect Crystals*. Amsterdam, 1964.

[164] R. A. De Souza and J. A. Kilner, "Oxygen transport in La1-xSrxMn1-yCoyO 3±δ perovskites Part I. Oxygen tracer diffusion," *Solid State Ionics*, vol. 106, no. 3–4, pp. 175–187, 1998, doi: 10.1016/s0167-2738(97)00499-2.

[165] I. Yasuda, K. Ogasawara, M. Hishinuma, T. Kawada, and M. Dokiya, "Oxygen tracer diffusion coefficient of (La, Sr)MnO3±δ," *Solid State Ionics*, vol. 86–88, no. PART 2, pp. 1197–1201, 1996, doi: 10.1016/0167-2738(96)00287-1.

[166] J. A. . Kilner, A. . Berenov, and J. Rossiny, "Diffusivity of the Oxide Ion in Perovskite Oxides," in *Perovskite Oxide for Solid Oxide Fuel Cells*, T. Ishihara, Ed. 2009, pp. 95–117.

[167] D. Neagu and J. T. S. Irvine, "Enhancing electronic conductivity in strontium titanates through correlated A and B-site doping," *Chem. Mater.*, vol. 23, no. 6, pp. 1607–1617, 2011, doi: 10.1021/cm103489r.

[168] M. J. Escudero, J. T. S. Irvine, and L. Daza, "Development of anode material based on La-substituted SrTiO3 perovskites doped with manganese and/or gallium for SOFC," *J. Power Sources*, vol. 192, no. 1, pp. 43–50, 2009, doi: 10.1016/j.jpowsour.2008.11.132.

[169] J. A. Kilner, "Fast oxygen transport in acceptor doped oxides," *Solid State Ionics*, vol. 129, no. 1, pp. 13–23, 2000, doi: 10.1016/S0167-2738(99)00313-6.

[170] R. Shiozaki, "Partial oxidation of methane over a Ni/BaTiO3 catalyst prepared by solid phasecrystallization.," *J. Chem. Soc. Faraday Trans.*, vol. 93, pp. 3235–3242, 1997.

[171] H. Tanaka *et al.*, "The intelligent catalyst having the self-regenerative function of Pd, Rh and Pt for automotive emissions control," *Catal. Today*, vol. 117, no. 1–3, pp. 321–328, 2006, doi: 10.1016/j.cattod.2006.05.029.

[172] H. Tanaka *et al.*, "Self-regenerating Rh- and Pt-based perovskite catalysts for automotive-emissions control," *Angew. Chemie - Int. Ed.*, vol. 45, no. 36, pp.

5998–6002, 2006, doi: 10.1002/anie.200503938.

[173] B. D. Madsen, W. Kobsiriphat, Y. Wang, L. D. Marks, and S. Barnett, “SOFC Anode Performance Enhancement through Precipitation of Nanoscale Catalysts,” *ECS Trans.*, vol. 7, no. 1, pp. 1339–1348, 2007, doi: 10.1149/1.2729237.

[174] W. Kobsiriphat, B. D. Madsen, Y. Wang, M. Shah, L. D. Marks, and S. A. Barnett, “Nickel- and Ruthenium-Doped Lanthanum Chromite Anodes: Effects of Nanoscale Metal Precipitation on Solid Oxide Fuel Cell Performance,” *J. Electrochem. Soc.*, vol. 157, no. 2, p. B279, 2010, doi: 10.1149/1.3269993.

[175] G. Tsekouras, D. Neagu, and J. T. S. Irvine, “Step-change in high temperature steam electrolysis performance of perovskite oxide cathodes with exsolution of B-site dopants,” *Energy Environ. Sci.*, vol. 6, no. 1, pp. 256–266, 2013, doi: 10.1039/C2EE22547F.

[176] T. Liu *et al.*, “Robust redox-reversible perovskite type steam electrolyser electrode decorated with: In situ exsolved metallic nanoparticles,” *J. Mater. Chem. A*, vol. 8, no. 2, pp. 582–591, 2020, doi: 10.1039/c9ta06309a.

[177] T. S. Oh *et al.*, “Evidence and Model for Strain-Driven Release of Metal Nanocatalysts from Perovskites during Exsolution,” *J. Phys. Chem. Lett.*, vol. 6, no. 24, pp. 5106–5110, 2015, doi: 10.1021/acs.jpclett.5b02292.

[178] M. L. Toebes, J. H. Bitter, A. Jos Van Dillen, and K. P. De Jong, “Impact of the structure and reactivity of nickel particles on the catalytic growth of carbon nanofibers,” *Catal. Today*, vol. 76, no. 1, pp. 33–42, 2002, doi: 10.1016/S0920-5861(02)00209-2.

[179] F. Abild-Pedersen, J. K. Nørskov, J. R. Rostrup-Nielsen, J. Sehested, and S. Helveg, “Mechanisms for Catalytic Carbon Nanofiber Growth Studied by Ab Initio Density Functional Theory Calculations,” *Phys. Rev. B*, vol. 73, pp. 115419-1-115419–13, 2006, doi: 10.1103/PhysRevB.73.115419.

[180] L. Adijanto, V. B. Padmanabhan, R. J. Gorte, and J. M. Vohs, “Polarization-Induced Hysteresis in CuCo-Doped Rare Earth Vanadates SOFC Anodes,” *J. Electrochem. Soc.*, vol. 159, no. 11, pp. F751–F756, 2012, doi:

10.1149/2.042211jes.

[181] D. M. Bierschenk *et al.*, “Pd-substituted (La,Sr)CrO3-δ-Ce0.9Gd 0.1O2-δ solid oxide fuel cell anodes exhibiting regenerative behavior,” *J. Power Sources*, vol. 196, no. 6, pp. 3089–3094, 2011, doi: 10.1016/j.jpowsour.2010.12.050.

[182] A. K. Opitz *et al.*, “Enhancing electrochemical water-splitting kinetics by polarization-driven formation of near-surface iron(0): An in situ XPS study on perovskite-type electrodes,” *Angew. Chemie - Int. Ed.*, vol. 54, no. 9, pp. 2628–2632, 2015, doi: 10.1002/anie.201409527.

[183] A. K. Opitz *et al.*, “Understanding electrochemical switchability of perovskite-type exsolution catalysts,” *Nat. Commun.*, vol. 11, no. 1, pp. 1–10, 2020, doi: 10.1038/s41467-020-18563-w.

[184] M. B. Katz *et al.*, “Reversible precipitation/dissolution of precious-metal clusters in perovskite-based catalyst materials: Bulk versus surface re-dispersion,” *J. Catal.*, vol. 293, pp. 145–148, 2012, doi: 10.1016/j.jcat.2012.06.017.

[185] D. Neagu *et al.*, “Demonstration of chemistry at a point through restructuring and catalytic activation at anchored nanoparticles,” *Nat. Commun.*, vol. 8, no. 1, 2017, doi: 10.1038/s41467-017-01880-y.

[186] J. H. Kuo, H. U. Anderson, and D. M. Sparlin, “Oxidation-reduction behavior of undoped and Sr-doped LaMnO3: Defect structure, electrical conductivity, and thermoelectric power,” *J. Solid State Chem.*, vol. 87, no. 1, pp. 55–63, 1990, doi: 10.1016/0022-4596(90)90064-5.

[187] J. A. M. van Roosmalen and E. H. P. Cordfunke, “The defect chemistry of lamno3±δ. 4. defect model for lamno3+δ,” *Journal of Solid State Chemistry*, vol. 110, no. 1. pp. 109–112, 1994, doi: 10.1006/jssc.1994.1143.

[188] F. W. Poulsen, “Defect chemistry modelling of oxygen-stoichiometry, vacancy concentrations, and conductivity of (La1-xSrx)yMnO3±δ,” *Solid State Ionics*, vol. 129, no. 1, pp. 145–162, 2000, doi: 10.1016/S0167-2738(99)00322-7.

[189] H. Kamata, Y. Yonemura, J. Mizusaki, H. Tagawa, K. Naraya, and T. i. Sasamoto, “High temperature electrical properties of the perovskite-type oxide

La1 - xSrxMnO3 - d," *J. Phys. Chem. Solids*, vol. 56, no. 7, pp. 943–950, 1995, doi: 10.1016/0022-3697(95)00019-4.

[190] E. P. Murray, T. Tsai, and S. A. Barnett, "Oxygen transfer processes in (La,Sr)MnO3/Y2O3-stabilized ZrO2 cathodes: an impedance spectroscopy study," *Solid State Ionics*, vol. 110, no. 3–4, pp. 235–243, 1998, doi: 10.1016/S0167-2738(98)00142-8.

[191] Y. Ji, J. A. Kilner, and M. F. Carolan, "Electrical properties and oxygen diffusion in yttria-stabilised zirconia (YSZ)-La0.8Sr0.2MnO3±δ (LSM) composites," *Solid State Ionics*, vol. 176, no. 9–10, pp. 937–943, 2005, doi: 10.1016/j.ssi.2004.11.019.

[192] A. Fossdal, M. Menon, K. Wiik, M. Einarsrud, and T. Grande, "Crystal Structure and Thermal Expansion of La," *Transition*, vol. 1958, no. 7, pp. 1952–1958, 2004.

[193] T. Kawada, "Perovskite Oxide for Cathode of SOFCs," in *Perovskite Oxide for Solid Oxide Fuel Cells*, T. Ishihara, Ed. Springer, 2009.

[194] O. Yamamoto, "Stability of Perovskite Oxide Electrode with Stabilized Zirconia," *ECS Proc. Vol.*, vol. 1989–11, no. 1, pp. 242–253, 1989, doi: 10.1149/198911.0242pv.

[195] A. Mitterdorfer, "La2Zr2O7 formation and oxygen reduction kinetics of the La0.85Sr0.15MnyO3, O2(g)|YSZ system," *Solid State Ionics*, vol. 111, no. 3–4, pp. 185–218, 1998, doi: 10.1016/S0167-2738(98)00195-7.

[196] M. Mori *et al.*, "Reaction mechanism between lanthanum manganite and yttria doped cubic zirconia," *Solid State Ionics*, vol. 123, no. 1, pp. 113–119, 1999, doi: 10.1016/S0167-2738(99)00115-0.

[197] S. P. Simner, J. P. Shelton, M. D. Anderson, and J. W. Stevenson, "Interaction between La(Sr)FeO3 SOFC cathode and YSZ electrolyte," *Solid State Ionics*, vol. 161, no. 1–2, pp. 11–18, 2003, doi: 10.1016/S0167-2738(03)00158-9.

[198] S. B. Adler, "Limitations of charge-transfer models for mixed-conducting oxygen electrodes," *Solid State Ionics*, vol. 135, no. 1–4, pp. 603–612, 2000, doi:

10.1016/S0167-2738(00)00423-9.

[199] K. Yasumoto, Y. Inagaki, M. Shiono, and M. Dokiya, “An (La,Sr)(Co,Cu)O3-δ cathode for reduced temperature SOFCs,” *Solid State Ionics*, vol. 148, no. 3–4, pp. 545–549, 2002, doi: 10.1016/S0167-2738(02)00115-7.

[200] S. Wang, M. Katsuki, M. Dokiya, and T. Hashimoto, “High temperature properties of La0.6Sr0.4Co0.8Fe0.2O3-δ phase structure and electrical conductivity,” *Solid State Ionics*, vol. 159, no. 1–2, pp. 71–78, 2003, doi: 10.1016/S0167-2738(03)00027-4.

[201] L. W. Tai, M. M. Nasrallah, H. U. Anderson, D. M. Sparlin, and S. R. Sehlin, “Structure and electrical properties of La1-xSrxCo1-Fey03 . Part 1 . The system La0.8Sr0.2Co1-yFeyO3,” *Solid State Ionics*, vol. 76, no. 94, 1995.

[202] L. W. Tai, M. M. Nasrallah, H. U. Anderson, D. M. Sparlin, and S. R. Sehlin, “Structure and electrical properties of La1 - xSrxCo1 - yFeyO3. Part 2. The system La1 - xSrxCo0.2Fe0.8O3,” *Solid State Ionics*, vol. 76, no. 3–4, pp. 273–283, 1995, doi: 10.1016/0167-2738(94)00245-N.

[203] Y. Teraoka, H. M. Zhang, K. Okamoto, and N. Yamazoe, “Mixed ionic-electronic conductivity of La1−xSrxCo1−yFeyO3−δ perovskite-type oxides,” *Mater. Res. Bull.*, vol. 23, no. 1, pp. 51–58, 1988.

[204] J. Bae and B. C. H. Steele, “Properties of La Sr Co Fe O (LSCF) double layer 0.6 0.4 0.2 0.8 32d cathodes on gadolinium-doped cerium oxide (CGO) electrolytes I. Role of SiO2,” *Solid State Ionics*, vol. 106, pp. 247–253, 1998.

[205] H. Y. Tu, Y. Takeda, N. Imanishi, and O. Yamamoto, “Ln0.4Sr0.6Co0.8Fe0.2O 3-δ (Ln=La, Pr, Nd, Sm, Gd) for the electrode in solid oxide fuel cells,” *Solid State Ionics*, vol. 117, no. 3–4, pp. 277–281, 1999, doi: 10.1016/s0167-2738(98)00428-7.

[206] J. Gao, X. Liu, D. Peng, and G. Meng, “Electrochemical behavior of Ln0.6Sr0.4Co0.2Fe0.8O3-δ (Ln = Ce, Gd, Sm, Dy) materials used as cathode of IT-SOFC,” *Catal. Today*, vol. 82, no. 1–4, pp. 207–211, 2003, doi: 10.1016/S0920-5861(03)00234-7.

[207] C. C. Chen, M. M. Nasrallah, and H. U. Anderson, “Synthesis and Characterization of (CeO2) 0.8 (SmO1.5) 0.2 Thin Films from Polymeric Precursors,” *J. Electrochem. Soc.*, vol. 140, no. 12, pp. 3555–3560, 1993, doi: 10.1149/1.2221125.

[208] K. K. Hansen, “Evaluation of LSF based SOFC cathodes using cone-shaped electrodes and EIS,” *Solid State Ionics*, vol. 344, no. October 2019, p. 115096, 2020, doi: 10.1016/j.ssi.2019.115096.

[209] J.-D. Kim *et al.*, “Characterization of LSM-- YSZ composite electrode by ac impedance spectroscopy,” *Solid State Ionics*, vol. 143, pp. 379–389, 2001.

[210] J. A. Kilner, R. A. De Souza, and I. C. Fullarton, “Surface exchange of oxygen in mixed conducting perovskite oxides,” *Solid State Ionics*, vol. 86–88, no. PART 2, pp. 703–709, 1996, doi: 10.1016/0167-2738(96)00153-1.

[211] S. Linderoth, “Solid oxide cell R & D at Risø National Laboratory — and its transfer to technology,” pp. 61–66, 2009, doi: 10.1007/s10832-008-9458-6.

[212] M. Cassidy, “Trends in the processing and manufacture of solid oxide fuel cells,” *Wiley Interdiscip. Rev. Energy Environ.*, vol. 6, no. 5, 2017, doi: 10.1002/wene.248.

[213] Y. Chen *et al.*, “Layered YSZ/SCSZ/YSZ electrolytes for intermediate temperature SOFC Part I: Design and manufacturing,” *Fuel Cells*, vol. 12, no. 5, pp. 722–731, 2012, doi: 10.1002/fuce.201200008.

[214] J. C. Ruiz-Morales, D. Marrero-López, M. Gálvez-Sánchez, J. Canales-Vázquez, C. Savaniu, and S. N. Savvin, “Engineering of materials for solid oxide fuel cells and other energy and environmental applications,” *Energy Environ. Sci.*, vol. 3, no. 11, p. 1670, 2010, doi: 10.1039/c0ee00166j.

[215] E. D. Wachsman and K. T. Lee, “Lowering the temperature of solid oxide fuel cells.,” *Science*, vol. 334, no. 6058, pp. 935–9, 2011, doi: 10.1126/science.1204090.

[216] S. De Souza, S. J. Visco, and L. C. De Jonghe, “Thin-film solid oxide fuel cell with high performance at low- temperature,” vol. 98, pp. 57–61, 1997.

[217] D. Waldbillig, A. Wood, and D. G. Ivey, "Electrochemical and microstructural characterization of the redox tolerance of solid oxide fuel cell anodes," vol. 145, pp. 206–215, 2005, doi: 10.1016/j.jpowsour.2004.12.071.

[218] B. C. H. Steele, A. Atkinson, J. A. Kilner, N. P. Brandon, and R. A. Rudkin, "Fuel Cells," GB2368450B, 2004.

[219] K. Huang and S. C. Singhal, "Cathode-supported tubular solid oxide fuel cell technology: A critical review," *Journal of Power Sources*, vol. 237. pp. 84–97, 2013, doi: 10.1016/j.jpowsour.2013.03.001.

[220] N. P. Brandon *et al.*, "Development of metal supported solid oxide fuel cells for operation at 500-600°C," *J. Mater. Eng. Perform.*, vol. 13, no. 3, pp. 253–256, 2004, doi: 10.1361/10599490419135.

[221] M. C. Tucker, "Progress in metal-supported solid oxide fuel cells : A review," *J. Power Sources*, vol. 195, no. 15, pp. 4570–4582, 2010, doi: 10.1016/j.jpowsour.2010.02.035.

[222] H. J. Cho, K. J. Kim, Y. M. Park, and G. M. Choi, "Flexible solid oxide fuel cells supported on thin and porous metal," *Int. J. Hydrogen Energy*, vol. 41, no. 22, pp. 9577–9584, 2016, doi: 10.1016/j.ijhydene.2016.04.040.

[223] R. A. George and N. F. Bessette, "Reducing the manufacturing cost of tubular solid oxide fuel cell technology," *J. Power Sources*, vol. 71, no. 1–2, pp. 131–137, 1998, doi: 10.1016/s0378-7753(97)02735-3.

[224] N. Q. Minh, "Solid oxide fuel cell technology - Features and applications," *Solid State Ionics*, vol. 174, no. 1–4. pp. 271–277, 2004, doi: 10.1016/j.ssi.2004.07.042.

[225] N. H. Menzler, F. Tietz, S. Uhlenbruck, H. P. Buchkremer, and D. Stöver, "Materials and manufacturing technologies for solid oxide fuel cells," *Journal of Materials Science*, vol. 45, no. 12. pp. 3109–3135, 2010, doi: 10.1007/s10853-010-4279-9.

[226] D. Fray, A. Varga, S. Mounsey, and J. C. Tan, "Solid oxide fuel cells (SOFCs)," 2006. https://www.doitpoms.ac.uk/tlplib/fuel-cells/index.php (accessed Sep. 22,

2021).

[227] A. Hornés, M. Torrell, A. Morata, M. Kendall, K. Kendall, and A. Tarancón, "Towards a high fuel utilization and low degradation of micro-tubular solid oxide fuel cells," *Int. J. Hydrogen Energy*, vol. 42, no. 19, pp. 13889–13901, 2017, doi: 10.1016/j.ijhydene.2016.12.106.

[228] K. S. Howe, G. J. Thompson, and K. Kendall, "Micro-tubular solid oxide fuel cells and stacks," *J. Power Sources*, vol. 196, no. 4, pp. 1677–1686, 2011, doi: 10.1016/j.jpowsour.2010.09.043.

[229] K. Kendall, J. Newton, and M. Kendall, "Microtubular SOFC (mSOFC) System in Truck APU Application," *ECS Trans.*, 2015, doi: 10.1149/06801.0187ecst.

[230] F. G. E. Jones, P. A. Connor, A. J. Feighery, J. Nairn, J. Rennie, and J. T. S. Irvine, "SOFCRoll development at St. Andrews fuel cells Ltd.," *J. Fuel Cell Sci. Technol.*, vol. 4, no. 2, pp. 138–142, 2007, doi: 10.1115/1.2713770.

[231] M. Cassidy, "SOFCRoll Recent Development Overview," St. Andrews, 2017.

[232] F. G. E. Jones, "Tape Casting, Co-firing and Electrical Characterisation of a Novel Design Solid Oxide Fuel Cell: SOFCRoll," University of St Andrews, St Andrews, 2005.

[233] A. T. Tesfai, "Solid Oxide Fuel Cells (SOFCRoll) Single Cell Stack Design and Development," St Andrews, 2013.

[234] A. Auxemery, "Bodreaux Internship Final Report," 2011.

[235] M. Etches, "Bodreaux Internship Final Report," 2012.

[236] G. Dulbecco, "Bodreaux Internship Final Report," 2016.

[237] A. Limou, "Riennes Internship Final Report," 2017.

[238] M. Machado, "Masters Dissertation," 2014.

[239] M. Cassidy, M. MacHado, P. A. Connor, J. Nairn, C. Ni, and J. T. S. Irvine, "No Title," in *Proc. 11th Europ. SOFC Forum*, 2014.

[240] D. J. Doherty, "Masters Dissertation," 2015.

[241] M. Cassidy, D. J. Doherty, X. Yue, and J. T. S. Irvine, “Development of Tailored Porous Microstructures for Infiltrated Catalyst Electrodes by Aqueous Tape Casting Methods,” vol. 68, no. 1, pp. 2047–2056, 2015.

[242] A. Ruszin, “Masters Dissertation,” 2017.

[243] Malvern Instruments Limited, “Mastersizer 3000,” p. 20, 2013.

[244] A. M. F. R. Pinto, V. B. Oliveira, and D. S. Falcão, *Experimental methods of characterization*. 2018.

[245] “Scanning electron microscope,” *Wikipedia*, 2021. https://en.wikipedia.org/wiki/Scanning_electron_microscope (accessed Sep. 22, 2021).

[246] Schema MEB, Steff, ARTE, and MarcoTolo, “Diagram of a scanning electron microscope,” 2010. https://commons.wikimedia.org/wiki/File:Schema_MEB_(en).svg.

[247] L. Lu, “Studies of Anode Supported Solid Oxide Fuel Cells (SOFCs) Based on La- and Ca-Doped SrTiO 3 Lanying Lu This thesis is submitted in partial fulfilment for the degree of PhD,” 2015.

[248] R. E. Mistler and E. R. Twiname, *Tape Casting: Theory and Practice*. Wiley-American Ceramic Society, 2000.

[249] W. Jillek and W. K. C. Yung, “Embedded components in printed circuit boards: A processing technology review,” *Int. J. Adv. Manuf. Technol.*, vol. 25, no. 3–4, pp. 350–360, 2005, doi: 10.1007/s00170-003-1872-y.

[250] R. I. Tomov, T. Mitchell-Williams, C. Gao, R. V. Kumar, and B. A. Glowacki, “Performance optimization of LSCF/Gd:CeO2 composite cathodes via single-step inkjet printing infiltration,” *J. Appl. Electrochem.*, vol. 47, no. 5, pp. 641–651, 2017, doi: 10.1007/s10800-017-1066-1.

[251] Y. X. Liu, S. F. Wang, Y. F. Hsu, and P. Jasinski, “Characteristics of La0.8Sr0.2Ga0.8Mg0.2O3-Δ-supported micro-tubular solid oxide fuel cells with LaCo0.4Ni0.6-xCuxO3-Δ cathodes,” *Int. J. Hydrogen Energy*, vol. 43, no. 11,

pp. 5703–5713, 2018, doi: 10.1016/j.ijhydene.2018.01.170.

[252] H. Monzón, M. A. Laguna-Bercero, A. Larrea, B. I. Arias, A. Várez, and B. Levenfeld, “Design of industrially scalable microtubular solid oxide fuel cells based on an extruded support,” *Int. J. Hydrogen Energy*, vol. 39, no. 10, pp. 5470–5476, 2014, doi: 10.1016/j.ijhydene.2014.01.010.

[253] J. H. Song, S. Il Park, J. H. Lee, and H. S. Kim, “Fabrication characteristics of an anode-supported thin-film electrolyte fabricated by the tape casting method for IT-SOFC,” *J. Mater. Process. Technol.*, vol. 198, no. 1–3, pp. 414–418, 2008, doi: 10.1016/j.jmatprotec.2007.07.030.

[254] D. Montinaro *et al.*, “Tape casting fabrication and co-sintering of solid oxide ‘half cells’ with a cathode-electrolyte porous interface,” *Solid State Ionics*, vol. 177, no. 19-25 SPEC. ISS., pp. 2093–2097, 2006, doi: 10.1016/j.ssi.2006.01.016.

[255] D. J. Shanefield, *Organic Additives and Ceramic Processing;* Boston: Kluwer Academic Publishers, 1995.

[256] P. Boch and T. Chartier, “Tape Casting and Properties of Mullite and Zirconia-Mullite,” *J. Am. Ceram. Soc.*, vol. 74, no. 10, pp. 2448–52, 1991.

[257] H. Burrell, “Solubility Parameters,” *Interchem. rev.*, vol. 14, no. 1, pp. 3–16, 1955.

[258] R. E. Mistler, D. J. Shanefield, and R. B. Runk, “Tape Casting of Ceramics,” in *Ceramic Processing Before Firitzg*, New York: John Wiley & Sons, 1978, p. 417.

[259] W. R. Cannon, R. Beclter, and I. R. Milteslta, “Interactions Among Organic Additives Used for Tape casting,” *Adv. Ceram.*, vol. 26, pp. 525–41, 1989.

[260] F. G. E. Jones and J. T. S. Irvine, “Co-Fired SOFC Electrode- Electrolyte-Electrode Membrane Rolls, Combining Tubular and Planar Technologies,” in *Fifth European Solid Oxide Fuel Cell Forum*, 2002, pp. 123–121.

[261] D. Simwonis, A. Naoumidis, F. J. Dias, J. Linke, and A. Moropoulou, “Material characterization in support of the development of an anode substrate for solid

oxide fuel cells," *J. Mater. Res.*, vol. 12, no. 6, pp. 1508–1518, 1997, doi: 10.1557/JMR.1997.0207.

[262] A. Hagen, M. Menon, R. Barfod, P. V. Hendriksen, S. Ramousse, and P. H. Larsen, "Properties and performance of SOFCs produced on a pre-pilot plant scale," *Fuel Cells*, vol. 6, no. 2, pp. 146–150, 2006, doi: 10.1002/fuce.200500108.

[263] H. Wang, Z. Gao, and S. A. Barnett, "Anode-Supported Solid Oxide Fuel Cells Fabricated by Single Step Reduced-Temperature Co-Firing," *J. Electrochem. Soc.*, vol. 163, no. 3, pp. F196–F201, 2016, doi: 10.1149/2.03716023jes.

[264] N. Hedayat, D. Panthi, and Y. Du, "Fabrication of tubular solid oxide fuel cells by solvent-assisted lamination and co-firing a rolled multilayer tape cast," *Int. J. Appl. Ceram. Technol.*, vol. 15, no. 2, pp. 307–314, 2018, doi: 10.1111/ijac.12828.

[265] A. J. Jacobson, "Materials for Solid Oxide Fuel Cells †," pp. 660–674, 2010, doi: 10.1021/cm902640j.

[266] A. M. Soydan, Ö. Yıldız, A. Durğun, O. Y. Akduman, and A. Ata, "Production, performance and cost analysis of anode-supported NiO-YSZ micro-tubular SOFCs," *Int. J. Hydrogen Energy*, vol. 44, no. 57, pp. 30339–30347, 2019, doi: 10.1016/j.ijhydene.2019.09.156.

[267] J. T. S. Irvine, F. G. E. Jones, and P. A. Connor, "Improvements in Fuel Cells and Related Devices.," PCT/GB2002/004726, 2003.

[268] NETZSCH, "Dilatometer Series DIL 402 Expedis Select and Supreme Method, Instruments, Applications."

[269] C. A. Schneider, W. S. Rasband, and K. W. Eliceiri, "NIH Image to ImageJ: 25 years of image analysis," *Nat. Methods*, vol. 9, no. 7, pp. 671–675, 2012, doi: 10.1038/nmeth.2089.

[270] A. McNaughton, "Measuring Area Using Thresholds," 2010. http://occm.otago.ac.nz/resources/ImageJ-Thresholding.pdf.

[271] W. R. T. Ferreira, “ImageJ User Guide IJ 1.46r,” *IJ 1.46r*, p. 185, 2012, doi: 10.1038/nmeth.2019.

[272] S. Zhang, L. Bi, L. Zhang, C. Yang, H. Wang, and W. Liu, “Fabrication of cathode supported solid oxide fuel cell by multi-layer tape casting and co-firing method,” *Int. J. Hydrogen Energy*, vol. 34, no. 18, pp. 7789–7794, 2009, doi: 10.1016/j.ijhydene.2009.07.081.

[273] X. Zhou, K. Sun, J. Gao, S. Le, N. Zhang, and P. Wang, “Microstructure and electrochemical characterization of solid oxide fuel cells fabricated by co-tape casting,” *J. Power Sources*, vol. 191, no. 2, pp. 528–533, 2009, doi: 10.1016/j.jpowsour.2009.02.008.

[274] N. H. Menzler, J. Malzbender, P. Schoderböck, R. Kauert, and H. P. Buchkremer, “Sequential tape casting of anode-supported solid oxide fuel cells,” *Fuel Cells*, vol. 14, no. 1, pp. 96–106, 2014, doi: 10.1002/fuce.201300153.

[275] S. Le *et al.*, “Fabrication and evaluation of anode and thin Y2O3-stabilized ZrO2 film by co-tape casting and co-firing technique,” *J. Power Sources*, vol. 195, no. 9, pp. 2644–2648, 2010, doi: 10.1016/j.jpowsour.2009.11.039.

[276] S. F. Corbin, “Engineered Porosity via Tape Casting , Lamination and the Percolation of Pyrolyzable Particulates,” vol. 701, pp. 1693–1701, 1999.

[277] S. F. Corbin, J. Lee, and X. Qiao, “Influence of Green Formulation and Pyrolyzable Particulates on the Porous Microstructure and Sintering Characteristics of Tape Cast Ceramics,” vol. 47, pp. 41–47, 2001.

[278] Y.-M. Chiang, C. B. Dunbar, and W. D. Kingery, “Physical ceramics: principles for ceramic science and engineering,” *Choice Rev. Online*, vol. 34, no. 03, pp. 34-1566-34–1566, 1996, doi: 10.5860/choice.34-1566.

[279] C. G. Kuczynski, “Self-diffusion in Sintering of Metallic Particles,” *J. Met.*, vol. 1, no. 2, pp. 169–78, 1949.

[280] Anonimo, “Sintering : Grain Boundaries, Interfaces, and Porosity,” 2014.

[281] J. Rojek, S. Nosewicz, M. Maździarz, P. Kowalczyk, K. Wawrzyk, and D.

Lumelskyj, “Modeling of a Sintering Process at Various Scales,” *Procedia Eng.*, vol. 177, pp. 263–270, 2017, doi: 10.1016/j.proeng.2017.02.210.

[282] W. D. Kingery and M. Berg, “Study of the initial stages of sintering solids by viscous flow, evaporation-condensation, and self-diffusion,” *J. Appl. Phys.*, vol. 26, no. 10, pp. 1205–1212, 1955, doi: 10.1063/1.1721874.

[283] R. L. Coble, “Sintering crystalline solids. I. intermediate and final state diffusion models,” *J. Appl. Phys.*, vol. 32, no. 5, pp. 787–792, 1961, doi: 10.1063/1.1736107.

[284] D. L. Johnson, “New method of obtaining volume, grain-boundary, and surface diffusion coefficients from sintering data,” *J. Appl. Phys.*, vol. 40, no. 1, pp. 192–200, 1969, doi: 10.1063/1.1657030.

[285] T. Shulin, Z. Xiaomin, Z. Zhipeng, and W. Zhouzhi, “Driving force evolution in solid-state sintering with coupling multiphysical fields,” *Ceram. Int.*, vol. 46, no. 8, pp. 11584–11592, 2020, doi: 10.1016/j.ceramint.2020.01.187.

[286] A. Kumar, “Ceramics : Sintering and Microstructure,” *Ceram. Colloids*, pp. 1–15, 2008.

[287] W. D. Kingery, *Kinetics of High Temperature Processes*. New York: John Wiley & Sons, Inc., 1959.

[288] J. E. Burke, “Role of Grain Boundaries in Sintering,” *J. Am. Ceram. Soc.*, vol. 40, pp. 80–85, 1957.

[289] R. J. . Brook, “Fabrication Principles for the Production of Ceramics with Superior Mechanical Properties,” *Proc. Brit. Ceram. Soc.*, vol. 32, pp. 7–24, 1982.

[290] T. O’Haver, “peakfit.” Tom O’Haver (2021). peakfit.m (https://www.mathworks.com/matlabcentral/fileexchange/23611-peakfit-m), MATLAB Central File Exchange. Retrieved August 23, 2021., 2021, [Online]. Available: https://uk.mathworks.com/matlabcentral/fileexchange/23611-peakfit-m.

[291] R. D. Fierro, G. H. Golub, P. C. Hansen, and D. P. O'Leary, "Regularization by truncated total least squares," *SIAM J. Sci. Comput.*, vol. 18, no. 4, pp. 1223–1241, 1997, doi: 10.1137/S1064827594263837.

[292] M. Saccoccio, T. H. Wan, C. Chen, and F. Ciucci, "Optimal regularization in distribution of relaxation times applied to electrochemical impedance spectroscopy: Ridge and Lasso regression methods - A theoretical and experimental Study," *Electrochim. Acta*, vol. 147, pp. 470–482, 2014, doi: 10.1016/j.electacta.2014.09.058.

[293] J. Van Herle and R. Vasquez, "Conductivity of Mn and Ni-doped stabilized zirconia electrolyte," *J. Eur. Ceram. Soc.*, vol. 24, no. 6, pp. 1177–1180, 2004, doi: 10.1016/S0955-2219(03)00471-0.

[294] M. J. Jørgensen and M. Mogensen, "Impedance of Solid Oxide Fuel Cell LSM/YSZ Composite Cathodes," *J. Electrochem. Soc.*, vol. 148, no. 5, p. A433, 2002, doi: 10.1149/1.1360203.

[295] E. Siebert, A. Hammouche, and M. Kleitz, "Impedance spectroscopy analysis of La1-xSrxMnO3-yttria-stabilized zirconia electrode kinetics," *Electrochim. Acta*, vol. 40, no. 11, pp. 1741–1753, 1995, doi: 10.1016/0013-4686(94)00361-4.

[296] R. Barfod, A. Hagen, S. Ramousse, P. V. Hendriksen, and M. Mogensen, "Break down of losses in thin electrolyte SOFCs," *Fuel Cells*, vol. 6, no. 2, pp. 141–145, 2006, doi: 10.1002/fuce.200500113.

[297] M. Brown, S. Primdahl, and M. Mogensen, "Structure / Performance Relations for Ni / Yttria - Stabilized Zirconia Anodes for Solid Oxide Fuel Cells Structure / Performance Relations for Ni / Yttria-Stabilized Zirconia Anodes for Solid Oxide Fuel Cells," 2000.

[298] S. Primdahl and M. Mogensen, "Gas Conversion Impedance: A Test Geometry Effect in Characterization of Solid Oxide Fuel Cell Anodes," *J. Electrochem. Soc.*, vol. 145, no. 7, pp. 2431–2438, 1998, doi: 10.1149/1.1838654.

[299] M. R. Gauna, M. S. Conconi, S. Gomez, G. Suárez, E. F. Aglietti, and N. M. Rendtorff, "Monoclinic-tetragonal zirconia quantification of commercial

nanopowder mixtures by XRD and DTA," *Ceram. - Silikaty*, vol. 50, no. 4, pp. 318–325, 2015.

[300] I. R. Gibson, G. P. Dransfield, and J. T. S. Irvine, "Sinterability of commercial 8 mol% yttria-stabilized zirconia powders and the effect of sintered density on the ionic conductivity," *J. Mater. Sci.*, 1998, doi: 10.1023/A:1004435504482.

[301] L. Lu, C. Ni, M. Cassidy, J. T. S. Irvine, and M. C. and J. T. S. I. Lanying Lu, Chengsheng Ni, "Demonstration of high performance in a perovskite oxide supported solid oxide fuel cell based on la and Ca co-doped SrTiO3," *J. Mater. Chem. A*, vol. 4, no. 30, pp. 11708–11718, 2016, doi: 10.1039/c6ta04074h.

[302] M. D. Gross, J. M. Vohs, and R. J. Gorte, "Recent progress in SOFC anodes for direct utilization of hydrocarbons," *J. Mater. Chem.*, 2007, doi: 10.1039/b702633a.

[303] J. Wan, J. H. Zhu, and J. B. Goodenough, "La0.75Sr0.25Cr0.5Mn0.5O3-δ + Cu composite anode running on H2 and CH4 fuels," *Solid State Ionics*, vol. 177, no. 13–14, pp. 1211–1217, 2006, doi: 10.1016/j.ssi.2006.04.046.

[304] M. Watanabe, H. Uchida, and M. Yoshida, "Effect of Ionic Conductivity of Zirconia Electrolytes on the Polarization Behavior of Ceria-Based Anodes in Solid Oxide Fuel Cells," *J. Electrochem. Soc.*, vol. 144, no. 5, pp. 1739–1743, 1997, doi: 10.1149/1.1837671.

[305] A. E. Becerra-Toledo, J. A. Enterkin, D. M. Kienzle, and L. D. Marks, "Water adsorption on SrTiO 3(001): II. Water, water, everywhere," *Surf. Sci.*, vol. 606, no. 9–10, pp. 791–802, 2012, doi: 10.1016/j.susc.2012.01.010.

[306] Y. Yang, C. S. Lin, and W. D. Cheng, "Hydrogen adsorption induced antiferrodistortive distortion and metallization at the (001) surface of SrTiO3," *J. Appl. Phys.*, vol. 118, no. 10, 2015, doi: 10.1063/1.4930042.

[307] I. W. Boateng, R. Tia, E. Adei, N. Y. Dzade, C. R. A. Catlow, and N. H. De Leeuw, "A DFT+U investigation of hydrogen adsorption on the LaFeO3(010) surface," *Phys. Chem. Chem. Phys.*, vol. 19, no. 10, pp. 7399–7409, 2017, doi: 10.1039/c6cp08698e.

[308] A. Nenning, E. Navickas, H. Hutter, and J. Fleig, “Water-Induced Decoupling of Tracer and Electrochemical Oxygen Exchange Kinetics on Mixed Conducting Electrodes,” *J. Phys. Chem. Lett.*, vol. 7, no. 14, pp. 2826–2831, 2016, doi: 10.1021/acs.jpclett.6b00778.

[309] C. T. Campbell, “Metal films and particles on oxide surfaces: Structural, electronic and chemisorptive properties,” *J. Chem. Soc. - Faraday Trans.*, vol. 92, no. 9, pp. 1435–1445, 1996, doi: 10.1039/ft9969201435.

[310] R. Prins, “Hydrogen spillover. Facts and fiction,” *Chem. Rev.*, vol. 112, no. 5, pp. 2714–2738, 2012, doi: 10.1021/cr200346z.

[311] P. Blennow, K. K. Hansen, L. R. Wallenberg, and M. Mogensen, “Electrochemical characterization and redox behavior of Nb-doped SrTiO3,” *Solid State Ionics*, vol. 180, no. 1, pp. 63–70, 2009, doi: 10.1016/j.ssi.2008.10.011.

[312] R. A. De Souza, M. S. Islam, and E. Ivers-Tiffée, “Formation and migration of cation defects in the perovskite oxide LaMnO3,” *J. Mater. Chem.*, vol. 9, no. 7, pp. 1621–1627, 1999, doi: 10.1039/a901512d.

[313] Y. Gao, D. Chen, M. Saccoccio, Z. Lu, and F. Ciucci, “From material design to mechanism study: Nanoscale Ni exsolution on a highly active A-site deficient anode material for solid oxide fuel cells,” *Nano Energy*, vol. 27, pp. 499–508, 2016, doi: 10.1016/j.nanoen.2016.07.013.

[314] H.J.T. Ellingham, “Standard Gibb ’ s Energies of Formation for,” *J. Soc. Chem. Ind.(London)*, vol. 63, no. 125, p. 125, 1944.

[315] B. A. Boukamp, “Derivation of a Distribution Function of Relaxation Times for the (fractal) Finite Length Warburg . Electrochimica Acta Derivation of a Distribution Function of Relaxation Times for the (fractal) Finite Length Warburg .,” *Electrochim. Acta*, vol. 252, no. September 2017, pp. 154–163, 2018, doi: 10.1016/j.electacta.2017.08.154.

[316] Z. Stoynov, “Impedance modelling and data processing: structural and parametrical estimation,” *Electrochim. Acta*, vol. 35, no. 10, pp. 1493–1499,

1990.

[317] B. A. Boukamp and H. J. M. Bouwmeester, “Interpretation of the Gerischer impedance in solid state ionics,” *Solid State Ionics*, vol. 157, no. 1–4, pp. 29–33, 2003, doi: 10.1016/S0167-2738(02)00185-6.

[318] M. Gonzalez-Cuenca, W. Zipprich, B. A. Boukamp, G. Pudmich, and F. Tietz, “Impedance Studies on Chromite- Titanate Porous Electrodes under Reducing Conditions,” no. 3, pp. 256–264, 2001.

[319] N. Hildenbrand, P. Nammensma, D. H. A. Blank, H. J. M. Bouwmeester, and B. A. Boukamp, “Influence of configuration and microstructure on performance of La 2NiO4+δ intermediate-temperature solid oxide fuel cells cathodes,” *J. Power Sources*, vol. 238, pp. 442–453, 2013, doi: 10.1016/j.jpowsour.2013.03.192.

[320] A. M. Hussain, J. V. T. Høgh, W. Zhang, P. Blennow, N. Bonanos, and B. A. Boukamp, “Effective improvement of interface modified strontium titanate based solid oxide fuel cell anodes by infiltration with nano-sized palladium and gadolinium-doped cerium oxide,” *Electrochim. Acta*, vol. 113, pp. 635–643, 2013, doi: 10.1016/j.electacta.2013.09.066.

[321] W. C. Chueh and S. M. Haile, “Electrochemical studies of capacitance in cerium oxide thin films and its relationship to anionic and electronic defect densities,” *Phys. Chem. Chem. Phys.*, vol. 11, no. 37, pp. 8144–8148, 2009, doi: 10.1039/b910903j.

[322] J. Jamnik and J. Maier, “Treatment of the Impedance of Mixed Conductors Equivalent Circuit Model and Explicit Approximate Solutions,” *J. Electrochem. Soc.*, vol. 146, 1999.

[323] M. Casarin and V. M. Sglavo, “Effect of the current collector on performance of anode-supported microtubular solid oxide fuel cells,” *J. Fuel Cell Sci. Technol.*, vol. 12, no. 3, 2015, doi: 10.1115/1.4029875.

[324] H. Zeng, K. Nowicki, J. T. S. Irvine, Y. Shia, and N. Cai, “Fabrication and Characterization of a Small Tubular Solid Oxide Fuel Cell with the La0.43Ca0.37Ni0.06Ti0.94O3-γ Anode,” *ECS Trans.*, vol. 91, no. 1, pp. 447–

456, 2019, doi: 10.1111/j.1744-7402.2007.02127.x.

[325] S. P. Jiang, “A review of wet impregnation - An alternative method for the fabrication of high performance and nano-structured electrodes of solid oxide fuel cells,” *Mater. Sci. Eng. A*, vol. 418, no. 1–2, pp. 199–210, 2006, doi: 10.1016/j.msea.2005.11.052.

[326] W. Bujalski, C. M. Dikwal, and K. Kendall, “Cycling of three solid oxide fuel cell types,” *J. Power Sources*, 2007, doi: 10.1016/j.jpowsour.2007.01.029.

[327] K. Kendall, C. M. Dikwal, and W. Bujalski, “Comparative Analysis of Thermal and Redox Cycling for Microtubular SOFCs,” 2007, doi: 10.1149/1.2729257.

[328] D. Sarantaridis and A. Atkinson, “Redox cycling of Ni-based solid oxide fuel cell anodes: A review,” 2007, doi: 10.1002/fuce.200600028.

[329] M. Pihlatie, T. Ramos, and A. Kaiser, “Testing and improving the redox stability of Ni-based solid oxide fuel cells,” *J. Power Sources*, vol. 193, no. 1, pp. 322–330, 2009, doi: 10.1016/j.jpowsour.2008.11.140.

[330] R. U. Atangulov and I. V. Murygin, “Gas electrode impedance with slow adsorption and surface diffusion,” *Solid State Ionics*, vol. 67, pp. 9–15, 1993.

[331] B. A. Boukamp, M. Verbraeken, D. H. A. Blank, and P. Holtappels, “SOFC-anodes, proof for a finite-length type Gerischer impedance?,” *Solid State Ionics*, vol. 177, no. 26-32 SPEC. ISS., pp. 2539–2541, 2006, doi: 10.1016/j.ssi.2006.03.002.

[332] Y. Lu, C. Kreller, and S. B. Adler, “Measurement and Modeling of the Impedance Characteristics of Porous La[1−x]Sr[x]CoO[3−δ] Electrodes,” *J. Electrochem. Soc.*, vol. 156, no. 4, p. B513, 2009, doi: 10.1149/1.3079337.

[333] A. Schmid, G. M. Rupp, and J. Fleig, “How to Get Mechanistic Information from Partial Pressure-Dependent Current-Voltage Measurements of Oxygen Exchange on Mixed Conducting Electrodes,” *Chem. Mater.*, vol. 30, no. 13, pp. 4242–4252, 2018, doi: 10.1021/acs.chemmater.8b00597.

[334] B. A. Boukamp, “Fourier transform distribution function of relaxation times;

application and limitations," *Electrochim. Acta*, vol. 154, pp. 35–46, 2015, doi: 10.1016/j.electacta.2014.12.059.